



**University of Kerbala**  
**College of Science**  
**Department of Physics**

**Synthesis of SnO<sub>2</sub>/ CuO - rGO Nanostructures and  
Characterization of Their Gas Sensing Performance**

**A Thesis**

**Submitted to the College of Science of the University of Kerbala in  
Partial Fulfillment of the Requirements for the Degree of Doctor of  
Philosophy in Physics**

**By**

**Inam Abed Hammod**

**B.Sc. 2011**

**M.Sc. 2015**

**Supervised by**

**Prof. Dr. Khawla J. Tahir**

**Prof. Dr. Noor J. Ridha**

**2024 A.D/ September**

**1446 A.H/ Rabi Al-Awwal**

بِسْمِ اللَّهِ الرَّحْمَنِ الرَّحِيمِ

أَقْرَأْ بِاسْمِ رَبِّكَ الَّذِي خَلَقَ (١) خَلَقَ  
الْإِنْسَانَ مِنْ عَلَقٍ (٢) أَقْرَأْ وَرَبُّكَ  
الْأَكْرَمُ (٣) الَّذِي عَلَّمَ بِالْقَلَمِ (٤) عَلَّمَ  
الْإِنْسَانَ مَا لَمْ يَعْلَمْ (٥)

صدق الله العلي العظيم

سورة العلق (الاية ١-٥)

## ***Dedication...***

*I dedicate this work to the Lord, God. All that I have, all that I am, and all that I do is because of and for you.*

*To my mother and family who I love deeply with all my heart.*

*To my friends those who supported me with their love kindness, attention and encouragement.*

## Supervisor Certificate

We certify that the thesis entitled “**Synthesis of SnO<sub>2</sub>/CuO-rGO Nanostructures and Characterization of Their Gas Sensing Performance**” was prepared under our supervision by (**Inam Abed Hammod**) at the College of the Science/ University of Kerbala as a partial fulfilment of the requirements for the degree of Doctor of Philosophy of Science in Physics.

Signature: 

Name: Prof. Dr. Khawla J. Tahir

Title: Professor

Date: 15/10/2024

Signature: 

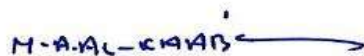
Name: Prof. Dr. Noor J. Ridha

Title: Professor

Date: 15/10/2024

In view of the available recommendations, I forward this thesis for debate by the examining committee.

Signature:



Name: Assist. Prof. Dr. Mohammed Abdulhussain AL-Kaabi

Title: Assistant Professor

Head of Physics Department, College of Science, University of Kerbala

Date: 17/10/2024

## Examination Committee Certification

We certify that we have read this thesis, entitled “Synthesis of SnO<sub>2</sub>/CuO - rGO Nanostructures and Characterization of their Gas Sensing Performance” and as an examining committee, examined the student “Inam Abed Hammod” on its contents and that in our opinion it is adequate for the partial fulfillment of the requirements for the degree of Ph.D. of Science in Physics.

Signature: 

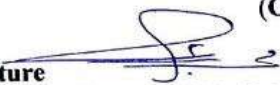
Name: **Dr. Ahmed M. Abdul-Lettif**

Title: Professor

Address: University of Kerbala, College of Science, Department of Physics.

Date: 7/10/2024

(Chairman)

Signature: 

Name: **Dr. Mohammed A. Kadhim**

Title: Professor

Address: University of Kerbala, College of Science, Department of Physics.

Date: 7/10/2024

(Member)

Signature: 

Name: **Dr. Ahmed K. Al-Kadumi**

Title: Professor

Address: University of Kerbala, College of Education for Pure Sciences.

Date: 7/10/2024

(Member)

Signature: 

Name: **Dr. Khawla J. Tahir**

Title: Professor

Address: : University of Kerbala, College of Science, Department of Physics.

Date: 7/10/2024

(Member & Supervisor)

Signature: 

Name: **Dr. Maysoon F. Alias**

Title: Professor

Address: University of Baghdad, College of Science, Department of Physics.

Date: / /

(Member)

Signature: 

Name: **Dr. Ammar S. Hameed**

Title: Assist Professor

Address: University of Kerbala, College of Science, Department of Physics.

Date: 7/10/2024

(Member)

Signature: 

Name: **Dr. Noor J. Ridha**

Title: Professor

Address: University of Kerbala, College of Science, Department of Physics.

Date: 7/10/2024

(Member & Supervisor)

Signature: 

Name: **Dr. Hassan Jameel Jawad AL-Fatlawy**

Title: Professor

Address: **Dean of the College of Science, University of Kerbala**

Date: / /

## *Acknowledgement*

*The first and deepest gratitude goes to Allah for his uncountable blessings, Lord of the whole creation and peace is upon his messenger Mohammad.*

*Firstly, I would like to express my sincere and great appreciation to my supervisors Prof. Dr. Khawla J. Tahir and Prof. Dr. Noor J. Ridha for suggesting this project, appreciable directions, help and support throughout the work.*

*I would like to thank the Head and the staff of Physics Department and the Dean of the College of Science for their support to perform this work.*

*My full thanks to all friends for their support and encouragement.*

*Finally, I am grateful to my lovely family, for their support and patience during my study.*

*To anyone who helped me in one way or another, and who contributed in making this thesis possible particularly.*

***Inam***

## Abstract

In this work SnO<sub>2</sub> / CuO- rGO nanostructures have been prepared as gas sensor using different techniques. The rGO, and CuO nanostructures were prepared by hydrothermal method then deposited on glass substrate utilizing dip coating technique. The third layer of SnO<sub>2</sub> was deposited on the thin film by pulsed laser deposition technique. The investigation of weight percentage of GO and annealing temperatures on the CuO-rGO nanocomposites were studied.

XRD results demonstrate that the reduction of GO has been done completely at 200 °C as preparation temperatures. Weak diffraction peaks related to rGO were observed in the CuO-rGO samples. The main diffraction peaks related to rGO, CuO, and SnO<sub>2</sub> appeared in the three layers thin film. The results of TGA analysis showed that the rGO samples were more stable than GO and the stability of CuO-rGO nanocomposites which decreasing with increasing the amount of GO while the CuO sample showed higher stability. FTIR spectra for GO, rGO, CuO, SnO<sub>2</sub>, CuO-rGO samples showed many peaks corresponding to O-H, C-H, C=C, C=O=C aromatic, C-C, CO-H, C-H and Cu-O, Sn-O bonds. A slight decrease in the peak intensity has been noted in the CuO-rGO samples.

FESEM and TEM results illustrated that the GO displays overlapped folded stoked layers but rGO appears in a plate-like structure with curved textures with more pores. CuO samples exhibited a rod shape. CuO-rGO samples showed a rod and spherical like shape depending on the amount of GO in the nanocomposites. SnO<sub>2</sub> appears in a spherical-like shape.

The EDS spectra of GO and rGO samples indicated that the atomic ratio of O:C in GO decreased as a result of the reduction of GO. The EDX characterization of the CuO samples revealed the presence of copper and oxygen. The EDX analysis of CuO- rGO samples showed that Cu, O, and C are the main elements for samples, and no other impurities. AFM results showed that the roughness of annealed GO thin film reduced after reduction but the surface roughness of annealed CuO thin film increased after increasing the preparation temperatures. High surface roughness was observed for annealed CuO -rGO thin films which were prepared at 200 °C.

The BET results demonstrated an increased in the surface area of GO after reduction but CuO samples showed low surface area with high pore diameter. CuO- rGO samples exhibited intermediate surface area with high pore diameter compared to CuO. All samples showed a direct band gap and UV-visible spectroscopy revealed a reduction in the energy gap of the CuO-rGO and a slight decrease was observing for the SnO<sub>2</sub>/CuO-rGO. I-V characteristics reveals a Schottky contact for all samples.

Gas sensor measurements showed that the CuO sensors were least sensitive to NH<sub>3</sub> gas, whereas rGO sensor shows relatively high sensitivity and the SnO<sub>2</sub>/rGO sensor has the highest sensitivity. The SnO<sub>2</sub>/ CuO- rGO, and SnO<sub>2</sub>/CuO, SnO<sub>2</sub>/rGO sensors were the most selective to H<sub>2</sub>S gas, whereas the SnO<sub>2</sub>/rGO sensor has the highest sensitivity. The best sensor toward both gases was SnO<sub>2</sub>/CuO- rGO which was improved after adding rGO, and it responded more quickly than the other samples.



# Contents

Acknowledgement.....	خطأ! الإشارة المرجعية غير معروفة.
Abstract.....	v
List of Tables .....	xii
List of Figures.....	xiv
List of Symbols .....	xix
List of abbreviations .....	xx
<b>Chapter One: Introduction.....</b>	<b>1</b>
1.1 Introduction.....	2
1.2 Literature Reviews.....	3
1.3 Aims of Study .....	9
<b>Chapter Two: Theoretical Part .....</b>	<b>10</b>
2.1 Metal Oxides Semiconductors .....	11
2.2 Tin Oxide (SnO <sub>2</sub> ) .....	12
2.3 Copper Oxide (CuO).....	13
2.4 Graphene Oxide (GO) and Reduced Graphene Oxide (rGO).....	14
2.5.1 Chemical Methods .....	18
2.5.2 Physical Methods .....	19
2.6 Crystallite Structure Determination of Nanomaterial .....	21
2.7 Optical Properties of Semiconductors .....	23
2.8 Applications of MOSs.....	25
2.9 Gas Sensors.....	26
2.10 Mechanism of MOSs Gas Sensor.....	27
2.11 Sensor Performance Toward Reducing Gases .....	31
2.11.1 Hydrogen Sulfide (H <sub>2</sub> S) Gas .....	31
2.11.2 Ammonia (NH <sub>3</sub> ) Gas .....	34
2.12 MOSs Heterojunctions .....	36
2.12.1 An Isotype Heterojunctions (p-n/ n-p).....	36
2.12.2 Isotype Homojunctions (n-n and p-p) .....	37
2.13 Characterization of Gas Sensor.....	38
2.13.1 Sensitivity .....	38
2.13.2 Selectivity .....	39

2.13.3 Stability .....	39
2.13.4 Response and Recovery Time .....	40
2.13.6 Operation Temperature .....	41
<b>Chapter Three: Experimental Work</b> .....	<b>42</b>
3.1 Introduction.....	43
3.2 Preparation of rGO.....	43
3.3 Preparation of CuO .....	45
3.4 Preparation of CuO- rGO Nanocomposites .....	45
3.5 Preparation of Substrates.....	46
3.6 Deposition of rGO, CuO, CuO-rGO on Glass Substrates.....	47
3.7 Compression of SnO <sub>2</sub> Powder.....	48
3.8 Deposition of SnO <sub>2</sub> by PLD.....	49
3.9 Samples Characterization .....	50
3.9.1 Energy Dispersive X-Ray Spectroscopy (EDX) .....	50
3.9.2 Fourier Transform Infrared Spectroscopy (FTIR) .....	51
3.9.3 X-Ray Diffraction (XRD) .....	52
3.9.4 Field Emission Scanning Electron Microscope (FESEM).....	52
3.9.5 Transmission Electron Microscopy (TEM) .....	53
3.9.6 Brunauer-Emmett-Teller (BET).....	53
3.9.7 Atomic Force Microscope (AFM).....	53
3.9.8 Film Thickness Measurements .....	54
3.9.9 Thermogravimetric Analysis (TGA) .....	54
3.9.10 Ultraviolet-Visible Spectroscopy (UV).....	55
3.11 Gas sensor .....	55
3.11.1 Interdigitated Electrodes (IDE) Deposition.....	55
3.11.2 Gas Sensor System Design.....	56
3.11.3 Procedure of Gas Sensing Measurement Testing .....	57
<b>Chapter Four: Results and Discussion</b> .....	<b>59</b>
4.1 Introduction.....	60
4.2 Energy Dispersive X-Ray Spectroscopy Analysis .....	61
4.2.1 GO and rGO Samples.....	61
4.2.2 CuO Samples .....	61

<b>4.2.3 CuO- rGO Samples.....</b>	<b>63</b>
<b>4.3 X-Ray Diffraction.....</b>	<b>65</b>
<b>4.3.1 Samples Prepared at 100 °C.....</b>	<b>66</b>
4.3.1.1 GO and rGO .....	66
4.3.1. 2 CuO .....	67
4.3.1. 3 CuO-rGO .....	69
<b>4.3.2 Samples Prepared at 200 °C.....</b>	<b>73</b>
4.3.2.1 rGO.....	73
4.3.2.2 CuO .....	74
4.3.2.3 CuO-rGO .....	76
4.3.2.4 SnO <sub>2</sub> /CuO - rGO.....	78
<b>4.4 Thermogravimetric Analysis (TGA).....</b>	<b>80</b>
<b>4.4.1 GO and rGO.....</b>	<b>80</b>
<b>4.4.2 CuO .....</b>	<b>81</b>
<b>4.4.3 CuO-rGO.....</b>	<b>83</b>
<b>4.5 FTIR- Spectroscopy .....</b>	<b>84</b>
<b>4.5.1 GO and rGO .....</b>	<b>84</b>
<b>4.5. 2 CuO .....</b>	<b>86</b>
<b>4.5.3 CuO-rGO.....</b>	<b>87</b>
<b>4.5.4 SnO<sub>2</sub>.....</b>	<b>88</b>
<b>4.6 FESEM Characterization.....</b>	<b>89</b>
<b>4.6.1 Samples Prepared at 100 °C.....</b>	<b>89</b>
4.6.1.1 GO and rGO .....	89
4.6.1.2 CuO .....	91
4.6.1.3 CuO- rGO .....	91
<b>4.6.2 Samples Prepared at 200 °C.....</b>	<b>96</b>
4.6.2.1 rGO.....	96
4.6.2.2 CuO .....	96
4.6.2.3 CuO -rGO .....	97
4.6.2.4 SnO <sub>2</sub> .....	99
<b>4.7 TEM Analysis .....</b>	<b>99</b>
<b>4.7.1 rGO.....</b>	<b>99</b>
<b>4.7.2 CuO .....</b>	<b>99</b>

<b>4.7.3 CuO- rGO .....</b>	<b>100</b>
<b>4.8 AFM Analysis .....</b>	<b>102</b>
<b>4.8.1 Samples Prepared at 100 °C.....</b>	<b>102</b>
4.8.1.1 GO and rGO .....	102
4.8.1.2 CuO .....	103
4.8.1.3 CuO- rGO .....	104
<b>4.8.2 Samples Prepared at 200 °C.....</b>	<b>106</b>
4.8.2.1 rGO.....	106
4.8.2.2 CuO .....	107
4.8.2.3 CuO- rGO .....	108
<b>4.9 BET analysis .....</b>	<b>111</b>
<b>4.9.1 Samples Prepared at 100 °C.....</b>	<b>111</b>
4.9.1.1 rGO.....	111
4.9.1.2 CuO .....	112
4.9.1.3 CuO- rGO .....	113
<b>4.9.2 Samples Prepared at 200 °C.....</b>	<b>115</b>
4.9.2.1 rGO.....	115
4.9.2.2 CuO .....	115
4.9.2.3 CuO- rGO .....	117
<b>4.10 UV-Visible Spectroscopy for Thin Films .....</b>	<b>119</b>
<b>4.10.1 UV-Visible Properties .....</b>	<b>119</b>
4.10.1.1 GO and rGO Thin Films.....	119
4.10.1.2 CuO and SnO <sub>2</sub> Thin Films .....	119
4.10.1.3 CuO- rGO and SnO <sub>2</sub> /CuO- rGO Thin Films .....	121
<b>4.10.2 Band gap Energy and Tauc Plot.....</b>	<b>121</b>
<b>4.11 Current-Voltage (I-V) Characteristics.....</b>	<b>123</b>
<b>4.12 Gas Sensor Measurements .....</b>	<b>124</b>
<b>4.12.1 NH<sub>3</sub> Sensor Measurement .....</b>	<b>125</b>
4.12.1.1 GO and rGO Sensors Measurements.....	125
4.12.1.2 CuO Sensors Measurements.....	129
4.12.1.3 CuO- rGO Sensors Measurements .....	131
4.12.1.4 SnO <sub>2</sub> / CuO Sensors Measurements .....	134
4.12.1.5 SnO <sub>2</sub> / rGO Sensors Measurements.....	136

4.12.1.6 SnO <sub>2</sub> / CuO- rGO Sensors Measurements .....	138
<b>4.12.2 H<sub>2</sub>S Gas Sensor Measurements.....</b>	<b>141</b>
4.12.2.1 SnO <sub>2</sub> / rGO Sensor Measurements.....	141
4.12.2.2 SnO <sub>2</sub> / CuO Sensor Measurements .....	143
4.12.2.3 SnO <sub>2</sub> / CuO- rGO Sensors Measurements .....	145
<b>4.13 Conclusions .....</b>	<b>148</b>
<b>4.14 Suggestions for Future Work.....</b>	<b>150</b>
<b>References .....</b>	<b>151</b>

## List of Tables

Table	Page
Table (2.1): Gas type effect on the sensor resistance for (n-type) and (p- type) materials	31
Table (3.1): Chemical materials	43
Table (4.1) Samples prepared hydrothermally with different parameters.	60
Table (4.2): EDX spectra of CuO- rGO samples prepared at 100 °C and 200 °C	65
Table (4.3): XRD data of rGO <sub>100</sub> before and after annealing	67
Table (4.4): XRD data of CuO <sub>100</sub> before and after annealing	69
Table (4.5): XRD data of CuO-rGO samples before and after annealing	72
Table (4.6): XRD data of rGO <sub>200</sub> before and after annealing	74
Table (4.7): XRD data of CuO <sub>200</sub> before and after annealing	75
Table (4.8): XRD data of CuO-rGO nanocomposite after annealing	78
Table (4.9): XRD data of SnO <sub>2</sub> / CuO- rGO nanostructure	80
Table (4.10): AFM data of GO and rGO <sub>100</sub> samples	103
Table (4.11): AFM data of CuO- rGO thin films prepared at 100 °C and annealed at 400°C	106
Table (4.12): AFM data of CuO- rGO thin films prepared at 200 °C and annealed at 400°C	110
Table (4.13): Thin film thickness measurements for different samples	110
Table (4.14): BET results of GO and rGO <sub>100</sub>	112
Table (4.15): BET results of CuO-rGO nanocomposites prepared at 100 °C	115
Table (4.16): BET results of CuO-rGO nanocomposites prepared at 200 °C	118
Table (4.17): GO and rGO gas sensor parameters with different operating temperatures	129
Table (4.18): CuO gas sensor parameters with different operating temperatures	130
Table (4.19): CuO-rGO gas sensor parameters with different operating temperatures	134
Table (4.20): SnO <sub>2</sub> / CuO gas sensor parameters with different operating temperatures	136
Table (4.21): SnO <sub>2</sub> / rGO gas sensor parameters with different operating temperatures	138
Table (4.22): SnO <sub>2</sub> / CuO-rGO gas sensors parameters with different operating	141

temperatures	
Table (4.23): SnO <sub>2</sub> / rGO gas sensors parameters with different operating temperatures	143
Table (4.24): SnO <sub>2</sub> / CuO gas sensors parameters with different operating temperatures	145
Table (4.25): SnO <sub>2</sub> / CuO-rGO gas sensors parameters with different operating temperatures	148

## List of Figures

Figure	Page
Figure (2.1): Schematic illustration of the rutile - structure of SnO <sub>2</sub>	13
Figure (2.2): CuO Crystal-structure	14
Figure (2.3): Conversion of graphene into GO and rGO	16
Figure (2.4): Schematic representation for the fabrication of nanomaterials	18
Figure (2.5): Basic principle of a typical XRD and Bragg's law	22
Figure (2.6): The optical transitions (a) allowed direct, (b) forbidden direct, (c) allowed indirect, (d) forbidden indirect	25
Figure (2.7): Mechanism of MOS gas sensor	29
Figure (2.8): Formation of electronic core – shell structures in (a) n-type, (b) p-type oxide semiconductors	30
Figure (2.9): The response curve of the MOS gas sensor	41
Figure (3.1): Schematic representation of the experimental work	44
Figure (3.2): Schematic diagram of the preparation process of rGO/CuO	46
Figure (3.3): (a) Dip-coating system, (b) the basic process of dip-coating	48
Figure (3.4): Electric furnace	48
Figure (3.5): The piston of powder compression: (a) piston, (b) mold, (c) powder pellets	49
Figure (3.6): Pulsed laser deposition system	50
Figure (3.7): (a) Sputtering system, (b) mask dimensions	56
Figure (3.8): Gas sensor system	58
Figure (3.9): Schematic diagram for gas sensor system	58
Figure (4.1): EDX spectrum and elemental mapping of (a) GO, (b) rGO <sub>100</sub> , and (c) rGO <sub>200</sub>	62
Figure (4.2): EDX spectrum of (a) CuO <sub>100</sub> , (b) CuO <sub>200</sub>	63
Figure (4.3): EDX spectrum of (a) S1, (b) S2, (c) S3, (d) S4, (e) S5, and (f) S6	65
Figure (4.4): XRD results of rGO <sub>200</sub> before and after annealing	67
Figure (4.5): XRD results of CuO <sub>200</sub> before and after annealing	68
Figure (4.6): XRD of CuO-rGO nanocomposites prepared at 100 °C before and after annealing at 400 °C	71



Figure (4.7): XRD results of rGO <sub>200</sub> before and after annealing at 400 °C	73
Figure (4.8): XRD results of CuO <sub>200</sub> before and after annealing at 400 °C	75
Figure (4.9): XRD results of CuO-rGO samples prepared at 200 °C after annealing at 400 °C	77
Figure (4.10): XRD results of SnO <sub>2</sub> /CuO - rGO nanostructure	79
Figure (4.11): TGA curves of GO, rGO <sub>100</sub> , and rGO <sub>200</sub>	82
Figure (4.12): TGA curves of CuO <sub>100</sub> and CuO <sub>200</sub>	82
Figure (4.13): TGA curves of CuO -rGO prepared at 100 °C: (a) before annealing, (b) after annealing at 400 °C	84
Figure (4.14): FTIR analysis for (a) GO, (b) rGO <sub>100</sub> , and (c) rGO <sub>200</sub> after annealing at 400 °C	86
Figure (4.15): FTIR analysis of CuO annealed at 400 °C	87
Figure (4.16): FTIR analysis of CuO-rGO nanocomposites annealed at 400 °C; (a) S4, and (b) S5	88
Figure (4.17): FTIR analysis of SnO <sub>2</sub>	89
Figure (4.18): High-resolution FESEM images of (a) GO, (b) rGO <sub>100</sub> before annealing, (c) rGO <sub>100</sub> after annealing at 400 °C	91
Figure (4.19): High-resolution FESEM images of CuO <sub>100</sub> , (a) before annealing, (b) after annealing at 400 °C	92
Figure (4.20): High-resolution FESEM images of S1, (a) before annealing, (b) after annealing at 400 °C	93
Figure (4.21): High-resolution FESEM images of CuO <sub>200</sub> after annealing	94
Figure (4.22): High-resolution FESEM images of S3, (a,) before annealing, (b) after annealing at 400 °C	95
Figure (4.23): High-resolution FESEM images of rGO <sub>200</sub> after annealing at 400 °C	96
Figure (4.24): High-resolution FESEM images of CuO <sub>200</sub> after annealing at 400 °C	97
Figure (4.25): High-resolution FESEM images of CuO- rGO after annealing at 400 °C; (a) S4, (b) S5, and (c) S6	98
Figure (4.26): SEM images of annealed SnO <sub>2</sub>	99
Figure (4.27): TEM images of rGO <sub>200</sub> annealed at 400 °C with different magnifications	100
Figure (4.28): TEM images of CuO <sub>200</sub> annealed at 400 °C with different magnifications	100
Figure (4.29): TEM images of CuO- rGO samples prepared at 200 °C and annealed at 400 °C with different magnifications	101

Figure (4.30): 3-D and 2-D images of AFM results annealed at 400 °C: (a) GO, and (b) rGO <sub>100</sub>	103
Figure (4.31): 3-D and 2-D images of AFM results of CuO <sub>100</sub> annealed at 400 °C	104
Figure (4.33): 3-D and 2-D image of AFM results of rGO <sub>200</sub> and annealed at 400 °C	107
Figure (4.34): 3-D and 2-D images of AFM results of CuO <sub>200</sub> and annealed at 400 °C	108
Figure (4.34): 3-D and 2-D images of AFM results of CuO <sub>200</sub>	113
Figure (4.35): 3-D and 2-D images of AFM results of: (a) S4, (b) S5, and (c) S6	110
Figure (4.36): N <sub>2</sub> - adsorption-desorption isotherms of (a) GO and (b) rGO <sub>100</sub> at 77 K. The inset shows the pore size distributions calculated using the BJH method	111
Figure (4.37): N <sub>2</sub> - adsorption-desorption isotherms of CuO <sub>100</sub> at 77 K. The inset shows the pore size distributions of CuO <sub>100</sub> calculated using the BJH method	113
Figure (4.38): N <sub>2</sub> - adsorption-desorption isotherms of (a) S1, (b) S2, (c) S3 at 77 K, and (d) the pore size distributions of S1, S2, S3 calculated using the BJH method	114
Figure (4.39): N <sub>2</sub> - adsorption-desorption isotherms of rGO <sub>200</sub> at 77 K. The inset shows the pore size distributions of rGO <sub>200</sub> calculated using the BJH method	116
Figure (4.40): N <sub>2</sub> - adsorption-desorption isotherms of CuO <sub>200</sub> at 77 K. The inset shows the pore size distributions of CuO <sub>200</sub> calculated using the BJH method	116
Figure (4.41): N <sub>2</sub> - adsorption-desorption isotherms of (a) S4, (b) S5, (c) S6 at 77 K, (d) the pore size distributions of samples calculated using the BJH method	118
Figure (4.42): UV-visible Spectra of the GO and rGO thin films	120
Figure (4.43): (a) UV-visible Spectra of the CuO thin films, (b) UV-visible Spectra of the SnO <sub>2</sub> thin films	120
Figure (4.44): UV-visible Spectra of: (a) CuO- rGO and (b) SnO <sub>2</sub> / CuO- rGO thin films	121
Figure (4.45): Tauc plots of the thin films	123
Figure (4.46): Current-Voltage characteristics of the thin films	124
Figure (4.47): Dynamic response of GO toward 100 ppm NH <sub>3</sub> gas at different working temperatures; (a) room temperature, (b) 100 °C, (c) 200 °C	125
Figure (4.48): (a) NH <sub>3</sub> gas sensitivity versus operating temperature for GO, and (b) response and recovery time versus operating temperatures	126

Figure (4.49): Dynamic response of rGO <sub>100</sub> toward 100 ppm NH <sub>3</sub> gas at different working temperatures; (a) room temperature, (b) 100 °C, (c) 200 °C	126
Figure (4.50): (a) NH <sub>3</sub> gas sensitivity versus operating temperature for rGO <sub>100</sub> , and (b) response and recovery time versus operating temperatures.	127
Figure (4.51): Dynamic response of rGO <sub>200</sub> toward 100 ppm NH <sub>3</sub> gas at different working temperatures; (a) room temperature, (b) 100 °C, (c) 200 °C	127
Figure (4.52): (a) NH <sub>3</sub> gas sensitivity versus operating temperature for rGO <sub>200</sub> , and (b) response and recovery time versus operating temperatures	128
Figure (4.53): Dynamic response of CuO toward 100 ppm NH <sub>3</sub> gas at different working temperatures; (a) room temperature, (b) 100 °C, (c) 200 °C	129
Figure (4.54): (a) NH <sub>3</sub> gas sensitivity versus operating temperature for CuO, and (b) response and recovery time versus operating temperatures	130
Figure (4.55): Dynamic response of S1 toward 100 ppm NH <sub>3</sub> gas at different working temperature; (a) room temperatures, (b) 100 °C, (c) 200 °C	132
Figure (4.56): (a) NH <sub>3</sub> gas sensitivity versus operating temperature for S1, and (b) response and recovery time versus operating temperatures	132
Figure (4.57): Dynamic response of S2 toward 100 ppm NH <sub>3</sub> gas at different working temperature; (a) room temperatures, (b) 100 °C, (c) 200 °C	132
Figure (4.58): (a) NH <sub>3</sub> gas sensitivity versus operating temperatures for S2, and (b) response and recovery time versus operating temperatures.	133
Figure (4.59): Dynamic response of S2 toward 100 ppm NH <sub>3</sub> gas at different working temperature; (a) room temperatures, (b) 100 °C, (c) 200 °C	133
Figure (4.60): (a) NH <sub>3</sub> gas sensitivity versus operating temperature for S3, and (b) response and recovery time versus operating temperature	133
Figure (4.61): Dynamic response of SnO <sub>2</sub> /CuO toward 47 ppm NH <sub>3</sub> gas at different working temperature; (a) 150 °C, (b) 200 °C, (c) 250 °C	135
Figure (4.62): (a) NH <sub>3</sub> gas sensitivity versus operating temperatures for SnO <sub>2</sub> /CuO, and (b) response and recovery time versus operating temperature	135
Figure (4.63): Dynamic response of SnO <sub>2</sub> /rGO toward 47 ppm NH <sub>3</sub> gas at different working temperature; (a) 150 °C, (b) 200 °C, (c) 250 °C	137
Figure (4.64): (a) NH <sub>3</sub> gas sensitivity versus operating temperatures for SnO <sub>2</sub> /rGO, and (b) response and recovery time versus operating temperature	137

Figure (4.65): Dynamic response of SnO <sub>2</sub> - S4 toward 47 ppm NH <sub>3</sub> gas at different working temperature; (a) 150 °C, (b) 200 °C, (c) 250 °C	139
Figure (4.66): (a) NH <sub>3</sub> gas sensitivity versus operating temperatures for SnO <sub>2</sub> -S4, and (b) response and recovery time versus operating temperature	140
Figure (4.67): Dynamic response of SnO <sub>2</sub> - S5 toward 47 ppm NH <sub>3</sub> gas at different working temperature; (a) 150 °C, (b) 200 °C, (c) 250 °C	140
Figure (4.68): (a) NH <sub>3</sub> gas sensitivity versus operating temperatures for SnO <sub>2</sub> -S5, and (b) response and recovery time versus operating temperature.	140
Figure (4.69): Dynamic response of SnO <sub>2</sub> /rGO toward 50 ppm H <sub>2</sub> S gas at different working temperature; (a) 150 °C, (b) 200 °C, (c) 250 °C	142
Figure (4.70): (a) H <sub>2</sub> S gas sensitivity versus operating temperatures for SnO <sub>2</sub> /rGO, and (b) response and recovery time versus operating temperatures	143
Figure (4.71): Dynamic response of SnO <sub>2</sub> /CuO toward 50 ppm H <sub>2</sub> S gas at different working temperature; (a) 200 °C, and (b) 250 °C	144
Figure (4.72): (a) H <sub>2</sub> S gas sensitivity versus operating temperatures for SnO <sub>2</sub> /CuO, and (b) response and recovery time versus operating temperatures.	145
Figure (4.73): Dynamic response of SnO <sub>2</sub> - S4 toward 50 ppm H <sub>2</sub> S gas at different working temperature; (a) 150 °C, (b) 200 °C and (c) 250 °C	147
Figure (4.74): (a) H <sub>2</sub> S gas sensitivity versus operating temperatures for SnO <sub>2</sub> -S4, and (b) response and recovery time versus operating temperatures	147
Figure (4.75): Dynamic response of SnO <sub>2</sub> - S5 toward 50 ppm H <sub>2</sub> S gas at different working temperature; (a) 150 °C, (b) 200 °C and (c) 250 °C	147
Figure (4.76): (a) H <sub>2</sub> S gas sensitivity versus operating temperatures for SnO <sub>2</sub> -S5, and (b) response and recovery time versus operating temperatures	148

## List of Symbols

$\lambda$	Wavelength
$n$	Refraction index
$\theta$	Bragg's angle
$D$	Crystallite size
$\beta$	Full width of the half maximum peak
$E_g$	Energy gap
$h\nu$	Incident photon energy
$I_0$	Incident photon intensity
$I$	Transmitted photon intensity
$\alpha$	Absorption coefficient
$t$	Thickness of the material
$k$	Wave number
$S$	Sensitivity
$R_a$	Resistance in air
$R_g$	Resistance in target gas
$\tau_{90}$	Sensor response time

## List of abbreviations

AFM	Atomic force microscopy
BET	Brunauer-Emmett-Teller
BJH	Barrent-Joyner-Halenda
CBM	Conduction band minimum
CVD	Chemical vapor deposition
EDX	Energy Dispersive X-Ray Spectroscopy
FESEM	Field Emission Scanning Electron Microscope
FTIR	Fourier Transform Infrared Spectroscopy
FWHM	Full width of the half maximum peak
HR-TEM	High resolution- tunneling electron microscopy
IDE	Interdigitated electrode
IDTs	Interdigitated transducers
JCPDS	Joint Committee on Powder Diffraction Standard
$L_D$	Debye length
LIBs	Lithium-ion batteries
MOS	Metal oxide semiconductor
pLD	Pulsed laser deposition
Ppm	Part per million
ppb	Part per billion
QWs	Quantum wires
rf	Radio frequency
SAW	Surface acoustic wave
SBH	Schottky barrier height
SEM	Scanning electron microscopy
SHG	Second Harmonic Generation
TEM	Transmission Electron Microscopy

TGA	Thermogravimetric Analysis
UV	Ultraviolet-Visible Spectroscopy
VBM	Valance band maximum
VOCs	Volatile organic compounds
XPS	X-ray photoelectron spectroscopy
XRD	X-ray diffraction

# **Chapter One**

## **Introduction**



## 1.1 Introduction

It is well known that the atmosphere contains numerous natural and synthetic chemical species, some of which are vital to the survival of organisms while the others are harmful to them [1]. Furthermore, indoor environments contain a multitude of volatile organic compounds (VOCs), including but not limited to methanol ( $\text{CH}_3\text{OH}$ ), benzene ( $\text{C}_6\text{H}_6$ ), acetone ( $\text{CH}_3\text{COCH}_3$ ), ethanol ( $\text{C}_2\text{H}_5\text{OH}$ ), and toluene ( $\text{C}_6\text{H}_5\text{CH}_3$ ), alongside inorganic gases such as carbon dioxide ( $\text{CO}_2$ ), nitrous oxides ( $\text{NO}_x$ ), and carbon monoxide ( $\text{CO}$ ). Recently, advancements in industrial sectors have increased recognition of the potential for hazardous gases to enter the human body by skin absorption or inhalation, subsequently entering the bloodstream or lungs may cause various cellular reactions and potentially give rise to health complications [2].

Hence, the global concern regarding air pollution has significantly increased [3]. It was necessary to design a gadget to effectively monitor air pollution and detect various substances in the surrounding environment. Numerous conventional approaches include the development of detecting devices that utilize auditory signals to alert individuals to the presence of hazardous gases. However, the reliability of these approaches is questionable due to the necessity of obtaining precise real-time measurements of the concentration of the gas being targeted [4, 5]. There is an increasing demand for the development of gas sensors that possess enhanced selectivity and sensitivity to detect contaminants in the environment effectively. These sensors should also exhibit robustness, accuracy, and cost-effectiveness [6, 7].

Gas sensors are categorized based on the sensing material employed in the sensor, which dictates the nature of the reaction between the sensing material and the gas being detected [8] including catalytic sensors [9], electrochemical sensor [10, 11], optical gas sensor [12, 13], infrared sensor [14, 15], acoustic wave gas sensor [16, 17]. The last and most prevalent variety of gas sensor is the metal oxide semiconductor gas sensor (MOS). This sensor is distinguished by its ability to detect various gases (transient organic compounds or inorganic compounds) at low concentrations in the range of part per million (ppm) or part per billion (ppb) [18]. MOSs is based on two functions that define their fundamental principle: first, the chemical reaction that occurs between sensing materials and target gases; second, the conversion of this chemical reaction into electrical signals due to a change in resistance [19].

## 1.2 Literature Reviews

Many researchers have adopted much work in gas sensors and their different applications, especially in protecting the environment from the risk of toxin gases. From this time, many efforts were oriented toward developing semiconductor gas sensors [5]. Here, several studies were listed:

**Verma et al. (2010)** [20] prepared two types of sensors: a SnO<sub>2</sub> film with a thickness of 90 nm loaded with a monolayer of copper oxide (CuO) with a thickness of 10 nm using radio frequency (rf) sputtering and pulsed laser deposition (PLD). The study revealed that the hydrogen sulfide (H<sub>2</sub>S) gas detection limit using a SnO<sub>2</sub> / CuO sensor was significantly improved in both PLD and sputtering techniques. Specifically, the sensor's sensitivity increased from approximately 147 to 2314 in the case of PLD and from around 14 to 211 in the case of sputtering. The increase in adsorbed oxygen

content on the surface of the sensing film at a low operating temperature of 100 °C can be attributed to the heterostructure and morphology of the sensing layer.

**Jundale et al. (2011)** [21] employed a sol-gel and spin-coating technique for coating a nano-film of CuO onto a glass substrate. The process involved the utilization of cupric acetate ( $\text{Cu}(\text{CH}_3\text{COO})_2$ ) as a precursor. The films underwent thermal treatment within the temperature range of 300 to 700 °C to enhance the performance of  $\text{H}_2\text{S}$  gas. The film subjected to a temperature of 700 °C demonstrated a response of around 25.2 when exposed to a 100 ppm gas concentration at a temperature of 200 °C. The CuO film appeared in a monoclinic-crystal structure, which is advantageous for sensing.

**Choi et al. (2012)** [22] reported the synthesis of  $\text{CuO}@ \text{SnO}_2$  nanofibers by utilizing an electrospinning technique for  $\text{H}_2\text{S}$  gas detection. The results demonstrated high response of ( $\sim 1.98 \times 10^4$ ) at 300 °C toward  $\text{H}_2\text{S}$  gas compared with bare  $\text{SnO}_2$  nanofibers with fast response and recovery time of about 1 seconds and 10 seconds, respectively. The formation of p-n heterojunctions between p and n types during the adsorption-desorption process of  $\text{H}_2\text{S}$  gas and the high specific surface area resulting from the one-dimensional nanofibers shape enhances the gas sensing performance.

**Hu et al. (2013)** [23] manufactured highly responsive rGO sensor for  $\text{NH}_3$  gas detection. In this study, GO was reduced chemically using polypyrrole which was dispersed in water and sonication for 1 hour at room temperature. The rGO sensor exhibited a 23% response towards 50 ppb  $\text{NH}_3$  gas, as evidenced by a rapid response time of around 1.4 seconds under ambient conditions. The observed improvement in sensor responsiveness can be

attributed to high surface area and the favorable adsorption of polypyrrole molecules onto the sensing film.

**Kumar and Gupta (2014)** [24] fabricated a pair of sensors using SnO<sub>2</sub> and SnO<sub>2</sub>-CuO thin films by PLD technique to detect H<sub>2</sub>S gas. The deposition process involves pressing powders of SnO<sub>2</sub> and CuO within a mold by applying a pressure of 110 MPa. The pellets of SnO<sub>2</sub> and CuO underwent annealing at 1350 °C and 400 °C, respectively, for 4 hours in a furnace. The targets were ablated using the Nd-YAG laser with a wavelength of 266 nm, operating at a pulse rate of 5 Hz and a fluence of 100 mJ/cm<sup>2</sup> with 310 shots for SnO<sub>2</sub> and 20 shots for CuO. The sensor's response exhibited an increase from  $1.4 \times 10^2$  to  $4.3 \times 10^3$  during 2 seconds after the introduction of CuO. The ability of H<sub>2</sub>S gas to penetrate the nanocomposite at a deeper level can be related to the film's surface shape, characterized by many pores. CuO can engage in sensing by creating a p-n junction between two oxides which prevents the movement of charge carriers and increases the sensor's resistance.

**Katoch et al. (2015)** [25] employed the technique of electrospinning to incorporating CuO/SnO<sub>2</sub> sensor. The sensor responded around 522 when exposed to 10 ppm of H<sub>2</sub>S gas at 300 °C. The response time of the sensor was measured to be one second. It was found that the interaction between CuO and SnO<sub>2</sub> results in the formation of a p-n junction and a transition in the semiconductor phase from CuO to the metallic state CuS which enhance sensitivity.

**Li et al. (2016)** [26] employed a hydrothermal approach to fabricate a porous CuO sensor to detect H<sub>2</sub>S gas at room temperature. The interaction

between CuO and H<sub>2</sub>S characterizes the sensor's performance, resulting in a phase transition from a semiconductor (CuO) to a metallic state (CuS). The sensor exhibited a response value 1.25% and response and recovery times of approximately 234 seconds and 76 seconds, respectively. Notably, the sensor demonstrated favorable selectivity towards H<sub>2</sub>S compared to other gases.

**Sakthivel et al. (2017)** [27] employed hydrothermal synthesis to produce CuO nano-rectangles to develop a room temperature NH<sub>3</sub> sensor. An approximate response of 0.98 was reported for an NH<sub>3</sub> gas concentration of around 100 ppm. The observed response in the sensor can be attributed to the high surface area (29 m<sup>2</sup>/g), which offers a more significant number of sites for the adsorption process. The primary attributes of this sensor are its ability to operate effectively at room temperature and remain unaffected by changes in humidity levels.

**Li et al. (2018)** [28] produced multi- layers sensor of rGO by simple and low-cost thermal reduction at 300 °C for 10 minutes. Thus, GO films with different layers (1, 2, 3, and 4 layers) were prepared. The two - layer sensors responded well to 50 ppm NH<sub>3</sub> gas and had a response time of 24 seconds, followed by one, three, and four- layers. The two - layer sensors have many flaws and adsorption sites. However, 3 and 4 layers generated rGO-sheet agglomeration and inhibited NH<sub>3</sub> adsorption, weakening gas sensor characteristics.

**Yin et al. (2019)** [29] proposed CuO@ rGO nanostructures with the assistance of microwaves under normal conditions. The homogenous suspension was obtained by dissolving copper acetate in GO solution and

stirring for 30 minutes. The CuO@ rGO sensors exhibit a response around 68.5 to H<sub>2</sub>S gas concentrations ranging from (1- 10) ppm within an operational temperature range of 50 to 150 °C. The improvement in the sensitivity of sensors towards low-concentration H<sub>2</sub>S can be attributed to the formation of substantial quantities of p-p heterojunctions and the hierarchical structure of CuO-coated rGO.

**Peng et al. (2020)** [30] used a simple hydrothermal technique to create a CuO sensor at 140 °C. The results showed that the sensor response primarily depended on the concentration of H<sub>2</sub>S gas and the sensor's working temperature. When the working temperature raised to 150 °C, the interaction rate increased, resulting in rapid recovery time. It was found that the response for the 5 ppm H<sub>2</sub>S gas was 10.9 at 150 °C, more significant than the other gases. This demonstrated the H<sub>2</sub>S gas's remarkable selectivity.

**Boroun et al. (2021)** [31] conducted a theoretical investigation utilizing a 3-D wire/shell architecture composed of SnO<sub>2</sub> and CuO to develop a sensor capable of detecting H<sub>2</sub>S gas, employing a (n-p-n) configuration. The primary emphasis of this investigation was directed towards the geometric characteristics of the sensor. The study revealed that rods, wires, and particle arrangement designs exhibited a more excellent response value than alternative configurations. Hence, the 2/ wires (n-p-n) junction responded towards H<sub>2</sub>S gas better than the single CuO and bi-layer designs. Based on the obtained results, it can be observed that the presence of an (n-p-n) junction significantly increases the resistance of the "two-wires" system in an air environment. It was found that the response of the 2/ wires (n -p- n) junction sensor was  $\sim 10^5$  at 10 ppm H<sub>2</sub>S gas at 150 °C, slightly matching with experimental studies.

**Jung et al. (2022)** [32] employed the thermal-evaporation technique to fabricate a CuO film with high porosity to detect H<sub>2</sub>S gas. A Cu source was used in the fabrication of porous Cu films. The films were subjected to annealing treatment in range of (400-700 °C) for 1 hour. The CuO film, which exhibited a porosity of 95.2%, had a response of approximately 2.7 with a recovery time of 514 seconds when exposed to 1.5 ppm of H<sub>2</sub>S gas at 325 °C. The enhanced sensor responses were obtained through many pores in the CuO layer, facilitating the transport of gas molecules into CuO sensor.

**Sun et al. (2022)**[33] fabricated a high response-H<sub>2</sub>S gas sensing by doping Cu with SnO<sub>2</sub>-rGO via a simple solvothermal method at 180 °C for 12 hours. A subsequent annealing procedure was carried out after the synthesis process at 400 °C for 2 hours. The sensor's sensitivity of around 156.7 at 120 °C has been observed for detect 10 ppm H<sub>2</sub>S gas. The observed high sensitivity value can be attributed to a (p-n-p) heterostructure offering numerous adsorption sites and vacancies. Additionally, incorporating Cu contributes to an increased surface area, while the proximity of a small grain size near Debye length (LD) enhances the sensor's performance. Furthermore, utilizing a large pore size facilitates faster response and recovery times for the sensor.

**Chaiyo (2023)** [34] investigated and analyzed the electrical characteristics of SnO<sub>2</sub> gas-sensing materials synthesized by a heating process. The (I-V) characteristics of the SnO<sub>2</sub> nonporous material indicated the presence of ohmic-contact properties. The findings showed that the conductivity increased after elevating the operational temperature to 250 °C. The response of ammonia gas was assessed at varying concentrations, precisely 70 ppm, 80 ppm, and 90 ppm. The corresponding measurements

were reported as 61%, 66%, and 71%, respectively. The sensor demonstrated an acceptable sensitivity towards  $\text{NH}_3$  gas at a concentration of 10 ppm, and this sensitivity was shown to rise proportionally with higher gas concentrations.

### 1.3 Aims of Study

The recent developments in technology and industry lead to further emission of toxic gases such as  $\text{H}_2\text{S}$  and  $\text{NH}_3$  that cause pollution to domestic environments even in a few tens of ppm, which is a hazard to human life. Therefore, highly sensitive and selective gas sensor devices by new preparation methods for practical implementation have been prepared with enhanced characteristics as follows:

- 1- Synthesis of sensing devices (rGO, CuO, CuO-rGO, and  $\text{SnO}_2/\text{CuO-rGO}$ ) by thermal method and pulsed laser deposition.
- 2- Studying the structural and morphological characterization of the prepared nanostructures.
- 3- Characterization of the synthesized sensors and study their sensing performance under reducing gases ( $\text{H}_2\text{S}$  and  $\text{NH}_3$ ).



# **Chapter Two**

## **Theoretical Part**

## 2.1 Metal Oxides Semiconductors

Metal oxide semiconductors (MOSs) represent a class of unique materials due to their electronic charge transport properties when compared to conventional covalent semiconductors such as silicon (Si). Metal oxide semiconductors are valence compounds with a high degree of ionic bonding. Their conduction band minimum (CBM) and valence band maximum (VBM) mainly consist of the metal (M) ns and oxygen (O) 2p orbital, respectively. The interaction between the metal and oxide orbitals results in significant disparity of the charge carrier transport [35]. MOSs nanostructures have attracted great attention because of their potential applications as sensors in domestic, industrial, and commercial fields due to their many essential properties like easy manufacture, low price, and small size. Due to the high surface-to-volume ratio and strong ability to adsorption, nano-sized compounds have demonstrated applicability in various sectors, including gas detection, solar cells, and many electronic instruments [36].

Metal oxides with semiconducting properties can be categorized as transition oxides like CuO, titanium dioxide ( $\text{TiO}_2$ ), Iron oxide ( $\text{Fe}_2\text{O}_3$ ), Nickel oxide (NiO), and (GO), and semi-transition oxides such as  $\text{SnO}_2$ , ZnO, and Indium (III) oxide ( $\text{In}_2\text{O}_3$ ) [37]. Metal oxides have wide band gaps, and typical electronic configurations are excellent candidate to be utilized as a sensing material in gas sensors due to the ease of producing electron-hole pairs [19]. Resistive sensors are MOSs that is distinguished by a high surface-to-bulk ratio. MOS shows reversible variations in conductivity due to changes in gas concentration, which provide information

about the composition of the surrounding environment. MOS can be classified as n-type such as ( $\text{SnO}_2$ ,  $\text{ZnO}$ ,  $\text{TiO}_2$ ,  $\text{WO}_3$ ) and p-type ( $\text{CuO}$ ,  $\text{NiO}$ ,  $\text{Cr}_2\text{O}_3$ ,  $\text{GO}$ ) depending on their behavior of ion absorption [38].

## 2.2 Tin Oxide ( $\text{SnO}_2$ )

$\text{SnO}_2$  nanostructure is an inorganic composition and one of the interesting MOSs. It has promising chemical and physical properties with a 3.6 eV band gap energy, and the conductivity is due to free electrons, making it an n-type semiconductor [39]. These unique features are frequently employed in many applications, such as catalysts, dye-based solar – cells, electrode materials, and gas sensors in thin film or bulk [40].  $\text{SnO}_2$  may be in various morphologies, including spherical, sheets, networks, microspheres, ribbons, and belts. Small spherical nanoparticles with high crystallinity have a greater significance than other morphologies due to increase the surface area [41].  $\text{SnO}_2$  is thermally stable and transparent in the visible range [42]. The powder of  $\text{SnO}_2$  appears in white and with a density of 6.9 g/cm and a molar mass of 150.7 g/mol with a high melting point of about 1630 °C. The rutile structure of  $\text{SnO}_2$  shows a tetragonal unit cell with lattice constants ( $a = b = 4.7374 \text{ \AA}$  and  $c = 3.1864 \text{ \AA}$ ). The unit cell is made up of two Sn atoms that are six fold coordinated and four O atoms that are threefold- coordinated [43]. In general, the conduction-type of semiconductor results from the formation of defects (impurities or deflection) in the structures. The surface of a metal oxide may be visualized as a cut crystal, which leads to break the bonds between atoms and topological defects arise on the surface. Other states result from alien species on the solid's surface and interaction with the surrounding gaseous.

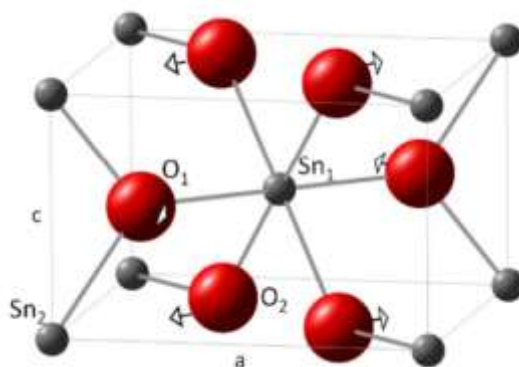


**Figure (2.1): Schematic illustration of the rutile - structure of SnO<sub>2</sub> [44].**

### 2.3 Copper Oxide (CuO)

Copper oxide (CuO) is a nontoxic (p-type) semiconductor with band gap values of about 1.2 eV. CuO has distinct features such as superconductivity, thermal stability, electrochemical solid behavior, cheap manufacturing cost, and photovoltaic properties. Furthermore, CuO may be found in various phases, including cupric oxide (CuO), cuprous oxide (Cu<sub>2</sub>O), and copper (III) oxide (Cu<sub>4</sub>O<sub>3</sub>). However, CuO and Cu<sub>2</sub>O phases are more useful in gas sensors [45]. CuO is characterized by good electrical, optical, magnetical, and physical properties that make it acquire great attention in many applications [46]. CuO powder appears in black and is unsolvable in water with a density of 6.4 g/cm<sup>3</sup>, melting point is 1330 °C, and mobility of about 10 cm<sup>2</sup>/Vs. CuO has a complicated tenorite-monoclinic crystal structure and has a unit cell with four molecules of CuO connected with different kinds of neighbor atoms with a lattice constant ( $a = 4.68 \text{ \AA}$ ,  $b = 3.41 \text{ \AA}$ ,  $c = 5.12 \text{ \AA}$ ). Figure (2.2) exhibits a crystal structure of CuO lattice. Specifically, the Cu atom is coordinated by four coplanar O atoms, forming a parallelogram [32, 47].

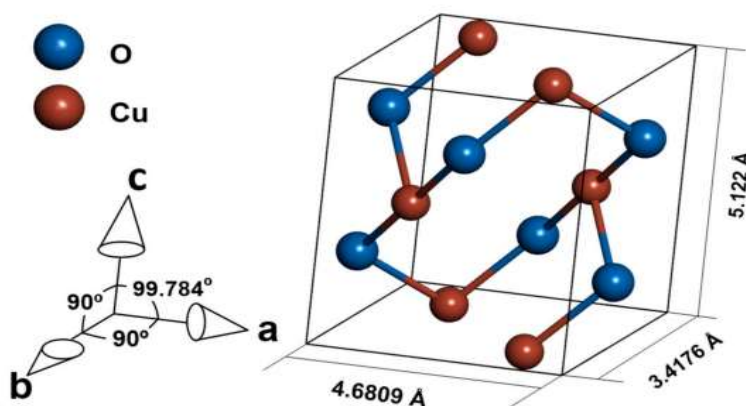


Figure (2.2): CuO Crystal-structure [48].

## 2.4 Graphene Oxide (GO) and Reduced Graphene Oxide (rGO)

Graphene is a two-dimensional arrangement of carbon atoms, forming a thin sheet of carbon known as an allotrope of graphite. The optimal arrangement of carbon atoms in graphene exhibits a hexagonal lattice structure, commonly called a "honeycomb" lattice. This unusual structure gives rise to several notable qualities, including high charge/hole mobility  $\sim 200,000 \text{ cm}^2/\text{vs}$ , a significant concentration of charge carriers, high thermal conductivity at ambient temperature of  $\sim 5000 \text{ W/mK}$ , high optical transmittance, a huge surface area of  $\sim 2620 \text{ m}^2/\text{g}$ , and electrical conductivity even at ambient temperatures [49]. Due to their unique properties, graphene and related materials are employed in various industries and technologies. These include solar cells, supercapacitors, adsorbents, photocatalysts, and sensors [50].

GO can be produced using chemical exfoliation of graphite. Graphene layers were incorporated into graphite by introducing multiple oxidizing agents, resulting in their subsequent separation. The formation of active functional groups, including epoxy, carboxyl, hydroxyl, and carboxylic acid

groups containing oxygen, induces a modification in the graphene lattice structure [51]. In addition to imperfections that make it an insulator due to its disrupted  $sp^2$  bonding networks. It can behave as a semiconductor depending on its oxidation level. It has a specific surface area of  $\sim 890 \text{ m}^2/\text{g}$  and low thermal conductivity at ambient temperature compared to graphene. Graphene delamination lowers the interaction between its layers, resulting in a larger space between them [23]. A distinction exists between GO and graphene regarding their respective solubility in water and other solvents.

Graphene has hydrophobic properties, whereas GO demonstrates hydrophilicity due to its active functional groups [52], which can be attributed to the increased interlunar distance or reduced interlunar  $\pi$ - $\pi$  interactions [53]. The band gaps of GO sheets are expected to be easily adjusted in a wide range from 0 to 4 eV by altering the arrangement, the relative ratio of the epoxy and hydroxyl groups, and external tensile strain.

On the other hand, GO possesses excellent optical transparency, and nonlinear optical features because of its heterogeneous atomic and electronic structures. One of the most exciting characteristics of GO is its ability to undergo partial reduction, resulting in the formation of graphene-like sheets called reduced graphene oxide (rGO). This reduction process involves the removal of oxygen-containing functional groups, leading to restoring a p-conjugated structure. The rGO exhibits electrical conductivity and possesses defect sites, making it beneficial for sensing applications [54]. One advantage of synthesizing graphene through the reduction of GO is the ability to manipulate several properties, including high electron mobility, electrical and thermal conductivity, stability, and high surface area, when compared to GO, by adjusting the degree of reduction.

There are three techniques for synthesizing rGO, including thermal reduction, chemical reduction, and electrochemical generation of rGO. Chemical reduction and electrochemical manufacture of rGO are two highly effective techniques for large-scale manufacturing [55]. However, the thermal reduction method is widely recognized as the most cost-effective and straightforward approach for synthesizing rGO. Thermal reduction of GO has been done in several environments, including ambient conditions, Ar-H<sub>2</sub> atmospheres, and ultrahigh vacuum settings N<sub>2</sub>, NH<sub>3</sub>- Ar [56]. Figure (2.3) illustrates the structure of graphene, GO, and rGO.

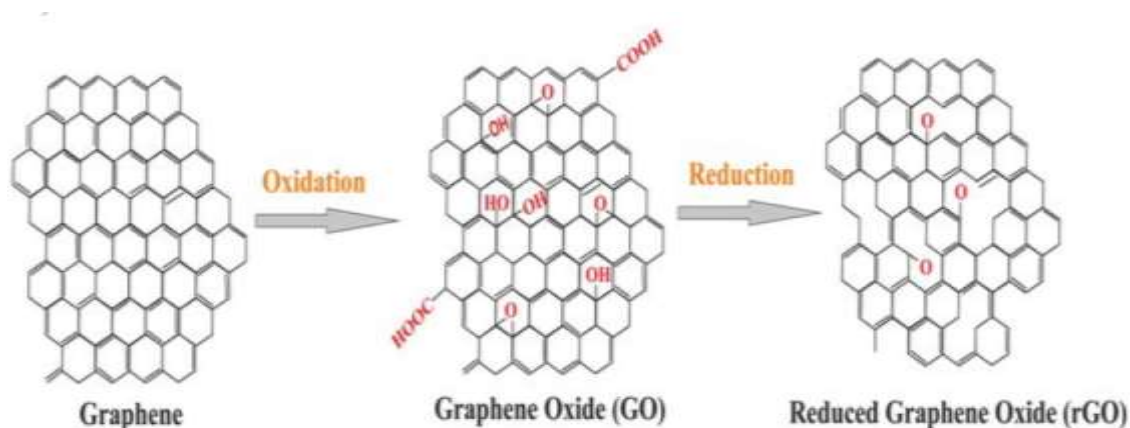


**Figure (2.3): Conversion of graphene into GO and rGO [57].**

rGO is produced by reducing GO using diverse reduction conditions and techniques. Researchers have employed numerous chemical and thermal reduction methodologies to enhance the electrochemical characterization of GO [58]. Currently, the chemical reduction of GO is achieved using a different reducing agent, including alcohol, hydrazine, hydroquinone, urea, hydriodic acid with acetic acid, sodium borohydride, sodium/potassium hydroxide, vitamin C, BSA, and aluminum/iron powder. Hence, selecting an appropriate reducing agent for this undertaking holds significant importance.

On the other hand, the thermal reduction of GO involves two distinct processes.

Firstly, an increase in carbon content by removing oxygen-containing functional groups. Secondly, it leads to the intercalation of carbon layers that are stacked together. When GO is subjected to abrupt thermal treatment at sufficiently high temperatures, it exhibits a structural change characterized by leading to release of oxygen-containing groups in the form of water. These gases generate pressure between the carbon [59]. vapor, CO, and CO<sub>2</sub> planes and induce shock, which causes the separation of closely packed carbon layers, commonly referred to as exfoliation. The thermal reduction of GO involves heating it in various atmospheres such as ultra-high vacuum, H<sub>2</sub>, Ar, and NH<sub>3</sub> or utilizing different heating sources like laser, microwave, and flashlight. Chemical and thermal reduction methodologies generally [23]. Employing chemical techniques makes possess distinct characteristics it possible to reduce GO in an aqueous environment. This reduction process leads to the formation of rGO, which can be modified with different organic functional groups or nanostructures. These modifications have the potential to improve the properties of rGO. While the degree of rGO during thermal reduction can be controlled by manipulating the time, heating temperature and gaseous environment [60].

## 2.5 Synthesis of Nanomaterial

There are two distinct approaches to manufacturing metal oxide nanoparticles, known as the "Top-down" and "Bottom-up" ways. These methods are based on experimental results. The top-down approach involves splitting more giant molecules into smaller, appropriate particles while



maintaining the original structure [61]. There are several drawbacks associated with this method, including high costs, defects, poor processing speeds, and limited suitability for large-scale production. The bottom-up approach involves constructing a structure by starting with its smallest components, such as atoms, molecules, and even nanoparticles, and gradually assembling them to form more complex systems. This approach is characterized by its cost-effectiveness compared to the top-down method, and improved consistency of the resulting product. The synthesis of nanostructured metal oxides can be achieved by chemical or physical processes [19], as shown in figure (2.4).

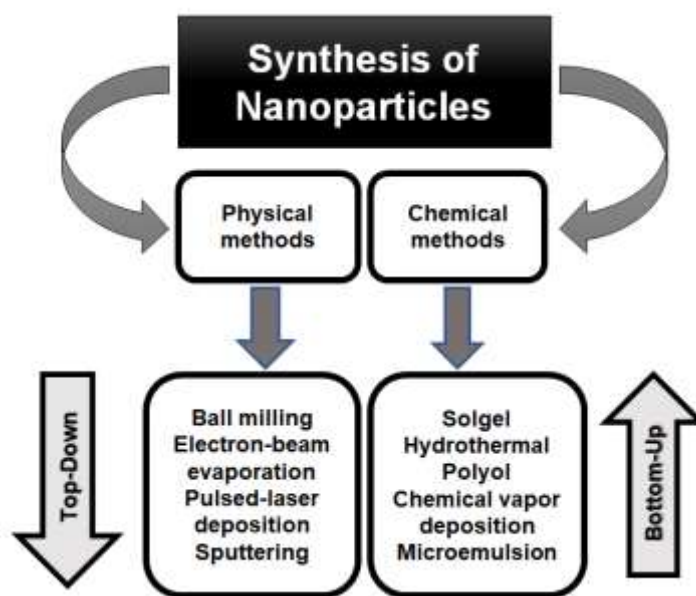


**Figure (2.4): Schematic representation for the fabrication of nanomaterial.**

### 2.5.1 Chemical Methods

Chemical methods involve several methods such as sol-gel method [62], chemical vapor deposition (CVD) [63], Solvothermal synthesis [64], hydrothermal method [65], and etc.

Hydrothermal is a commonly utilized synthesis process for fabricating nano-materials across various temperatures. In this experimental method, the reactants are dissolved in water within a sealed system in a pressurized container, such as an autoclave, lined with Teflon material. After that, the reactants experience a heterogeneous reaction under increased pressure. The temperature within the autoclave can gradually expand beyond the boiling point by increasing the vapor pressure within the chamber. The hydrothermal synthesis method is frequently used to produce nanospheres, nanowires, nanosheets, and nanorods [59].

The primary benefit of this technique involves its simplicity, ability to effectively control the procedure through liquid-phase or multiphase chemical reactions while maintaining high vapor pressures and minimizing the loss of nanomaterial, as a single-step synthetic process, and environmental reliability. This approach's drawbacks involve using costly equipment, including an autoclave and high temperatures at the limit of 300 °C [66].

### **2.5.2 Physical Methods**

Physical methods are an efficient top-down preparation process for creating nanoparticles and amorphous materials from bulk materials which include ball milling [67], electrospinning [68], sputtering [69], pulsed laser deposition [70], and etc.

Sputtering is thought to be an efficient process for creating nanomaterial thin films. The sputtering deposition process involves the bombardment of the target surface by intense gaseous ions, resulting in the physical ejection of tiny atom groups. These groups' size depends on the energy of the

impacting gaseous ions. The sputtering process can be executed using several methods, including magnetron, radio-frequency, and DC diode sputtering [71]. Typically, sputtering is conducted within a vacuum chamber, wherein the sputtering gas is introduced. The cathode target is subjected to a high voltage, causing the collision between free electrons and the gas, generating gas ions. The ions with positive charge experience a significant acceleration within the electric field as they move toward the cathode target. Upon reaching the target, these ions repeatedly collide with it, expelling atoms from the target's surface [72]. Benefits of sputtering include stability of deposition rate, uniform deposition with defect covering, excellent adhesion to thin films, and deposition can occur on metals, alloys, compounds, and insulators. Thin films of oxide and nitride can be made from reactive sputters like  $O_2$  and  $N_2$ . The disadvantage of ion beam sputtering is that it cannot produce a uniform-thickness large-area film. Additionally, the sputtering mechanism is excessively complicated and expensive [73].

Laser ablation is a physical technique employed to fabricate nanostructures by a top-down approach. This technique involves the targeted emission of pulsed laser beam towards the substrate, resulting in the formation of nanoparticles by the ablation process. The target surface absorbs Laser beam energy, resulting in electronic excitations. In addition, due to the extremely low thermal conductivity of the target, it is difficult to lose energy in a short period; therefore, photon energy is converted into chemical and thermal energy. As a consequence, the surface temperature of the target rises to  $3500\text{ }^\circ\text{C}$  within just a small volume of the target, leading to the rapid evaporation, ionization, and decomposition of the target material

[74]. Various parameters, including pulse duration, wavelength, irradiance, and repetition rate, influence the interaction between laser and substrate. This method can produce a variety of nanomaterial, including ceramics, carbon nanomaterial, metal nanoparticles, and oxide composites [75]

There are numerous reasons for using a PLD, the most important of which is that a PLD can readily generate the energy necessary for a material to convert into plasma. Equally important is the laser's operating wavelength; thin film growth can be done at many wavelengths, although most thin film growth is done between (200 – 400 nm) laser wavelengths when considering a laser for PLD. The basic reason for choosing these wavelengths is that most of the materials utilized for PLD have substantial absorption in these regions [76].

The main advantages of this technique are the capacity to regulate only laser energy density and pulse repetition rate during deposition, the ability to sequentially ablate targets to create multi-layered films of diverse materials, and the ability to control film thickness to atomic monolayer by number of pulses. One limitation of PLD is its relatively low average deposition rate, and costly to apply thin layers of material. Challenges associated with the equipment setup include its complexity, limited compatibility with different materials, high energy consumption, lack of uniformity, and sensitivity to substrate temperature [77].

## **2.6 Crystallite Structure Determination of Nanomaterial**

X-ray diffraction (XRD) is essential for determining material crystallite structures and phase composition. The incident X-rays directed with appropriate wavelengths and angles onto crystalline objects and generated

patterns with highly concentrated peaks of reflected radiation. These peaks are comparable to the distances between atoms and hence provide an exceptional tool for investigating this particular length scale. The phase shift results in either constructive or destructive interferences was indicated by the  $2\theta$  deviation. It was suggested that incident X-ray radiation would generate a Bragg peak by constructive interference of reflections from different planes. Constructive interference occurs when the phase shift is a multiple of  $2\pi$ . This process can be mathematically described using Bragg's law [78].

$$n\lambda = 2 d \sin \theta \quad (2.1)$$

$n = 1, 2, 3, \dots$  which represents the refraction order,  $\theta =$  Bragg's angle.

As described by Scherer's formula, the crystalline size ( $D$ ) of a particle in a polycrystalline film is measured by the full width of the half maximum peak (FWHM),  $\beta$  (in radians) [79].

$$D = \frac{0.94 \lambda}{\beta \cos \theta} \quad (2.2)$$

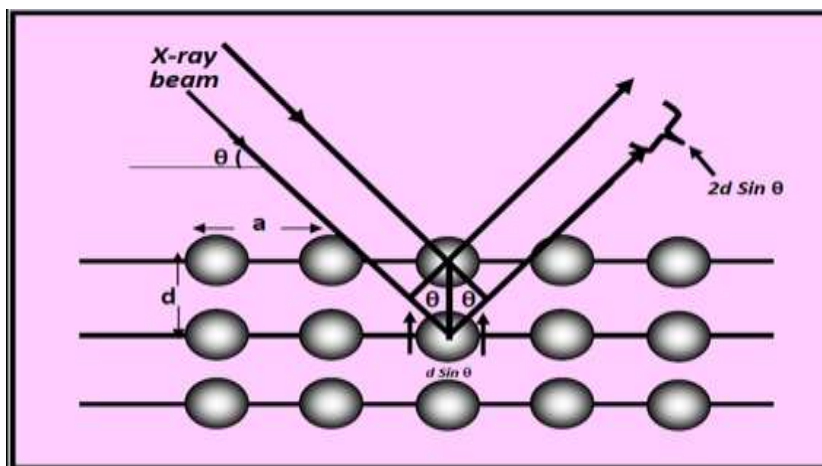


Figure (2.5): Basic principle of a typical XRD and Bragg's law [80].

## 2.7 Optical Properties of Semiconductors

The absorption spectrum provides valuable insights into the characteristics of semiconductor materials, including the nature of transitions, permittivity, energy gap, and several optical properties. When light interacts with a semiconductor, it is possible to be absorbed by the material. The probability of absorption depends on the energy of the photons ( $E = h\nu$ ), where  $h$  represents Planck's constant and  $\nu$  represents the frequency of the incident photons. This absorption occurs when there is an electronic transition from the valence band to the crystal's conduction band. This transition begins at the absorption edge, corresponding to the minimum energy difference between the lowest level of the conduction band and the highest level of the valence band [80]. If the energy of a photon is greater than or equal to the  $E_g$ , the photon can engage in an interaction with a valence electron. This interaction results in the elevation of the electron from the valence band to the conduction band, consequently generating an electron-hole pair. The maximum wavelength ( $\lambda$ ) of the incident photon responsible for generating the electron-hole pair is denoted as follows [81].

$$\lambda_{nm} = hc/E_g = 1240/E_g \quad (2.3)$$

The exponential decay of photon flux intensity with distance  $t$  within the semiconductor can be described using the Beer-Lambert equation [82]:

$$I = I_0 e^{-\alpha t} \quad (2.4)$$

Where:  $I_0$  and  $I$ : the incident and the transmitted photon intensity, respectively.

$\alpha$ : the absorption coefficient.

t: the thickness of the material.

The transitions between the valence and conduction bands can be classified directly and indirectly according to the Tauc equation [22]:

$$\alpha h\nu = \beta(h\nu - E_g)^r \quad (2.5)$$

Where  $\beta$ : a constant inversely proportional to r

$$r = \frac{1}{2} \text{ (allowed direct transition) }, \frac{3}{2} \text{ (forbidden direct transition)}$$

$$= 2 \text{ ( allowed indirect transition ) }, 3 \text{ (forbidden indirect transition).}$$

In general, direct transitions involve the transfer of an electron between initial and final states with the same wave vector value, denoted as  $\Delta k = 0$ , to conserve momentum. The absorption coefficient associated with this transition takes values from  $10^4$  to  $10^5 \text{ cm}^{-1}$ . The direct transition occurs within both crystalline and polycrystalline semiconductors.

The allowed direct transition occurs when an electron undergoes a direct transition from the valence band's highest point to the conduction band's lowest point, with both the starting and final states having wave vectors equal to zero. Forbidden direct transitions can occur within the same wave vector state, provided that the wave vector is not equal to zero [83].

Indirect transitions happen when the conduction band's minima and valence band's maxima are not at the same k value. In such cases, the role of phonons becomes imperative for the preservation of crystal momentum, so  $h\nu = E_g \pm E_p$ , where  $E_p$  is the emitted or absorbed phonon energy and  $\alpha$  takes the value between 1 and  $10^4 \text{ cm}^{-1}$ . Direct transfers are allowed from

the valence band's top to the conduction band's bottom. Disallowed indirect transitions are prohibited from any location other than the top of the valence band to any point other than the bottom of the conduction band [84]. Figure (2.6) illustrates the optical transitions.

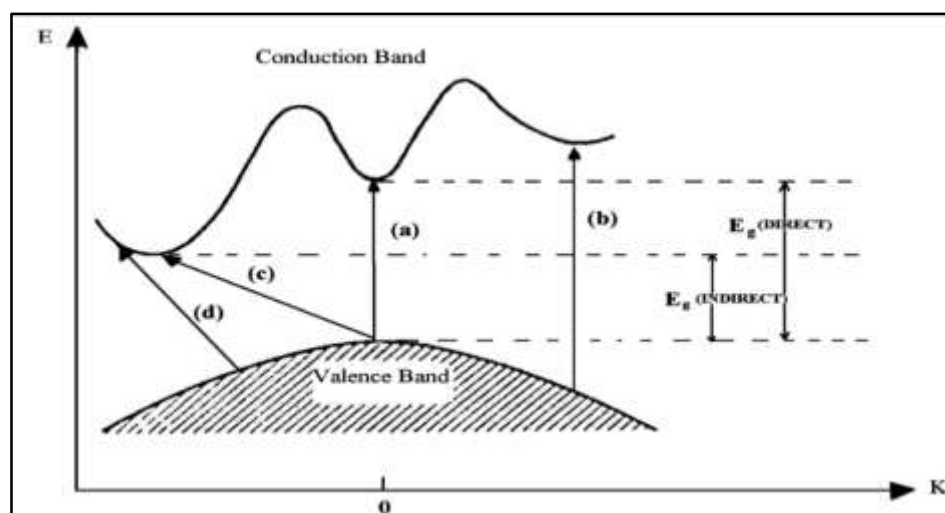


**Figure (2.6):** The optical transitions (a) allowed direct, (b) forbidden direct, (c) allowed indirect, (d) forbidden indirect [85].

## 2.8 Applications of MOSs

Metal oxide nanoparticles are an important type of nanomaterial that broadly impact science and technology due to their unique characteristics, including a high surface-to-volume ratio, a huge surface area, and their abundance on earth [86]. The applications of MOSs depend on the distinguishable properties of each oxide; here are some of them:

- 1- Lithium-ion batteries (LIBs):  $\text{SnO}_2$  has been considered as one of the most important materials used as an anode for high-implementation LIBs [87].
- 2- Photodetector: CuO is an ideal choice for visible-light photodetectors due to its low band gap of 1.2 eV, availability, and mechanical



- stability resulting from its atomic structure. This makes it both high-performing and cost-effective [88].
- 3- Solar cells:  $\text{SnO}_2$  got much attention in this field due to its high mobility, good conductivity, large optical bandgap, and excellent transmittance over a wide visible spectrum range [89].  $\text{TiO}_2$ ,  $\text{ZnO}$ , and  $\text{CuO}$  are also greatly used in this field [90].
  - 4- Catalysis:  $\text{CuO}$ 's reducibility and surface reactivity are vital in determining its high catalytic performance [91].
  - 5- Biomedical applications: Including treatment and diagnosis. GO and rGO play a vital role in this application due to their high surface area, stability, solubility, and excellent biocompatibility [92].
  - 6- Gas sensors: The sensors' performance can be improved by making the particles as small as possible. The plurality of metal oxides used in gas sensors are  $\text{SnO}_2$ ,  $\text{CuO}$ , GO,  $\text{TiO}_2$ ,  $\text{ZnO}$  ... [34].

## 2.9 Gas Sensors

Concerns for a clean and healthy atmosphere in regions ranging from households to the global level have pushed researchers to develop a broad spectrum of gas sensors in recent years. Gas detection is imperative to handle these challenges effectively [93]. The vast majority of gases in the atmosphere, such as ( $\text{O}_2$ ,  $\text{N}_2$ ,  $\text{H}_2\text{O}$ ,  $\text{CO}$ ,  $\text{CO}_2$ ,  $\text{NO}_x$ , etc...) are colorless and odorless. However, it is impossible to differentiate all types of gases based on bodily organs, many of which are essential to our survival, while numerous others are detrimental. Vital gases such as  $\text{O}_2$  and  $\text{H}_2\text{O}$  should be preserved at acceptable levels in living environments. In contrast, dangerous gases such as  $\text{CO}$  should be kept below a particular level to avoid toxicity. As far as lighter hydrocarbons and  $\text{H}_2$  are concerned, their evaporation

following leakage into the air is one of the key concerns addressed by the employment of gas sensors [94]. A gas sensor is a system that detects the presence of atmospheric gases. By altering the material's resistance within the detection device in response to the gas concentration, the sensor produces a difference in potential that can be used to calculate the output voltage [95]. These devices are sensitive to a wide range of combustible and toxic gases, and they have been successfully implemented in numerous fields, including climate, safety, security, process-monitoring equipment, and medical equipment [96]. In recent years, there has been a growing trend in utilizing MOSs with sizes ranging from 1 nm to 100 nm for gas sensing applications, primarily due to their size-dependent features.

Nanomaterial possesses distinctive characteristics due to their catalytic, optical, mechanical, magnetic, and electrical capabilities. In addition, these materials exhibit a high surface area-to-mass ratio. Moreover, novel physical and chemical characteristics manifest when particles are reduced to the nanoscale scale [96]. The size and geometry of semiconductor nanoparticles have been observed to influence the passage of electrons and holes. The increased demand for the manufacture of nanoparticles for gas sensor development can be attributed to several factors, including their high crystalline structure, the ability to incorporate noble metal doping, and their competitive manufacturing rate [97].

## **2.10 Mechanism of MOSs Gas Sensor**

Semiconductor gas sensors consist of metal oxides and are utilized to detect the concentration of a specific gas by monitoring the electrical resistance of the electronic device. These changes in conductivity can be

measured with the electrodes [98]. The sensing mechanism of MOS comprises two essential functions: receptor and transducer parts. The receptor function transfers chemical information from target gas molecules and sensitive layer surfaces into energy that the transducer transforms into electrical parameters, specifically resistance, and capacitance in the form of voltage or current, that may be measured in terms of its magnitude, frequency, and phase. [5]. MOSs can be categorized into n-type and p-type semiconductors according to the behavior of oxygen ionosorption [36, 86]. In an n-type, the material exhibits excess free electrons compared to the number of holes present. The designation of these materials as n-type arises from the fact that electrons possess a negative charge. In a material with p-type, the dominant charge carriers are holes. The term "p-type" denotes a material or semiconductor in which most charge carriers are positively charged holes [6].

The process of oxygen adsorption on the surface of the n-type metal oxide results in the formation of a depletion layer in the surrounding air. This process leads to a rise in the resistance of the sensor. In the presence of gas, it is expected that a reaction will occur either with the oxygen that has been pre-adsorbed or with the metal oxide, resulting in a modification in the thickness of the depletion layer. The thickness of the depletion layer is commonly referred to as the Debye length ( $\lambda_D$ ), and any alterations in its dimensions impact the sensor's conductivity [37]. Figure (2.8) shows the mechanism of the MOS gas sensor.

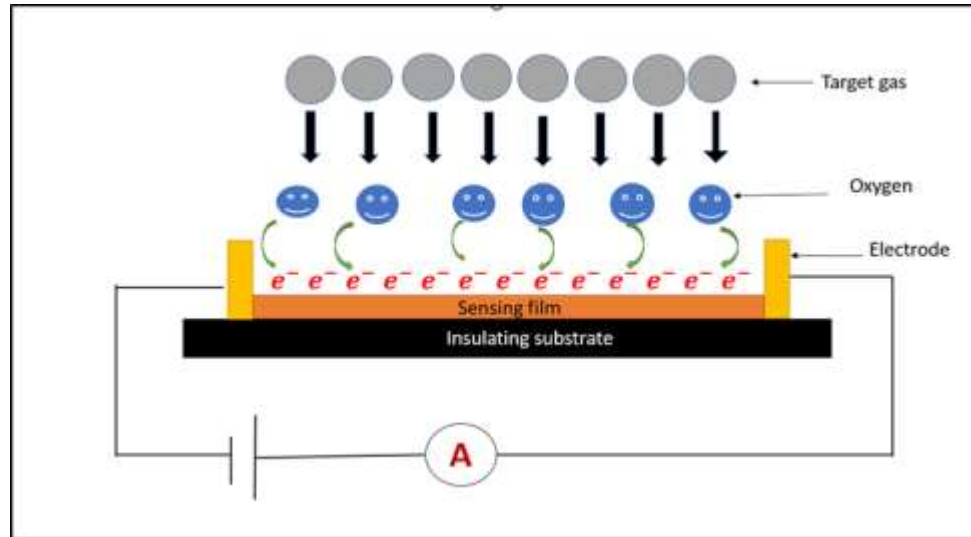
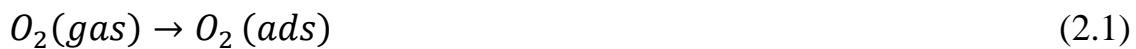


**Figure (2.7): Mechanism of MOS gas sensor.**

At 100 °C or higher, the adsorption of oxygen on the surface results in the formation of molecular species (ions) through the capture of an electron from the conduction band of the active layer at the surface. This interaction is expressed by the following equations [99]:



In the case of a p-type semiconductor, the enhanced conductivity is attributed to an excessive carrier concentration. The sensors' responses to the exposure to the target gases were analyzed using the electron-depletion-layer/hole-accumulation-layer theory [100]. Upon being exposed to reductive gases, including (H<sub>2</sub>S, H<sub>2</sub>, CH<sub>4</sub>, NH<sub>3</sub>, C<sub>2</sub>H<sub>5</sub>OH, CO, and acetone), n-type semiconductors undergo a surface interaction between negative

oxygen species and the reductive gases, resulting in the return of electrons back to the depleted oxides which cause an increase in the conductivity.

While for oxidizing gases such as ( $\text{Cl}_2$ ,  $\text{NO}_x$ , and  $\text{SO}_2$ ), it can enhance resistance by increasing electron depletion. In a p-type semiconductor, most of the charge carriers are positive holes. This means that the opposite effects are seen with the material: it becomes more conductive when an oxidizing gas is present by increasing the number of positive holes, and it becomes more resistant when a reducing gas is present by decreasing the concentration of holes' charge carriers [85].

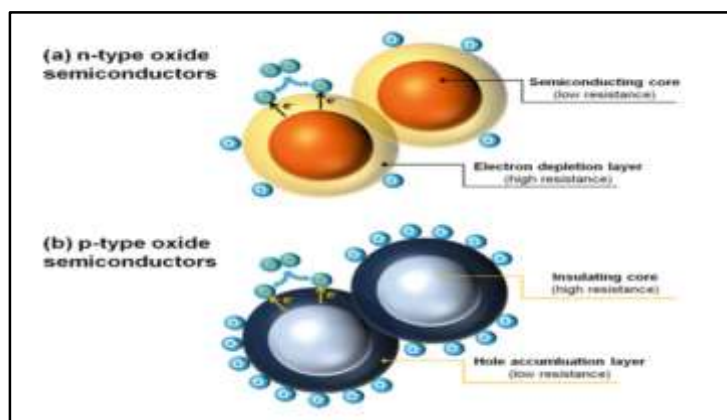


**Figure (2.8): Formation of electronic core – shell structures in (a) n-type, (b) p-type oxide semiconductors [101].**

The material's grain and particle boundary size directly influence the sensitivity and response time. Oxygen on the surface of metal oxide can be adsorbed, leading to the extraction of electrons from the material. Consequently, this phenomenon induces a modification in the resistivity. The resistivity of the p-type material exhibits a drop compared to the bulk material, while the resistivity of the n-type material demonstrates an increase. In the case of tiny grain sizes, it is possible to regard the grain as

having negligible bulk area, attributing the entire grain to the surface area. Alternatively, when the size of the grains is sufficiently enormous to have little impact on resistance or conductivity, it is possible to see the surface as possessing a consistent resistance. This model is anticipated to apply to n-type and p-type sensors [102].

The following table summarizes how the gas type affects the sensor's resistance.

**Table (2.1): Gas type effect on the sensor's resistance for (p-type) and (n-type) materials.**

Type of gas	Semiconductor - type	Resistance
<b>Reducing - gas</b>	n-type	decrease
	p-type	increase
<b>Oxidizing - gas</b>	n-type	increase
	p-type	decrease

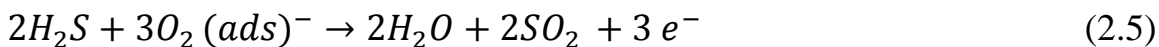
## 2.11 Sensor Performance toward Reducing Gases

### 2.11.1 Hydrogen Sulfide (H<sub>2</sub>S) Gas

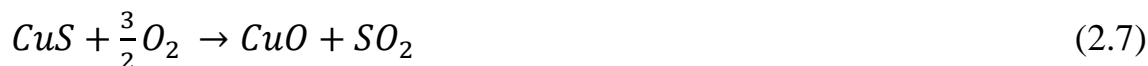
H<sub>2</sub>S is a toxic, colorless, flammable and hazardous gas with a pungent odor reminiscent of decaying eggs. This scent can be produced by sewage, hot springs, food processing, and more than 70 industries, including metal extraction, coal processing, and natural gas creation. The American Conference of Government Industrial Hygienists has determined the threshold limit value of H<sub>2</sub>S gas at 10 ppm. H<sub>2</sub>S is a gas that contaminates the air and harms human health, even at low levels 10 ppm. The concentrations that humans can smell in the air are between (0.0005 and 0.3

ppm). Concentrations above 20 ppm can irritate the upper respiratory tract [103].

Additionally, H<sub>2</sub>S is a crucial diagnostic marker for problems like diabetes, liver cirrhosis, irritation of the eyes, and asthma, even when present at ppb concentrations [29]. Therefore, there is a need for an H<sub>2</sub>S gas sensor that can provide a rapid and highly sensitive response [24]. Reducing gases—such as H<sub>2</sub>S, interact with desorbing oxygen ions on the metal's surface to release electrons as they flow through the metal oxide's surface, which enhances the conductivity and results in the creation of sulfur dioxide (SO<sub>2</sub>) according to eq. (2.5) [104].



Metal oxides exhibit significant chemical species detection capabilities. This method has an important drawback: the unspecific interaction of the MOX surface with the surrounding atmosphere results in redox reactions involving electrical resistance modulation. Integrating MOS heterostructure in sensors is a viable option for improving sensitivity and selectivity. CuO/SnO<sub>2</sub> heterostructure excelled in H<sub>2</sub>S detection [24]. The reaction between CuO and H<sub>2</sub>S does not adhere to a typical redox process but instead involves a thermally activated exchange of anions to produce CuS. The reversibility of this change occurs in an atmosphere abundant in oxygen, and it can be briefly explained by:



CuO acts as a p-type semiconductor, while SnO<sub>2</sub> acts as an n-type semiconductor. When these two semiconductors are brought together to form a p-n junction, a depletion zone is created between them. The properties of this depletion zone are determined by the relative positions of the Fermi levels of the two semiconductors. Modifying the structure and content of the metal oxides leads to changes in the Fermi level and the depletion zone. Consequently, the electrical characteristics of the entire heterostructure undergo significant alteration. When exposed to H<sub>2</sub>S, CuO undergoes a process called sulphuration, resulting in the formation of a molecule called Cu<sub>x</sub>O<sub>z</sub>S<sub>y</sub>. Eventually, this compound transforms into CuS, which exhibits metallic properties (eq. (2.6)). Under these circumstances, the heterostructure transforms from a conventional p-n junction to a metal-semiconductor interface. The impact of this phenomenon on the sensors' electrical properties can be greater than that induced by conventional redox surface reactions in MOSs [27]. Simultaneously, the CuO and H<sub>2</sub>S gas reaction enhances the sensor's selectivity performance by creating significant oxygen vacancies to uphold charge neutrality.

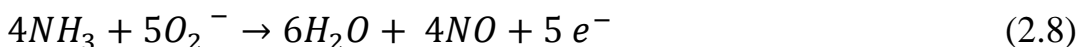
Nevertheless, CuO-doped SnO<sub>2</sub> typically occurs at elevated temperatures higher than 180 °C, resulting in raised power consumption of the sensor. Two-dimensional carbon materials known as rGO have demonstrated their effectiveness in enhancing the performance of MOS gas sensing devices at low temperatures. This is because of its significant surface-to-volume ratio, high charge carrier mobility, the presence of active defect sites, and its ability to detect the adsorption and desorption of single molecules. Moreover, the chemical modification using metal and MOS nanoparticles



enables the effortless identification of numerous analyses at low concentration levels [33].

### 2.11.2 Ammonia (NH<sub>3</sub>) Gas

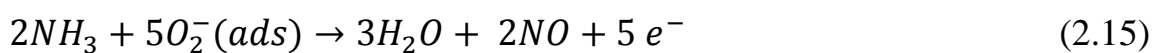
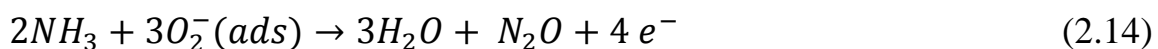
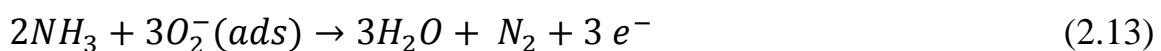
NH<sub>3</sub>, a toxic gas, is generated in numerous industrial processes and through the natural decomposition of organic waste. NH<sub>3</sub> is a commonly utilized industrial refrigeration gas in food and beverage. NH<sub>3</sub>, a favored refrigerant, offers high efficiency and stability at low cost. Although beneficial, these benefits come with health dangers such as skin, eye, throat, and lung irritation, damage, and worker safety concerns. Continuous exposure to 35 ppm NH<sub>3</sub> poses a significant risk to human health. Ingesting ammonia can result in corrosive damage to the oral cavity, esophagus, and gastrointestinal tract. Direct contact with very concentrated ammonia might result in skin or eye irritation and burns [105]. Due to its role as a reducing gas, ammonia exhibits a change in resistance when it passes over the surface of the MOS sensor, depending on whether it is p-type or n-type. The reaction clearly characterizes the mechanism for gas detection in MOS's - NH<sub>3</sub> [102].



According to the theoretical and simulation studies, NH<sub>3</sub> is inherently a weak charge transfer molecule compared to other gases. During interaction with a p-type oxide, such as CuO or rGO, as a reducing agent, NH<sub>3</sub> donates a lone electron pair to p-type, leading to the decrease of charge carrier density in the conduction - band and increasing the resistance of the devices [106]. The addition of rGO-CuO led to an improvement in the sensing response. This can be attributed to the increased adsorption sites (dangling

bonds) caused by surface imperfections and the larger surface area. When rGO and CuO come into contact, electrons are transported from rGO to CuO due to their different work functions (5.3 eV for CuO and 4.7 eV for rGO), causing a band bending at the interface. rGO influences the electron density of CuO, which increases sensor resistance when exposed to NH<sub>3</sub> [107].

In the case of n-type like SnO<sub>2</sub>, in air, the SnO<sub>2</sub> sensor has high initial resistance because oxygen at its surface captures almost free electrons. Thus, the SnO<sub>2</sub> nonporous surface has low free electron concentration. Additionally, oxygen atoms become ions. Thus, the space charge region width increased. As the reaction equation (2.9-2.12) demonstrated, oxygen ions reacted with ammonia gas on the SnO<sub>2</sub> nonporous surface, narrowing the space charge region width. The SnO<sub>2</sub> resistance dropped after this reaction released free electrons from the previous reaction onto its surface [34].



## 2.12 MOSs Heterojunctions

Irrespective of the specific gas sensor material employed, achieving optimal performance across all parameters presents a challenge. Heterojunctions can be constructed by integrating multiple MOS materials, resulting in the acquisition of complementary benefits and enhancement of gas sensing capabilities. Implementing this particular technique can enhance the response by heightened catalytic activity, the establishment of electron depletion layers, increased adsorption sites, and alterations in the band structure resulting from heterojunctions. Heterojunctions can be categorized into p–n junctions, n–n junctions, and p–p junctions based on the combination of metal-oxide-semiconductors (MOSs) involved [38].

### 2.12.1 An Isotype Heterojunctions (p-n/ n-p)

An isotype heterojunctions refers to a composite structure comprising two semiconductors. In this structure, a secondary phase p-type semiconductor is joined with a primary phase n-type semiconductor to form a hetero-junction of p-n type. Alternatively, the combination can be arranged to make a hetero-junction of n-p type. Electrons migrate from regions of higher energy to those of lower energy. In contrast, holes, in turn, migrate in the opposite direction until a state of equilibrium is attained, as dictated by the difference in Fermi energy levels, which leads to band bending [108]. This energy shift can alter the p- and n-side energy structures, making them more sensitive. A depletion layer is formed between two semiconductors due to the electric field caused by the polarity mismatch between the n and p regions. As a result of the rising potential, charge carriers can move across the junction.

Therefore, resistance will grow in this area. Due to the bending of both sides of the energy level, a potential barrier and a space charge zone are formed when the Fermi level in an n-type region is higher than in a p-type region [109]. Jin et al. [110] developed a gas sensor for acetylene ( $C_2H_2$ ) using a heterojunction of rGO-loaded  $SnO_2$  synthesized using a hydrothermal process. The synthetic materials were tested to sense gases at temperatures ranging from (100 to 300 °C) and with different concentrations of  $C_2H_2$  gas. This sensor showed a better response of 12.4 to 50 ppm gas at 180 °C. It was found that adding rGO would improve the ability of metal oxide-based gas sensors to detect  $C_2H_2$  because of the formation of a p-n junction between two oxides.

### 2.12.2 Isotype Homojunctions (n-n and p-p)

Isotype transition is a homojunction between two similar semiconductors (n - n or p - p) with different work functions. The transfer of charge carriers, whether electrons or holes, occurs towards the Fermi level with the lowest energy. This process creates a depletion layer (or an accumulation layer) consisting of either electrons or holes. The principle of n-n homojunction is that making the carrier accumulation area facilitates oxygen adsorption onto the surface and grows the carrier depletion region. Consequently, the initial resistance rises, thereby enabling the detection of reducing gas [111]. Several studies have demonstrated enhanced gas detection capabilities utilizing (n-n) homo-junctions. Naik et al. [112] introduced a sensor array composed of ZnO and  $SnO_2$ . The experimental procedure recorded a response of 109 for both acetone and ethanol gases when subjected to a temperature of 300 °C. In the case of a p-p homo-junctions, a hole

accumulation layer and a hole depletion layer combine at the interface of two junctions. Adsorbed oxygen ions inject holes into the barrier layer. As a result, the thickness of the barrier layer decreases, resulting in a drop in resistance [113]. Yin et al. [114] employed a microwave-assisted methodology to synthesize nanoparticles of CuO-rGO. Upon exposure to a concentration of 10 ppm of H<sub>2</sub>S gas at 100 °C, the sensor exhibited a response of around 68.5. The potential augmentation of sensor response can be attributed to a p-p heterojunction between two materials. The distinct work functionalities exhibited by the two oxides lead to the movement of holes towards CuO, where they recombined with electrons released by the H<sub>2</sub>S vapor. This procedure continues until the Fermi level achieves a state of equilibrium. Consequently, a decrease in the concentration of holes occurs, leading to an increase in resistance.

## 2.13 Characterization of Gas Sensor

### 2.13.1 Sensitivity

Sensitivity refers to the capacity of a device to measure changes in a physical and chemical attribute of the sensing material when exposed to a specific concentration of gas. Different formulas can express the sensitivity:

$$\text{For reducing gases: } S = \frac{R_a}{R_g} \quad (2.6)$$

$$\text{For oxidizing gases: } S = \frac{R_g}{R_a} \quad (2.7)$$

$$\text{Or: For reducing gases: } S (\%) = \frac{|R_a - R_g|}{R_g} * 100\% \quad (2.8)$$

$$\text{For oxidizing gases: } S (\%) = \frac{|R_g - R_a|}{R_a} * 100\% \quad (2.9)$$

Where  $R_a$  and  $R_g$  are the resistance in air and the target gas, respectively [37]. The porosity of the sensitive material, the working temperature, the presence of dopants, and the crystallite size all significantly impact the gas sensors' sensitivity. Since most of the sensing processes happen on the surface of the sensitive material, one of the first things that need to be done to make the sensor more sensitive is to control the particle size of semiconductor materials. Nanocrystallites materials have the strongest sensor signals because they have a large specific surface area, resulting in an increased adsorption process [85].

### 2.13.2 Selectivity

The semiconductor layer's selectivity refers to its ability to differentiate between various target gases or a single gas within a gas mixture. Gas sensor selectivity can be enhanced by applying annealing as a post-processing step or by modifying the surface by doping oxides to other metal oxides or doping with different catalytic additions to improve the adsorption capabilities towards the desired target gases [115].

### 2.13.3 Stability

Stability is the sensor's ability to sustain its sensitivity and response behavior over time. According to the application, the time could range from hours to years. Stability can be represented in terms of sensor response drift. The environmental variables and measurement conditions must be comparable for good stability values. Sensor stability can be classified as either active or passive. The term "active stability" or "reproducibility" refers to sensor properties over a specific period under operating settings that

may include high temperatures and the presence of a known analytic. Passive stability is associated with keeping sensitivity and selectivity following regular storage conditions, such as room temperature and ambient humidity [36].

#### **2.13.4 Response and Recovery Time**

The response time refers to the duration required for the sensor to respond to a sudden alteration in the gas concentration. The sensor response ( $\tau_{90}$ ) time is the duration required for the sensor to attain 90% of its maximum reading after exposure to a specific gas concentration corresponding to its maximum sensitivity. The recovery time refers to the duration required for the signal to revert to its original value following a zero decrease in the target gas concentration [98]. The response and recovery times can be shortened by doping metal oxides with metals like Pd and Ag [117].

#### **2.13.5 Detection Limit**

The detection limit is the lowest possible gas concentration that a sensor element can detect. The resolution of a device is equal to the difference in concentration that must be of the most insufficient magnitude for it to be seen by a sensor. The sensitivity and the noise levels of a sensor's response determine its detection limit. In gas sensors, it is commonly believed that a response signal three times larger than the noise level represents the limit of detection [5].

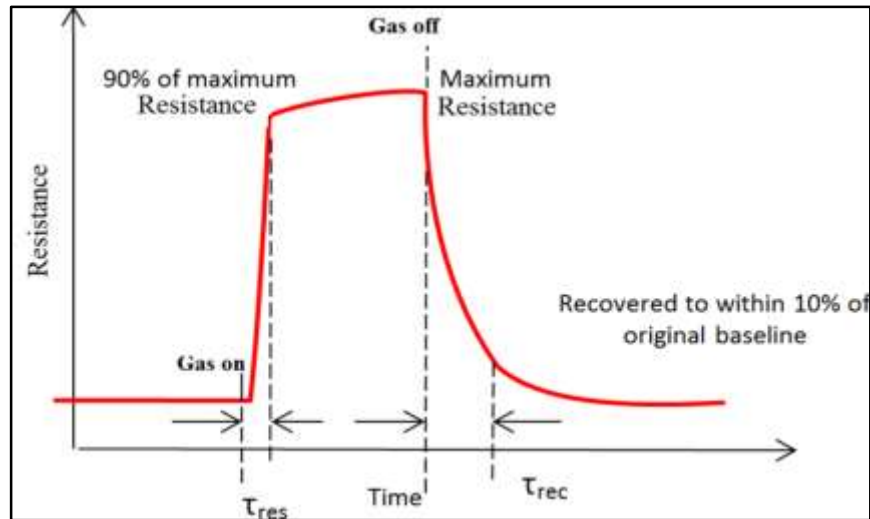


**Figure (2.9):** The response curve of the MOS gas sensor [85].

### 2.13.6 Operation Temperature

It is widely acknowledged that the chemical and physical properties of MOSs are significantly influenced by the temperature at which they are operated. Regarding chemo-resistive gas sensors, the operational temperature plays a crucial role in governing the reaction kinetics, conductivity, and electron mobility. Typically, conventional MOS gas sensors are commonly operated above the room temperature range of (200-500 °C). The values vary according to the type of material and gas that will be detected. This is mainly attributed to the necessity of thermal energy to facilitate surface redox reactions and exceed the activation energy barrier [6]. High operating temperatures can cause energy waste and safety risks when exposed to explosive and combustible gases, limiting the applications of MOS gas sensors due to their high sensitivity. The high- operation temperature also causes sensor signal drift, leading to inaccurate readings. Thus, MOS gas sensor development focuses on reducing operating temperature while maintaining sensitivity [116].



# **Chapter Three**

## **Experimental Work**

### 3.1 Introduction

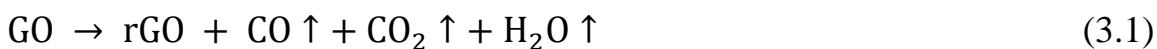
This chapter describes the experimental procedures of preparation of metal oxide semiconductors and setup of gas sensor devices. The chemical materials which used in our work are reported in table (3.1). Figure (3.1) illustrates a schematic representation of the practical work approach.

**Table (3.1): Chemical materials.**

Material	Molecular formula	Molecular weight (gram/mol)	Purity	Company
Graphene oxide	GO	124.91	99%	BDH
Cupric nitrate trihydrate	Cu (NO <sub>3</sub> ) <sub>2</sub> .3H <sub>2</sub> O	241.6	99%	Chemicals Ltd Poole England,
Tin oxide	SnO <sub>2</sub>	150.71	99%	ALPHA
Sodium hydroxide	NaOH	39.997	99%	CHEMIKA in INDIA

### 3.2 Preparation of rGO

GO powder was reduced thermally by the hydrothermal method: 2 grams of GO powder were dissolved in 100 mL of deionized water and sonicated for 30 minutes until the powder was completely dissolved in the water. After 30 minutes of stirring, the solution was transferred to a 100 mL sealed autoclave and heated in an oven to 100 °C for four hours. Following five washes with ethanol and distilled water, the product was dried in a furnace at 100 °C for one hour. The reaction occurs according to the equation:



This procedure was repeated at 200 °C to investigate the temperature at which GO was reduced to rGO.

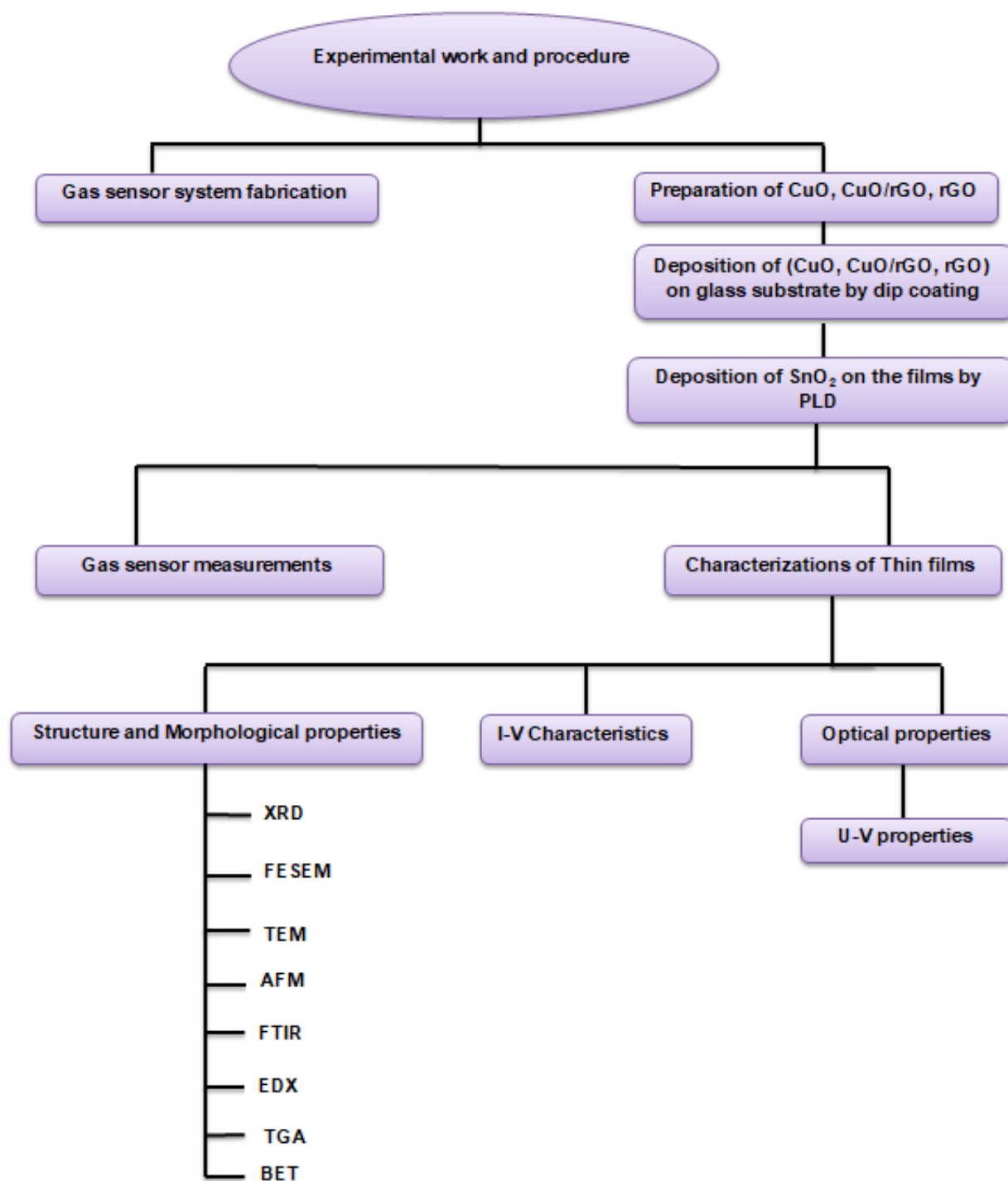
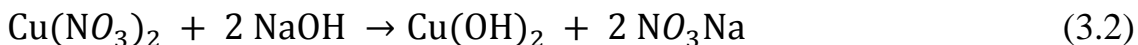


Figure (3.1): Schematic representation of the experimental work.

### 3.3 Preparation of CuO

To synthesize CuO powder using the hydrothermal process, a mass of 2 grams of  $\text{Cu}(\text{NO}_3)_2 \cdot 3\text{H}_2\text{O}$  powder was dissolved in 100 mL of deionized water, and the resulting solution was subjected to sonication for 30 minutes. The solution color turns blue. Following this, a carefully prepared solution of sodium hydroxide (NaOH) with a concentration of 1 M was gradually added to the system under continuous stirring for 30 minutes. The pH value of the composites was observed to be 10, indicating an alkaline characteristic. The solution has undergone thermal treatment in a 100 mL autoclave and exposed to a temperature of 100 °C for 4 hours. The final product was subjected to a sequence of five washes using ethanol and distilled water until it reached pH 7, followed by a further drying procedure at 100 °C for one hour. This reaction can be described as the following equations:



This procedure was repeated at 200 °C to investigate the effect of temperature on the formation of CuO.

### 3.4 Preparation of CuO- rGO Nanocomposites

The synthesis of CuO- rGO was accomplished by a single-step hydrothermal method. Initially, 0.5 grams of GO powder was subjected to ultrasonic dispersion in 100 mL of deionized water for 30 minutes, forming a uniform brown-colored solution. Subsequently, 2 grams of  $\text{Cu}(\text{NO}_3)_2 \cdot 3\text{H}_2\text{O}$  was introduced into the acquired dispersion, stirring for 15 minutes. Subsequently, a solution of NaOH (1 M) was gradually introduced

into the mixture while maintaining constant stirring for an additional duration of 30 minutes. The pH value of the composites was determined and recorded as 9. Subsequently, the resultant mixture was transferred into a sealed autoclave with a volume of 100 mL and subjected to thermal treatment in an oven set at a temperature of 100 °C for 4 hours. The composite material was subjected to five washes using ethanol and deionized water until it achieved a pH of 7. The final product was dried in the furnace at 100 °C for one hour. The schematic representation of the fabrication process is depicted in figure (3.2). Different amounts of GO (1 gram, 2 grams) were employed to clarify its impact on the nanocomposites. This procedure was repeated at 200 °C to investigate the effect of temperature on the nanocomposites.

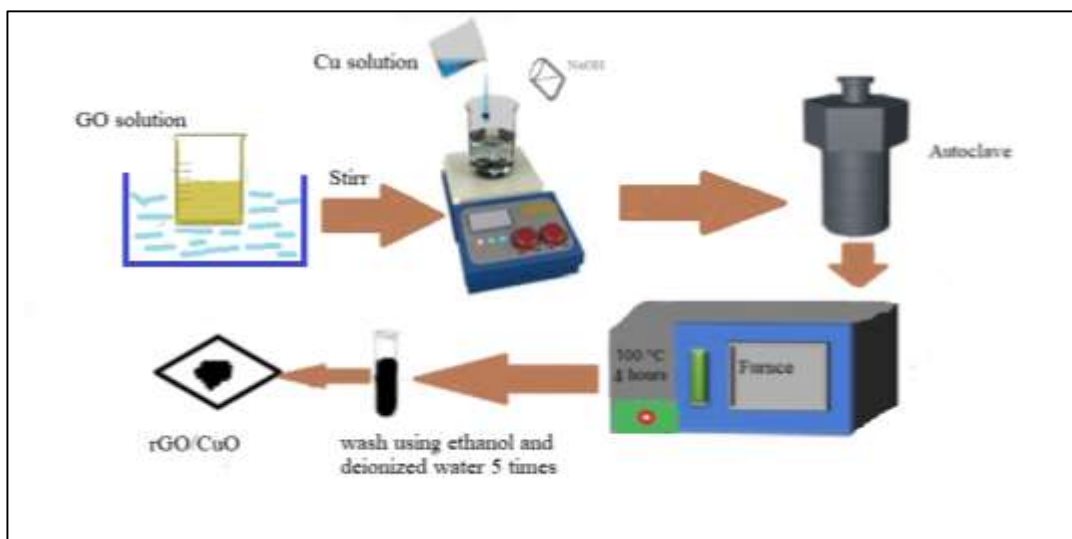


**Figure (3.2): Schematic diagram of the preparation process of rGO/CuO.**

### 3.5 Preparation of Substrates

The selection of glass as a substrate was based on its transparency of light and low cost. The glass substrate was cut to 2.5 cm × 2.5 cm. The substrates underwent a cleaning process involving immersion in a detergent solution,

distilled water, and alcohol, then sonication for 30 minutes. The substrates were washed with distilled water and dried on a hot plate for 10 minutes.

### **3.6 Deposition of rGO, CuO, CuO-rGO on Glass Substrates**

Figure (3.3) shows the dip coating technique that has been chosen for the deposition of thin metal oxide films due to its simplicity and cost-effectiveness, ranging from a few nanometers to a micrometer. It can produce a homogeneous film with a large area, high crystallinity, excellent thickness, and phase purity at surrounding deposition conditions.

Following the preparation of the substrate, 100 mL was taken from each sample and subjected to sonication for 30 minutes to achieve a uniform solution. This methodology involves a series of sequential steps. Initially, the glass substrates were immersed in a 100 mL beaker containing solutions with an average rate of 0.11 mm/s. The subsequent procedure involved maintaining the substrate within the beaker for 5 minutes. The third step involved pulling the sample at the same speed. The final step entails subjecting the sample to a drying process at a temperature of 90 °C on a hot plate for 10 minutes. This procedure facilitates the evaporation of the solvent and achieves the desired outcome of an ultra-thin layer. This process is iterated five times for each sample to acquire a uniform thin layer. The deposited films undergo annealing in an electric furnace at 400 °C for two hours.

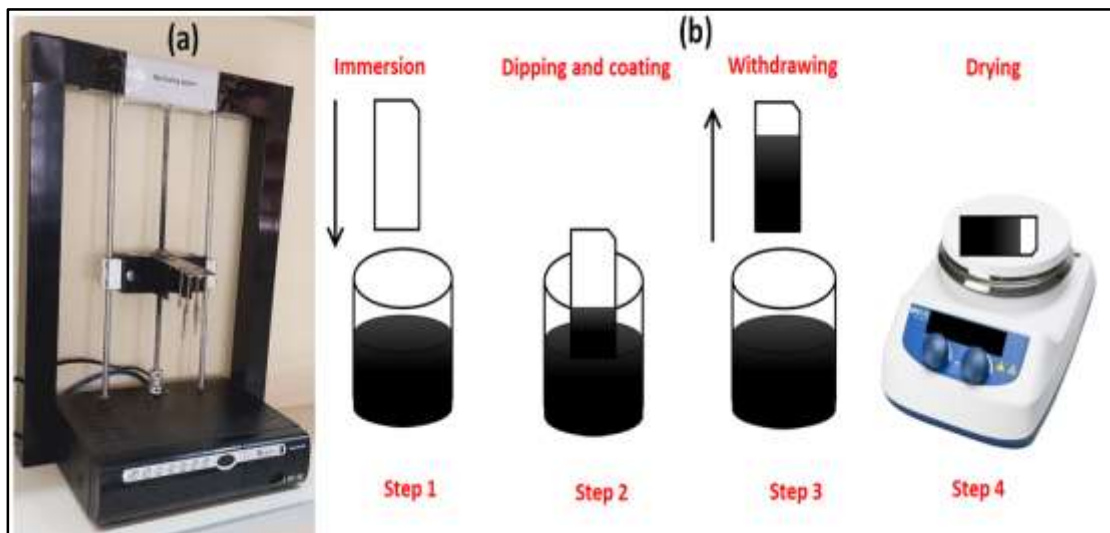


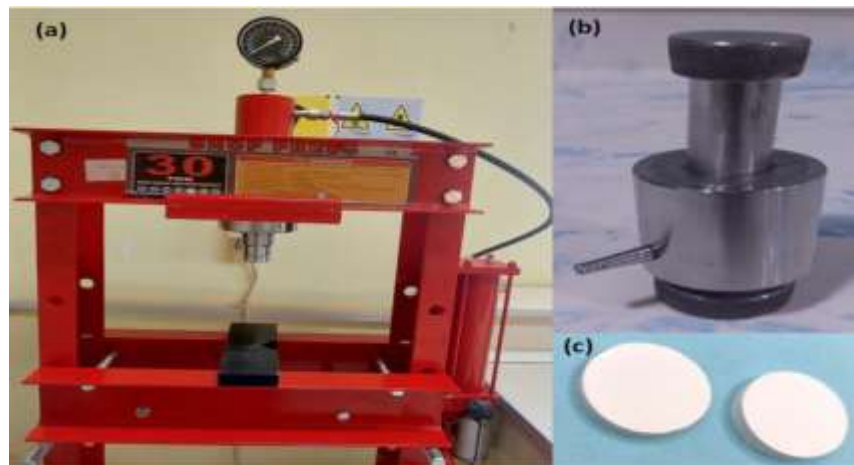
Figure (3.3): (a) Dip-coating system, (b) the basic process of dip-coating.



Figure (3.4): Electric furnace [117].

### 3.7 Compression of SnO<sub>2</sub> Powder

Compression procedures were carried out utilizing a device designed specifically for this objective. The tool employed in this investigation is a steel cylindrical mold with an internal diameter of 20 mm, as illustrated in figure (3.5). Following the insertion of 3 grams of SnO<sub>2</sub> material into the mold, it was compressed at a rate of 10 tons for 10 minutes to produce a disc of 20 mm in diameter and 3 mm in thickness; this disc will be utilized as a PLD target after annealing it to 1000 °C for two hours.



**Figure (3.5): The piston of powder compression: (a) piston, (b) mold, (c) powder pellets.**

### 3.8 Deposition of SnO<sub>2</sub> by PLD

The experimental technique employed for this work was PLD, which involved the utilization of a Q-switched pulsed (Nd: YAG) laser Second Harmonic Generation (SHG) as shown in Figure (3.6). The laser operates at a repetition rate of 6 Hz and emits laser pulses with duration of 10 ns at a wavelength of 1064 nm. The PLD setup includes a laser, a chamber of reaction, a vacuum pump, a target (SnO<sub>2</sub>), and a substrate. The primary vacuum chamber is a stainless - steel chamber with a diameter of 30 cm. It is highly evacuated, with a pressure of 10<sup>-3</sup> mbar. The chamber is securely attached to an HSS-stainless steel flange, which has a groove with an O-ring for vacuum sealing. Additionally, there is a feed-through in the base of the flange for electrical connections. These connections allow controlling of the motor rotation and the substrate heater and are connected to an external power supply. The target was placed parallel to the substrate, and the pump evacuated the chamber into a vacuum. The target was mounted on a rotating target holder to provide uniform ablation with minimum change in the target



surface geometry. At the same time, the substrate was held stationary on a substrate holder. The distance between the substrate and the target was fixed at 3.5cm. The target was exposed to laser radiation at a  $45^\circ$  angle of incidence using a laser beam operating under vacuum conditions of  $10^{-3}$  mbar. When the laser beams hit the target, the temperature rises until it reaches a state of ionization (the plasma state). At this point, the atoms move from the surface of the target to the substrate, and we get a thin coating with strong adherence. The laser fluence was  $2.8 \text{ J/cm}^2$ , and the number of pulses was 120 for all samples.



**Figure (3.6): Pulsed laser deposition system.**

## **3.9 Samples Characterization**

### **3.9.1 Energy Dispersive X-Ray Spectroscopy (EDX)**

An indispensable tool for ascertaining the elemental composition of a particular surface area on which a stationary electron beam is concentrated is EDX. This method is frequently combined with SEM, which measures the elemental composition of the samples which observed by energy dispersive

X-ray spectroscopy. The elemental composition was done using EBSD Instrument: FESEM- Imaging-EDS-Mapping-Line-EBSD/Germany and all the samples under testing were in powdered form.

### 3.9.2 Fourier Transform Infrared Spectroscopy (FTIR)

The FTIR spectroscopy analysis was conducted using FTIR – 8400S (Shimadzu), which studied harmonic vibrations using the mid-infrared area between the frequency range of 400 to 4000  $\text{cm}^{-1}$ . The samples were prepared using the potassium bromide (KBr) procedure, in which the samples were ground into a powder and mixed with KBr powder. Crushing KBr is crucial to prevent light dispersion caused by the substantial dimensions of the KBr crystals. Subsequently, the mixture was crushed using a mechanical die press to shape a pellet with a translucent appearance. A sample holder was used to secure the pellet, allowing the IR laser to flow through it.

FTIR is a non-destructive technique for determining the specific effective groups in organic and inorganic materials such as polymers and metal oxides. The sample is analyzed using an infrared beam that passes through it, and the absorption of radiation is calculated as a function of frequency. The wavelength at which the specimen absorbs infrared radiation is shown in the FTIR spectrum. This permits the effective groups, chemical bonding, molecular structure, and chemicals in the sample to be identified. The prepared samples were examined at the University of Kerbala, College of Science.

### 3.9.3 X-Ray Diffraction (XRD)

XRD, SHEMADZU / Japan, was utilized for characterizations the structural properties of the thin films. XRD is an essential technique to analyze the phases and crystalline structures of various materials. It is possible to determine the Miller index, position of diffraction peak, and relative intensity of unidentified substances by comparing diffraction data and the diffraction pattern provided by the Joint Committee on Powder Diffraction Standard (JCPDS). The X-ray diffractions were performed with a Philips X-ray diffractometer system, which measures intensity as a function of Bragg's angle. The radiation source is Cu K $\alpha$  with a wavelength of (1.5406 Å), a current of (30 mA), and a voltage of (40 KV). The scanning angle was adjusted in the range of (10 - 80) degrees at a scanning rate of 4-degree/min rate.

### 3.9.4 Field Emission Scanning Electron Microscope (FESEM)

The FESEM is a versatile tool that may be employed for high-resolution and magnification imaging of many materials, enabling the analysis of sample structure and the surface topography and morphology, which uses electrons instead of light to compose images. A high-energy electron beam originates from the electron gun in a vacuum column positioned above the sample's surface. When the electron beam is directed toward the target surface, the interaction between the low-angle backscattered electrons and the surface atoms generates diverse electronic signals. For chemical composition determination and elemental analysis and mapping, EBSD Instrument: FESEM- Imaging-EDS-Mapping-Line-EBSD/Germany was used to examine the prepared samples.

### **3.9.5 Transmission Electron Microscopy (TEM)**

TEM is a microscopy technique that uses high-energy electrons to pass through specimens, providing detailed information about the morphology, composition, and crystallography of the samples. TEM is a vital tool for confirming the production of nanocomposites. This microscopy operates on the same fundamental premise as light microscopy, with the main difference being the use of electrons instead of photons, resulting in the generation of shorter wavelengths. TEM Instrument ZEISS LEO 912 AB/Germany was utilized to examine samples in this work.

### **3.9.6 Brunauer-Emmett-Teller (BET)**

The establishment of a surface area analysis method was based on the BET theory, named after Stephen Brunauer, Paul Hugh Emmett, and Edward Teller. These researchers expanded upon Langmuir's theory by applying it to a multilayer of absorbed gases. They assumed that the absorbed gas layers do not interact with one another. This particular technique is employed for approximating surface areas. The BET theory works for systems with multilayer adsorption and usually uses inert gases that don't react chemically with material surfaces to measure the area of a particular surface. Nitrogen is the gaseous adsorbate that used for BET surface testing. This work conducts BET analysis at 77 K, corresponding to nitrogen's boiling point ( $N_2$ ) using BET/BJH Micromeritics MicroActive for TriStar II Plus Microtrac Bel Cor BEISORP Min.

### **3.9.7 Atomic Force Microscope (AFM)**

AFM, an early iteration of scanning probes, was pivotal in advancing nanotechnology. It was employed to investigate the morphological

characteristics of the thin film being deposited. A typical atomic force microscope comprises a microfabricated cantilever with a sharp tip that features on the surface of a sample that can bend. A laser beam hits the back of the cantilever. It bounces back into a set of Photodetector, enabling the measurement of the deflection of the cantilever and then turning that information into a picture of the surface. The image was analyzed with software to determine the grain size and surface roughness. The data collection for this study was conducted using AFM/ SPM DualScope™ DS/Germany with N<sub>2</sub> gas at 77 K.

### **3.9.8 Film Thickness Measurements**

The film thickness and topography were determined by atomic force microscopy (AFM), which measured and scanned its surface with a tiny probe. The scratch-and-scan approach involves using a hard tool, such as a needle or scalpel, to remove the thin film layer until the underlying substrate is exposed. Then, a thorough scan of the scratch should be conducted. The scanned image might be utilized to determine the thickness of the thin film through a cross-sectional profile. It is imperative to ensure that the thin film is entirely removed through scratching while also ensuring that the substrate underlying the thin film remains unscratched.

### **3.9.9 Thermogravimetric Analysis (TGA)**

The TGA technology is employed to assess the alterations in the mass of specimens in correlation with variations in their temperatures. This method facilitates the determination of the degradation temperature of the materials and the breakdown point of any solvent residues that may be present within

the samples. The TGA measurements were combined with DTA to facilitate the identification of any phase transitions that may occur in the material during the heating process. This study investigates the thermal stability of the nanocomposites in a nitrogen atmosphere, with a temperature range (25 – 800 °C) with an increase of 50 °C  $min^{-1}$  by TGA/DTA/DTG Mettler-Toledo USA.

### 3.9.10 Ultraviolet-Visible Spectroscopy (UV)

The UV-visible absorption spectrum of all samples was recorded for the range of (190-1200 nm) by Shimadzu-UV-VIS Spectra-photometer UV-1900i in Kerbala University, College of Science, Department of Physics.

## 3.11 Gas sensor

### 3.11.1 Interdigitated Electrodes (IDE) Deposition

Sensor fabrication involves a specific mask made of a stainless-steel plate with a thickness of 0.5 mm, which must be placed on the top of the film's surface. A pair of electrodes made of gold in the shape of fringes, was deposited on the top of a thin film by the sputtering deposition method using the mask. PVD is ion plating, which involves extracting ions using plasma to create an ion beam. In a conventional ion beam deposition system, gold ions are generated through plasma sputtering of a cathode onto the surface of the substrate to be coated using an ion source. Samples of glass containing the film were placed on the base, where the target was the gold material inside the chamber designated for deposition. Each electrode has 10 fringes with a spacing of 200  $\mu m$ . The width of the fringes was 350  $\mu m$ . Figure (3.7) illustrates the sputtering system and IDE.

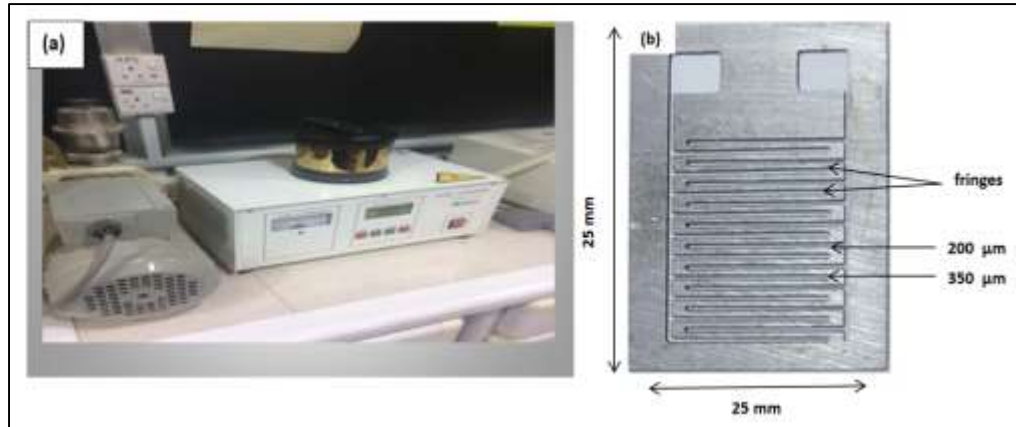


**Figure (3.7): (a) Sputtering system, (b) mask dimensions.**

### 3.11.2 Gas Sensor System Design

Figure (3.8) illustrates the gas sensor system which includes three parts:

- The gas chamber to be examined has a sensing film and is constructed from a cylindrical stainless-steel chamber with a diameter of 20 cm and a height of 20 cm. The total volume of the chamber is 6.28 liter. The chamber is evacuated using a rotary pump. The device is equipped with an inlet to facilitate the input of the tested gas and an air admittance valve to enable ambient air entry following evacuation. The establishment of electrical connections to the heater, thermocouple, and sensor electrodes is facilitated by a multi-pin feed through located at the base of the chamber. The working temperature of the sensor was regulated by utilizing a heater-controlled thermocouple located within the chamber. The sensor heaters were connected to an external power supply, allowing accurate temperature setting and control.
- An injection system comprises mass flow controllers, pressure regulators, and a timer. This system controls the gas flow inside the

chamber using an electric valve. The chamber is connected to the carrier gas using Teflon tubing.

The measurement system enables monitoring of the sensor's electrical resistance during gas exposure. The work involved utilizing a digital millimeter, a power supply, and a personal computer. The purpose was to evaluate the changes in sensor resistance resulting from exposure to a mixture of nitrogen and target gas facilitated by flow meters. The electrical measurements are acquired using a printed circuit board and positioned below the chamber. Figure (3.9) illustrates a schematic diagram for the gas sensor system.

### 3.11.3 Procedure of Gas Sensing Measurement Testing

1. The test chamber is opened, and the sensor is set on the heater. The electrical connections between the pin feed through, sensor spring-loaded pins, and thermocouple are done. Then, the chamber has been closed.
2. The rotary pump then turns on to evacuate the test chamber to around  $1 \times 10^{-1}$  bar. A temperature controller is used to set the sensor's desired operating temperature.
3. Set the carrier gas (air or analytic gas) flow rate utilizing the mass flow controllers.
4. Subsequently, the gas with a predetermined concentration in the mixing chamber is introduced into the test chamber by turning on the two-way valve.
5. The resistance fluctuation of the sensor in a known concentration of test gas with the air mixing ratio is measured using two flow meters.



6. Following the reading, the mass flow rate was deactivated in order to restore the sensor's current to its original value,  $R_0$ .

7. These measurements are performed for the additional temperatures.



Figure (3.8): Gas sensor system.

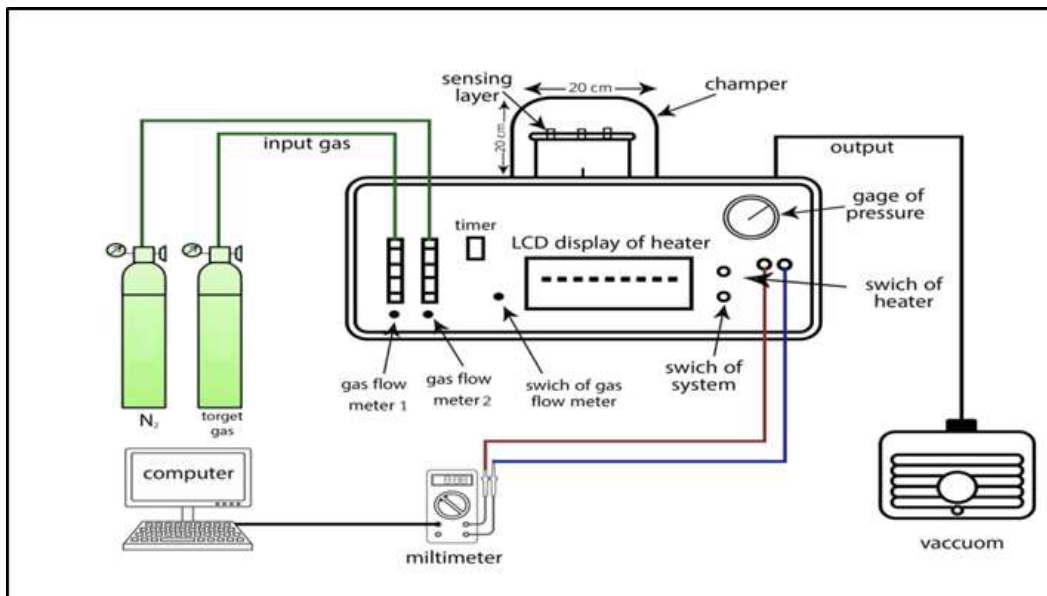


Figure (3.9): Schematic diagram for gas sensor system.

# **Chapter Four**

## **Results and Discussion**

## 4.1 Introduction

This chapter will show the comprehensive experimental results and sensing performance characteristics of thin films made from rGO, CuO, and SnO<sub>2</sub>/ CuO-rGO nanoparticles when exposed to NH<sub>3</sub> and H<sub>2</sub>S gases. The effect of optimization of preparation temperature on the morphology, structure, and optical characteristics will be presented. An investigation will be carried out on key aspects of sensor properties. The factors to consider are sensitivity, response and recovery time, and the optimal working temperature. Table (4.1) shows all prepared samples with different amount of GO and preparation temperatures.

**Table (4.1) Samples prepared hydrothermally with different parameters.**

Molecular formula	Sample	Temperature (°C)	Time of preparation(hour)
rGO pure	rGO <sub>100</sub>		
(0.25:1) rGO: CuO	S1		
(0.5:1) rGO: CuO	S2	100	
(1:1) rGO: CuO	S3		
CuO pure	CuO <sub>100</sub>		4
rGO pure	rGO <sub>200</sub>		
(0.25:1) rGO: CuO	S4		
(0.5:1) rGO: CuO	S5	200	
(1:1) rGO: CuO	S6		
CuO pure	CuO <sub>200</sub>		

## 4.2 Energy Dispersive X-Ray Spectroscopy Analysis

### 4.2.1 GO and rGO Samples

EDX analysis was conducted to confirm the basic structure of the synthetic composites generated using the hydrothermal process. Figure (4.24) displayed the EDX spectra of GO and rGO samples. The GO sample results, shown in figure (4.1-a), indicated that the atomic ratio of O:C in GO was 15.79:84.21. The ratio reduced to 12.66:87.33, indicating a reduction in oxygen in rGO<sub>100</sub> as a result of the reduction process. When the preparation temperature reached 200 °C, the O:C ratio decreased to 7.53:92.46 as a result of the reduction of GO and the loss of active functional groups.

### 4.2.2 CuO Samples

Figure (4.2) shows the chemical composition of the CuO prepared at 100 °C and 200 °C by hydrothermal method. The EDX characterization of the CuO<sub>100</sub> reveals the presence of copper and oxygen in the rod-like structure with the atomic ratio of Cu:O at 52.75:47.24, proving the existence CuO. No other impurities are shown which confirms the purity of the final product. No essential changes have been observed on the CuO<sub>200</sub> sample which was prepared at 200 °C which has an atomic ratio of 53.25:46.74 as shown in figure (4.2).

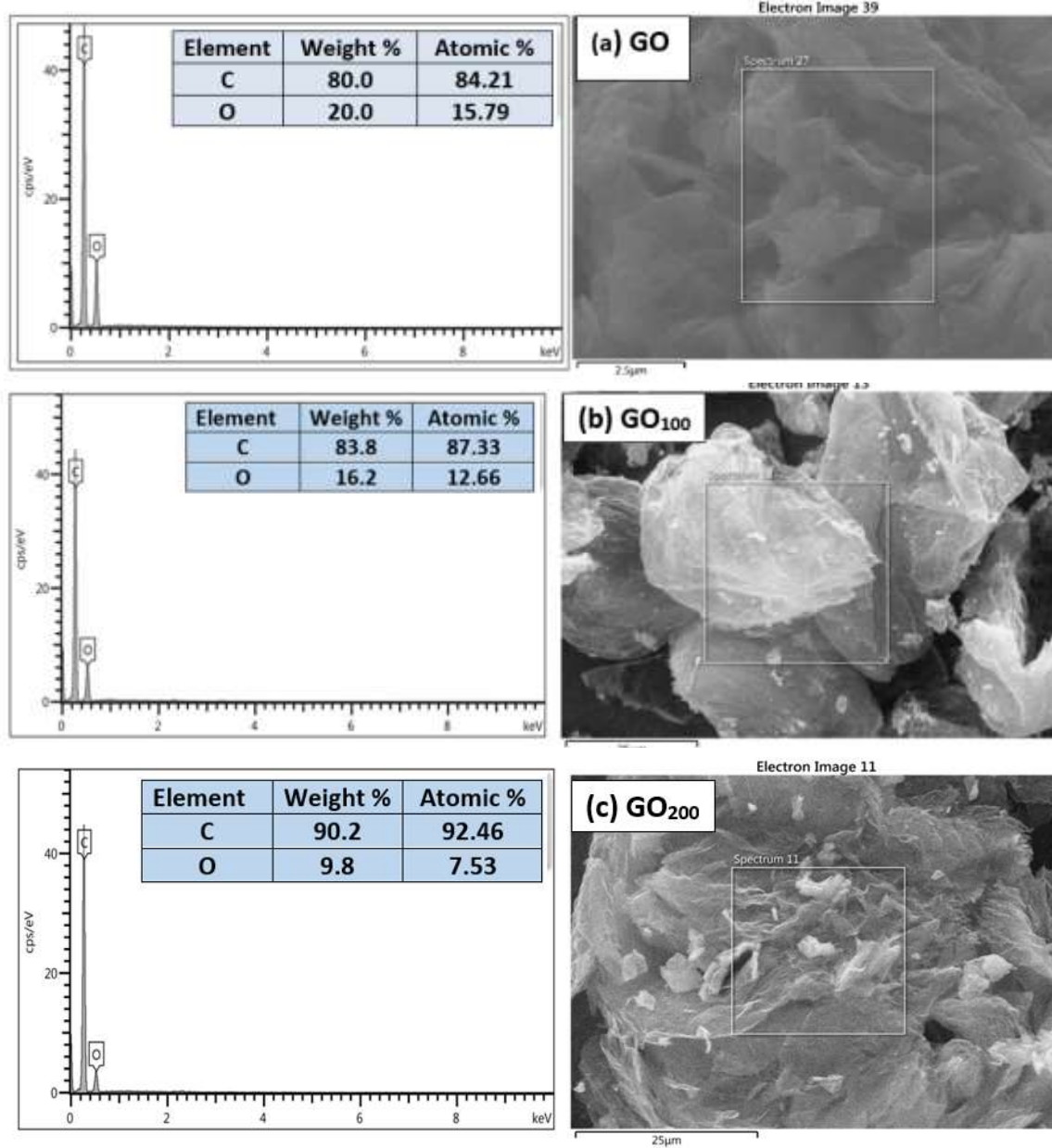


Figure (4.1): EDX spectrum and elemental mapping of (a) GO, (b) rGO<sub>100</sub>, and (c) rGO<sub>200</sub>.

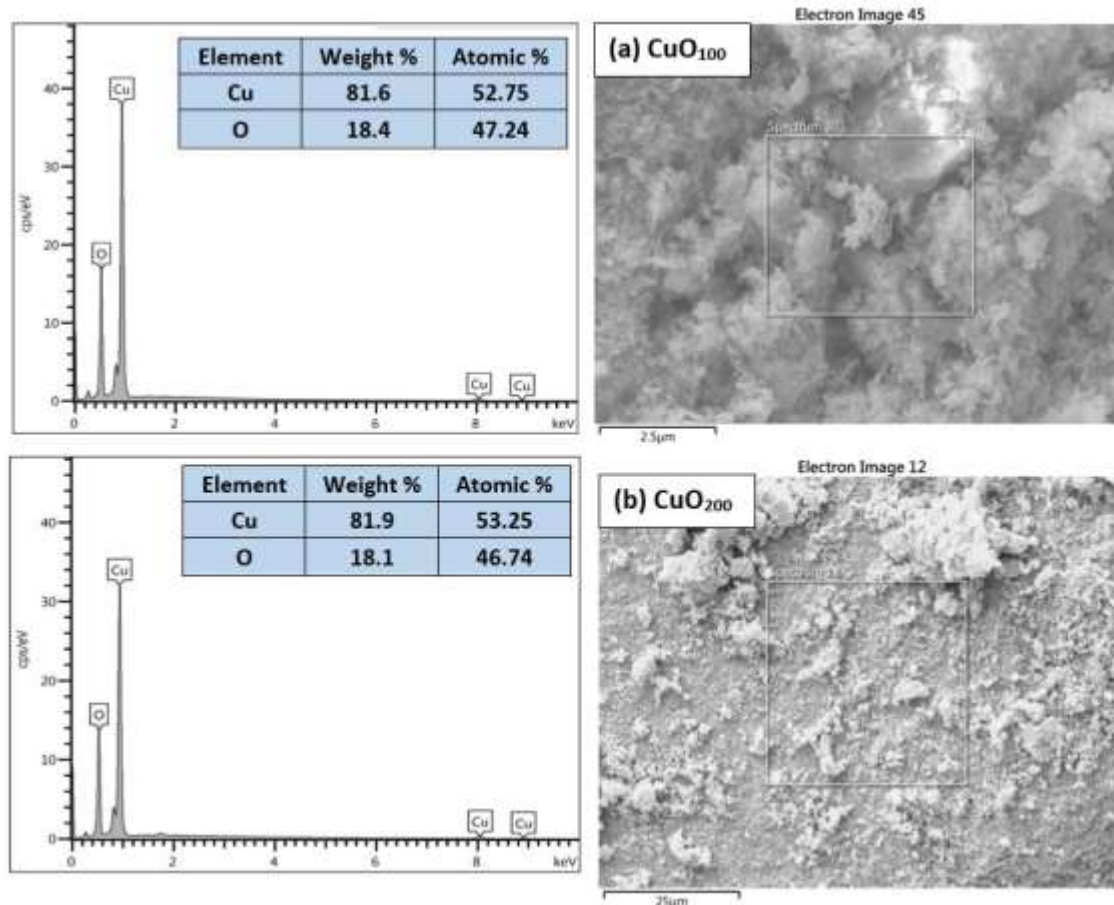
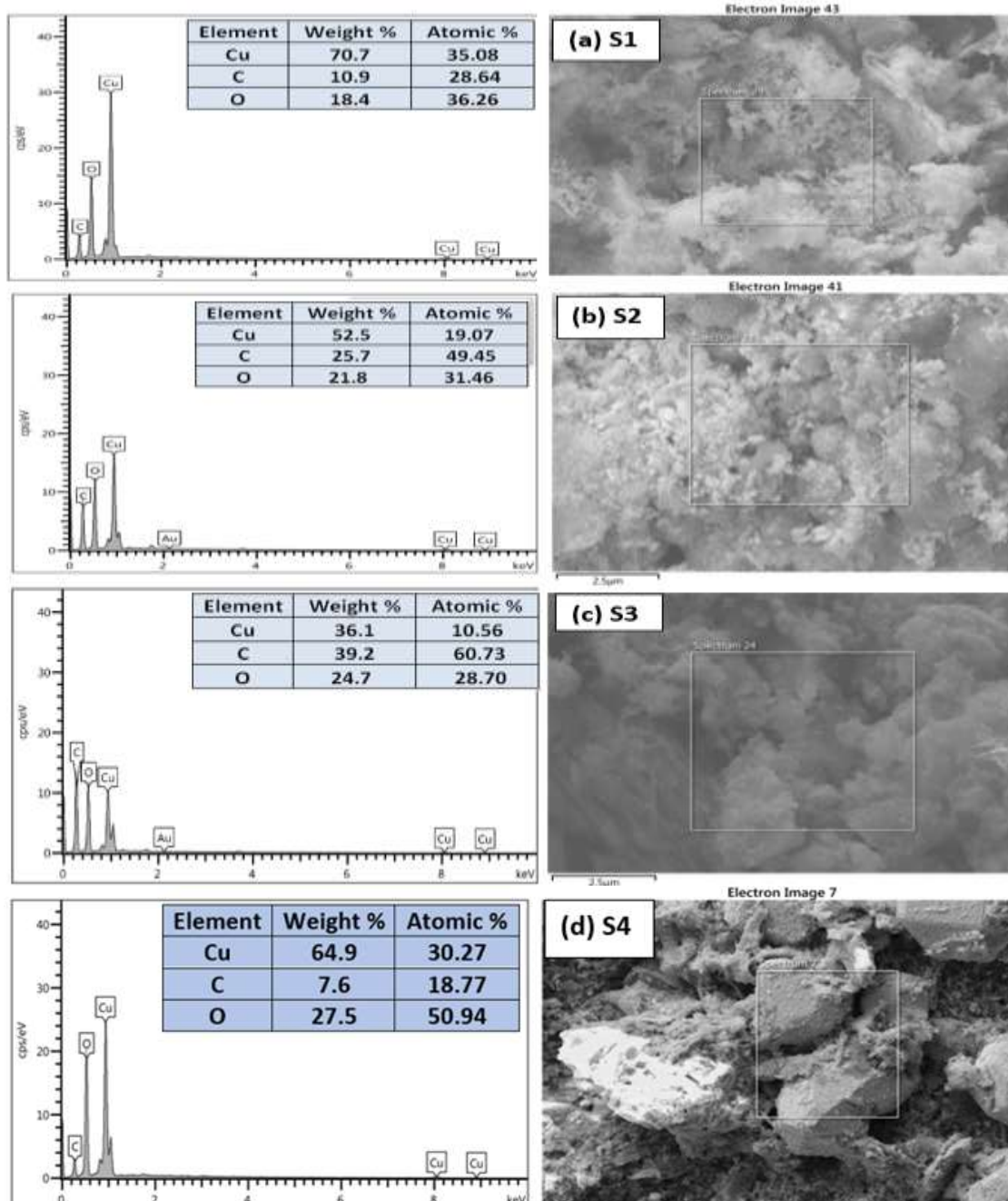


Figure (4.2): EDX spectrum of (a)  $\text{CuO}_{100}$ , (b)  $\text{CuO}_{200}$ .

### 4.2.3 CuO- rGO Samples

To prove the interstitial structure (elementary structure) of the synthetic composites previously prepared by hydrothermal method, EDX was performed and showed that Cu, O, and C are the main elements for samples S1, S2, and S3, and no other impurities as shown in figure (4.3, a- c). This indicates the successful production of nanocomposites. Figure (4.3, d-f) shows the main elements of CuO- rGO prepared at 200 °C. A difference in the weight and atomic percentages of Cu and C were observed in samples S4, S5, and S6.

The atomic percentages of Cu, O, and C are shown in Table (4.8). The decrease in copper content in samples corresponds to an increase in GO concentration in the nanocomposites.



Continued...

Continued

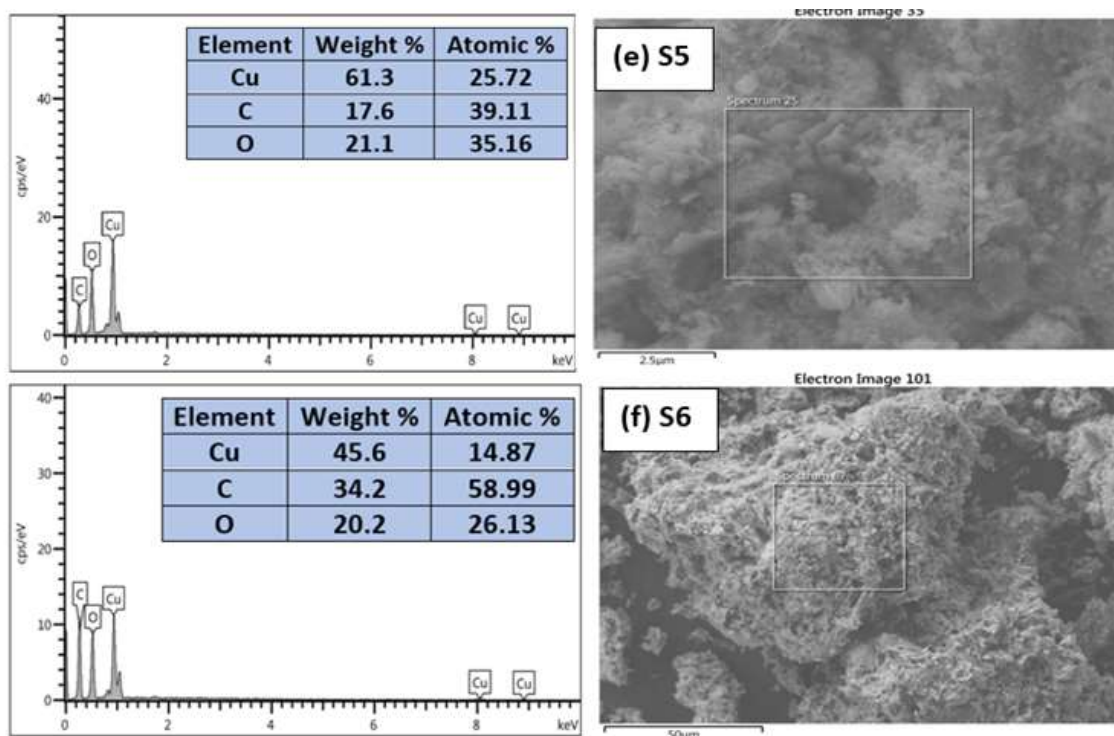


Figure (4.3): EDX spectrum of (a) S1, (b) S2, (c) S3, (d) S4, (e) S5, and (f) S6.

Table (4.2): EDX spectra of CuO- rGO samples prepared at 100 °C and 200 °C

Sample	Cu Atomic%	C Atomic%	O Atomic%
S1	35.08	28.64	36.26
S2	19.07	49.45	31.46
S3	10.56	60.73	28.70
S4	30.27	18.77	50.94
S5	25.72	39.11	35.16
S6	14.87	58.29	26.13

### 4.3 X-Ray Diffraction

To study the impact of temperature on the prepared samples, two different temperatures were chosen for preparation: 100 °C and 200 °C. As prepared and after annealing samples were examined using XRD as follow:



### 4.3.1 Samples Prepared at 100 °C

#### 4.3.1.1 GO and rGO

Figure (4.4) displays the XRD results of GO, as prepared and after annealing at 400 °C of rGO powder. The main diffraction peaks associated with GO had been found at  $2\theta$  of  $17.02^\circ$  (001),  $42.44^\circ$  (100), and  $77.96^\circ$  (110), which closely matched the JCPDS card (00-001-0646) for graphite. Thermal reduction at 100 °C resulted in the creation of a new, weak peak at  $25.02^\circ$  (002), which is associated with the exfoliation of GO. This observation had indicated a partial reduction. After thermal annealing to 400 °C the intensity of the peak of GO decreased and was observed at  $11.69^\circ$ . From the figure, it can be inferred that the peaks associated with GO suggest an insufficient reduction of graphene oxide at 100 °C, even after annealing which in agreement with [118].

After thermal reduction, eliminating some oxygen-active groups from the GO leads to a significant shift in lattice constant, d-spacing, and crystal size, as indicated in Table (4.3). It can be seen from this table that the average crystallite size increases after annealing. The increase in the crystallite size confirms recrystallization of the atoms into lattice structure due to thermal energy generated by annealing process. This energy helps atoms to align themselves into the plane with lowest free surface energy, and small crystallites were aggregated after annealing to form larger crystallites which improved upon annealing [119]. The average size of rGO before and after annealing was 4.2 nm, and 25.9 nm, respectively.

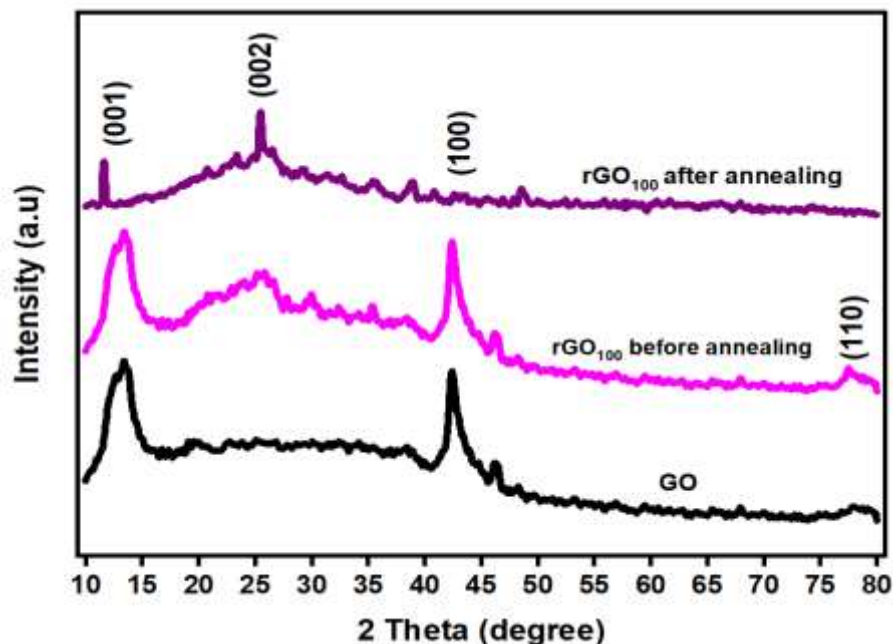


Figure (4.4): XRD-results of GO and rGO<sub>100</sub> before and after annealing at 400 °C.

Table (4.3): XRD data of rGO<sub>100</sub> before and after annealing.

		Before annealing			After annealing				
2θ (°)	d (Å)	(hkl)	FWHM (°)	Crystallite size (nm)	2θ (°)	d (Å)	(hkl)	FWHM (°)	Crystallite size (nm)
13.4	6.724	(001)	2.532	3.2	13.69	7.562	(001)	0.280	29.6
25.5	3.586	(002)	3.686	2.3	25.50	3.489	(002)	0.381	22.2
42.5	2.096	(100)	2.333	3.8					
77.6	1.230	(110)	1.440	7.3					
<b>Average crystallite size</b>				<b>4.2</b>	<b>Average crystallite size</b>				<b>25.9</b>

#### 4.3.1. 2 CuO

The main peaks of the as prepared and annealed CuO are illustrated in figure (4.5). It can be seen that the single phase of CuO (tenorite) can be observed with distinct diffraction peaks at 2θ of 32.6°, 35.48°, 38.72°,

48.68°, 53.2°, 58.1 °, 61.55°, 66.2°, 68°, 72°, 75.127° corresponding to (110), (-111), (111), (-112), (-202), (020), (202), (-113), (022), (220), (311) with lattice constant  $a = 4.684 \text{ \AA}$ ,  $b = 3.0425 \text{ \AA}$ ,  $c = 5.129 \text{ \AA}$  according to JCPDS card (00-005-0661) of CuO. No noticeable alterations had been detected following the process of annealing, except an augmentation in the intensity and distinctness of the peaks.

This suggests an enhancement in the crystalline structure after annealing. Table (4.4) shows the XRD data before and after annealing for CuO<sub>100</sub>. It was found that the average crystallite size increased from 11.3 nm to 11.4 nm after annealing, which matches well with previous studies [119].

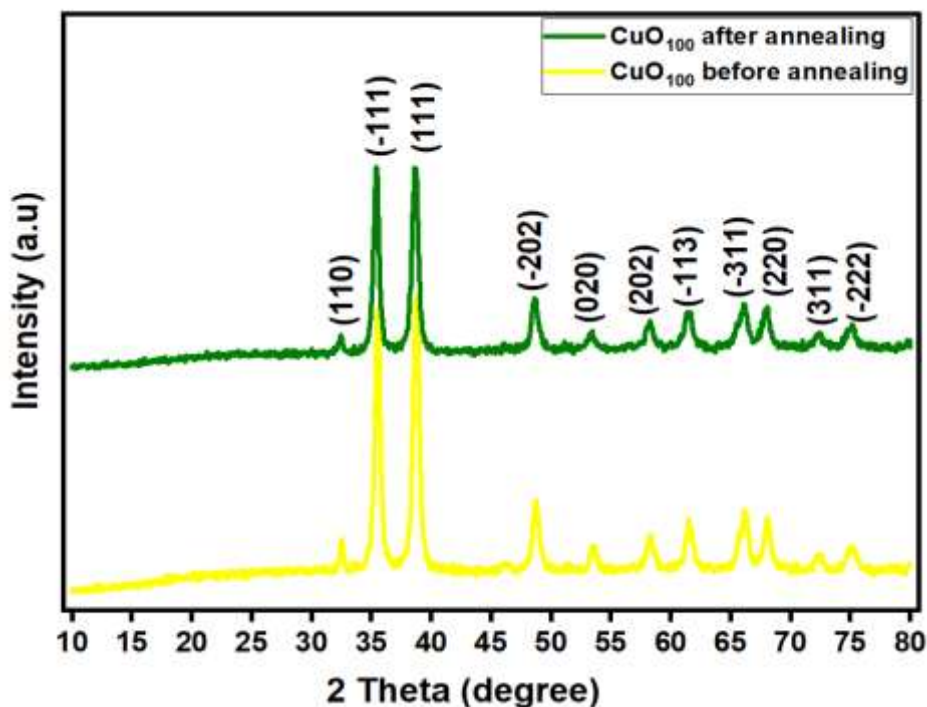


Figure (4.5): XRD of CuO<sub>100</sub> nanocomposites before and after annealing at 400 °C.

**Table (4.4): XRD data of CuO<sub>100</sub> before and after annealing.**

Before annealing					After annealing				
2θ (°)	d (Å)	(hkl)	FWHM (°)	Crystallite size (nm)	2θ (°)	d (Å)	(hkl)	FWHM (°)	Crystallite size (nm)
32.4	2.75	(110)	0.450	17.6	32.4	2.758	(110)	0.493	16.1
35.4	2.530	(-111)	0.539	14.6	35.4	2.531	(-111)	0.571	13.8
38.6	2.323	(111)	0.598	13.0	38.6	2.362	(111)	0.586	13.3
48.6	1.866	(-202)	0.619	12.2	48.6	1.869	(-202)	0.558	11.4
53.5	1.714	(020)	0.685	10.8	53.3	1.751	(020)	0.690	10.7
58.2	1.582	(202)	0.681	10.6	58.2	1.583	(202)	0.635	11.4
61.6	1.506	(-113)	0.695	10.2	61.5	1.507	(-113)	0.663	10.7
66.0	1.410	(-311)	0.764	9.1	66.1	1.414	(-311)	0.664	10.4
68.1	1.376	(220)	0.792	8.6	68.1	1.378	(220)	0.647	10.6
72.4	1.304	(311)	0.648	10.3	72.3	1.304	(311)	0.684	9.7
75.1	1.262	(-222)	0.921	7.1	75.2	1.265	(-222)	0.851	7.7
<b>Average crystallite size</b>				<b>11.3</b>	<b>Average crystallite size</b>				<b>11.4</b>

### 4.3.1. 3 CuO-rGO

The impact of the amount of GO on the formation of CuO-rGO nanocomposites can be demonstrated using XRD analysis of the samples (0.5 gram, 1 gram, and 2 gram of graphene oxide added to copper nitrate). The samples are named (S1, S2 and S3) respectively, for simplicity. Figure (4.6) shows the XRD results of all samples before and after annealing. S1 showed high-intensity peaks with a single phase of CuO with lattice constant  $a = 4.684 \text{ \AA}$ ,  $b = 3.0425 \text{ \AA}$ ,  $c = 5.129 \text{ \AA}$ , which is consistent with the data from JCPDS card (00-005-0661) of CuO. A small and weak peak appeared at  $2\theta$  equal to  $42^\circ$  (100) due to disordered stacking for rGO layers in the composites, which is consistent with previous work [120].

In the case of S2, a strong and sharp peak at  $2\theta$  of  $36.54^\circ$  (211) related to cubic phase of  $\text{Cu}_2\text{O}$  with d-spacing of  $2.5 \text{ nm}$ , in addition to other weak and small peaks at  $42.329^\circ$  (220) and  $77.417^\circ$  (422) plans accordance with the JCPDS card (00-002-1067). These results were similar in to that reported in [121]. No peaks related to rGO appeared for this sample perhaps because of strong peak of  $\text{Cu}_2\text{O}$  and low diffraction intensity of rGO in the nanocomposites.

Two phases were observed for the S3 sample, tenorite ( $\text{CuO}$ ) and cuprite ( $\text{Cu}_2\text{O}$ ), and the tenorite phase was predominated. The peak corresponding to  $\text{Cu}_2\text{O}$  was observed at  $29^\circ$  (200) according to the JCPDS card (00-002-1067) of  $\text{Cu}_2\text{O}$ . Other weak and broad peaks related to GO appeared at  $16^\circ$  (001),  $26^\circ$  (002), and  $42^\circ$  (100) due to an increase in the amount of GO in the nanocomposites. These results correspond with [122].

The XRD analysis of S1 did not reveal any shift in the peak positions after annealing, except for an increase in crystallinity. In contrast, only one phase of tenorite has been detected in the case of S2, suggesting a rise in the crystallites during annealing, but two phases of  $\text{CuO}$  were observed in the case of S3. The distinct peak of rGO exhibits a significant decrease in intensity or completely vanishes in all three samples. This can be ascribed to the strong effect of  $\text{CuO}$ , which effectively inhibited the growth of rGO. These results correspond with [123]. Upon annealing, the reduction of GO was not completely achieved, leading to the presence of a weak diffraction peak that remained. The size of the nanostructures can be substantially modified by altering the amount of GO present in them. These results correspond with previously obtained [124]. Moreover, annealing led to a rise in the average crystallite size for all samples. These findings align with

earlier research [125]. Table (4.5) shows the XRD data for all samples before and after annealing. The average crystallite size for samples S1, S2, and S3 was 11.6 nm, 27.3 nm, and 14.9 nm, respectively, before annealing and 12.3 nm, 27.4 nm, and 25.3 nm after annealing.

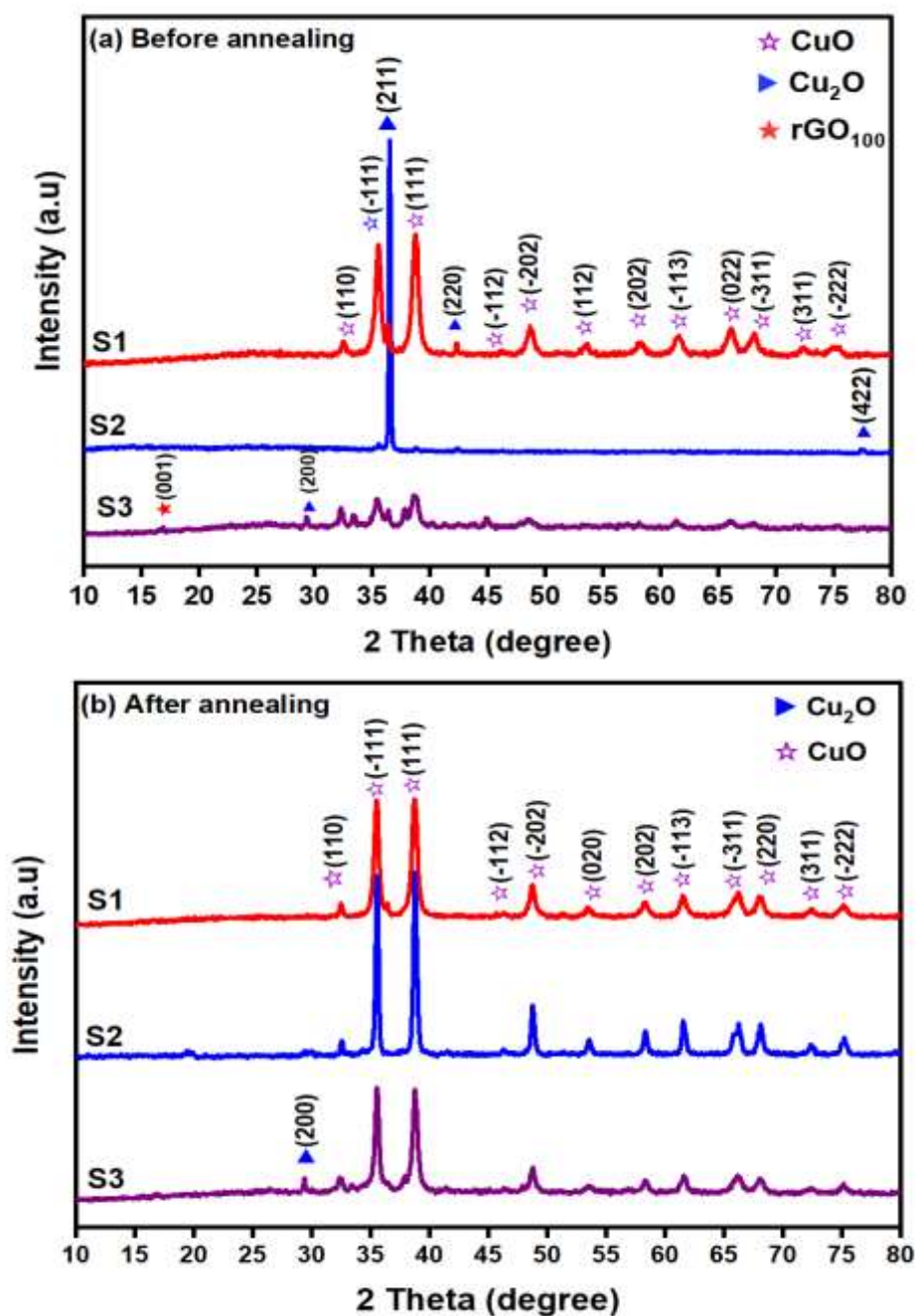


Figure (4.6): XRD of CuO-rGO nanocomposites prepared at 100 °C before and after annealing at 400 °C

Table (4.5): XRD data of CuO-rGO samples before and after annealing.

Sample	Before annealing					After annealing				
	2 $\theta$ (°)	d(Å)	(hkl)	FWHM (°)	Crystallite size (nm)	2 $\theta$ (°)	d(Å)	(hkl)	FWHM (°)	Crystallite size (nm)
S1	32.0	2.70	(110)	0.310	20.2	32.0	2.75	(110)	0.436	18.2
	35.4	2.03	(-111)	0.602	13.1	35.0	2.53	(-111)	0.504	15.6
	38.7	2.31	(111)	0.600	11.9	38.7	2.31	(111)	0.563	13.8
	42.3	2.13	(100)	0.430	17.9	48.7	1.86	(-202)	0.530	14.1
	48.7	1.86	(-202)	0.736	10.2	53.0	1.71	(020)	0.580	12.6
	53.0	1.71	(020)	0.630	11.6	58.2	1.58	(202)	0.600	11.9
	58.2	1.58	(202)	0.898	8.0	61.5	1.50	(-113)	0.599	11.8
	61.5	1.50	(-113)	0.823	8.6	66.0	1.41	(-311)	0.611	7.6
	66.0	1.41	(-311)	0.861	8.0	68.0	1.35	(220)	0.633	10.8
<b>Average crystallite size</b>					<b>11.6</b>	<b>Average crystallite size</b>				
S2	36.5	2.46	(211)	0.233	33.3	32.5	2.75	(110)	0.219	36.3
	42.4	2.13	(220)	0.284	27.2	35.5	2.52	(-111)	0.261	30.2
	77.5	1.23	(422)	0.307	21.0	38.7	2.32	(111)	0.308	20.4
						48.1	1.88	(-202)	0.232	32.0
						53.5	1.71	(020)	0.316	22.4
						58.2	1.58	(202)	0.346	20.9
						61.5	1.50	(-113)	0.217	32.8
						66.0	1.41	(-311)	0.220	30.8
						68.0	1.37	(220)	0.4	17.1
					72.3	1.30	(311)	0.316	21.1	
					75.1	1.26	(-222)	0.213	30.8	
<b>Average crystallite size</b>					<b>27.3</b>	<b>Average crystallite size</b>				
S3	16.7	5.27	(111)	0.410	20.0	26.5	3.36	(002)	0.483	17.6
	26.6	2.62	(002)	0.700	11.5	29.4	3.03	(200)	0.264	32.4
	29.3	3.03	(200)	0.446	17.9	32.4	2.75	(110)	0.43	20.0
	32.3	2.76	(110)	0.508	15.6	35.5	2.52	(-111)	0.338	25.7
	36.3	2.26	(211)	0.496	15.8	36.5	2.45	(111)	0.155	56.3
	38.7	2.32	(111)	0.715	10.9	38.8	2.31	(-112)	0.487	18.0
	42.5	2.12	(100)	0.480	16.0	41.4	2.17	(100)	0.326	27.1
	44.9	2.01	(-112)	0.468	16.3	46.4	1.95	(-112)	0.511	17.6
	48.5	1.87	(-202)	0.468	7.9	48.7	1.86	(-202)	0.445	20.4
	51.2	1.78	(112)	0.200	37.3	53.8	1.71	(020)	0.308	30.1
	53.0	1.70	(020)	0.720	10.2	58.3	1.58	(202)	0.433	21.9
	58.1	1.58	(202)	0.542	13.3	61.3	1.51	(-113)	0.261	36.9
	61.4	1.50	(-113)	0.620	11.5	65.9	1.41	(-311)	0.64	15.4
	66.0	1.41	(-311)	0.800	8.6	68.0	1.37	(220)	0.594	16.8
	68.0	1.36	(220)	0.400	17.1	72.3	1.30	(311)	0.353	29.1
72.3	1.30	(311)	0.540	12.4	75.1	1.26	(-222)	0.542	19.3	
75.1	1.25	(-222)	0.566	11.5						
<b>Average crystallite size</b>					<b>14.9</b>	<b>Average crystallite size</b>				

### 4.3.2 Samples Prepared at 200 °C

#### 4.3.2.1 rGO

The XRD results of rGO produced at 200 °C and annealed at 400 °C had depicted in figure (4.7). The primary diffraction peak attributed to GO vanished, whereas peaks corresponding to  $2\theta$  values of  $24.93^\circ$  (002),  $43.11^\circ$  (100), and  $78.01^\circ$  (110) were detected. These results correspond with [126]. These peaks closely resembled the ones specified in the JCPDS card (00-001-0646) for graphite.

Thermal reduction at a temperature of 200 °C led to the creation of distinct and strong peaks, indicating the full exfoliation of GO. A noticeable crystallinity enhancement was observed after two hours of thermal annealing. This result signifies the effective process of reduction.

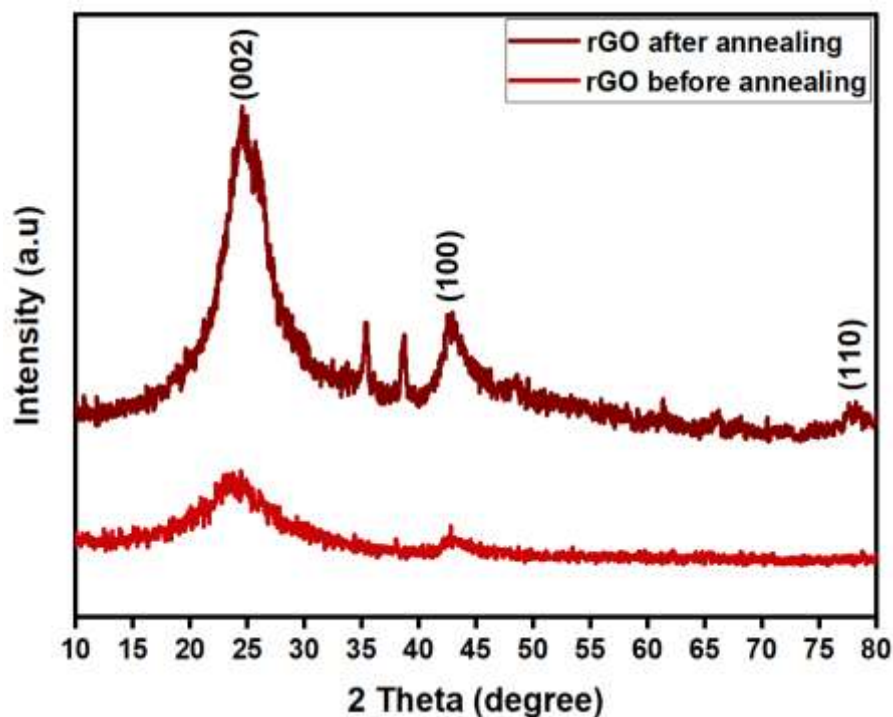


Figure (4.7): XRD results of rGO<sub>200</sub> before and after annealing at 400 °C



The d-spacing and crystallite size are presented in Table (4.6) before and after annealing. The average crystallite size had been calculated before and after annealing as 3.4 nm and 3.8 nm.

**Table (4.6): XRD data of rGO<sub>200</sub> before and after annealing.**

Before annealing					After annealing				
2θ (°)	d (Å)	(hkl)	FWHM (°)	Crystallite size (nm)	2θ (°)	d (Å)	(hkl)	FWHM (°)	Crystallite size (nm)
24.9	3.568	(002)	4.280	1.9	23.7	3.841	(002)	2.880	2.8
43.1	2.096	(100)	3.686	3.7	43.0	2.097	(100)	1.880	4.7
78.0	1.223	(100)	2.240	4.6					
<b>Average crystallite size</b>				<b>3.4</b>	<b>Average crystallite size</b>				<b>3.8</b>

#### 4.3.2.2 CuO

The main peaks of the as-prepared and annealed CuO are illustrated in figure (4.8). It can be seen that the single phase of CuO (tenorite) has been observed with distinct diffraction peaks at 2θ of 32.42°, 35.42°, 38.72°, 48.67°, 53.36°, 58.24°, 61.52°, 66.16°, 67.92°, 72.32°, 75.1° corresponding to (110), (-111), (111), (-202), (020), (202), (-113), (-311), (220), (311), (-222) with lattice constant  $a = 4.684 \text{ \AA}$ ,  $b = 30425 \text{ \AA}$ ,  $c = 5.129 \text{ \AA}$ , according to JCPDS card (00-005-0661) of monoclinic CuO. No significant changes have been detected after the annealing process, except an increase in the intensity of the peaks. This suggests an enhancement in the crystalline structure after annealing. Table (4.7) shows the XRD data before and after annealing for CuO<sub>200</sub>. It was found that the average crystallite size increased from 13.8 nm to 26.9 nm after thermal treatment, which matches well previous studies [127].

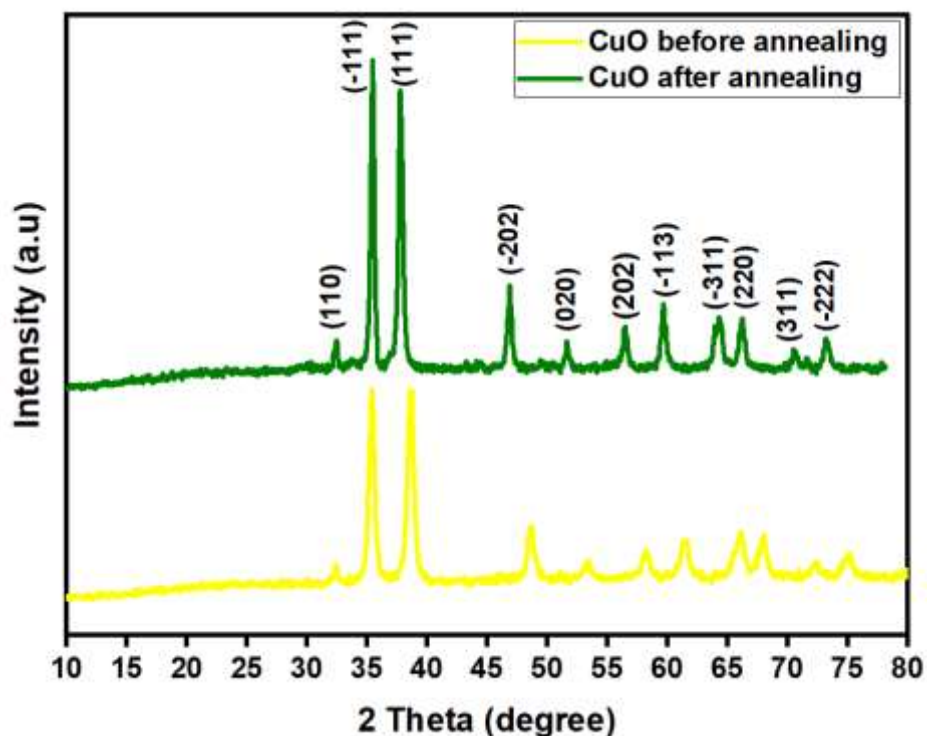


Figure (4.8): XRD results of CuO<sub>200</sub> before and after annealing at 400 °C

Table (4.7): XRD data of CuO<sub>200</sub> before and after annealing.

Before annealing					After annealing				
2θ (°)	d (Å)	(hkl)	FWHM (°)	Crystallite size (nm)	2θ (°)	d (Å)	(hkl)	FWHM (°)	Crystallite size (nm)
32.4	2.708	(110)	0.493	17.0	32.3	2.758	(110)	0.377	22.9
35.4	2.531	(-111)	0.571	10.2	35.5	2.558	(-111)	0.341	25.5
38.6	2.326	(111)	0.636	13.8	38.7	2.321	(111)	0.401	21.9
48.6	1.869	(-202)	0.608	12.8	48.6	1.869	(-202)	0.391	23.2
53.3	1.710	(020)	0.690	12.4	53.4	1.711	(020)	0.297	31.2
58.2	1.583	(202)	0.735	12.9	58.2	1.581	(202)	0.357	26.6
61.5	1.507	(-113)	0.793	12.1	61.4	1.506	(-113)	0.388	23.8
66.1	1.414	(-311)	0.831	11.9	66.1	1.414	(-311)	0.468	21.3
67.9	1.378	(220)	0.747	13.3	68.0	1.377	(220)	0.468	21.3
72.3	1.304	(311)	0.664	15.4	72.4	1.303	(311)	0.360	28.5
75.1	1.265	(-222)	0.856	12.2	75.4	1.259	(-222)	0.226	46.4
<b>Average crystallite size</b>				<b>13.8</b>	<b>Average crystallite size</b>				<b>26.9</b>

### 4.3.2.3 CuO-rGO

The effect of GO on the formation of CuO-rGO nanocomposites can be demonstrated using XRD analysis of the samples (0.5 gram, 1 gram, and 2 gram of graphene oxide added copper nitrate) prepared at 200 °C. Figure (4.9) shows the XRD results of all samples after annealing. S4 sample showed high-intensity peaks with a single phase of CuO with lattice constant  $a = 4.684 \text{ \AA}$ ,  $b = 30425 \text{ \AA}$ ,  $c = 5.129 \text{ \AA}$  which is consistent with the data from JCPDS card (00-005-0661) of CuO. A small and weak peak appeared at  $2\theta$  equal to  $42.26^\circ$  (100) due disordered stacking for rGO layers in the composites, consistent with previous work [120].

In the case of S5, a strong and sharp peak at  $2\theta$  of  $36.46^\circ$  (211) related to cubic phase of  $\text{Cu}_2\text{O}$  with d-spacing of 2.46 nm, in addition to other peaks at  $42.279^\circ$  (220),  $73.45^\circ$  (332), and  $77.29^\circ$  (422) plans in accordance with the JCPDS card (00-002-1067). In addition to weak peaks related to the tenorite phase of CuO at  $2\theta$  of  $35.56^\circ$  (111), and  $38.8^\circ$  (-111).

Two phases were observed for the sample S6, tenorite (CuO) and cuprite ( $\text{Cu}_2\text{O}$ ), and the tenorite phase was predominated. The peak corresponding to  $\text{Cu}_2\text{O}$  was observed at  $29.98^\circ$  (200),  $36.89^\circ$  (211),  $42.3^\circ$  (220),  $73.84^\circ$  (332),  $77.64^\circ$  (422) according to the JCPDS card (00-002-1067) of  $\text{Cu}_2\text{O}$ . Other peaks related to CuO appeared at  $39.19^\circ$  (111), and  $61.7^\circ$  (-113). It was found from these results that two phases of CuO appeared even after annealing in the case of samples S5 and S6. The distinct peak of rGO exhibits a significant decrease in intensity in sample S4 and completely vanishes in samples S5 and S6. This can be ascribed to the strong effect of  $\text{Cu}_2\text{O}$  and CuO, which effectively inhibited the growth of rGO [128]. Upon annealing, the reduction of CuO and GO was

completely achieved, indicating the successful preparation method. The size of the nanocomposites can be substantially modified by altering the amount of GO present in them.

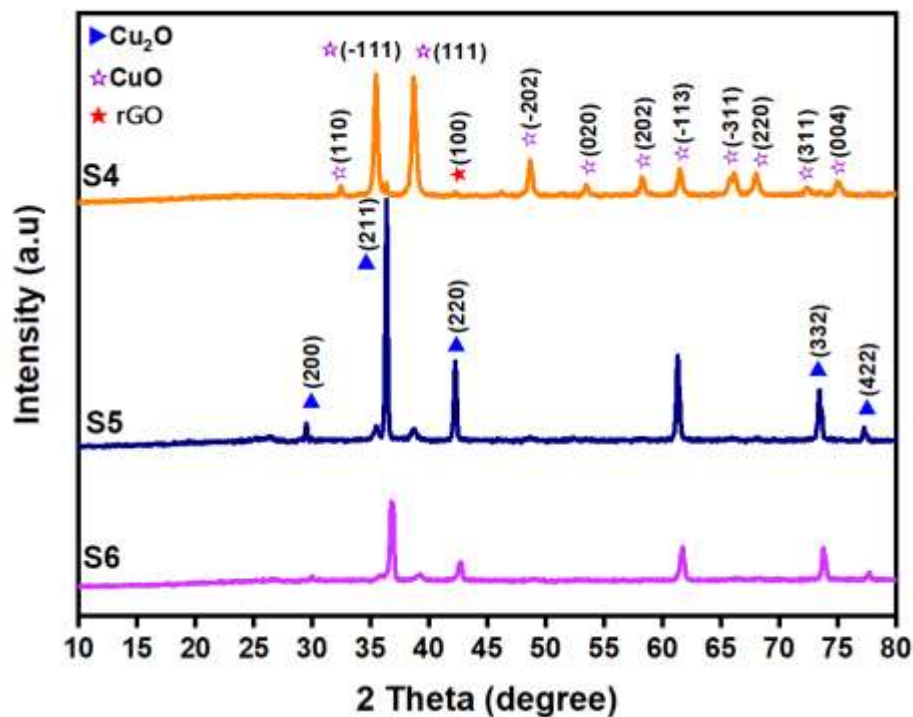


**Figure (4.9): XRD results of CuO-rGO samples prepared at 200 °C after annealing at 400 °C**

Table (4.8) shows the XRD data for all samples after annealing. The average crystallite size for samples S4, S5, and S6 was 26 nm, 40.8 nm, and 28.1 nm, respectively.

**Table (4.8): XRD data of CuO-rGO nanocomposite after annealing.**

Sample	2 $\theta$ (°)	d (Å)	(hkl)	FWHM (°)	Crystallite size (nm)
S4	32.4	2.753	(110)	0.307	28.1
	35.4	2.527	(-111)	0.340	25.6
	38.7	2.322	(111)	0.385	22.8
	42.2	2.136	(100)	0.328	27.1
	48.6	1.868	(-202)	0.366	24.8
	53.4	1.712	(020)	0.348	26.6
	58.2	1.581	(202)	0.370	25.6
	61.5	1.506	(-113)	0.377	25.6
	66.1	1.41	(-311)	0.353	28.0
	68.0	1.377	(220)	0.399	25.0
	72.3	1.304	(311)	0.364	28.2
	75.0	1.264	(040)	0.436	23.9
<b>Average crystallite size</b>					<b>26</b>
S5	29.5	3.021	(200)	0.186	46.1
	35.5	2.528	(-111)	0.342	25.4
	36.4	2.487	(211)	0.199	43.8
	38.7	2.319	(111)	0.28	31.4
	42.2	2.136	(220)	0.211	42.1
	61.3	1.51	(-113)	0.221	43.6
	73.4	1.288	(332)	0.229	45.2
	77.2	1.233	(422)	0.217	48.9
<b>Average crystallite size</b>					<b>40.8</b>
S6	29.9	2.978	(200)	0.353	24.3
	36.8	2.436	(211)	0.366	23.8
	39.1	2.296	(111)	0.553	15.9
	42.3	2.14	(220)	0.226	39.3
	61.7	1.502	(-113)	0.323	29.9
	73.8	1.282	(332)	0.296	35.0
	77.6	1.228	(422)	0.373	28.5
<b>Average crystallite size</b>					<b>28.1</b>

#### 4.3.2.4 SnO<sub>2</sub>/CuO - rGO

Figure (4.10) shows the structure SnO<sub>2</sub>/CuO-rGO thin film. It can be seen that the diffraction peaks corresponding to tetragonal SnO<sub>2</sub> and the sharp peaks related to monoclinic CuO both present in the composite. In addition

to the peaks indexed to rGO. These peaks were observed at  $2\theta$  of  $20^\circ$ ,  $26.4^\circ$ ,  $31.5^\circ$ ,  $33.6^\circ$ ,  $35.16^\circ$ ,  $38.2^\circ$ ,  $43.28^\circ$ ,  $49.12^\circ$ ,  $51.5^\circ$ ,  $54.88^\circ$ ,  $58^\circ$ ,  $63.32^\circ$ ,  $75.08^\circ$  corresponding to (002), (110), (110), (101), (-111), (111), (100), (-202), (211), (220), (202), (-113), (004) according to JCPDS cards (41-1445), (00-001-0646), and (00-005-0661) of  $\text{SnO}_2$ , rGO, and CuO respectively. No impurity peaks for other phase were appeared.

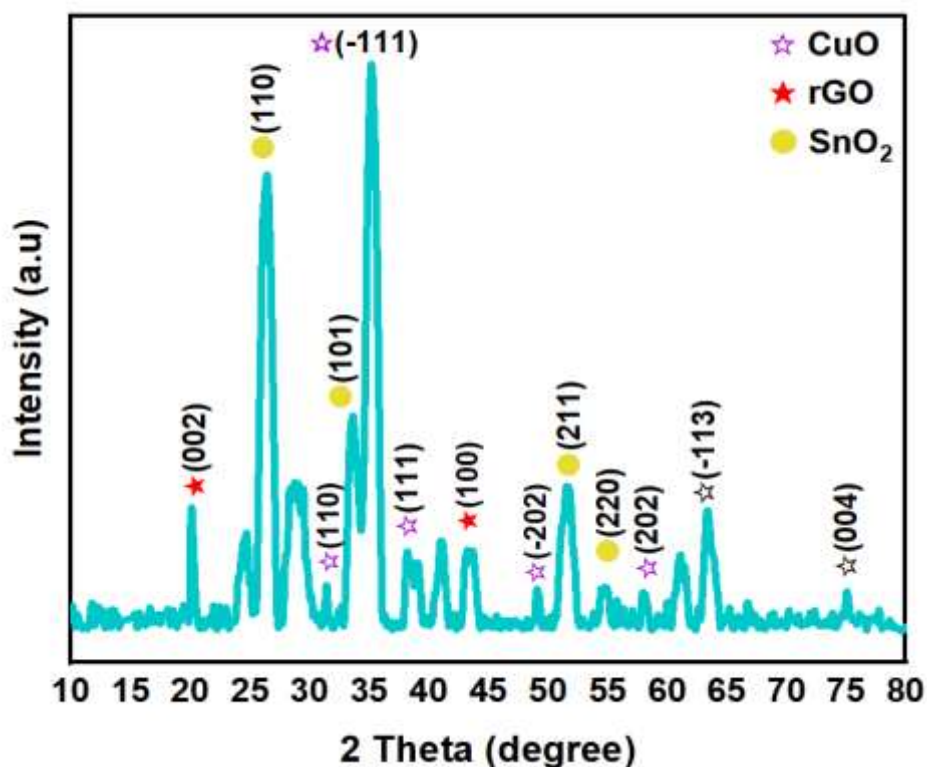


Figure (4.10): XRD results of  $\text{SnO}_2/\text{CuO}$  - rGO nanostructure.

Table (4.9) shows the XRD data of  $\text{SnO}_2/\text{CuO}$  - rGO. It was found that the average crystallite size about 31.4 nm.

**Table (4.9): XRD data of SnO<sub>2</sub>/ CuO- rGO nanostructure.**

2θ (°)	d (Å)	(hkl)	FWHM (°)	Crystallite size(nm)
20.0	4.435	(002)	0.760	11.0
26.4	3.368	(110)	0.940	9.0
31.5	2.865	(110)	0.140	61.5
33.6	2.651	(101)	0.440	19.6
35.1	2.545	(-111)	0.766	11.3
38.2	2.315	(111)	0.140	62.7
43.2	2.078	(100)	0.160	55.7
49.1	1.841	(-202)	0.400	22.8
51.5	1.768	(211)	0.200	46.0
54.8	1.674	(220)	0.280	33.3
58.0	1.587	(202)	0.480	19.7
63.3	1.463	(-113)	0.640	15.2
75.0	1.260	(004)	0.260	40.2
<b>Average crystallite size</b>				<b>31.4</b>

#### 4.4 Thermogravimetric Analysis (TGA)

The thermal stability of the samples was tested under Nitrogen atmosphere at a temperature between (50 – 900 °C) with a temperature rise of 50°C min<sup>-1</sup>.

##### 4.4.1 GO and rGO

Figure (4.11) shows the thermal stability of GO, rGO<sub>100</sub>, and rGO<sub>200</sub>. The TGA curve of the GO exhibited a progressive reduction in mass as a result of many sequential decomposition processes, ultimately reaching a 70 % decrease after being heated to 800 °C. Initially, when heating the sample to 100 °C, approximately 10 % of its weight was reduced due to moisture evaporation. Upon additional heating to 480 °C, there was no notable decrease in weight due to a stable product during this phase. Subjecting the

material to additional heating at temperatures over 500 °C causes a weight reduction, reaching 60 % of its initial value at 675 °C. The weight loss persisted via additional heating until it reached approximately 50 % at a temperature of 750 °C due to the removal of some active functional groups and the reduction of GO. At a temperature of 800 °C, the most significant weight reduction was seen, amounting to 30 % of its initial weight. The drop in GO mass was primarily due to oxygen-containing functional groups' pyrolysis, which produced steam, CO<sub>2</sub>, and CO [129].

The TGA curve of rGO<sub>100</sub> shows a 58% weight decrease at (100- 800 °C) due to oxygen extraction from active groups (CO, CO<sub>2</sub>, and H<sub>2</sub>O). The elimination exerts significant pressure on the layers, causing them to split due to heat that produces thermal energy [130]. A slight reduction in mass of around 5% was detected in the rGO<sub>200</sub> sample within the temperature range of (100 – 600 °C), extending up to 600 °C. The degradation of rGO<sub>200</sub> was observed to be 27%. These results were similar to those previously obtained [131]. Furthermore, at 800 °C, there was no significant drop in weight percentage observed after that. The decrease in mass was attributed to the limited quantity of active groups that were still present and the combustion of the carbon [132]. Based on the experiments, it can be inferred that the breakdown temperature of GO was lower than that of rGO.

#### 4.4.2 CuO

Figure (4.12) illustrates the TGA graph of CuO. The TGA of CuO<sub>100</sub> revealed a decrease in weight of around 3% within the temperature range of (100 °C – 500 °C). This drop can be attributed to the evaporation of volatile components. Once the temperature reached (550°C - 750 °C), there was a slight decrease of 1%. After 750 °C, a slight loss of mass about 1.25% was



observed. The  $\text{CuO}_{200}$  exhibited a weight loss of around 2.25% between temperatures of 100 °C and 500 °C. However, it demonstrated thermal stability between 500 °C to 750 °C. Following this temperature, there was a slight weight reduction, around 1.19%. The TGA curves of both samples show that the CuO was thermally stable.

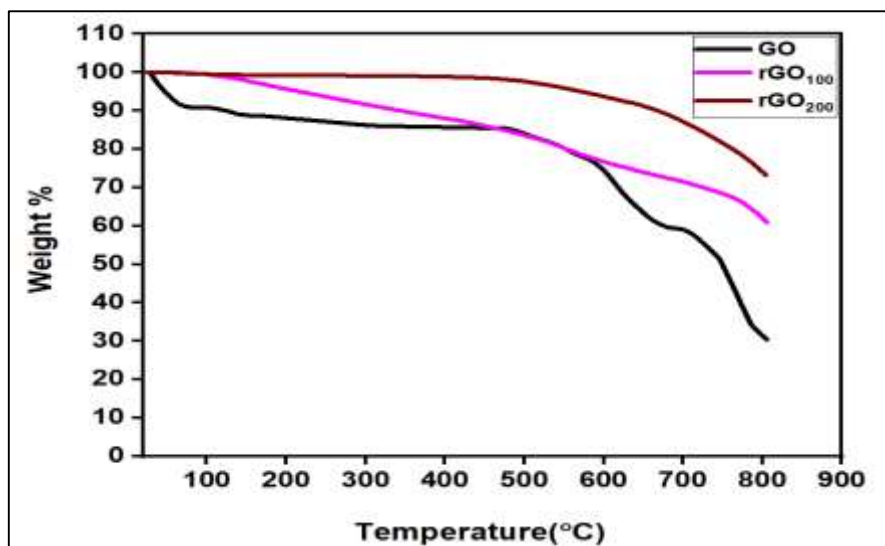


Figure (4.11): TGA curves of GO, rGO<sub>100</sub>, and rGO<sub>200</sub>.

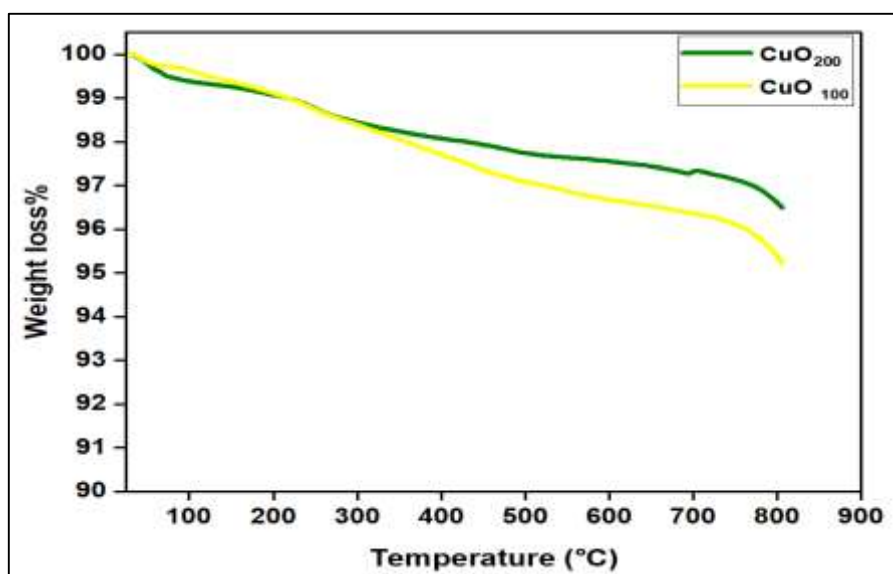
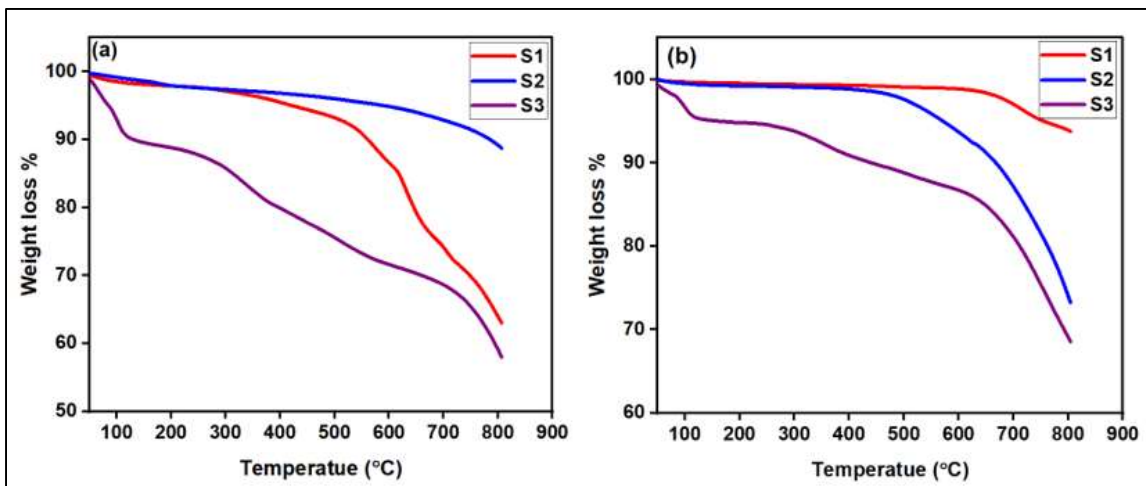


Figure (4.12): TGA curves of CuO<sub>100</sub> and CuO<sub>200</sub>.

### 4.3 CuO-rGO

Figure (4.13) demonstrates the impact of annealing on the TGA curves of samples S1, S2, and S3, to examine the thermal stability of the samples. Before annealing, as shown in figure (4.13-a), the S1 and S2 samples exhibited a weight reduction of 5% to 7% at temperatures lower than 450 °C. The reduction in weight of the nanocomposites is attributed to the process of water evaporation. Subsequently, the weight loss percentage at 800 °C increased to 37% for S1 and 14% for S2, suggesting the deterioration of oxygen-containing functional groups within the composite material [133]. No weight loss was observed over 800 °C. For S3, the weight loss caused by moisture absorption rose to 11% at a temperature of 150 °C as the GO ratio in the nanocomposites increased.

Gradual weight loss reaching 42% occurred at 800 °C due to carbon combustion in the composite. Following the annealing process at a temperature of 400 °C, as shown in figure (4.13-b), both S1 and S2 demonstrated thermal stability across the range of 100 °C to 500 °C. At temperatures up to 800 °C, S1 showed a weight reduction of approximately 6%, whereas S2 exhibited a significant weight loss of 27%. This can be attributed to the removal of carbon from the nanocomposites. The weight loss increased when the GO weight in sample S3 was increased. The weight of S3 gradually decreased due to various disintegration processes, ultimately resulting in a 32% loss after being heated to 800 °C. A weight loss of 13% was initially recorded between temperatures of 100 °C and 600 °C, followed by an additional weight loss of around 19% up to temperature of 800 °C.



**Figure (4.13):** TGA curves of CuO -rGO prepared at 100 °C: (a) before annealing, (b) after annealing at 400 °C.

## 4.5 FTIR- Spectroscopy

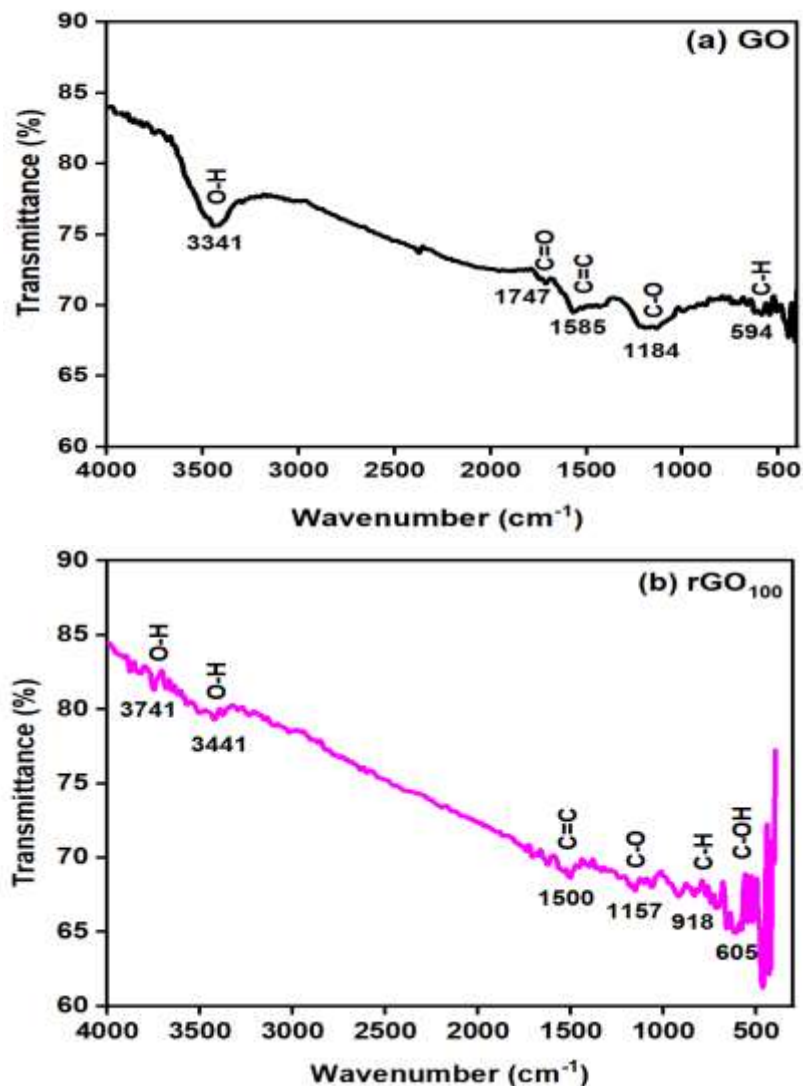
### 4.5.1 GO and rGO

Figure (4.14) shows the FTIR of GO and rGO annealed at 400 °C for two hours. The GO spectrum exhibited a significant peak at  $3341\text{ cm}^{-1}$ , attributed to the OH (hydroxyl) stretching caused by the water molecules trapped between the graphene layers during production. The presence of bands, such as C=O, C-OH (hydroxyl), and C-O (epoxy), within the carbon layers indicates the existence of significant quantities of oxygen-containing functional groups in GO [134].

The aromatic C=C band can represent the skeleton vibration of the graphene plane. The presence of an ineffective band with a peak at  $450\text{ cm}^{-1}$  may be attributed to the production of amorphous carbon nanoclusters [135]. The spectra of rGO<sub>100</sub> demonstrated a significant decrement in the intensity of the bands compared to GO. It was obvious that the peak C=O for carboxyl at  $1747\text{ cm}^{-1}$  vanished. This could be attributed to partially removing the oxygen-containing functional groups and deoxygenation [130].

The appearance of additional peaks at  $918\text{ cm}^{-1}$  and  $605\text{ cm}^{-1}$  can be related to rGO. Increasing the reduction temperature to  $200\text{ }^{\circ}\text{C}$  led to reduce the hydroxyl group in GO.

Consequently, the absorption peak at wave number  $3741\text{ cm}^{-1}$  decrease, indicates the skeleton vibration of the OH group. The peak at  $2330\text{ cm}^{-1}$  represents the restored carbon basal planes after thermal reduction [136]. Compared to GO, hydrothermal treatment lowered the absorbance peak at  $3441\text{ cm}^{-1}$  in rGO samples, indicating effective hydroxyl group elimination. These results correspond with previous works [137].



Continued

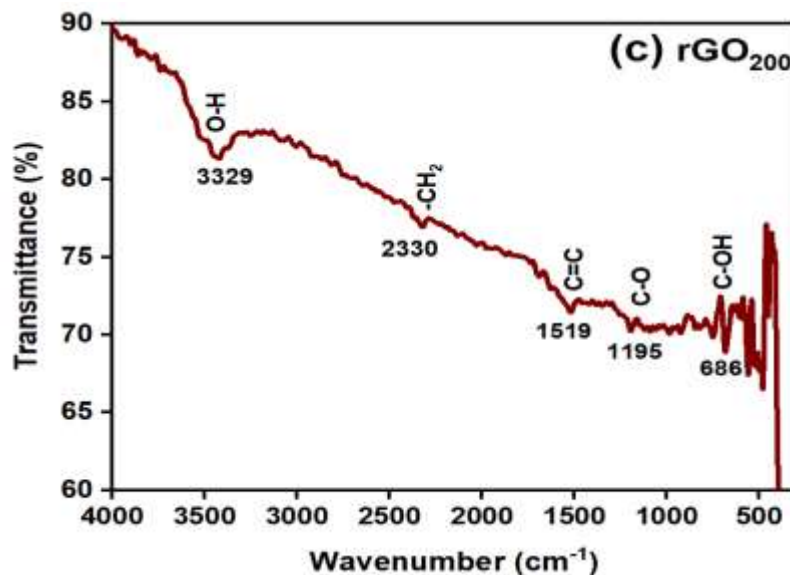


**Figure (4.14): FTIR analysis for (a) GO, (b) rGO<sub>100</sub>, and (c) rGO<sub>200</sub> after annealing at 400 °C.**

#### 4.5.2 CuO

Figure (4.15) illustrates the FTIR of CuO after annealing at 400 °C. The vibrations peak around 3742 cm<sup>-1</sup> was related to the stretching vibrations of hydroxyl O-H bonds induced by water absorption in the composites during preparation. The peak at 2360.9 cm<sup>-1</sup> is due to the symmetric and anti-symmetric stretching vibrations of CH<sub>2</sub> [138], in addition to the bond at 1519 cm<sup>-1</sup> corresponding to C=O stretching of the carboxylate ion bond to the CuO. The band that appeared at 1161 cm<sup>-1</sup> represents the covalent bond between -OH and C, as indicated in previous work [101]. The absorption peaks at 659 cm<sup>-1</sup>, 505 cm<sup>-1</sup>, and 420 cm<sup>-1</sup> were perhaps due to Cu-O bond vibration in the monoclinic phase of CuO, which signifies the presence of a metal-oxide group in the composites [139].

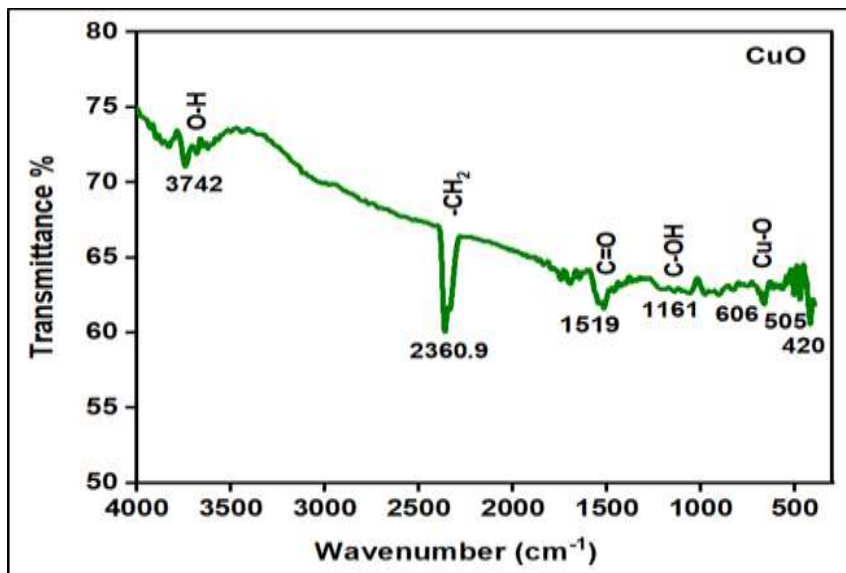


Figure (4.15): FTIR analysis of CuO annealed at 400°C

#### 4.5.† CuO-rGO

The FTIR analysis of CuO-rGO for samples S4 and S5, which underwent annealing at 400 °C, is depicted in figure (4.16). The S4 sample exhibits a distinct absorption peak at 3410  $\text{cm}^{-1}$ , attributed to the stretching and bending vibrations of the hydroxyl groups and water molecules on the surface. Furthermore, 1465  $\text{cm}^{-1}$  ascribed to the stretching vibration of C-OH of alcohol indicated the formation of CuO-rGO nanocomposites. Other peaks such as 609  $\text{cm}^{-1}$  and 516  $\text{cm}^{-1}$  confirmed that the cuprous ions were securely attached to the graphene oxide layers [138]. For sample S5, an increment in the amount of GO in the nanocomposites led to an increment of the functional groups, as appeared in figure (4.16-b). The absorption peaks at 2360  $\text{cm}^{-1}$  represent symmetric stretching vibrations of  $\text{CH}_2$  [123]. The vibration of the Cu–O bond was confirmed by the presence of the peak at 547  $\text{cm}^{-1}$ [140, 141].

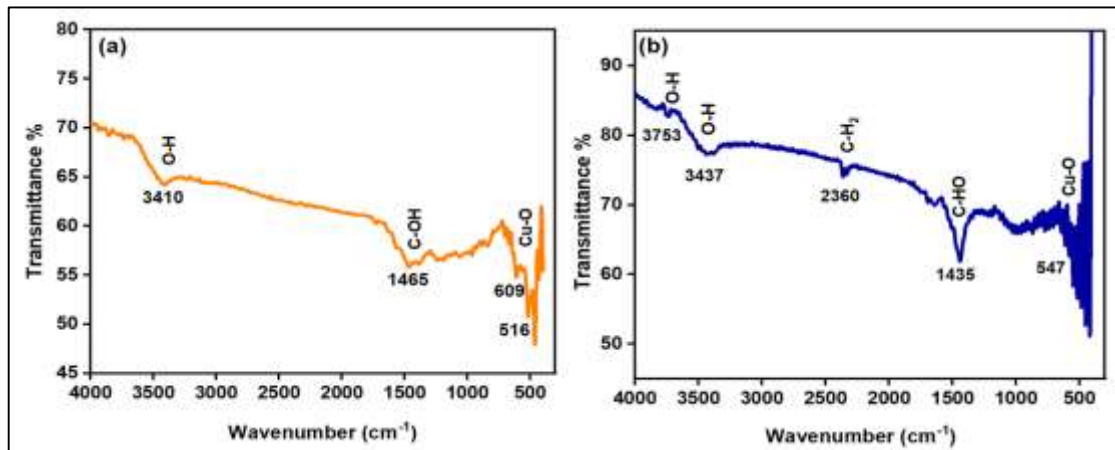


Figure (4.16): FTIR analysis of CuO-rGO nanocomposites annealed at 400 °C; (a) S4, and (b) S5.

#### 4.5.4 SnO<sub>2</sub>

The FTIR spectra of SnO<sub>2</sub> is shown in figure (4.17). The band at 3433 cm<sup>-1</sup> indicates the hydroxide -OH groups of the nanocomposites. The weak peak revealed the presence of CO<sub>2</sub> at 2349 cm<sup>-1</sup>, which corresponds to the O=C=O bond. The peak at 1647 cm<sup>-1</sup> corresponds to the H-O-H water molecule found in the atmosphere [142]. The strong bonding observed at a wavenumber of 609 cm<sup>-1</sup> is attributed to the Sn-O stretching vibrational mode of the asymmetric Sn-O-Sn bond [143].

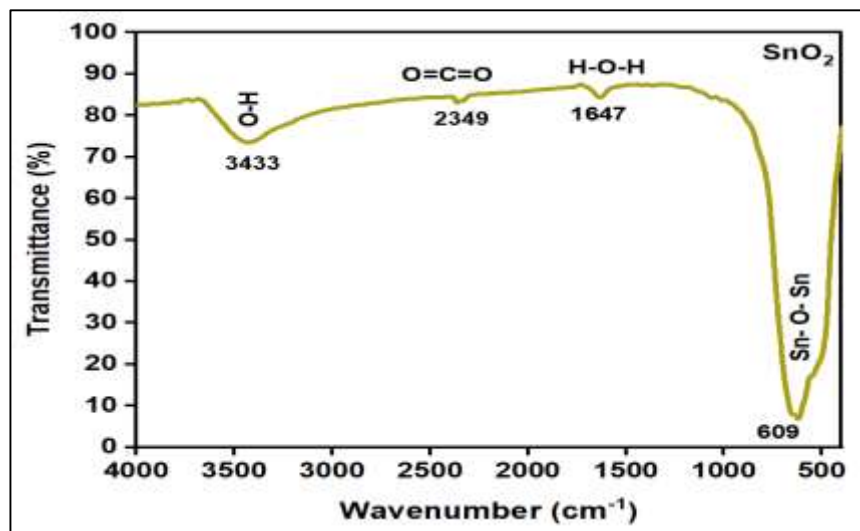


Figure (4.17): FTIR analysis of SnO<sub>2</sub>.

## 4.6 FESEM Characterization

### 4.6.1 Samples Prepared at 100 °C

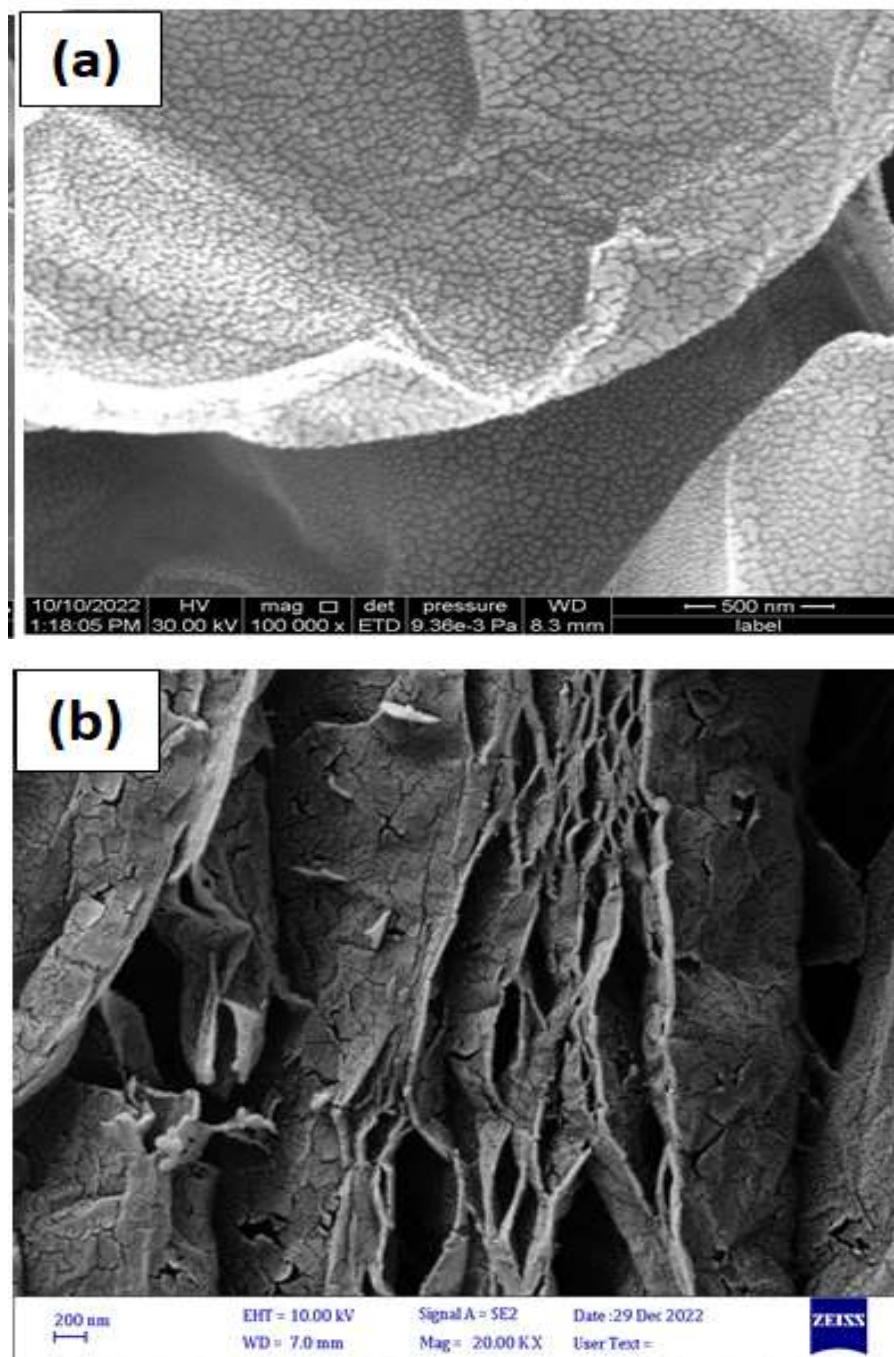
#### 4.6.1.1 GO and rGO

The GO and rGO<sub>100</sub> samples were analyzed using High-resolution FESEM characterization to investigate their structure and surface morphology before and after annealing, as shown in figure (4.18). Figure (4.18-a) displays several overlapped folded stoked graphene oxide layers. Applying heat treatment at 100 °C resulted in the consolidation and compaction of the GO layers, forming a plate-like structure with curved textures with more pores, as appeared in figure (4.18-b).

The average thickness of the layers was about 35.5 nm. The rGO layers formed agglomerates in a plate-like shape, resulting in a structure with increased flaws. These defects were caused by the breakdown of oxygen groups during thermal annealing, suggesting a reduction of GO. This is shown in figure (4.18-c); eliminating oxygen-containing groups can form



rGO sheets. The decrease of van der Waals interlayer interaction would facilitate the split of GO layers, forming thin rGO sheets containing fewer graphene layers than GO [78].



Continued...

Continued

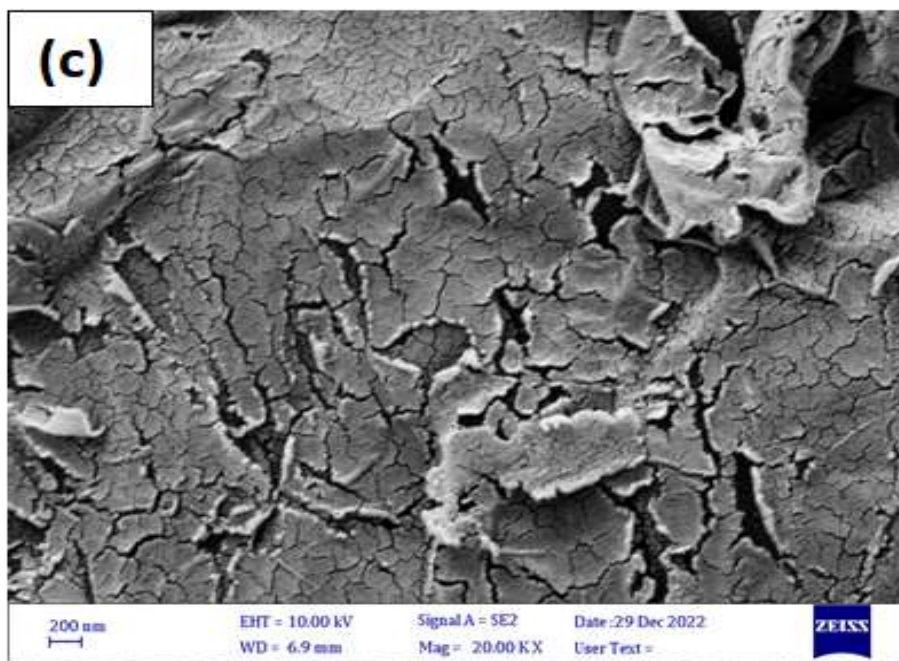


**Figure (4.18):** High-resolution FESEM images of (a) GO, (b) rGO<sub>100</sub> before annealing, (c) rGO<sub>100</sub> after annealing at 400 °C

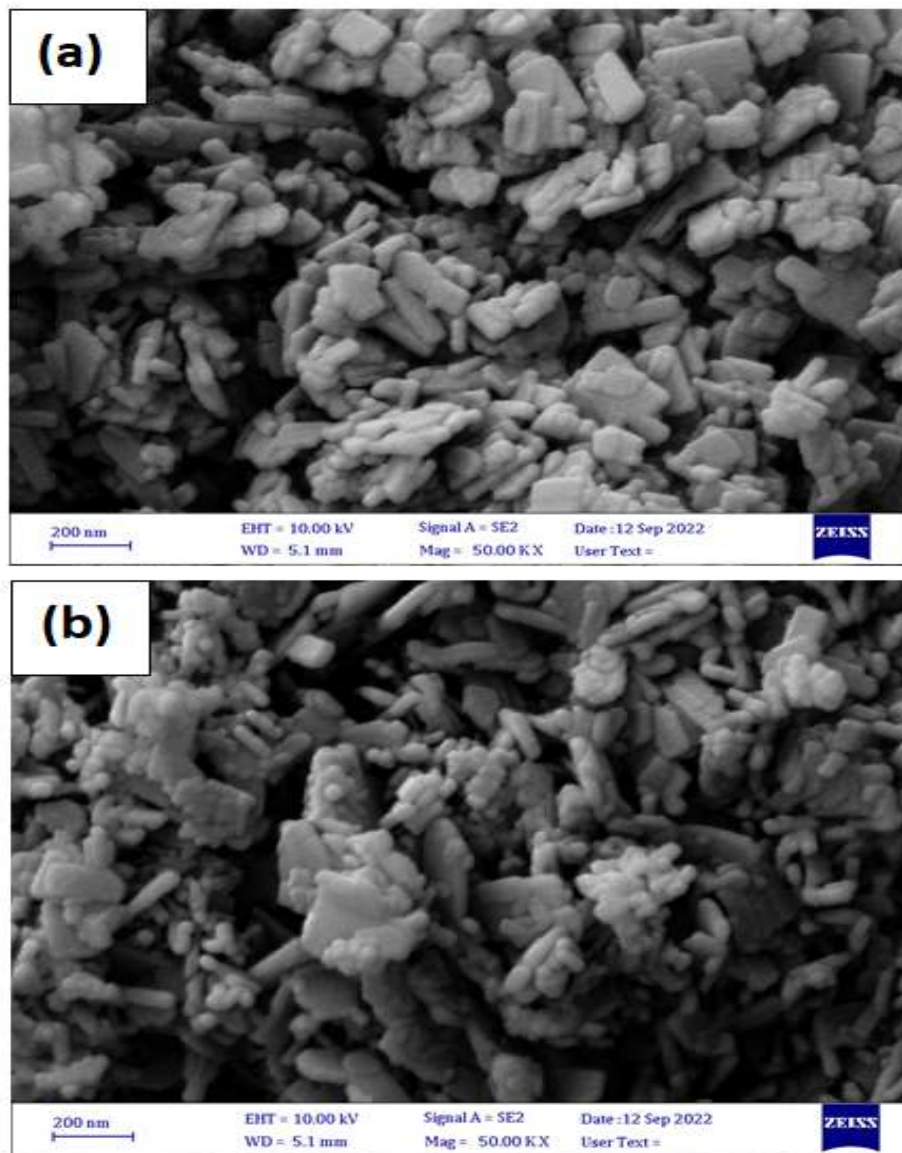
#### 4.6.1.2 CuO

Figure (4.19) shows the FESEM of CuO<sub>100</sub> before and after annealing. It is clear from figure (4.19-a) that CuO<sub>100</sub> exhibited a nanorods structure with an average diameter of 51 nm and length of 170 nm. After annealing, these structures agglomerated on the surface, appearing as larger particles, and the average diameter increased to 59 nm as shown in figure (4.19-b).

#### 4.6.1.3 CuO- rGO

The impact of the GO quantity on the CuO- rGO nanocomposites was illustrated in figures (4.20), (4.21), and (4.22). S1 had a morphology characterized by a small rod-shaped structure on its surface with an average diameter of about 34 nm. When subjected to annealing at a temperature of 400 °C, the nanorods structure experiences accumulation, creating larger

particles with 37 nm in diameter that form a spherical structure, as in figure (4.20, a, b).



**Figure (4.19): High-resolution FESEM images of CuO<sub>100</sub>, (a) before annealing, (b) after annealing at 400 °C**

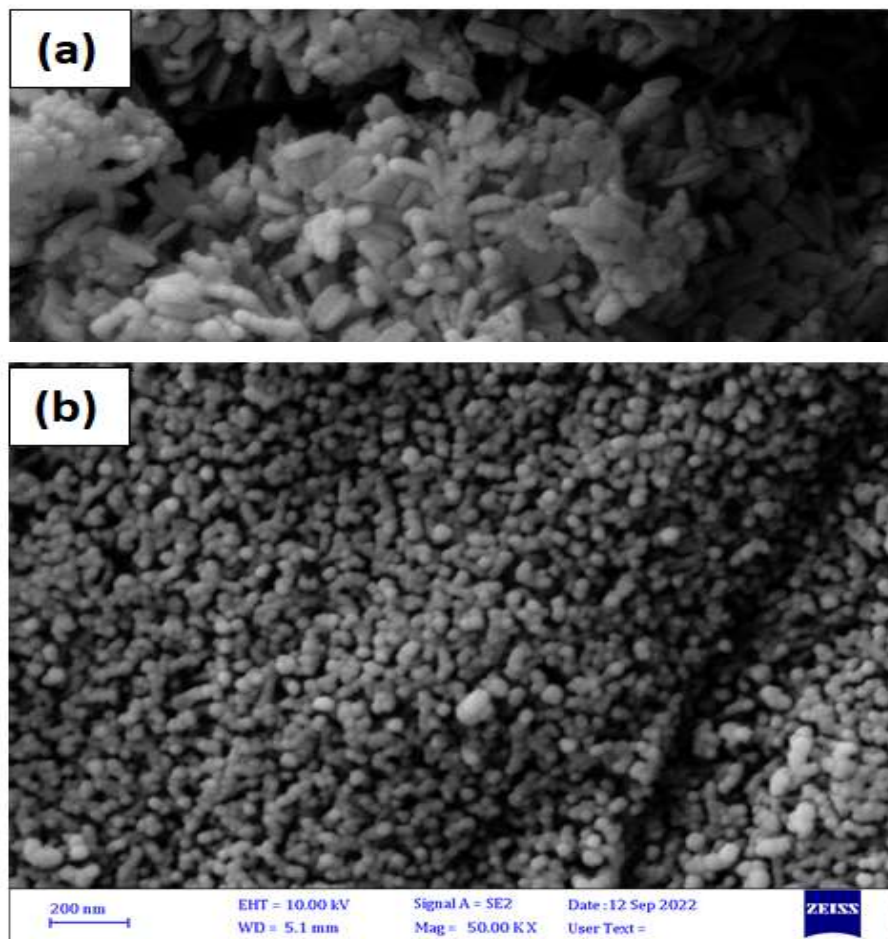


**Figure (4.20): High-resolution FESEM images of S1, (a) before annealing, (b) after annealing at 400 °C**

Upon increasing the quantity of GO to 1 gram, S2 sample, the long nanorods decreased resulting in an irregular structure with an average size of 52 nm as shown in figure (4.21-a). Then the structure totally transformed to a spherical shape with an increment in size to 92 nm upon annealing, as shown in figure (4.21-b). At a weight fraction of 2 grams in figure (4.22), the GO forms a semi-rod-like structure that completely coats the surface of the rGO sheets. The average diameter of this structure was in the range of 41 nm. This structure coalesces into sizable agglomerations with a spherical morphology following heat treatment. As a result, the quantity of small

particles is reduced, increasing the number of large particles with a diameter of about 63 nm.

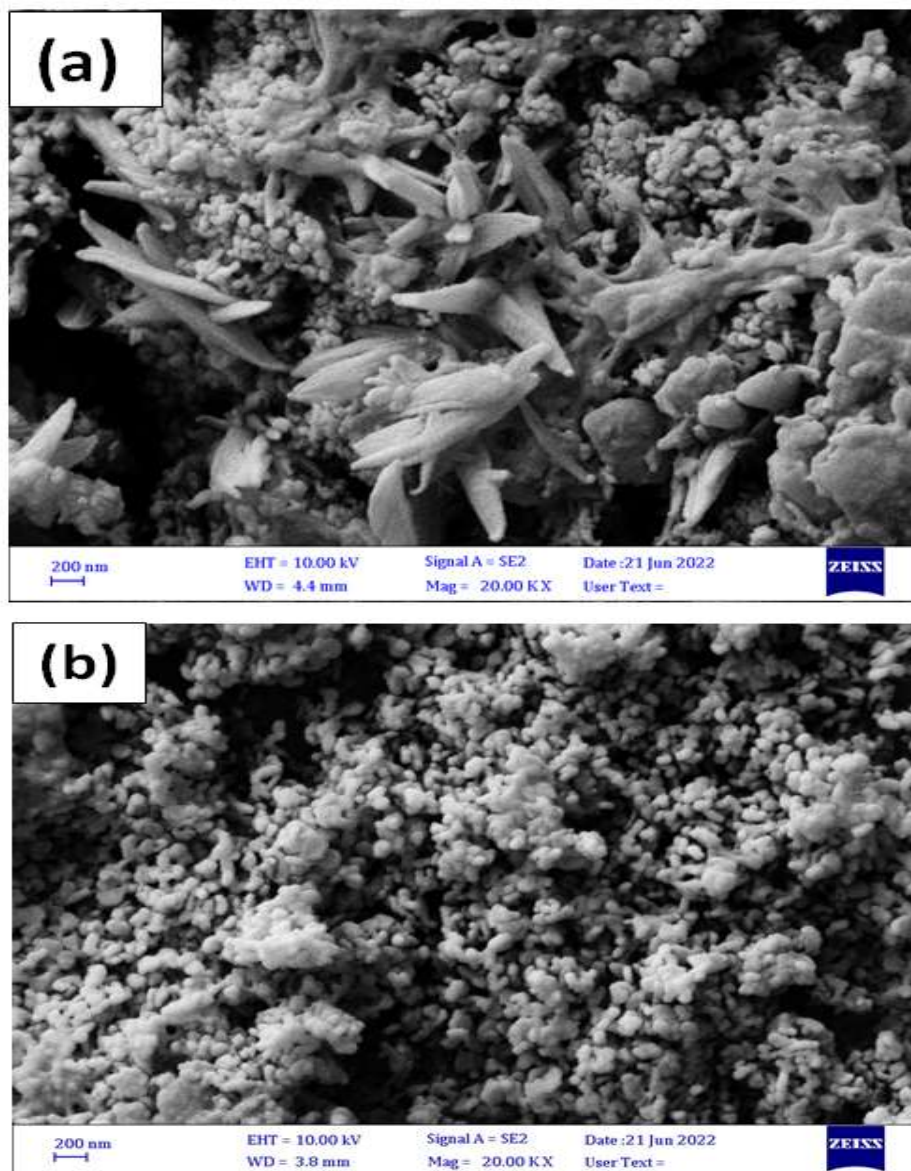


**Figure (4.21): High-resolution FESEM images of S2, (a) before annealing, (b) after annealing at 400 °C**

The purpose of NaOH in the reaction was to facilitate the connection between GO and CuO through hydrothermal treatment, hence promoting the generation of electrons on the surface of GO. During this stage, reducing  $\text{Cu}^{+2}$  and GO forms CuO and rGO nanocomposites. As previous studies discussed, the temperatures influence this reaction. The average size of [144] all three samples was observed to be within the nanoscale range, as confirmed by XRD results.

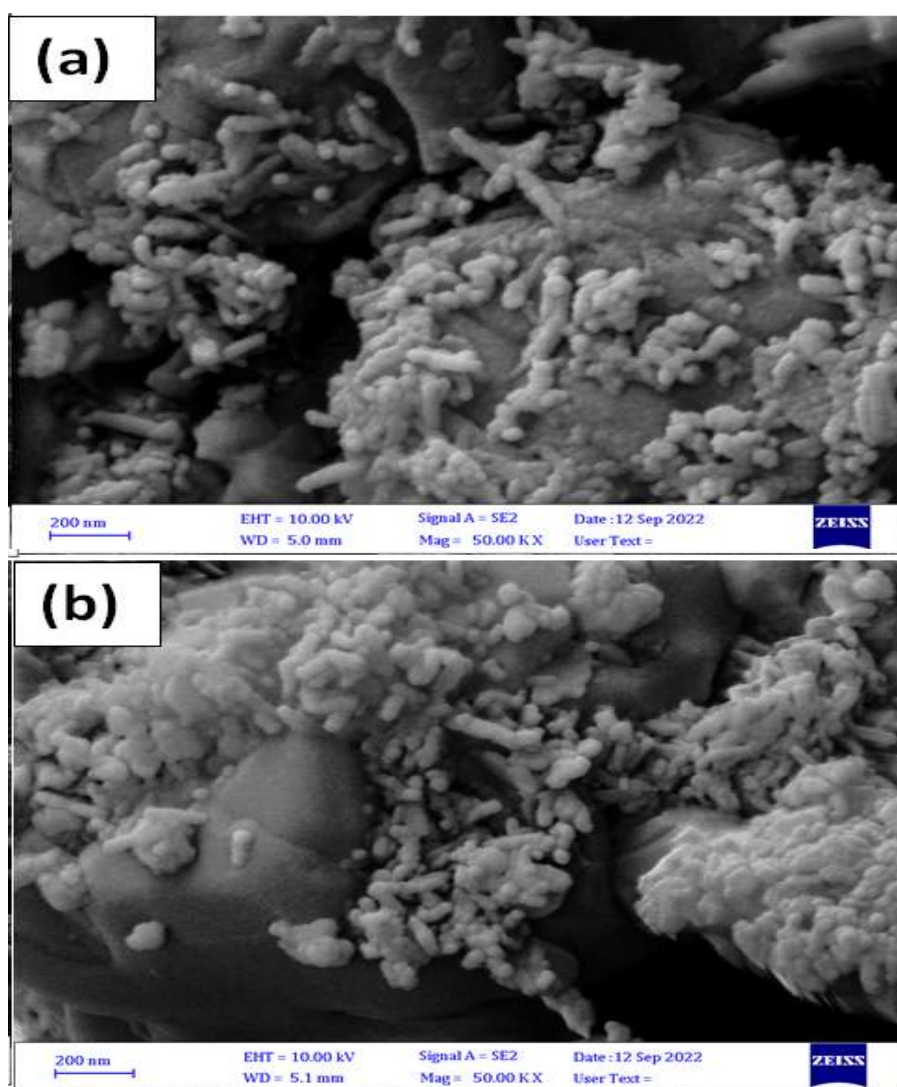


**Figure (4.22): High-resolution FESEM images of S3, (a) before annealing, (b) after annealing at 400 °C**

## 4.6.2 Samples Prepared at 200 °C

### 4.6.2.1 rGO

The morphology of the annealed samples was analyzed using a high-resolution FESEM. Figure (4.23) illustrates a crumpled plate-like structure of rGO<sub>200</sub> after raising the preparation temperature to 200 °C. The breakdown of oxygen-active groups and increased space between layers resulted in a notable alteration in morphology with an average thickness of 77 nm. These results were in agreement with previous studies [146]. This decreased reaction between the planes weakened the van der Waals force [147]. This suggests that the GO was reduced successfully, which was inferred by XRD and FTIR results.

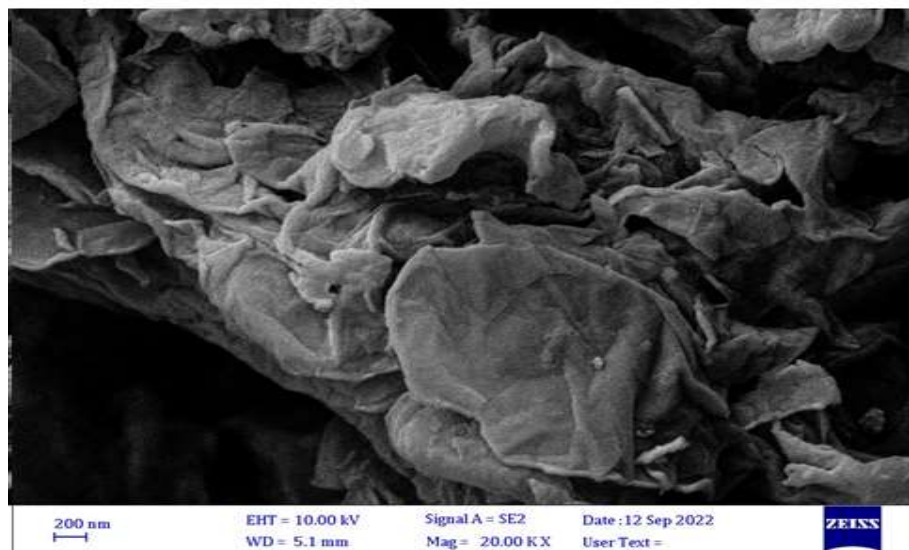


**Figure (4.23): High-resolution FESEM images of rGO<sub>200</sub> after annealing at 400 °C**

### 4.6.2.2 CuO

The morphology of the annealed sample was analyzed using a high-resolution FESEM. Figure (4.24) shows a rod-like structure of CuO<sub>200</sub> after raising the preparation temperature to 200 °C with an average particle size of a few nanometers, confirming the results of XRD. These results were the

same as when CuO was prepared at 100 °C and in agreement with the previous study which used the same preparation method but larger particles were obtained [148].

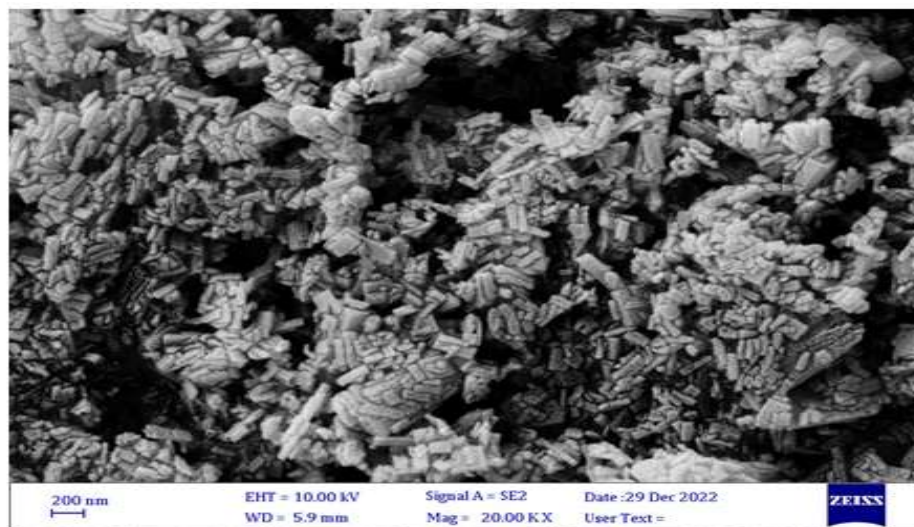


**Figure (4.24): High-resolution FESEM images of CuO<sub>200</sub> after annealing at 400 °C.**

#### 4.6.2.3 CuO -rGO

The effect of the GO quantity on the CuO- rGO nanocomposites after annealing at 400 °C is shown in figure (4.25). Figure (4.25- a) shows that an S4 nanorods structure can be observed on the surface of rGO with high accumulation and an average size of over 27 nm. After increasing the quantity of GO to 1 gram, as shown in figure (4.25- b), the S5 sample underwent a significant transformation in its nanocomposites structure. This led to a uniform and spherical-like shape with an average size of approximately 52 nm. The rise in average size resulted from the aggregation of small particles. In figure (4.25- c), when the weight fraction increases by 2 grams, the CuO particles merge to form large, uneven clusters. These clusters cover the surface of the rGO sheets and reduce the number of folds in the rGO nanosheets [149]. The study revealed a reduction in the average particle size to approximately 37 nm.



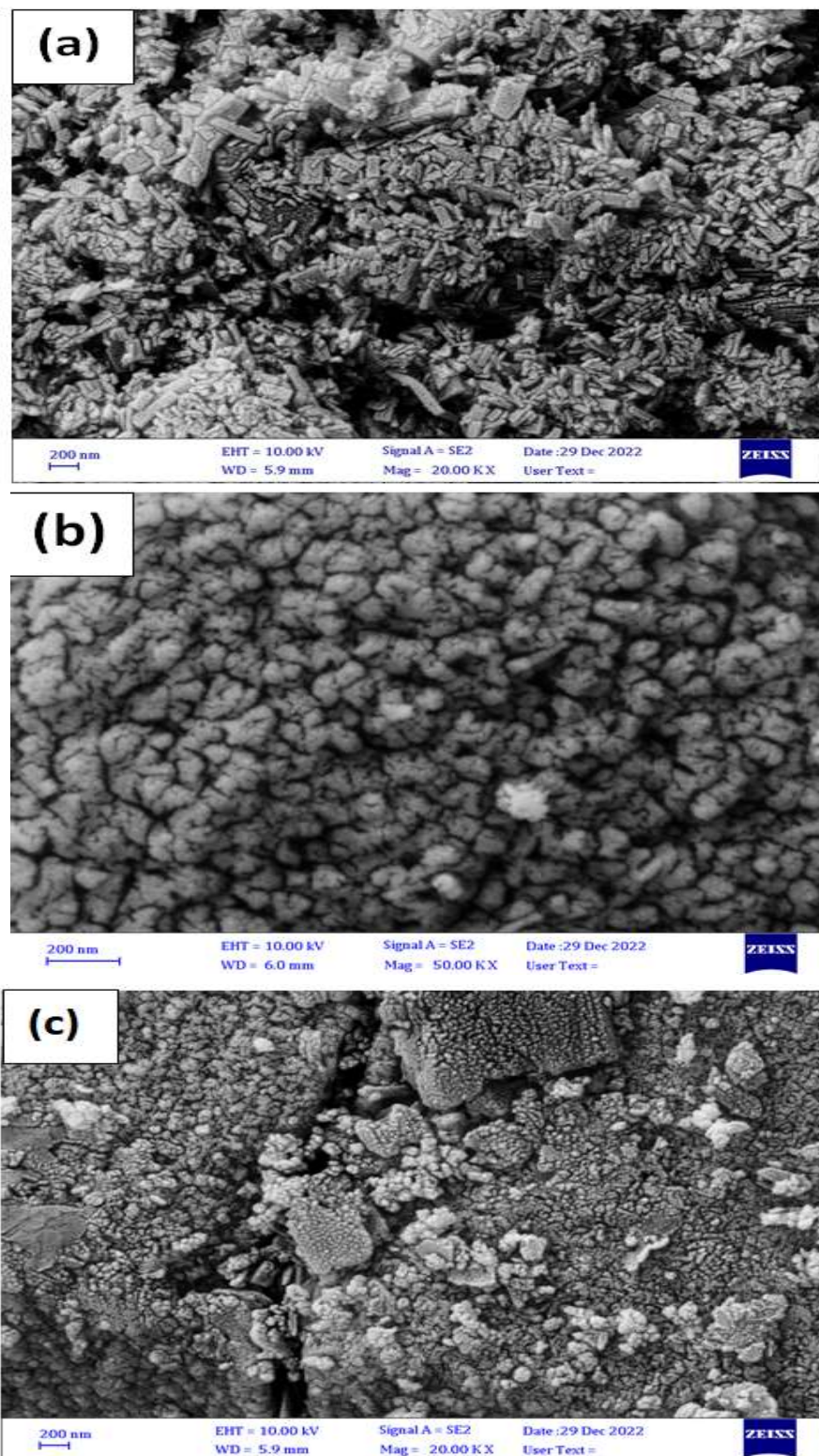


**Figure (4.25): High-resolution FESEM images of CuO- rGO after annealing at 400 °C; (a) S4, (b) S5, and (c) S6.**

#### 4.6.2.4 SnO<sub>2</sub>

The morphology of the SnO<sub>2</sub> film annealed at 1000 °C and deposited by PLD is shown in figure (4.26). It was clear from the figure that a spherical-like shape was observed with larger agglomerations. The average particle size was about 60.56 nm. This result was similar to that indicated in previous study [150] when the SnO<sub>2</sub> prepared by chemical precipitation method.

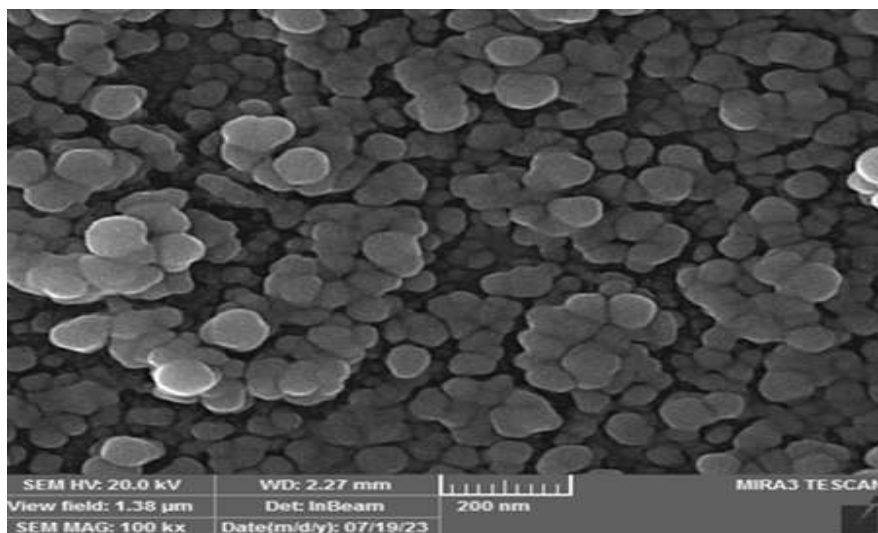


Figure (4.26): SEM images of annealed SnO<sub>2</sub>.

### 4.7 TEM Analysis

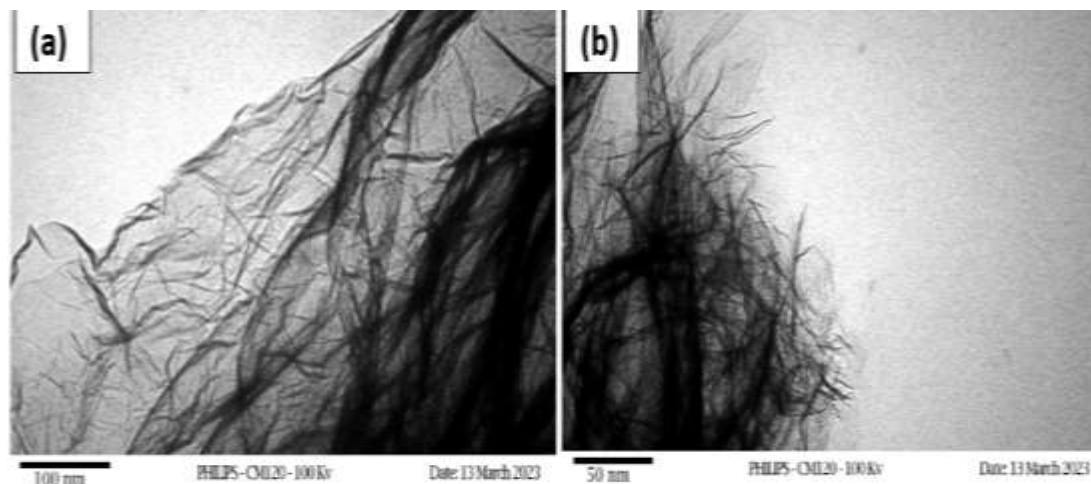
#### 4.7.1 rGO

Figure (4.27) illustrates the TEM of rGO prepared at 200 °C and annealed at 400 °C with different magnifications. The peeling process from GO to rGO<sub>200</sub> caused bending of the stacked layers of graphene sheets, resulting in wrinkled surface patterns and irregular and crashing shape. These results were in agreement with [151].

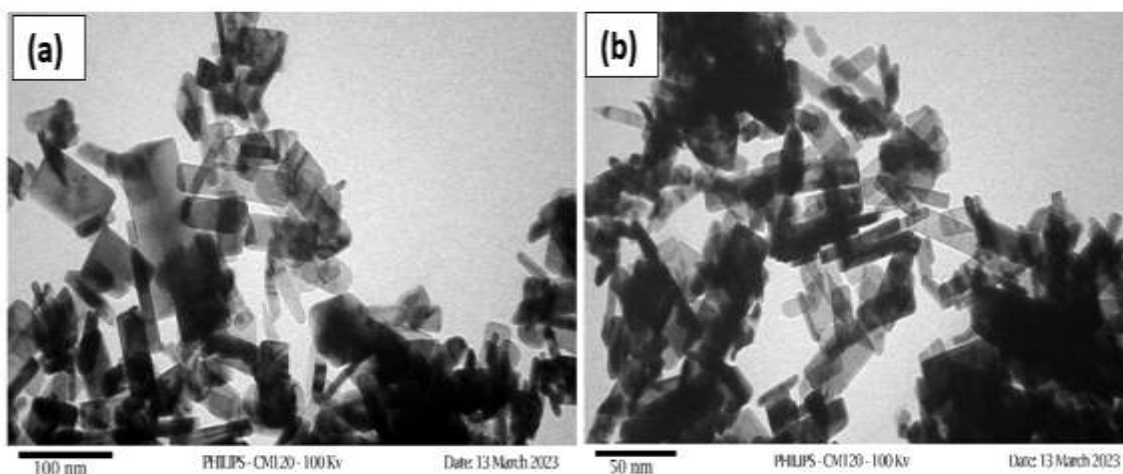
#### 4.7.2 CuO

Figure (4.28) illustrates the TEM of CuO prepared at 200 °C and annealed at 400 °C with different magnifications. From the obtained images, we can

observe a large quantity of uniform nanoparticles in a rod-like shape with high agglomerations.



**Figure (4.27): TEM images of rGO<sub>200</sub> annealed at 400 °C with different magnifications.**



**Figure (4.28): TEM images of CuO<sub>200</sub> annealed at 400 °C with different magnifications.**

### 4.7.3 CuO- rGO

Figure (4.29) demonstrates the impact of the GO weight on the CuO-rGO nanocomposites prepared at 200 °C and annealed at 400 °C, depicted at various magnifications. The TEM images in figure (4.29-a) reveal that a rod-

like structure has completely coated the surface of rGO with a significant amount of CuO, enhancing the SEM results of S4. A different shape is shown in figure (4.29-b). With increasing the weight of GO in the nanocomposites, a transformation in shape to a spherical form is clearly evident. CuO grains are dispersed between rGO sheets, showing a strong interaction between the two compounds with significant agglomeration leading to an increase in particle size. Figure (4.29-c) shows the TEM images of sample S6 after increasing the weight of GO. The spherical formations were randomly distributed across the surface and edges of the rGO sheets. The remained functional groups that are present on the rGO sheets serve as ligands that facilitate the attachment of CuO particles.

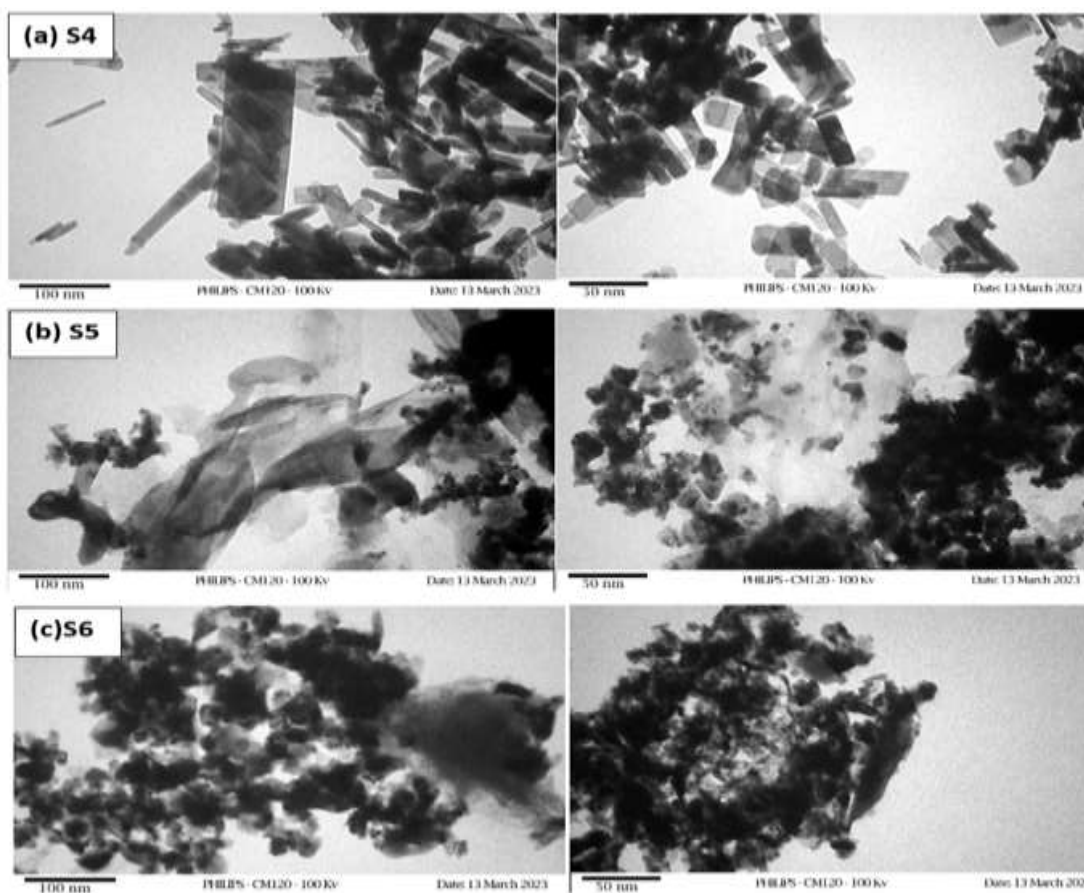


**Figure (4.29): TEM images of CuO- rGO samples prepared at 200 °C and annealed at 400 °C with different magnifications.**

## 4.8 AFM Analysis

### 4.8.1 Samples Prepared at 100 °C

AFM analysis was utilized to examine the surface characteristics of the thin films fabricated at 100 °C using the dip coating technique and subsequently annealed at 400 °C for two hours.

#### 4.8.1.1 GO and rGO

Figure (4.30) displays the surface characteristics of GO and rGO thin films deposited on a glass substrate using the dip coating process and then annealed at 400 °C for two hours. The AFM results depicted the roughness and surface topography of both GO and rGO samples. The 2-D and 3-D images of GO are shown in figure (4.30-a). The surface of GO was rough and had many wrinkles. The mean square, roughness, and height obtained from the AFM results are 19.35 nm, 15.75 nm, 7.85 nm respectively. After reduction at 100 °C, the GO displayed a reduction in root mean square and roughness as a result of exfoliation and removal of some oxygen-active groups as illustrated in figure (4.30-b). This eliminated some edges and wrinkles on the surface. The surface roughness of rGO<sub>100</sub> reported at 3.91 nm which was less than that of GO and higher than that reported before [40]. The mean square, roughness, and height obtained from the AFM results are illustrated in Table (4.10).

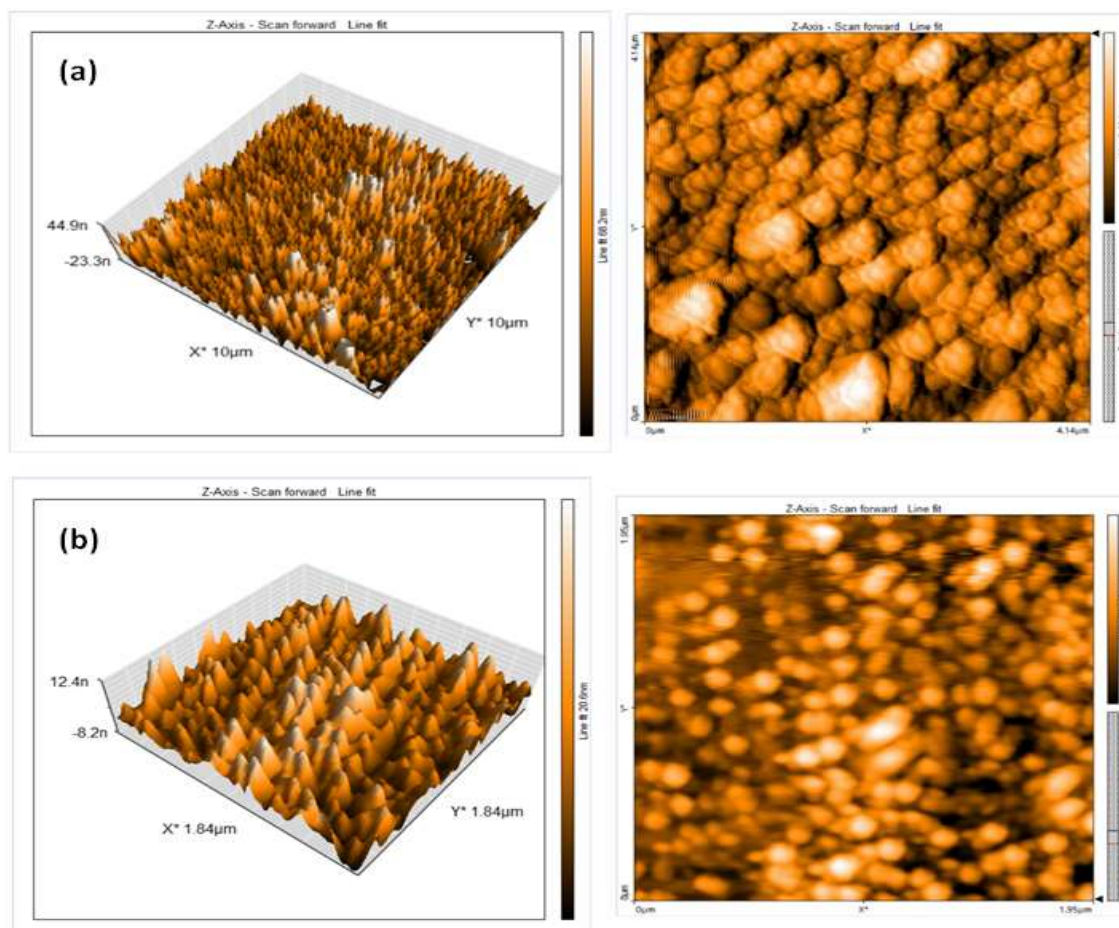


**Figure (4.30): 3-D and 2-D images of AFM results annealed at 400 °C: (a) GO, and (b) rGO<sub>100</sub>.**

**Table (4.10): AFM data of GO and rGO<sub>100</sub> samples.**

Sample	Root mean square (nm)	Roughness (nm)	Height of peak (nm)
GO	19.35	15.57	7.86
rGO <sub>100</sub>	5.14	3.91	2.88

#### 4.8.1.2 CuO

Figure (4.31) displays the surface characteristics of CuO thin films deposited on a glass substrate using the dip-coating process and then annealed at 400 °C for two hours.

The AFM results showed the roughness and surface topography of CuO sample. The 2-D and 3-D images showed rough surface of annealed film of CuO. The root mean square, roughness, and height obtained from the AFM results are 25.22 nm, 19.81 nm, 10.22 nm respectively. These results differ from those obtained recently when CuO film was prepared by so- gel method and deposited by dip coating process. The film showed high roughness of 77.4 nm [153].

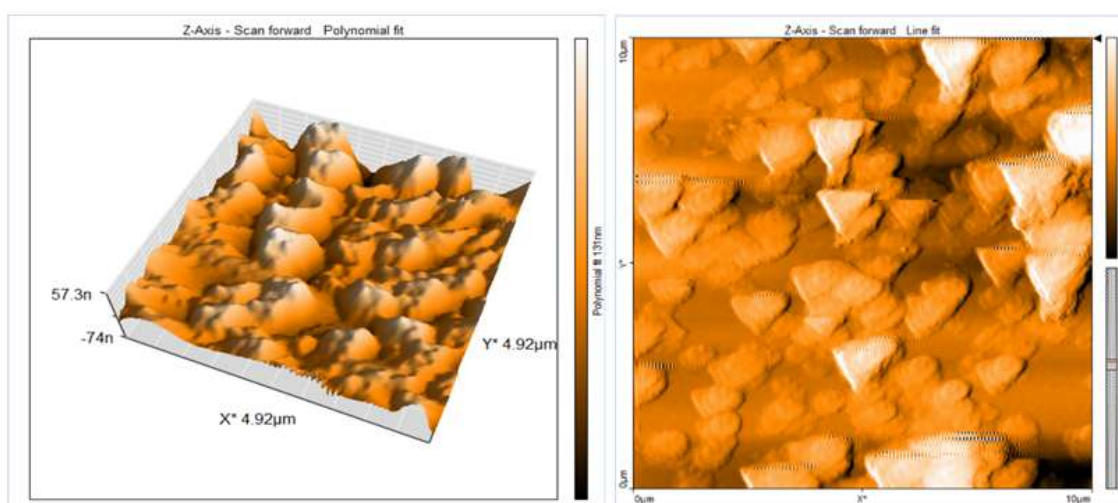
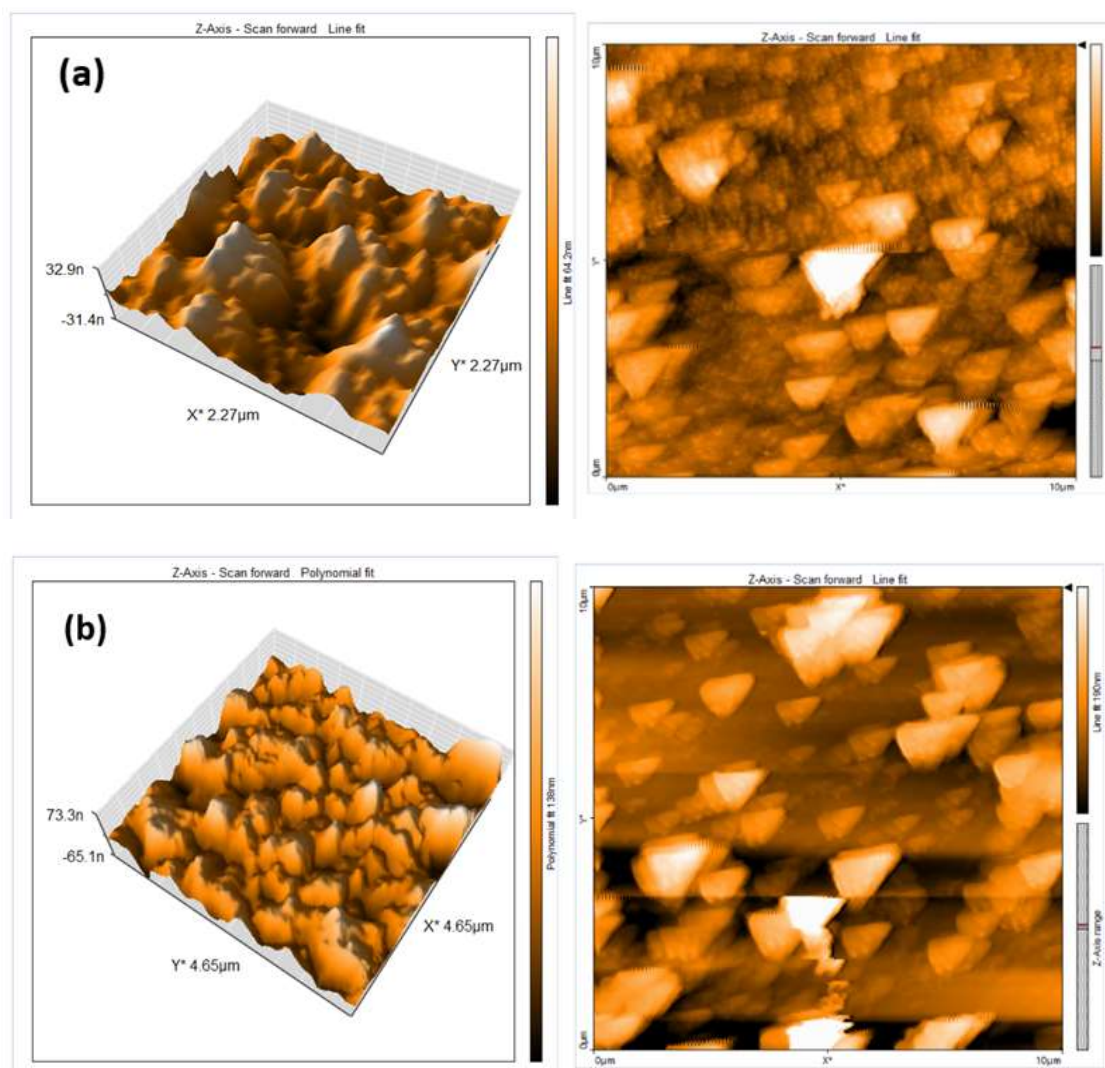


**Figure (4.31):3-D and 2-D images of AFM results of CuO<sub>100</sub> annealed at 400 °C.**

#### 4.8.1.3 CuO- rGO

Figure (4.32) displays the 2-D and 3-D images of CuO- rGO nanocomposites. As shown in figure (4.36-a), the surface of S1, as exhibits several peaks and valleys due to the deposition of nanoparticles, resulting in significant height variation. The surface has an average roughness of 27.81 nm, with a peak height around 144.4 nm. Increasing the weight percentage of GO in sample S2 resulted in the creation of many peaks and valleys on the surface, with heights of around 54.44 nm, leading to an increase in roughness to 116.1 nm (see figure 4.32- b).

Further increase in the GO amount resulted in a reduction of the roughness surface to around 31.62 nm with relatively high peaks, as depicted in figure (4.32- c). The results showed that roughness can be altered by combining rGO with CuO, resulting in nanocomposites with greater roughness than pure CuO and rGO which is in agreement with [174]. Table (4.11) displays the results of AFM of the three samples.



Continued...



Continued

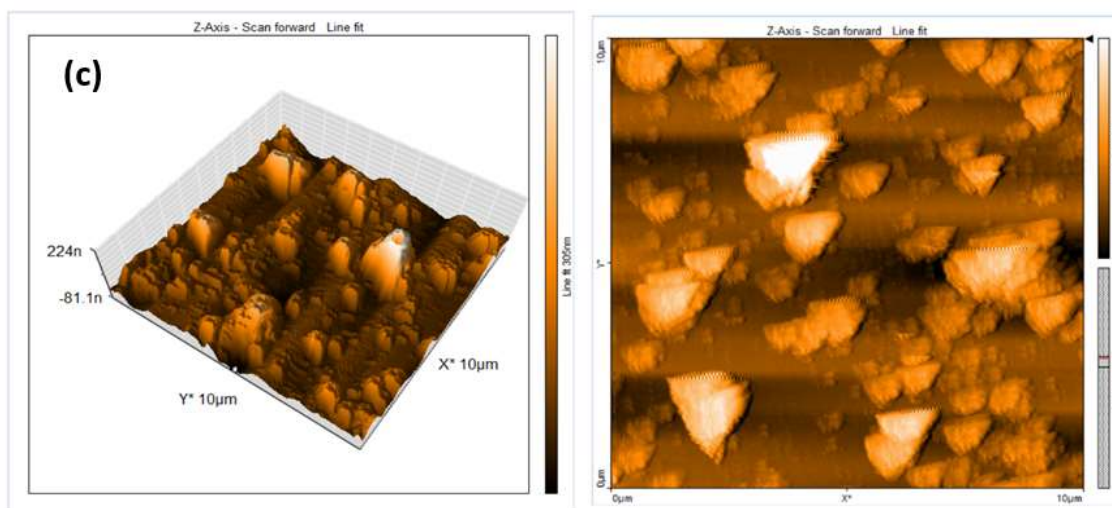


Figure (4.32): 3-D and 2-D images of AFM results of: (a) S1, (b) S2 (c) and S3.

Table (4.11): AFM data of CuO- rGO thin films prepared at 100 °C and annealed at 400 °C.

Sample	Root mean square (nm)	Roughness (nm)	Height of peak (nm)
S1	39.30	27.81	149.40
S2	223.30	116.1	54.44
S3	43.93	31.62	135.80

## 4.8.2 Samples Prepared at 200 °C

AFM analysis was utilized to examine the surface characteristics of the thin films fabricated at 200 °C using the dip coating technique and subsequently annealed at 400 °C for two hours.

### 4.8.2.1 rGO

Figure (4.33) displays 2-D and 3-D images of rGO thin films fabricated at 200 °C and deposited on a glass substrate using the dip coating technique and annealed at 400 °C. At a preparation temperature of 200 °C, several functional groups were eliminated resulting in thicker layers and increased surface roughness due to deoxidation. The surface roughness reached 10.14

nm, the root mean square was 13.02 nm, and the peak height was around 1.02 nm. The results closely align with other reduction methods such as magnetron sputtering in the HCl agent [155] and biological reduction of GO [156]. The thin film's thickness was determined to be 42.34 nm.

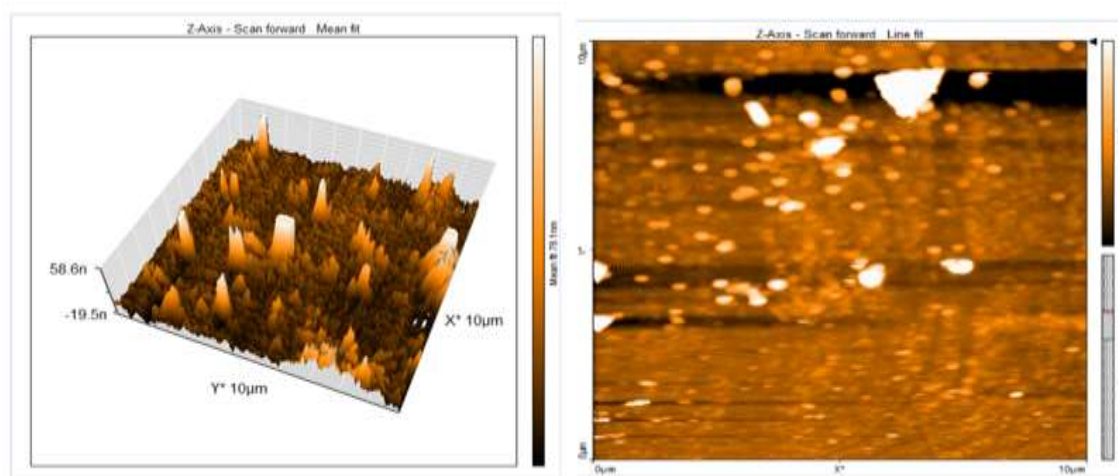


**Figure (4.33): 3-D and 2-D image of AFM results of rGO<sub>200</sub> and annealed at 400 °C.**

#### 4.8.2.2 CuO

Figure (4.34) shows AFM images of a CuO thin film produced at 200 °C on a glass substrate using the dip coating process, followed by annealing at 400 °C for two hours. At a preparation temperature of 200 °C, a notable increase in peak height and roughness was observed in both the 2-D and 3-D images. The surface of CuO<sub>200</sub> was higher than that of CuO<sub>100</sub>. The results suggest that raising the temperature to 200 °C leads to an increase in grain size and subsequently an increase in surface roughness during annealing [157]. The average values for root mean square, roughness, peak height, and thickness are 29.87 nm, 21.44 nm, 13.17 nm, and 62.69 nm, respectively.

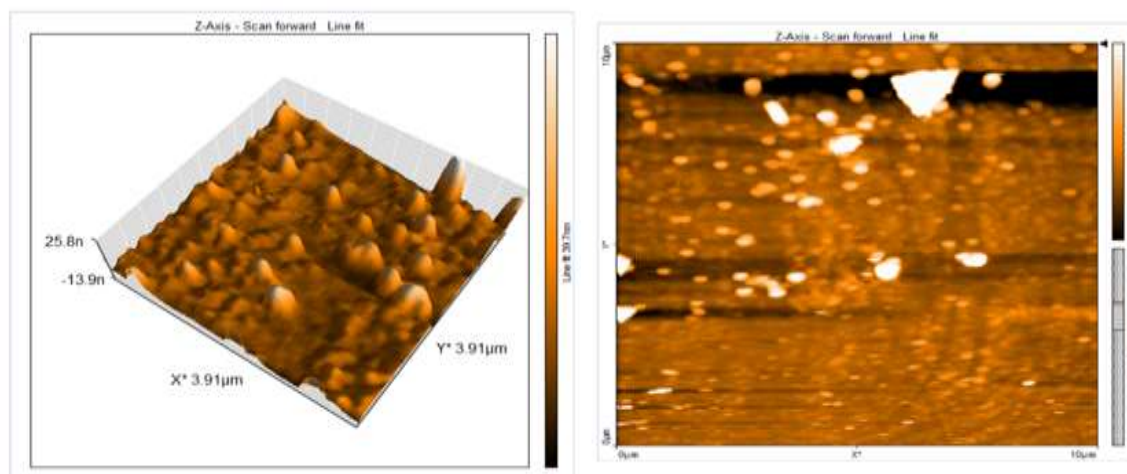
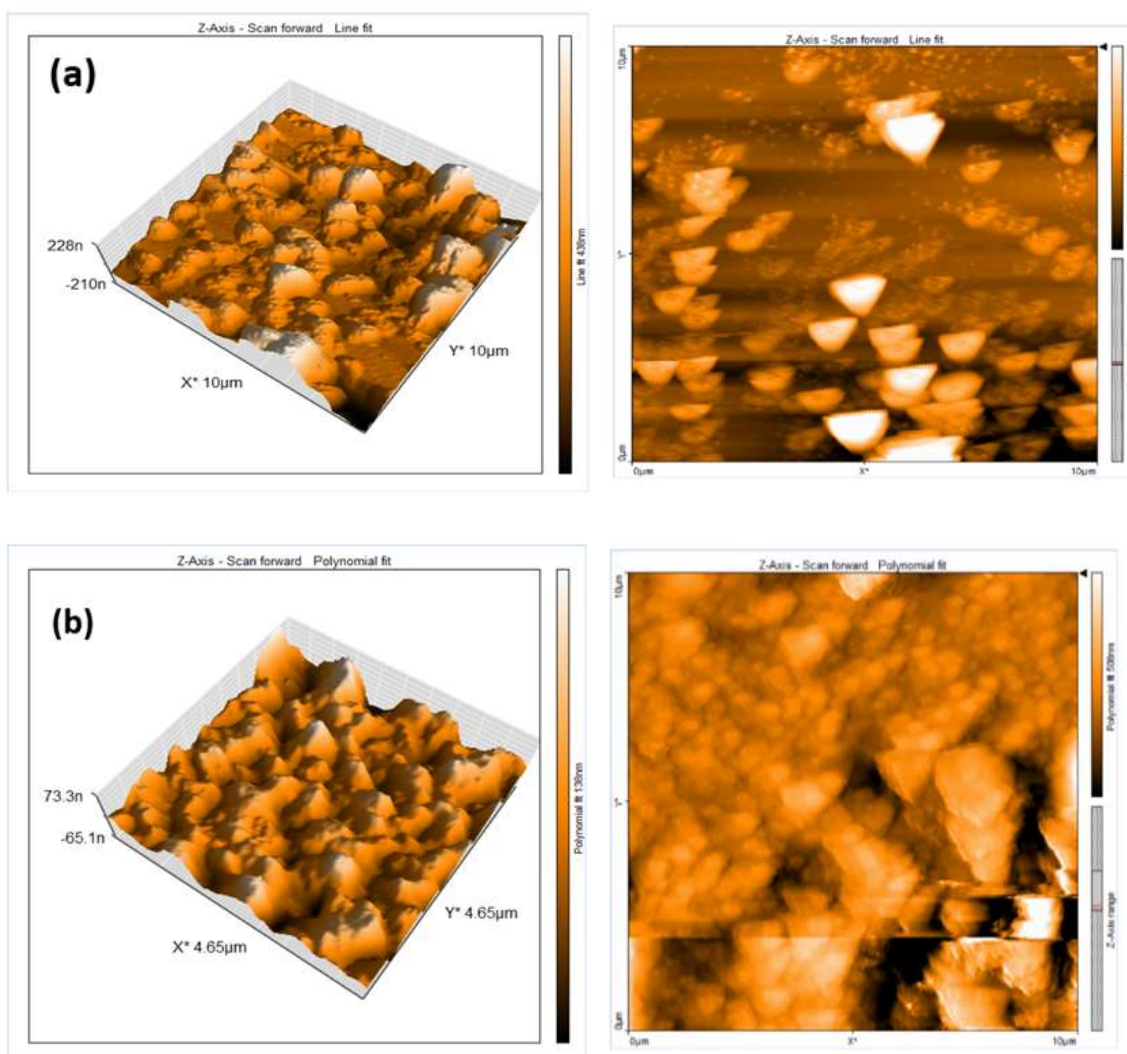


Figure (4.34): 3-D and 2-D images of AFM results of CuO<sub>200</sub> and annealed at 400 °C.

#### 4.8.2.3 CuO- rGO

Figure (4.35) displays the 2-D and 3-D images of CuO- rGO thin films prepared at 200 °C using the dip coating technique and subsequently annealed at 400 °C for two hours. The surface of S4 was rough with an average roughness of 51.40 nm, as shown in figure (4.35-a), with low height of peak. Increasing the weight percentage of GO in sample S5 resulted in the creation of many peaks and valleys on the surface, with heights of around 47.64 nm leading to great increase in roughness to 144.4 nm (see figure 4.35-b). Further increase in the GO amount resulted in a reduction of the rough surface to around 61.42 nm with very high peaks, as depicted in figure (4.35-c). The results showed that roughness of samples prepared at 200 °C were greater than that prepared at 100 °C.

A notable increase in roughness was noticed with the S5 compared to other samples. This was attributed to the presence of Cu ions being firmly anchored in the interfacial layers of GO which resulted in the difference in the topology of CuO -rGO [158]. The thickness of sample S4 measured to be 92.72 nm and increase 278.4 nm after deposition of SnO<sub>2</sub> above it by PLD. Table (4.12) displays the data of AFM of the three samples measured using AFM macroscopy.



Continued...

Continued

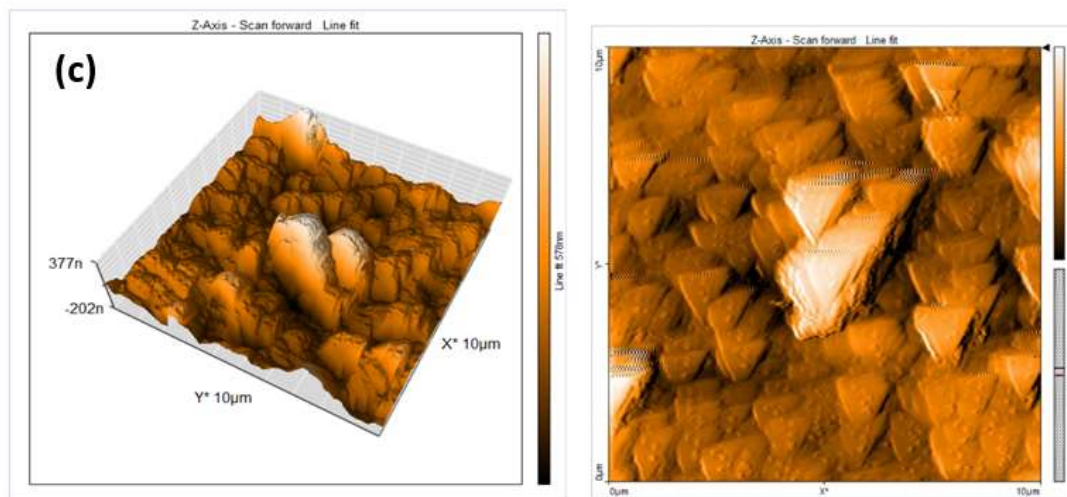


Figure (4.35): 3-D and 2-D images of AFM results of: (a) S4, (b) S5, and (c) S6.

Table (4.12): AFM data of CuO- rGO thin films prepared at 200 °C and annealed at 400 °C.

Sample	Root mean square (nm)	Roughness (nm)	Height of peak (nm)
S4	68.59	51.40	12.23
S5	223.30	144.40	47.64
S6	87.04	61.42	254.5

Table (4.13) displays the average thickness of thin films measured using AFM microscopy.

Table (4.13): Thin film thickness measurements for different samples.

Sample	Thickness (nm)
rGO <sub>200</sub>	42.34
CuO <sub>200</sub>	61.69
SnO <sub>2</sub>	86.30
CuO- rGO	92.72
SnO <sub>2</sub> / CuO-rGO	278.4

## 4.9 BET analysis

### 4.9.1 Samples Prepared at 100 °C

#### 4.9.1.1 rGO

The BET results demonstrate the impact of temperature on the adsorbed  $N_2$  in connection with pressure, as depicted in figure (4.36). The samples' adsorption isotherm is classed as type (IV) based on the Brunauer-Emmett-Teller classification, suggesting a mesoporous structure. The analysis shows that GO has a specific surface area of  $55.53 \text{ m}^2/\text{g}$ . Following the initial thermal reduction at  $100 \text{ }^\circ\text{C}$  and annealing at  $400 \text{ }^\circ\text{C}$ , the isotherm curve of rGO indicates its porous nature and exhibits a hysteresis loop [159]. The hysteresis loops of the produced samples revealed that the H3 hysteresis was indicated the existence of slit-shaped pores as observed in the FESEM images. The isotherms did not exhibit any limiting adsorption at high relative pressure.

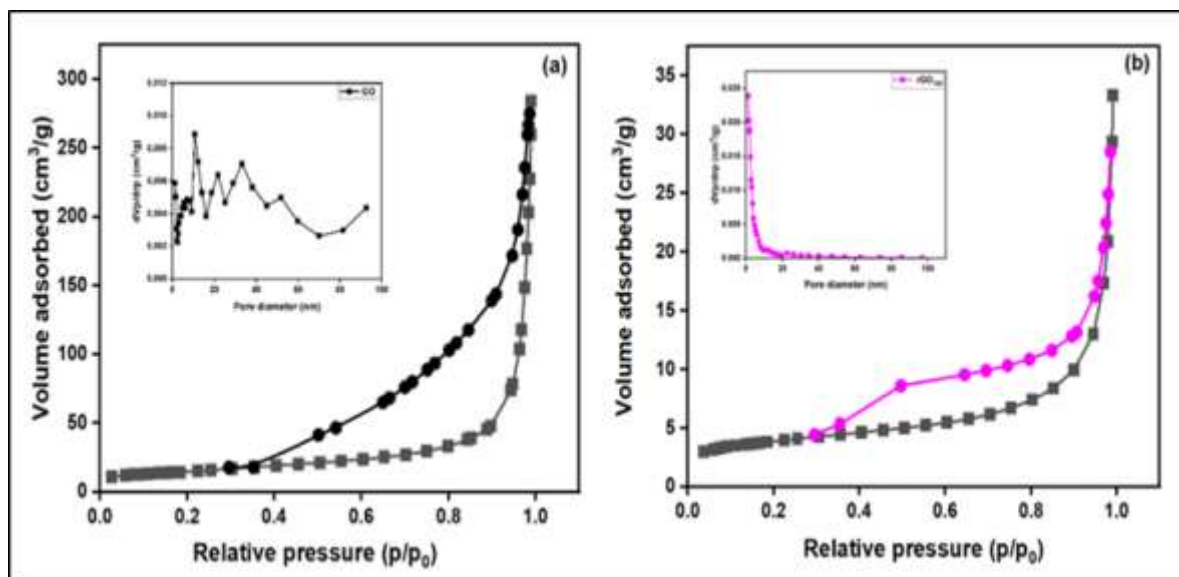


**Figure (4.36):  $N_2$  - adsorption–desorption isotherms of (a) GO and (b)  $rGO_{100}$  at  $77 \text{ K}$ . The inset shows the pore size distributions calculated using the BJH method.**

Table (4.13) summarises the BET results. This analysis indicated that the surface area of GO<sub>100</sub> was 118.99 m<sup>2</sup>/g as shown in figure (4.36-b) which was higher than that of GO. High BET surface area of GO and rGO<sub>100</sub> provides plenty of active sites for accelerating the sensing reactions as well [160]. The pore size distribution derived from the N<sub>2</sub> - adsorption isotherm using the BJH model was displayed in the inset figures, confirming the presence of micro- and mesoporous in the GO and rGO samples but the pore diameter was reduced to 3.99 nm after reduction as illustrated in table below.

**Table (4.14): BET results of GO and rGO<sub>100</sub>.**

Sample	Surface area (m <sup>2</sup> g <sup>-1</sup> )	Pore diameter (nm)	Total pore volume (cm <sup>3</sup> g <sup>-1</sup> )
GO	52.532	32.895	0.432
rGO <sub>100</sub>	118.990	3.991	0.118

#### 4.9.1.2 CuO

Figure (4.37) shows the N<sub>2</sub> adsorption–desorption isotherms of CuO prepared at 100 °C and annealed at 400 °C to confirm the existence of macropores and mesoporous in the sample. The isotherm curve of the sample exhibits an H3 hysteresis loop, suggesting the existence of significant mesoporous and macropores, which can be classified as type IV according to the international union of pure and applied chemistry (IUPAC) classification [161].

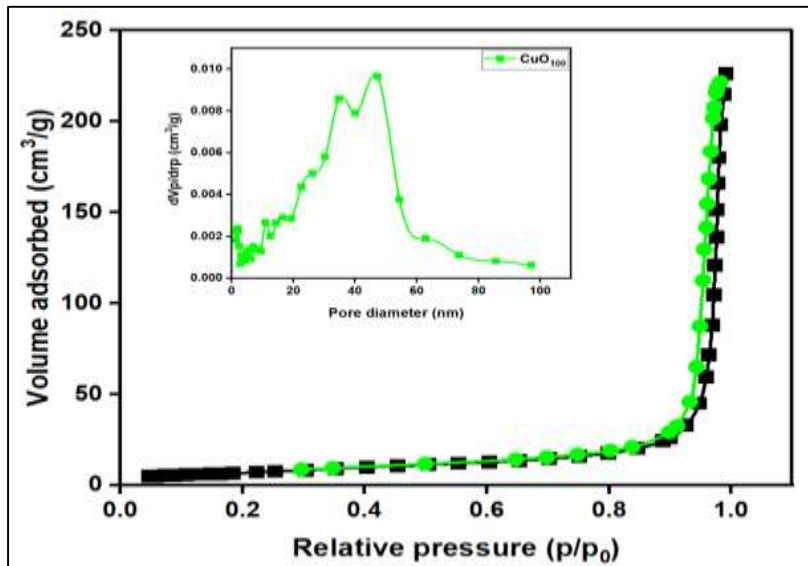


**Figure (4.37):** N<sub>2</sub> - adsorption–desorption isotherms of CuO<sub>100</sub> at 77 K. The inset shows the pore size distributions of CuO<sub>100</sub> calculated using the BJH method.

Based on the BET measurements, CuO has a mesoporous structure characterized by big pores and a relatively small surface area. The results showed that CuO nanoparticles had a BET surface area of 26.157 m<sup>2</sup>/g, which was higher than that reported previously [162], a pore diameter of 52.218 nm, and a pore volume of 0.341 cm<sup>3</sup>/g.

#### 4.9.1.3 CuO- rGO

The N<sub>2</sub> adsorption- desorption isotherms of CuO- rGO nanocomposites generated at 100 °C and annealed at 400 °C are depicted in figure (4.38) to verify the presence of microspores and mesoporous in the sample. The isotherm curves of the three samples exhibited H3 hysteresis loop, suggesting the presence of significant mesoporous. These mesoporous can be classified as type IV according to the IUPAC classification. Figure (4.38-a) indicates that sample S1 had a relatively small surface area of around 17.468 m<sup>2</sup>/g and a large pore diameter of 53.292 nm. This can be attributed to the low amount of rGO in the nanocomposites. By increasing the amount of GO in the nanocomposites, the specific surface area of S2 increased to



31.944 m<sup>2</sup>/g, but there was a slight decrease in the pore diameter, as shown in figure (4.38- d). The results were comparable to those obtained by [163]. With the increase in the amount of GO in sample S3, the BET surface area decreased to 10.379 m<sup>2</sup>/g. This reduction can be attributed to the weight loss observed in the temperature range of 100 - 600 °C, which is caused by the decomposition of rGO in the nanocomposites, as revealed by the TGA data. The Barrett–Joyner–Halenda (BJH) analysis revealed that the predominant pore diameter was approximately 31.507 nm, with an average pore volume of 0.081 cm<sup>3</sup>/g, as depicted in the figure (4.38-d). Table (4.15) illustrated the BET results of the three samples.

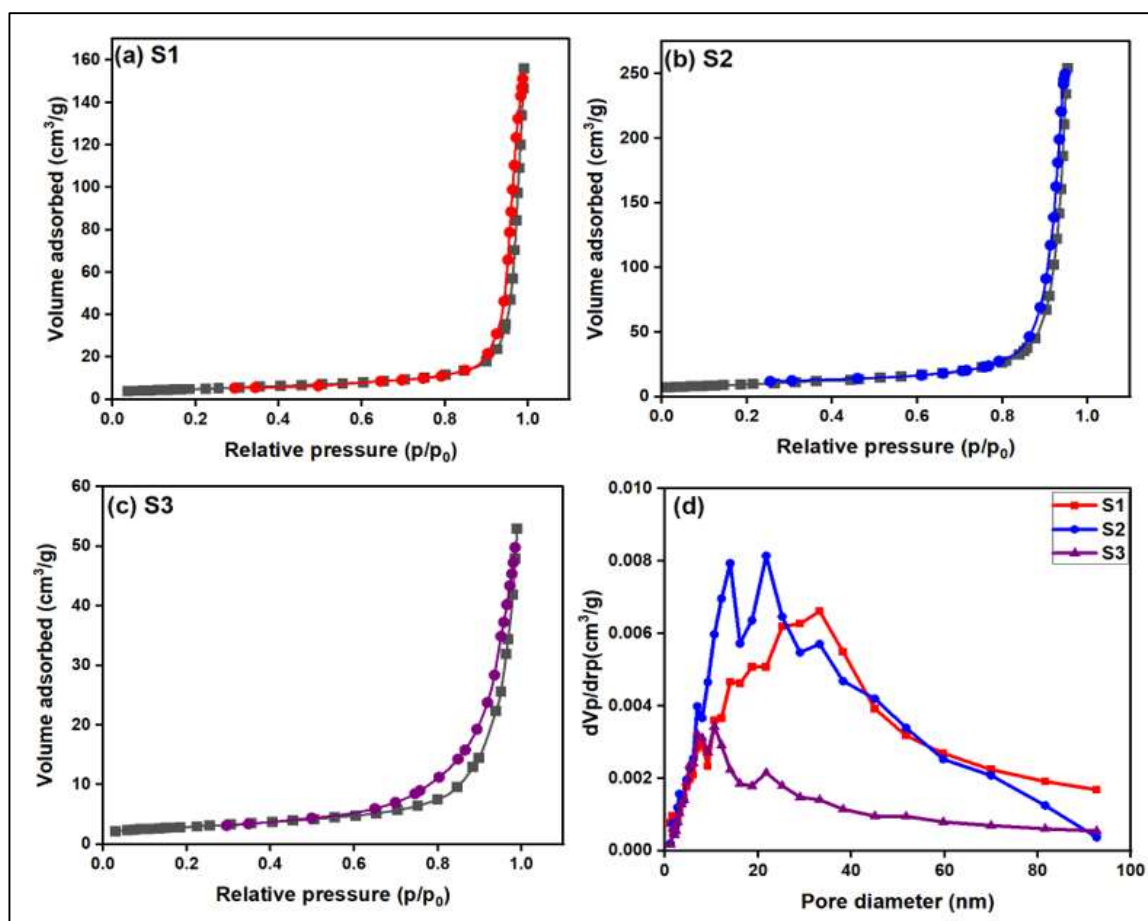


Figure (4.38): N<sub>2</sub> - adsorption–desorption isotherms of (a)S1, (b)S2, (c) S3 at 77 K, and (d) the pore size distributions of S1, S2, S3 calculated using the BJH method.

**Table (4.15): BET results of CuO- rGO nanocomposites prepared at 100 °C**

Sample	Surface area (m <sup>2</sup> g <sup>-1</sup> )	Pore diameter (nm)	Total pore volume (cm <sup>3</sup> g <sup>-1</sup> )
S1	17.468	53.292	0.232
S2	31.944	46.646	0.372
S3	10.379	31.507	0.081

## 4.9.2 Samples Prepared at 200 °C

### 4.9.2.1 rGO

The N<sub>2</sub> adsorption–desorption isotherms of rGO prepared at 200 °C and annealed at 400 °C for two hours were illustrated in figure (4.39). rGO<sub>200</sub> showed type-IV adsorption isotherms in the relative pressure indicating to the sheet-like particles and slit-like pores. The pore size distribution derived from the N<sub>2</sub> adsorption isotherm using the BJH model is also displayed in the inset figure (4.39) confirming the presence of mesoporous. The specific surface area of rGO<sub>200</sub> was about 195.28 m<sup>2</sup>/g, which was higher than that of rGO prepared at 100 °C and that reported by [159], when GO reduced at 900 °C. High surface area due to many oxygen functional groups on its surface that can become adsorption sites for gas. The average pore diameter and pore volume were 28.779 nm, and 1.408 cm<sup>3</sup>/g respectively.

### 4.9.2.2 CuO

The N<sub>2</sub> adsorption-desorption isotherms of CuO, which were synthesized at a temperature of 200 °C and then annealed at 400 °C for two hours, are shown in figure (4.40). The isotherm curves of CuO<sub>200</sub> exhibited a hysteresis loop, suggesting the presence of significant mesoporous and macropores, which can be classified as type IV isotherm. The computed specific BET surface area of CuO<sub>200</sub> was 15.233 m<sup>2</sup>/g. The obtained results were lower

than that of  $\text{CuO}_{100}$ . In addition, the BJH method was used to determine the average pore-size distributions and pore diameter of  $\text{CuO}_{200}$ . The results showed that the average pore diameter was 50.46 nm and the pore volume was  $0.192 \text{ m}^3/\text{g}$ , as indicated in the inset figure (4.40).

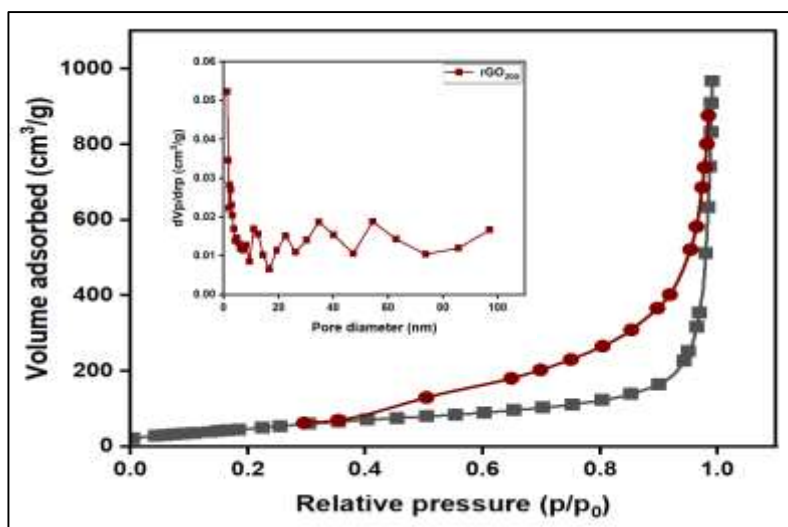


Figure (4.39):  $\text{N}_2$  - adsorption–desorption isotherms of  $\text{rGO}_{200}$  at 77 K. The inset shows the pore size distributions of  $\text{rGO}_{200}$  calculated using the BJH method.

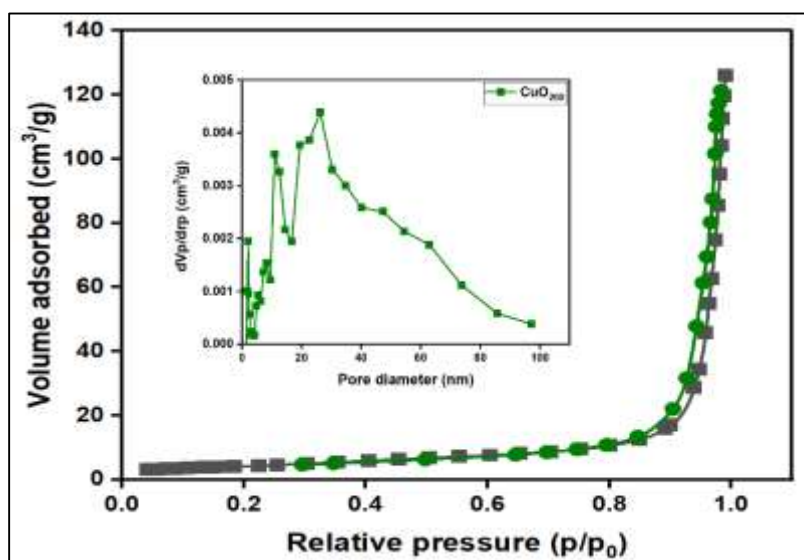
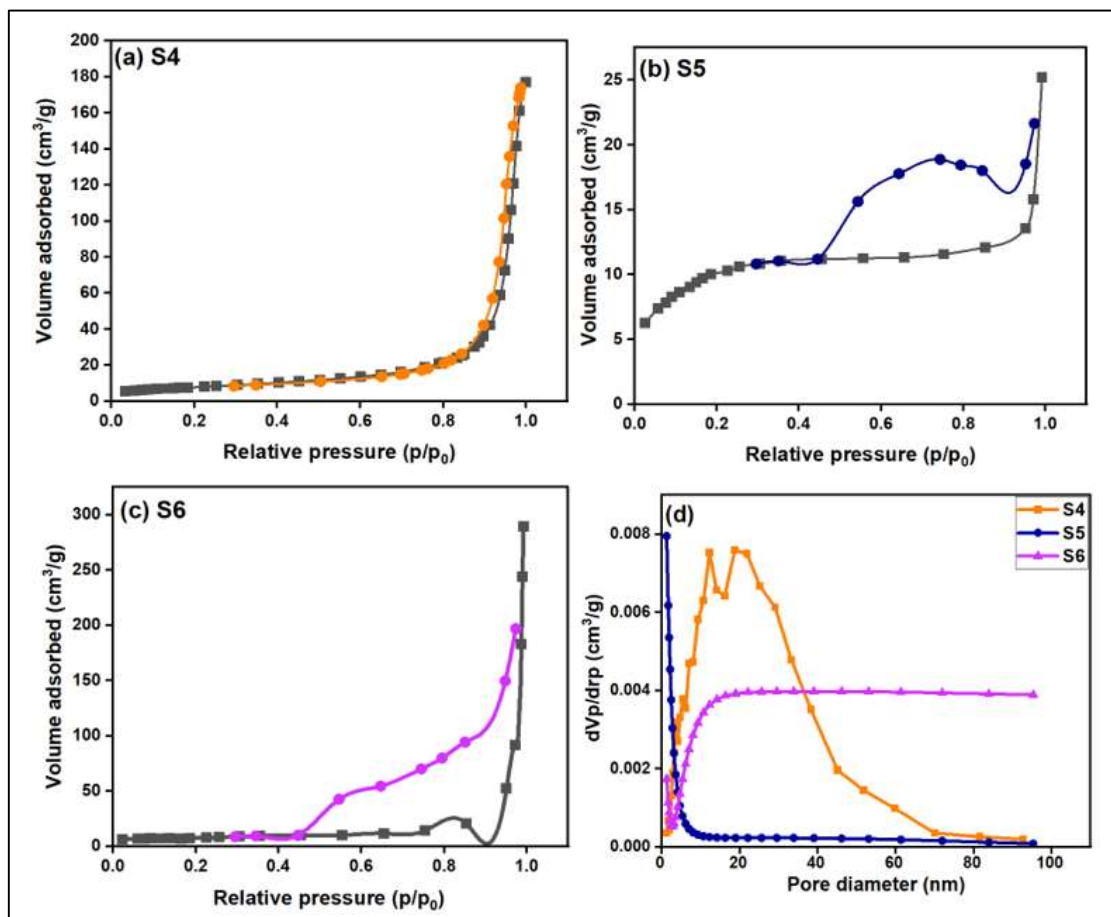


Figure (4.40):  $\text{N}_2$  - adsorption–desorption isotherms of  $\text{CuO}_{200}$  at 77 K. The inset shows the pore size distributions of  $\text{CuO}_{200}$  calculated using the BJH method.

### 4.9.2.3 CuO- rGO

The N<sub>2</sub> adsorption- desorption isotherms of CuO- rGO nanocomposites generated at 200 °C and annealed at 400 °C are depicted in figure (4.41) to verify the presence of macropores and mesoporous in the sample. The isotherm curves of the three samples exhibited a hysteresis loop, suggesting the presence of significant mesoporous. These mesoporous can be classified as type IV according to the IUPAC classification. Figure (4.41- a) indicated that S4 sample had a relatively high surface area of around 27.926 m<sup>2</sup>/g which was higher than that of S1 with a smaller pore diameter of 36.968 nm. By increasing the amount of GO in the nanocomposites, the specific surface area of S5 increased to 36.116 m<sup>2</sup>/g, with an increase in the pore diameter, as shown in the figure (4.41- d) revealing the H2 hysteresis loop [164]. With increase in the amount of GO in sample S6, the BET surface area decreased to 28.149 m<sup>2</sup>/g.

The Barrett–Joyner–Halenda (BJH) analysis revealed that the predominant pore diameter was approximately 55.597 nm, with an average pore volume of 0.391 m<sup>3</sup>/g as depicted in the inset figure (4.41- d). From the results of all samples, it can be said that the three samples exhibited enhancement in the surface area after doping with rGO compared with pristine CuO. The relatively large specific surface area benefits the gas sensor process by providing additional active adsorption sites for gas and accelerating the redox reaction on the surface of CuO- rGO, leading to the improvement response. Table (4.16) illustrates the BET results of the three samples.



**Figure (4.41):** N<sub>2</sub> - adsorption–desorption isotherms of (a) S4, (b) S5, (c) S6 at 77 K, (d) the pore e distributions of samples calculated using the BJH method.

**Table (4.16):** BET results of CuO- rGO nanocomposites prepared at 200 °C

Sample	Surface area (m <sup>2</sup> g <sup>-1</sup> )	Pore diameter (nm)	Total pore volume (cm <sup>3</sup> g <sup>-1</sup> )
S4	27.926	36.968	0.258
S5	36.116	41.189	0.378
S6	28.149	55.597	0.391

## 4.10 UV-Visible Spectroscopy for Thin Films

The optical properties of the thin films deposited on glass substrate have been investigated. The optical properties include the UV-Visible absorption and Tauc plot analysis.

### 4.10.1 UV-Visible Properties

#### 4.10.1.1 GO and rGO Thin Films

Figure (4.42) shows the UV-visible spectra of GO and rGO thin films. As shown in figure (4.42), GO has two peaks at 232.5 nm and 321 nm, which are related to ( $\pi$ - $\pi^*$  transition) of (C=C) bonds and ( $n$ - $\pi^*$  transitions) of (C=O) bonds [165], [166]. Figure (4.42) showed rGO prepared at 100 °C and annealed at 400 °C for two hours. For rGO<sub>100</sub>, due to the partial reduction of GO and the elimination of oxygen-functional groups, a red shift in ( $\pi$ - $\pi^*$  transition) may occur and disappearance ( $n$ - $\pi^*$  transitions) of (C=O) bonds and an increase in aromatic rings leads to easier electron excitation at lower energy [162]. As preparation temperature goes up, absorptivity goes down, but there is no change in wave lengths less than 400 nm [167]. The rGO<sub>200</sub> film absorption was observed between 200- 300 nm and was absent ( $n$ - $\pi^*$  transitions) due to the reduction of GO.

#### 4.10.1.2 CuO and SnO<sub>2</sub> Thin Films

The UV-visible absorption spectrum of CuO and SnO<sub>2</sub> thin films are shown in figure (4.43). It is clear from figure (4.43-a) that CuO films exhibit a relatively high absorption in the visible region ranging from 400 to 800 nm. The absorption peak of CuO prepared at 100 °C is at around 280 nm [168] . Shifting in the absorption spectrum of CuO has been observed after increasing the preparation temperature to 200 °C and the peak was seen at

244 nm. The UV-visible absorption spectrum of SnO<sub>2</sub> thin films deposited by PLD is shown in figure (4.43- b). High absorption peak was observed in the range of 300 nm and decreases with increasing the wavelength [169].

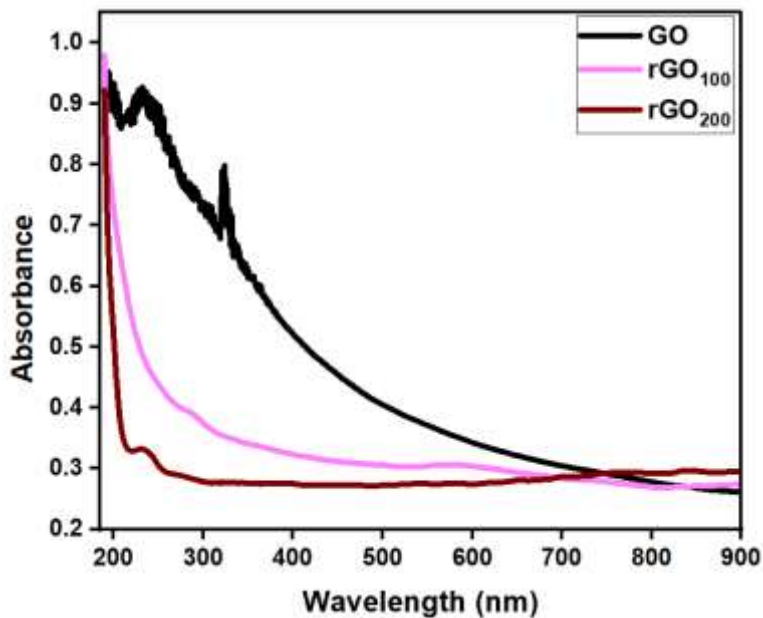


Figure (4.42): UV-visible Spectra of the GO and rGO thin films.

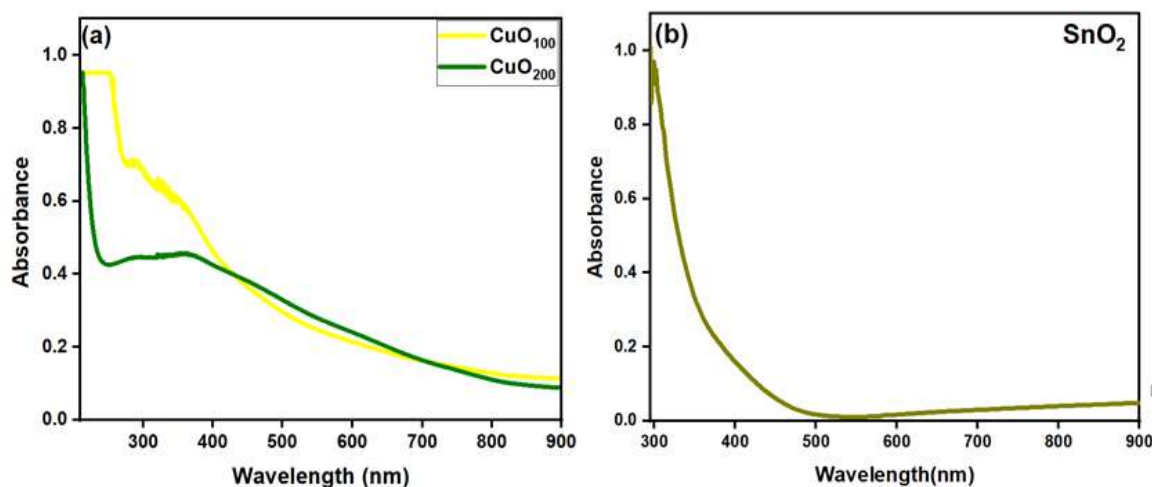
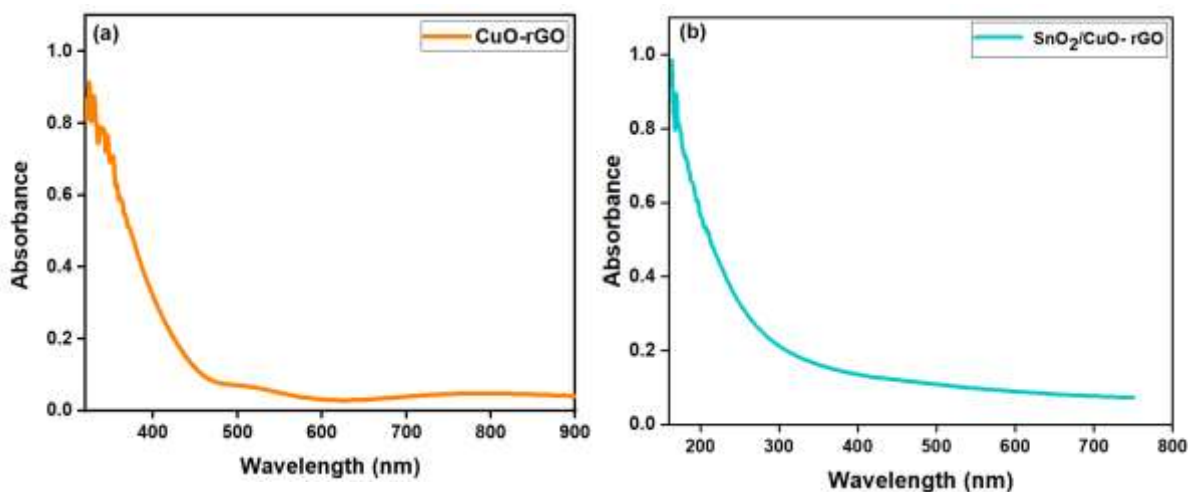


Figure (4.43): (a) UV-visible Spectra of the CuO thin films, (b) UV-visible Spectra of the SnO<sub>2</sub> thin films.

### 4.10.1.3 CuO- rGO and SnO<sub>2</sub> /CuO- rGO Thin Films

Figure (4.44-a) displays the UV-visible absorption spectrum of CuO-rGO thin films that were prepared at 200 °C and subsequently annealed at 400 °C for two hours. The absorption peak of the CuO- rGO thin film exhibits a red shift of 322 nm in comparison to pure CuO. The presence of a red-shifted indicates a decrease in the GO content in the nanostructure. The primary absorbance peak of CuO nanoparticles has seen a shift towards a lower wavelength (300 nm), suggesting changes in the structure of the CuO nanoparticles [170]. After deposition of third layer of SnO<sub>2</sub>, a small shift in the absorption peak around 312 nm has been observed in comparison with CuO- rGO as shown in figure (4.44-b).



**Figure (4.44): UV-visible Spectra of: (a) CuO- rGO and (b) SnO<sub>2</sub>/ CuO- rGO thin films.**

### 4.10.2 Band gap Energy and Tauc Plot

A high absorption region ( $\alpha > 10^4 \text{ cm}^{-1}$ ) thus direct transition has been observed related to the absorption coefficient  $\alpha$  using Tauc's equation [39]



for all samples. Band gap can be calculated by the intercept of tangent of  $(\alpha h\nu)^2$  and the photon energy.

Figure (4.45) shows the variation of  $(\alpha h\nu)^2$  versus photon energy ( $h\nu$ ) of incident radiation for rGO<sub>200</sub>, CuO<sub>200</sub>, SnO<sub>2</sub>, CuO- rGO and SnO<sub>2</sub>/ CuO- rGO. This figure shows that the value of optical energy gap of rGO<sub>200</sub> was equal to 4.68 eV and the value of optical energy gap of CuO<sub>200</sub> was equal to 4.45 eV which was larger than the bulk value (1.2 eV). The increase in band gap of CuO was due to decreased in particle size [171] which was calculated by Scherer equation. As shown in figure (4.45), the calculated band gap of SnO<sub>2</sub> was 3.7 eV which is in agreement with published value of bulk SnO<sub>2</sub> [172]. The computed band gap of the CuO- rGO composite was 2.95 eV as shown in figure, which was smaller than the individual band gaps of pure rGO and CuO. The observed result can be related to the heightened surface charge interaction between rGO and CuO, which leads to a shift in the optical energy gap towards longer wavelengths. Consequently, this shift results in a reduction of the band gap in the CuO- rGO [173].

The computed band gap of the SnO<sub>2</sub>/ CuO- rGO composite was 3.5 eV, which was greater than CuO- rGO and smaller than the individual band gaps of pure rGO and CuO due to an increase in particle size as calculated previously in XRD results.

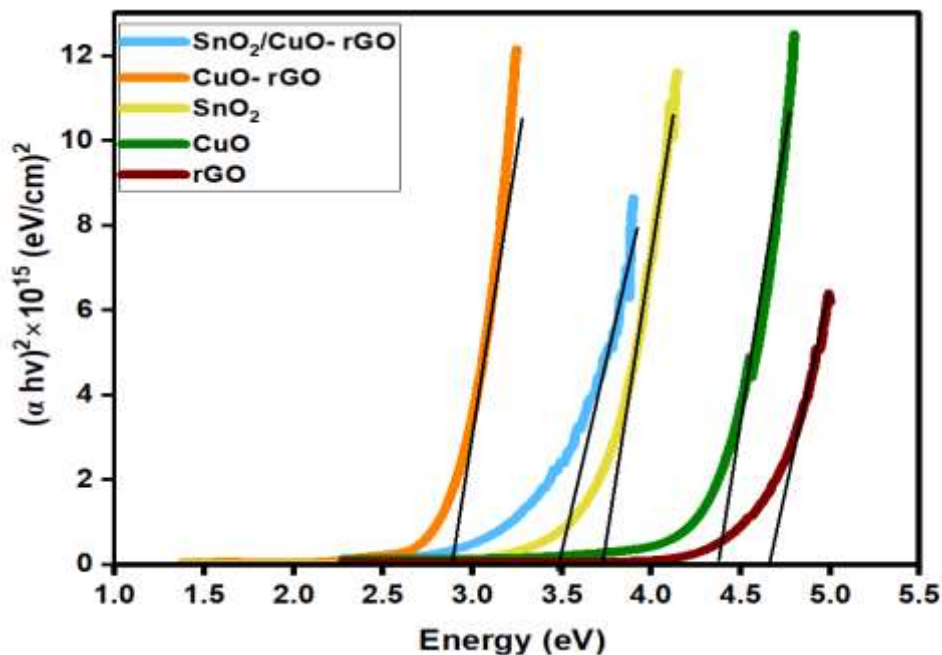


Figure (4.45): Tauc plots of the thin films.

#### 4.11 Current-Voltage (I-V) Characteristics

Current–Voltage characteristics of SnO<sub>2</sub>/ CuO- rGO, CuO- rGO, CuO, rGO, and SnO<sub>2</sub> thin films were investigated under the dark condition. The measurements were taken using the two-probe method with applied voltage ranging from -5 to 5 V, as depicted in figure (4.46). The figure shows that Au electrodes (5.1 eV) have a larger work function than that of SnO<sub>2</sub> (4.2 eV), rGO (4.6 eV), and CuO (4.8 eV), indicating Schottky contact generation. Under experimental conditions, all samples displayed Schottky contact behavior with a slight resistivity change. The non-linear I-V curve relation shown in figure is important for gas detecting devices since it directly influences gas sensor sensitivity. Detecting different target gases and improving sensing performance requires modulating Schottky barrier height (SBH) at the metal-semiconductor junction. Many parameters can

affect electrical contact and thus the sensitivity, such as electrode resistance, which can be modified by electrode thickness or distance [174].

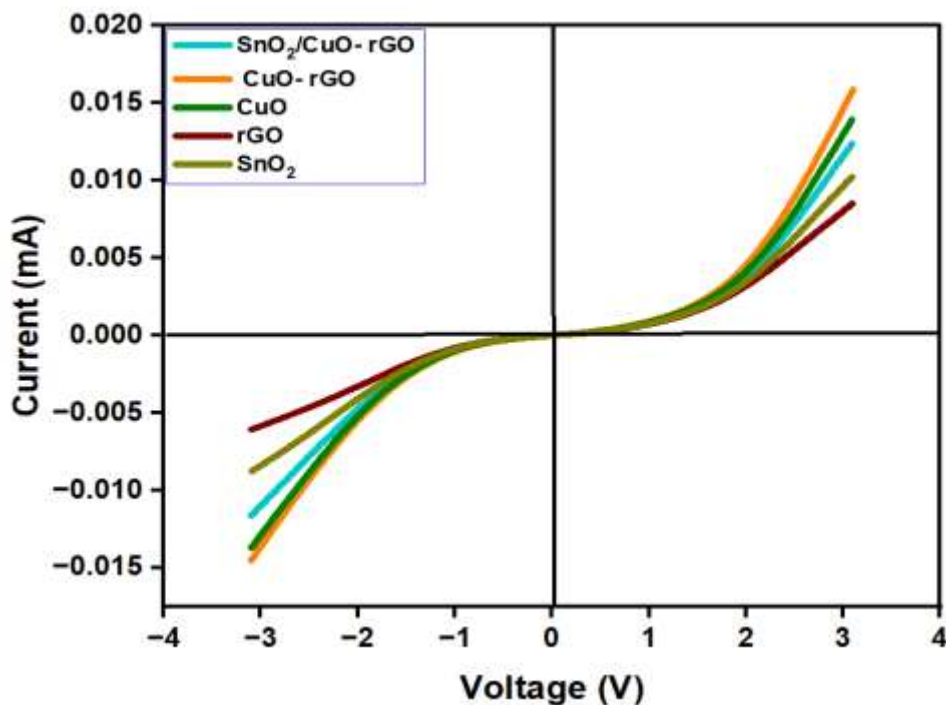


Figure (4.46): Current–Voltage characteristics of the thin films.

## 4.12 Gas Sensor Measurements

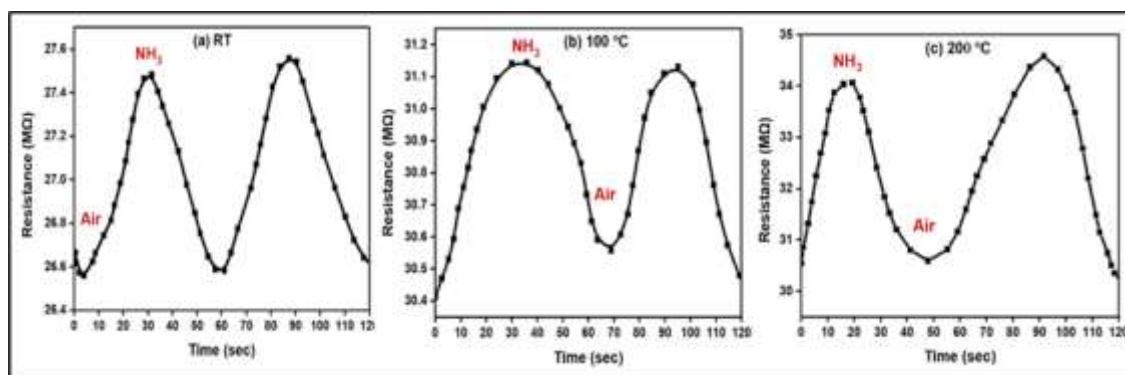
The gas-sensing characteristics of sensors have been examined by measuring the resistance across sensors while the gas mixtures were flowing through them. The chamber was continuously ventilated with dry air at a consistent rate during the measurements. Prior to introducing the target gas into the chamber, the chamber underwent a purging process with dry N<sub>2</sub> for approximately half hour. This was done to eliminate any remaining gas molecules that could affect the gas-detecting behavior.

## 4.12.1 NH<sub>3</sub> Sensor Measurement

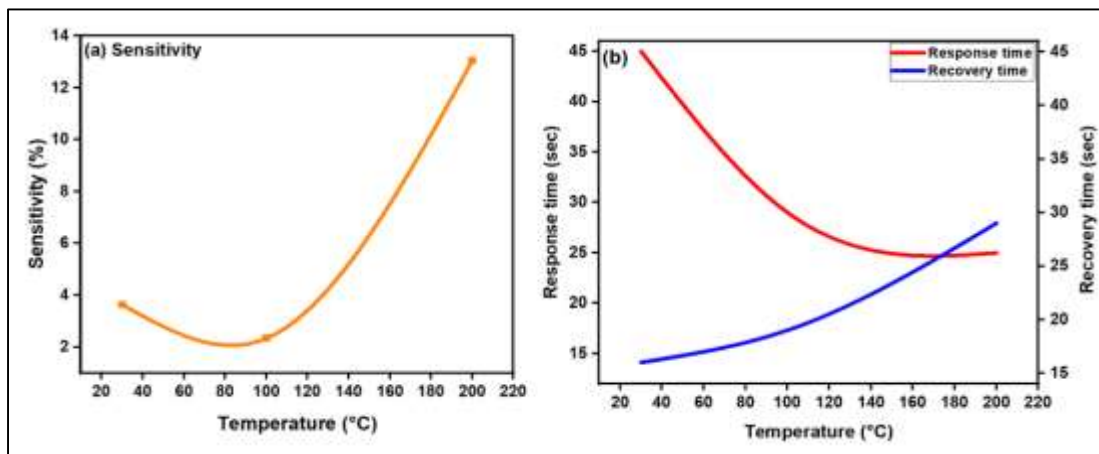
### 4.12.1.1 GO and rGO Sensors Measurements

The gas-sensing characteristics of GO and rGO sensors had been examined by measuring the resistance across sensors at various temperatures (RT, 100 °C, and 200 °C) while the gas mixtures were flowing through them. Figure (4.47) shows the response of the GO sensor for 100 ppm of NH<sub>3</sub> gas at different operation temperatures.

The increase in the response of the sensor had been observed when sample was exposed to NH<sub>3</sub> gas (reducing gas). The NH<sub>3</sub> gas contributed with a pair of valence electrons to GO which acts as a p-type sensor, this modifies the charge carriers in the p-type GO causing a decrease of holes concentration and this rises the electrical resistivity. These results agreed with previously published work [175]. Figure (4.48) shows the variation of NH<sub>3</sub> gas sensitivity, response and recovery time versus operating temperature for GO sensor toward NH<sub>3</sub> gas. This figure shows that the sensitivity increases with increasing operation temperature reaching maximum values at 200 °C.

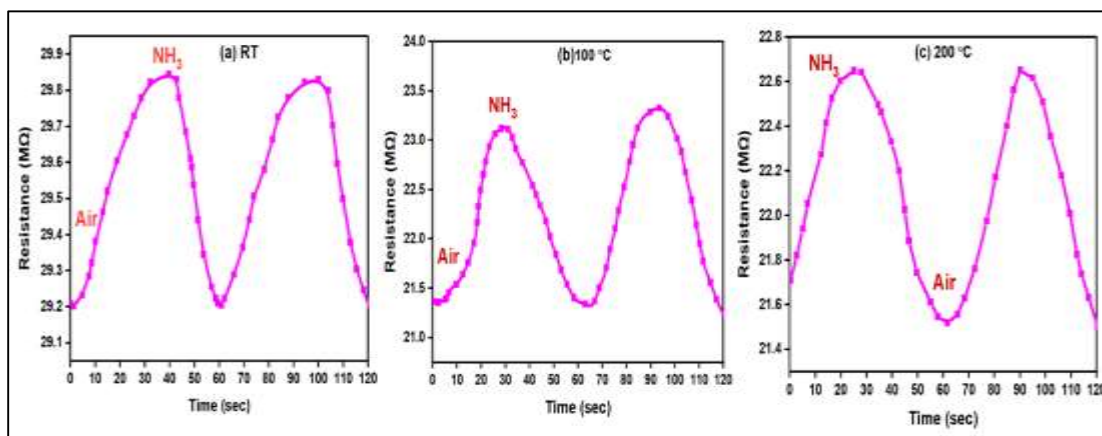


**Figure (4.47): Dynamic response of GO toward 100 ppm NH<sub>3</sub> gas at different working temperatures; (a) room temperature, (b) 100 °C, (c) 200 °.**



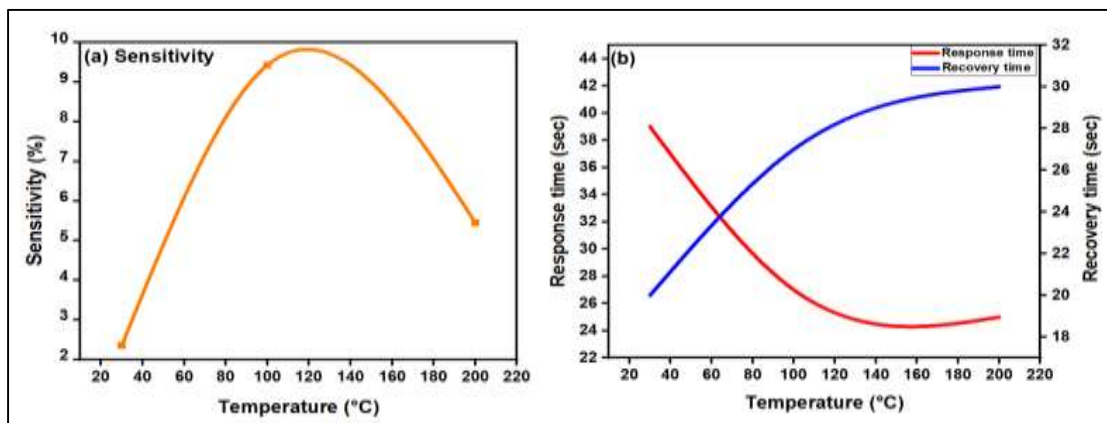
**Figure (4.48): (a)  $\text{NH}_3$  gas sensitivity versus operating temperature for GO, and (b) response and recovery time versus operating temperatures.**

The response of the  $\text{rGO}_{100}$  sensor for 100 ppm of  $\text{NH}_3$  gas at different operation temperatures is shown in figure (4.49). The increase in the response of the sensor was observed when sample exposed to  $\text{NH}_3$  gas which acts as a p-type semiconductor.



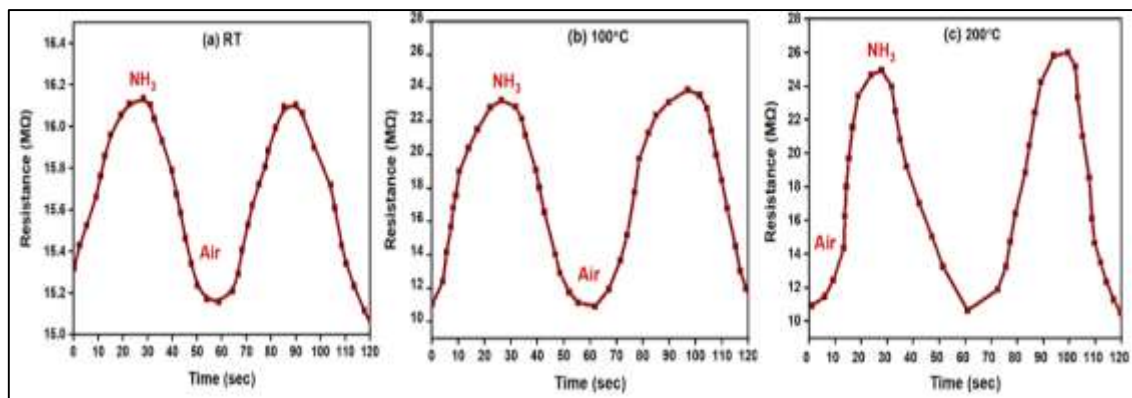
**Figure (4.49): Dynamic response of  $\text{rGO}_{100}$  toward 100 ppm  $\text{NH}_3$  gas at different working temperatures; (a) room temperature, (b) 100 °C, (c) 200 °C.**

Figure (4.50) shows the variation of  $\text{NH}_3$  gas sensitivity, response and recovery time versus operating temperature for  $\text{rGO}_{100}$  sensor toward  $\text{NH}_3$  gas. This figure shows that the sensitivity increases with increasing operation temperature reaching maximum values at  $100\text{ }^\circ\text{C}$  then decreases after increase operation temperature to  $200\text{ }^\circ\text{C}$ .



**Figure (4.50): (a)  $\text{NH}_3$  gas sensitivity versus operating temperature for  $\text{rGO}_{100}$ , and (b) response and recovery time versus operating temperatures.**

Figure (4.51) shows the response of the  $\text{rGO}_{200}$  sensor for 100 ppm of  $\text{NH}_3$  gas at different operation temperatures. When sample exposure to  $\text{NH}_3$  gas, an increase in the response of the sensor was observed as a p-type semiconductor.



**Figure (4.51): Dynamic response of  $\text{rGO}_{200}$  toward 100 ppm  $\text{NH}_3$  gas at different working temperatures: (a) room temperature, (b)  $100\text{ }^\circ\text{C}$ , (c)  $200\text{ }^\circ\text{C}$ .**

Figure (4.52) shows the variation of  $\text{NH}_3$  gas sensitivity, response and recovery times versus operating temperature for  $\text{rGO}_{200}$  sensor toward  $\text{NH}_3$  gas. This figure shows that the sensitivity increases with increasing operation temperature reaching maximum values at  $200\text{ }^\circ\text{C}$ . It was observed from all above results that  $\text{rGO}_{200}$  sensor exhibited higher response than GO and  $\text{rGO}_{100}$  with fast response and recovery times. The enhanced sensitivity for this sensor is due to the small crystal size oxygen, high roughness, the presence of pores like slits, and high surface area exposure to gas target as mentioned in XRD, AFM, FESEM, and BET results. The sensitivity of the present work is higher than that reported by [176]. The results indicate that the sensor's response is enhanced when using rGO with a higher degree of reduction as a sensing material for  $\text{NH}_3$ .

Table (4.17) shows GO and rGO gas sensor parameters (sensitivity, response time and recovery time with different operating temperatures.

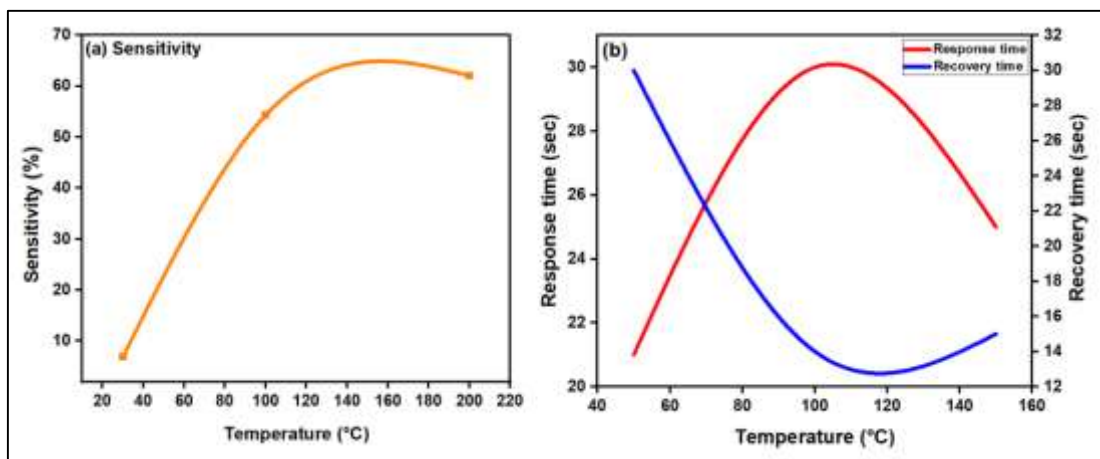


**Figure (4.52): (a)  $\text{NH}_3$  gas sensitivity versus operating temperature for  $\text{rGO}_{200}$ , and (b) response and recovery time versus operating temperatures.**

**Table (4.17): GO and rGO gas sensor parameters with different operating temperatures.**

Sample	Operating Temperature (°C)	Sensitivity (%)	Response time (sec)	Recovery time (sec)
GO	RM	3.63	45	16
	100	2.34	29	19
	200	13.04	25	29
rGO <sub>100</sub>	RM	2.35	39	20
	100	9.42	27	27
	200	5.44	25	30
rGO <sub>200</sub>	RM	6.93	21	30
	100	54.32	30	14
	200	62.02	25	15

#### 4.12.1.2 CuO Sensors Measurements

Figure (4.53) shows the response of the CuO sensor prepared at 100 °C for 100 ppm of NH<sub>3</sub> gas at different operation temperatures.

The increase in the response of the sensor was observed when sample was exposed to NH<sub>3</sub> gas which acts as a p-type semiconductor.

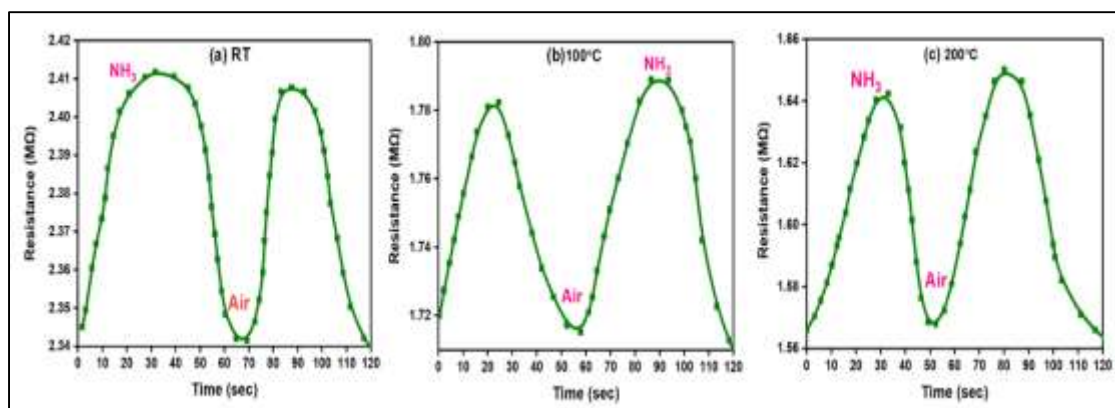


**Figure (4.53): Dynamic response of CuO<sub>100</sub> toward 100 ppm NH<sub>3</sub> gas at different working temperatures; (a) room temperature, (b) 100 °C, (c) 200 °C.**



Figure (4.54) shows the variation of  $\text{NH}_3$  gas sensitivity, response and recovery time versus operating temperature for CuO sensor toward  $\text{NH}_3$  gas. This figure shows the increment of CuO sensitivity by increasing operation temperature up to 5.32% at 200 °C. These results were lower than reported before [177]. The low response of this sensor was due to high agglomerated structures on the surface, appearing as larger particles as mentioned by FESEM results, led to the reduction of the spaces between them, which cause reducing the gas diffusion and sensing reaction [178] in addition to decrease in surface area exposure to gas target as appeared from BET measurements.

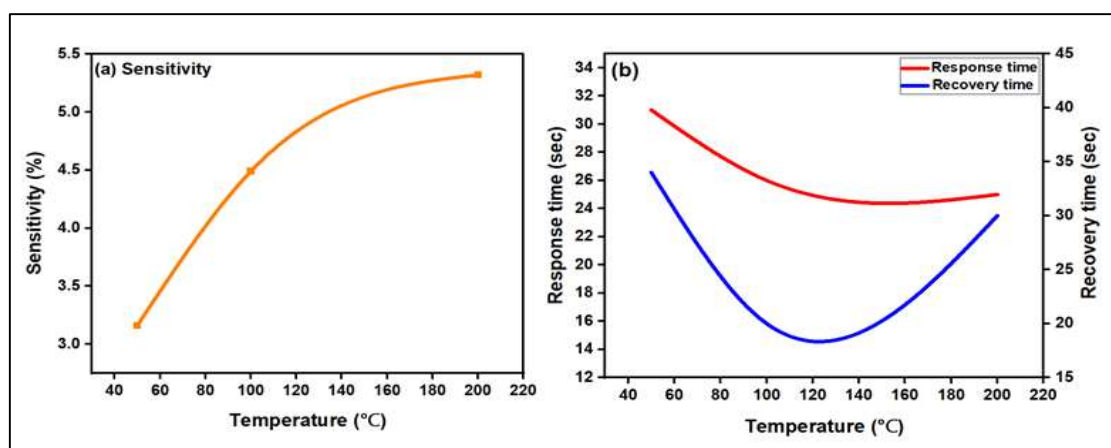


**Figure (4.54): (a)  $\text{NH}_3$  gas sensitivity versus operating temperature for CuO, and (b) response and recovery time versus operating temperatures.**

Table (4.18) shows CuO gas sensor parameters (sensitivity, response time and recovery time) with different operating temperatures.

**Table (4.18): CuO gas sensor parameters with different operating temperatures.**

Sample	Operating Temperature (°C)	Sensitivity (%)	Response time (sec)	Recovery time (sec)
CuO	RM	3.16	31	34
	100	4.49	26	20
	200	5.32	25	30

### 4.12.1.3 CuO- rGO Sensors Measurements

Figures (4.55), (4.56), (4.57), (4.58), (4.59), (4.60) show the response, sensitivity, response and recovery times of the CuO- rGO sensors prepared at 100 °C for 100 ppm of NH<sub>3</sub> gas at different operation temperatures. The sensor sensitivity of the three sensors (S1, S2, S3) exhibited low values at room temperature, with recorded values of 5.95, 9.13, and 6.42 for samples S1, S2, and S3, respectively, as evident from figures. The high response of the S2 sensor was due to high stability, small crystal size, high roughness, and larger surface area than S1, and S3 as indicated from XRD, TGA, AFM, and BET results.

The porous structure of rGO, which appeared from FESEM results, provides more active sites for NH<sub>3</sub> molecules adsorption/desorption, enhancing the interaction surface area and accelerating carrier transfer during gas sensing reactions [179]. The sensing response decreased when the temperature was subsequently raised to 100 °C. When the temperature was raised to 200 °C, there was a little increase in sensitivity for samples S1, S2, and S3. This change can be related to the release of oxygen at higher temperatures due to desorption [180].

The optimal operating temperature of CuO-rGO sensors is around room temperature. Results had showed that sensor response is influenced by the weight ratio of GO in nanocomposites. The CuO with incorporated rGO demonstrated a markedly enhanced sensory responsiveness in comparison to pure rGO<sub>100</sub> and CuO<sub>100</sub>. In addition, sample S2 exhibited a rapid reaction and recovery time of 21 seconds and 15 seconds, respectively, which were faster than the response and recovery times that seen in prior studies

conducted at room temperature [121]. Table (4.19) shows all sensors' estimated sensitivity, response, and recovery times.

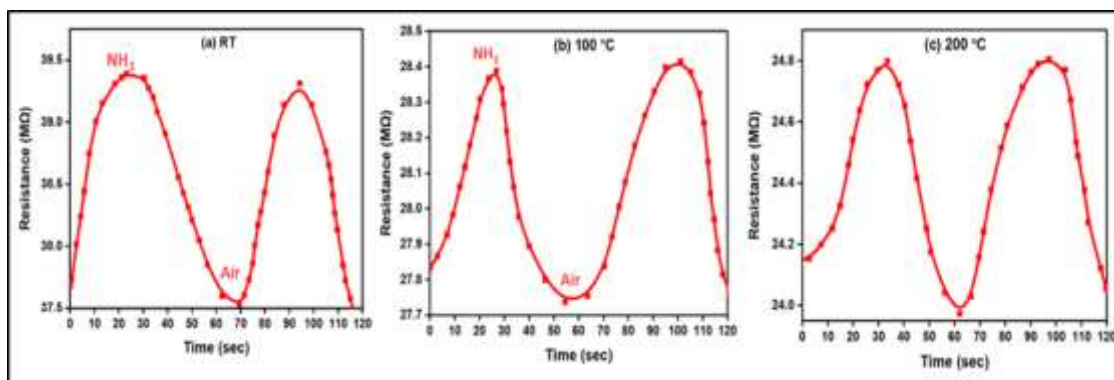


Figure (4.55): Dynamic response of S1 toward 100 ppm  $\text{NH}_3$  gas at different working temperature; (a) room temperature, (b) 100 °C, (c) 200 °C.

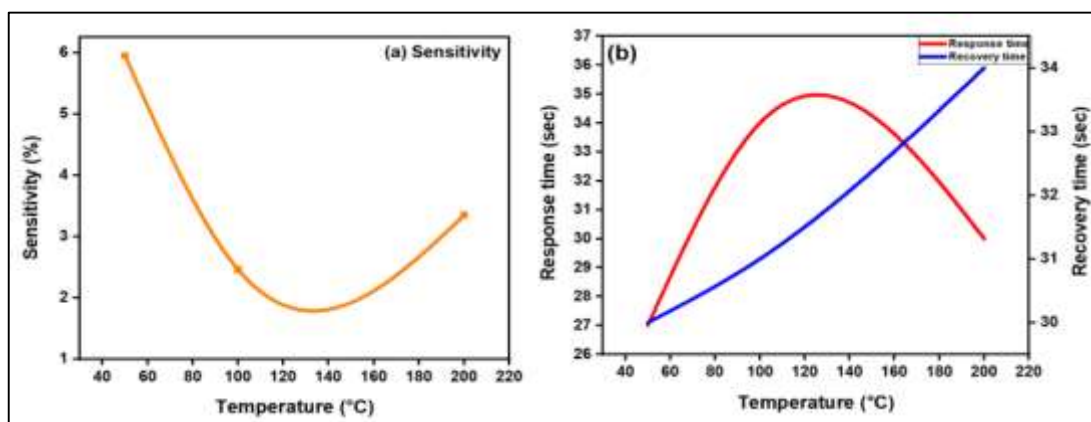


Figure (4.56): (a)  $\text{NH}_3$  gas sensitivity versus operating temperature for S1, and (b) response and recovery time versus operating temperatures.

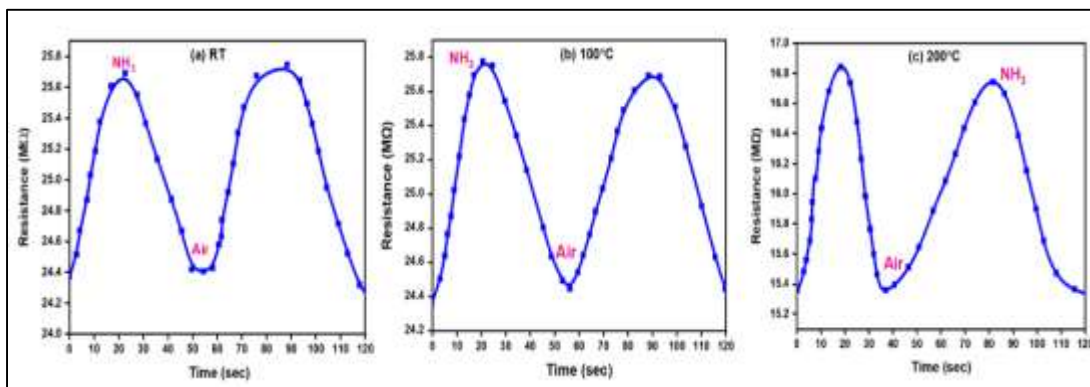


Figure (4.57): Dynamic response of S2 toward 100 ppm  $\text{NH}_3$  gas at different working temperature; (a) room temperatures, (b) 100 °C, (c) 200 °C.

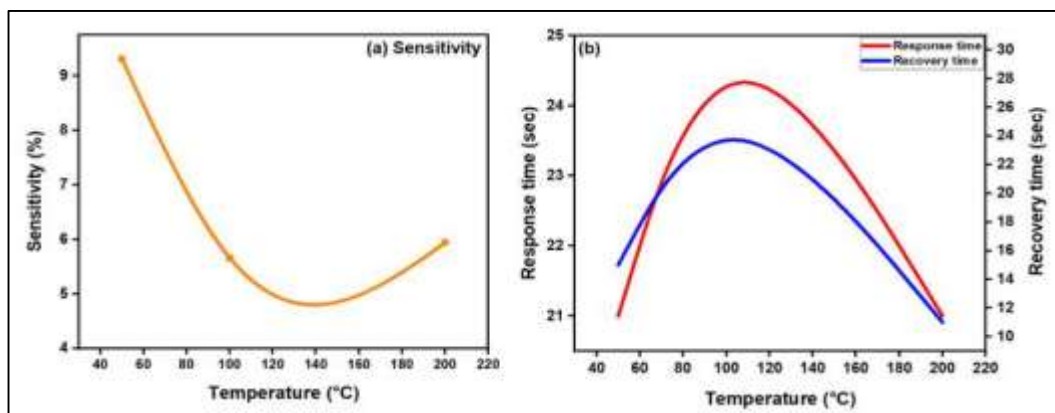


Figure (4.58): (a)  $\text{NH}_3$  gas sensitivity versus operating temperatures for S2, and (b) response and recovery time versus operating temperatures

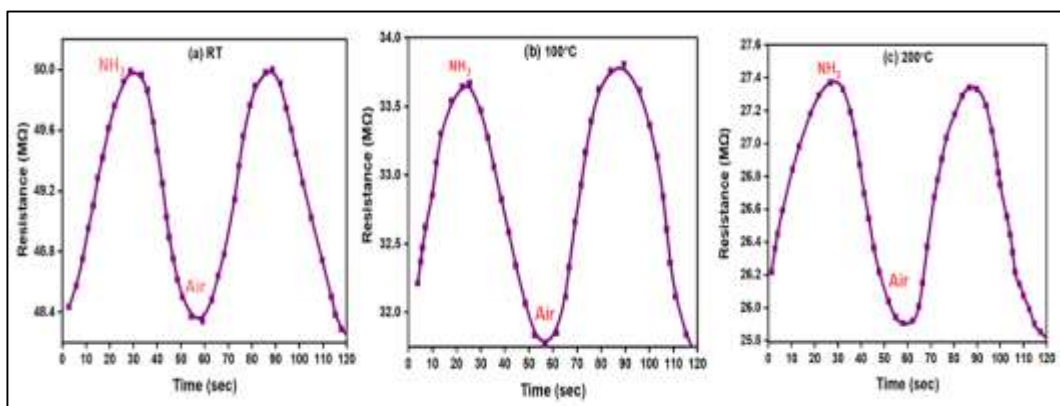


Figure (4.59): Dynamic response of S3 toward 100 ppm  $\text{NH}_3$  gas at different working temperature; (a) room temperatures, (b) 100 °C, (c) 200 °C.

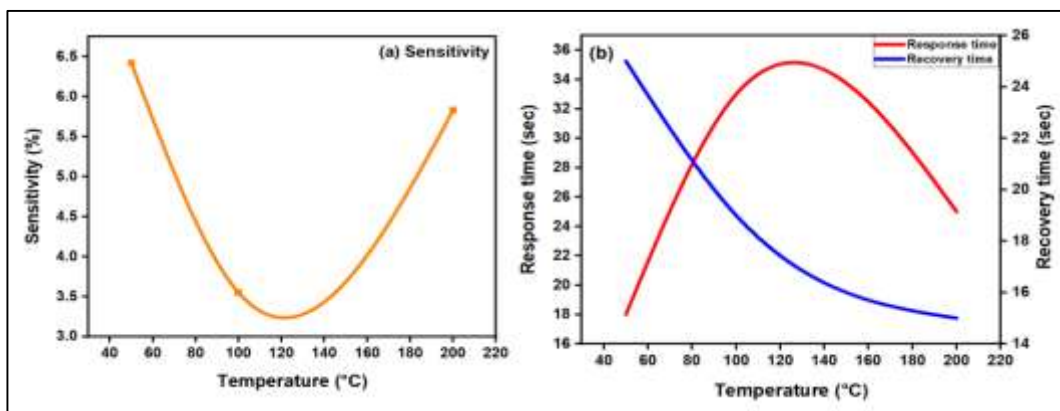


Figure (4.60): (a)  $\text{NH}_3$  gas sensitivity versus operating temperature for S3, and (b) response and recovery time versus operating temperature.

**Table (4.19): CuO-rGO gas sensor parameters with different operating temperatures.**

Sample	Operating Temperature	Sensitivity	Response time	Recovery time
	(°C)	(%)	(sec)	(sec)
S1	RM	5.95	27	30
	100	2.46	34	31
	200	3.35	30	34
S2	RM	9.31	21	15
	100	5.66	26	29
	200	5.94	21	11
S3	RM	6.42	18	25
	100	3.55	33	19
	200	5.83	25	15

#### 4.12.1.4 SnO<sub>2</sub>/ CuO Sensors Measurements

Figures (4.61) and (4.62) display the sensitivity, response, and recovery times of the SnO<sub>2</sub>/CuO sensors when exposed to 47 ppm of NH<sub>3</sub> gas at various operating temperatures (150 °C, 200 °C, 250 °C). This sensor exhibited no response at room and low temperatures, with the initial response at 150 °C. Subsequently, a decrease in sensitivity was seen with increasing temperature, as depicted in figure (4.62-a).

The behavior of this sensor was opposite to previous sensors, as it shows a decrease in resistance when exposed to NH<sub>3</sub> gas. Figure (4.61) demonstrates that the addition of SnO<sub>2</sub> to the CuO thin film enhances the sensitivity of CuO. CuO is classified as a p-type semiconductor, while SnO<sub>2</sub> is categorized as an n-type semiconductor. Consequently, n-p junctions are created, causing a depletion region to occur at the interface. This results in a confined pathway for the conduction of charge carriers, leading to a high value of sensor resistance [181].

Nevertheless, the addition of CuO to the SnO<sub>2</sub> film leads to a more significant reduction in sensor resistance when exposed to NH<sub>3</sub> gas. This can be due to the improved transfer of NH<sub>3</sub> gas molecules onto the surface of SnO<sub>2</sub>, facilitated by the presence of CuO catalysts dispersed throughout the film. Table (4.20) shows the sensor's estimated sensitivity, response, and recovery times. It is important to point out that the time taken by SnO<sub>2</sub>/CuO thin film sensor to achieve 90% of the total resistance was achieved in 20 sec, while the time required returning to baseline resistance reduced to 10 sec. These results were higher than that obtained by [182].

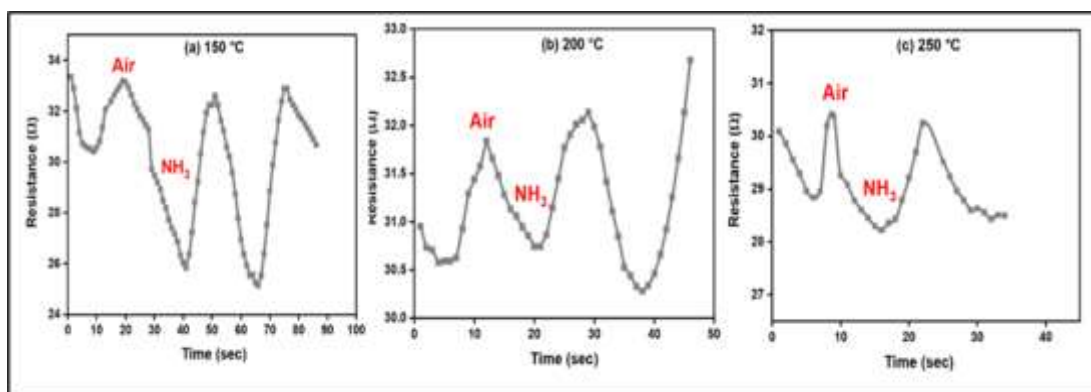


Figure (4.61): Dynamic response of SnO<sub>2</sub>/CuO toward 47 ppm NH<sub>3</sub> gas at different working temperature; (a) 150 °C, (b) 200 °C, (c) 250 °C.

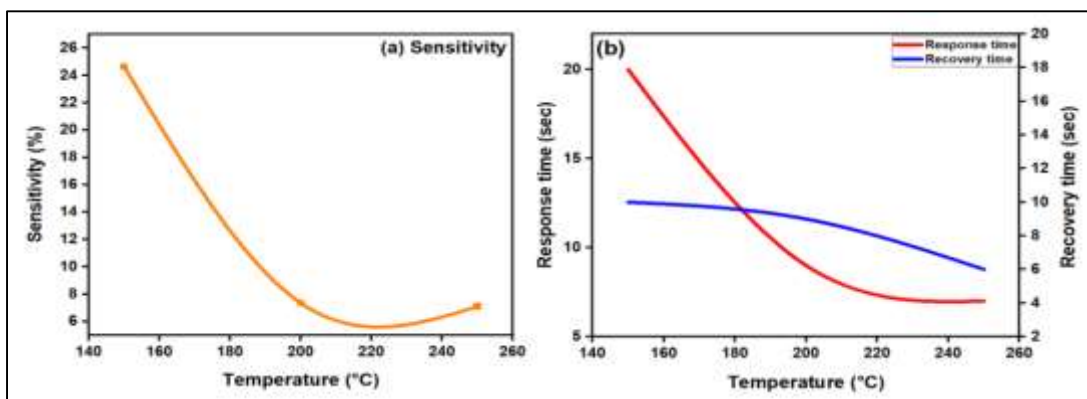


Figure (4.62): (a) NH<sub>3</sub> gas sensitivity versus operating temperatures for SnO<sub>2</sub>/CuO, and (b) response and recovery time versus operating temperature.

**Table (4.20): SnO<sub>2</sub>/ CuO gas sensor parameters with different operating temperatures.**

Sample	Operating Temperature (°C)	Sensitivity (%)	Response time (sec)	Recovery time (sec)
SnO <sub>2</sub> /CuO	150	24.63	20	10
	200	7.34	9	9
	250	7.10	7	6

#### 4.12.1.5 SnO<sub>2</sub>/ rGO Sensors Measurements

The sensitivity, response time, and recovery time of the SnO<sub>2</sub>/rGO sensors when exposed to 47 ppm of NH<sub>3</sub> gas at different operating temperatures (150 °C, 200 °C, 250 °C) are shown in figures (4.63) and (4.64).

This sensor displayed very weak response at room and low temperatures, with the initial response occurring at 150 °C. Following that, there was a rise in sensitivity with increasing the temperature to 200 °C. However, a decrease in sensitivity was observed at 250 °C, as depicted in figure (4.64-a). Upon exposure to NH<sub>3</sub>, an n-p heterojunction would be formed at the interface of SnO<sub>2</sub> and rGO sheet leading to the creation of a barrier at the interface of n-type SnO<sub>2</sub> and p-type rGO nanosheets. SnO<sub>2</sub> has excellent gas sensing properties as its conductivity is altered upon the adsorption of target gas molecules onto preadsorbed oxygen species on the oxide surface. When a reducing gas such as NH<sub>3</sub> is adsorbed onto the surface of SnO<sub>2</sub>, it releases a small number of conduction electrons. This leads to the transfer of electrons from SnO<sub>2</sub> to rGO, which in turn reduces the potential barrier between SnO<sub>2</sub> particles. As a result, the carrier concentration of SnO<sub>2</sub>

increases, leading to an increase in conductivity and a further decrease in resistance [183].

The superior sensing capabilities of SnO<sub>2</sub> compared with [183] were primarily ascribed to the catalytic properties of rGO, high surface roughness, porosity, and large surface area, which facilitated the adsorption through rapid response time and intermediate recovery time as shown in Table (4.21).

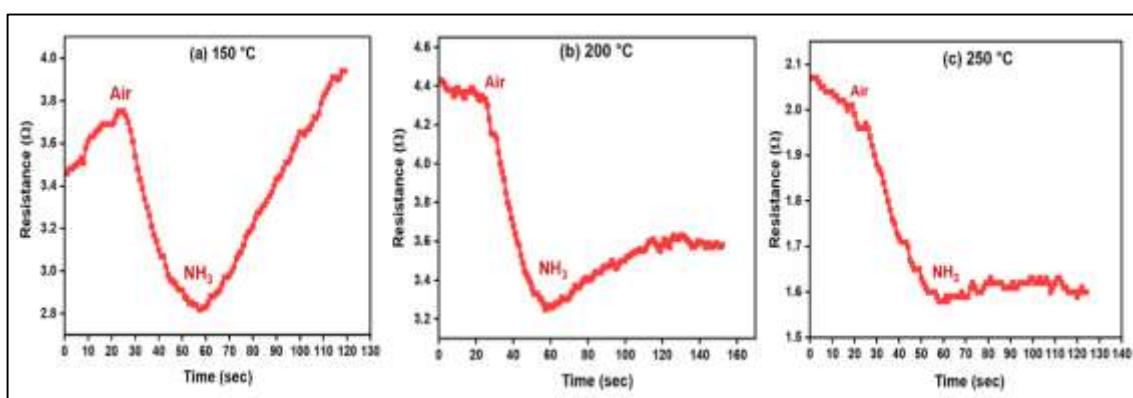


**Figure (4.63):** Dynamic response of SnO<sub>2</sub>/rGO toward 47 ppm NH<sub>3</sub> gas at different working temperature; (a) 150 °C, (b) 200 °C, (c) 250 °C.

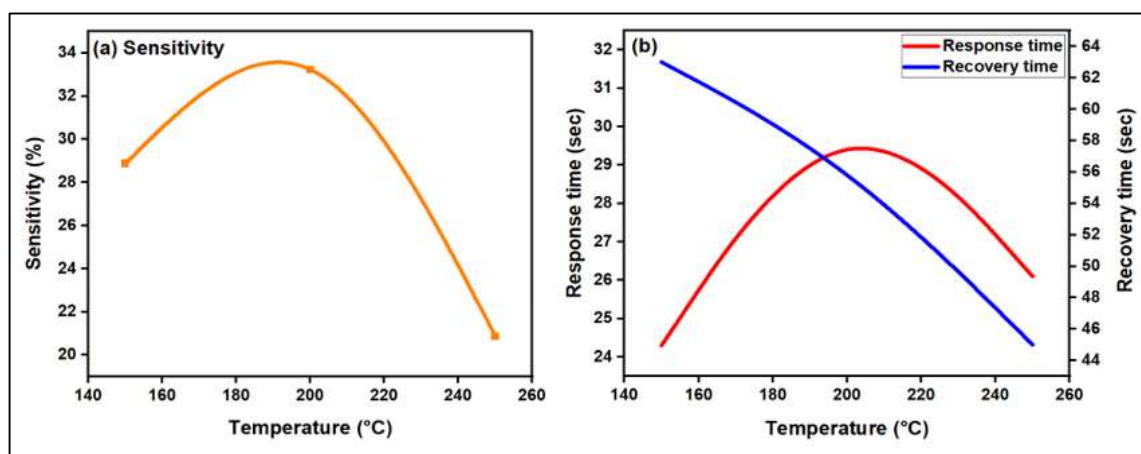


**Figure (4.64):** (a) NH<sub>3</sub> gas sensitivity versus operating temperatures for SnO<sub>2</sub>/rGO, and (b) response and recovery time versus operating temperature.



**Table (4.21): SnO<sub>2</sub>/ rGO gas sensor parameters with different operating**

Sample	Operating Temperature (°C)	Sensitivity (%)	Response time (sec)	Recovery time (sec)
SnO <sub>2</sub> /rGO	150	28.86	24.3	63
	200	33.23	31.5	56.7
	250	20.85	26.1	45

**temperatures.**

#### 4.12.1.6 SnO<sub>2</sub>/ CuO- rGO Sensors Measurements

The sensitivity, response time, and recovery time of the SnO<sub>2</sub>/ CuO- rGO sensors when exposed to 47 ppm of NH<sub>3</sub> gas at different operating temperatures (150 °C, 200 °C, 250 °C) are shown in figures (4.65) and (4.66), (4.67), and (4.68). These sensors display low response at room and low temperatures, with initial response at 150 °C. SnO<sub>2</sub>/ S4 and SnO<sub>2</sub>/S5 sensors showed a decrease in sensitivity as the temperature increased up to 250 °C as depicted in figures (4.66-a) and (4.68-a).

High sensitivity was observed at 150 °C with fast response and recovery time for the two sensors; then, the sensitivity dropped to low a value at 250 °C. SnO<sub>2</sub>/ S4 sensor with low amount of GO exhibited high response compared to SnO<sub>2</sub>/S5 sensor. This gives an indication that the weight percentage of GO greatly affected the sensitivity of the nanostructure. In air, the resistance of SnO<sub>2</sub>/ S4 and SnO<sub>2</sub>/ S5 increases compared to CuO, rGO, CuO- rGO, SnO<sub>2</sub>/ CuO, and SnO<sub>2</sub>/ rGO sensors. It can be attributed to the presence of heterojunctions (specifically n-p junctions), which enhance the adsorption and decomposition of O<sub>2</sub>. As a result, a larger concentration of

chemisorbed oxygen is formed on the surface, increasing the thickness of the depletion layer. After exposure to  $\text{NH}_3$  gas, it reacts with surface negative oxygen species, and releases electrons to conduction band of  $\text{SnO}_2$ . Additionally, electrons enter the conduction band of rGO and CuO, resulting in increased conductivity. The presence of heterojunctions enhances catalytic activity by increasing adsorption sites.

The  $\text{SnO}_2/\text{S4}$  surface exhibits higher adsorbed oxygen vacancies, that contributed to increased charge density near the valence and conduction bands, narrowing the band gap of  $\text{SnO}_2$  and facilitating gas adsorption and activation [185]. The mesoporous structure of S4 incorporated  $\text{SnO}_2$ , the higher BET surface area, and the high surface roughness contributes to gas diffusion. This gives oxygen molecules more sites to interact with inner grains and lowers the activation energy of gas sensing, which accelerates the reaction between  $\text{NH}_3$  and oxygen molecules that have been adsorbed. Table (4.22) shows the sensor's estimated sensitivity, response, and recovery times.

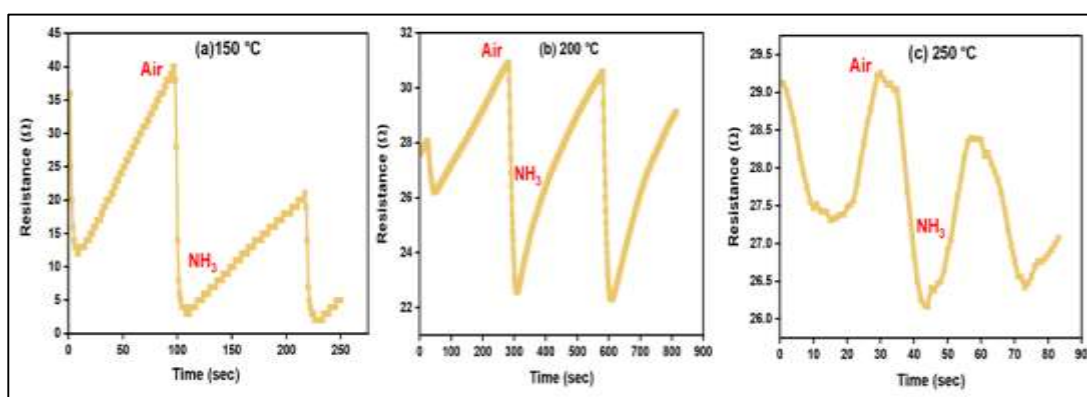


**Figure (4.65): Dynamic response of  $\text{SnO}_2/\text{S4}$  toward 47 ppm  $\text{NH}_3$  gas at different working temperature; (a) 150 °C, (b) 200 °C, (c) 250 °C.**

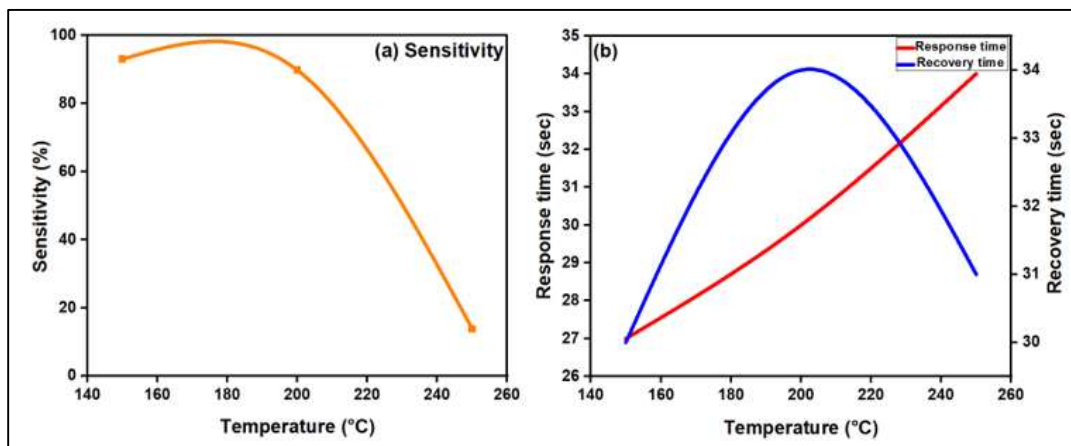


Figure (4.66): (a) NH<sub>3</sub> gas sensitivity versus operating temperatures for SnO<sub>2</sub>/S4, and (b) response and recovery time versus operating temperature.

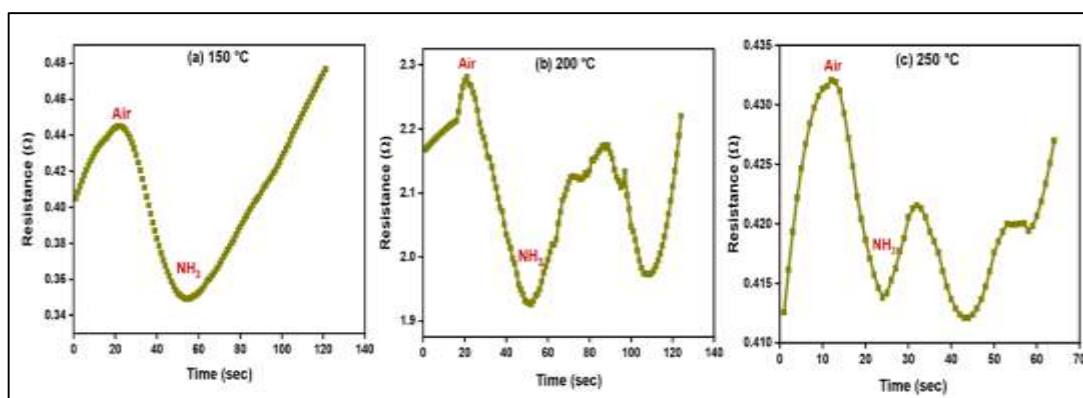


Figure (4.67): Dynamic response of SnO<sub>2</sub>/S5 toward 47 ppm NH<sub>3</sub> gas at different working temperature; (a) 150 °C, (b) 200 °C, (c) 250 °C.

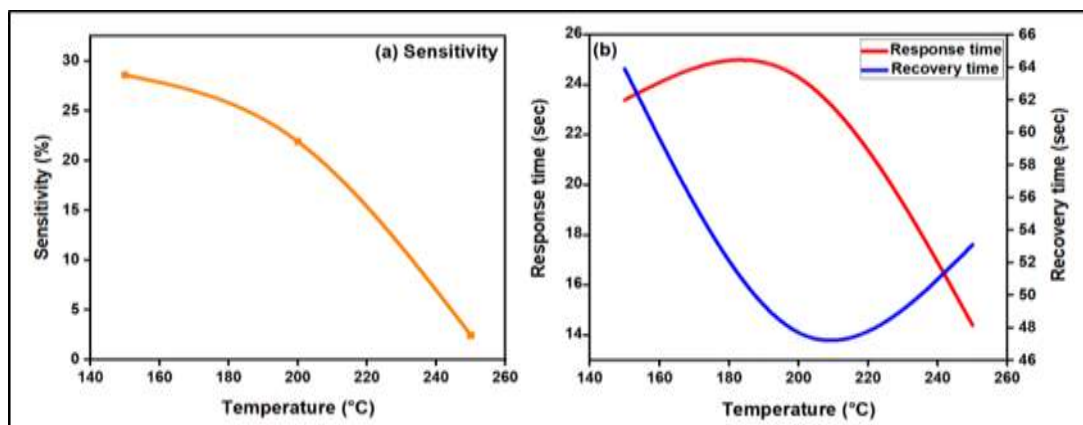


Figure (4.68): (a) NH<sub>3</sub> gas sensitivity versus operating temperatures for SnO<sub>2</sub>-S5, and (b) response and recovery time versus operating temperature.

**Table (4.22): SnO<sub>2</sub>- rGO/ CuO gas sensors parameters with different operating temperatures.**

Sample	Operating Temperature (°C)	Sensitivity (%)	Response time (sec)	Recovery time (sec)
SnO <sub>2</sub> -S4	150	93.05	27	30
	200	89.79	30	34
	250	13.79	34	31
SnO <sub>2</sub> -S5	150	28.57	23.4	63.9
	200	21.89	24.3	47.7
	250	2.43	14.4	53.1

## 4.12.2 H<sub>2</sub>S Gas Sensor Measurements

### 4.12.2.1 SnO<sub>2</sub> / rGO Sensor Measurements

The sensitivity, response time, and recovery time of the SnO<sub>2</sub>/rGO sensors when exposed to 50 ppm of H<sub>2</sub>S gas at different operating temperatures (150 °C, 200 °C, 250 °C) are shown in figures (4.69) and (4.70). This sensor displays weak response at room temperature and low temperatures; therefore, it was neglected. The excellent response occurs at 150 °C. Following that, there was a drop in sensitivity as the temperature increased up to 250 °C as depicted in figure (4.70-a). Upon exposure to H<sub>2</sub>S gas, an n-p heterojunction would be formed at the interface of SnO<sub>2</sub> and rGO sheet leading to the creation of a barrier at the interface of n-type SnO<sub>2</sub> and p-type rGO nanosheets. SnO<sub>2</sub> has excellent gas sensing properties as its conductivity is altered upon the adsorption of target gas molecules onto preadsorbed oxygen species on the oxide surface. When a reducing gas such as H<sub>2</sub>S is adsorbed onto the surface of SnO<sub>2</sub>, it releases a conduction electron. This leads to the transfer of electrons from SnO<sub>2</sub> to rGO, which in turn reduces the potential barrier between SnO<sub>2</sub> particles. As a result, the carrier concentration of SnO<sub>2</sub> increases, leading to an increase in

conductivity and a further decrease in resistance. The electron flow across the interfaces of SnO<sub>2</sub> /rGO nanocomposites was improved due to the excellent transport capacity of rGO, ensuring good adsorption of H<sub>2</sub>S molecules which led to an overall enhancement of both the chemical and electrical interactions between SnO<sub>2</sub> and H<sub>2</sub>S molecules [186]. The superior sensing capabilities of SnO<sub>2</sub>/ rGO were primarily ascribed to the catalytic properties of high surface area rGO, which facilitated the adsorption through rapid response time of about 12.6 sec and intermediate recovery time of 76seconds as shown in Table (4.23). The addition of rGO nanosheets reduces the working temperature of pristine SnO<sub>2</sub> semiconductor material to 150 °C, overcoming its high operating temperature. This result was better than that obtained by other works [187].

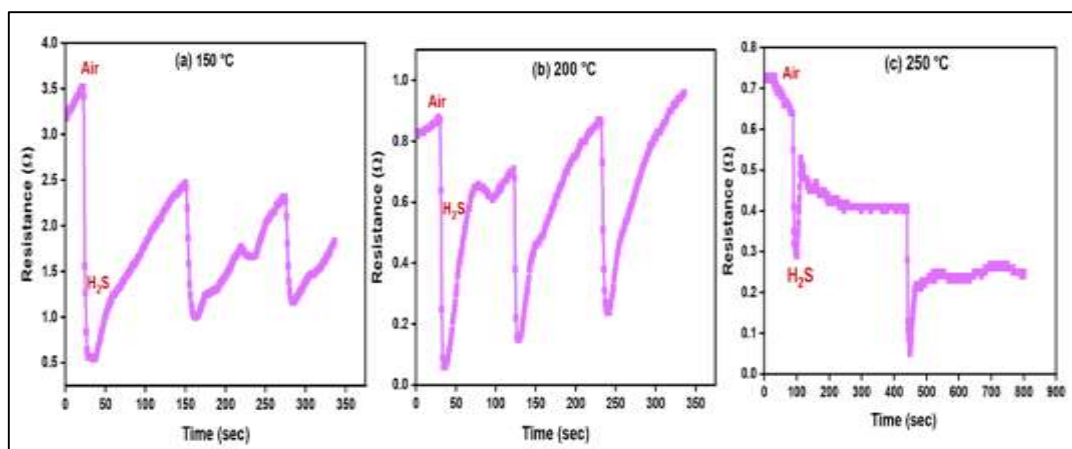


**Figure (4.69): Response of SnO<sub>2</sub> /rGO toward 50 ppm of H<sub>2</sub>S gas at different operating temperatures ;(a) 150 °C, (b) 200 °C, and (c) 250 °C.**

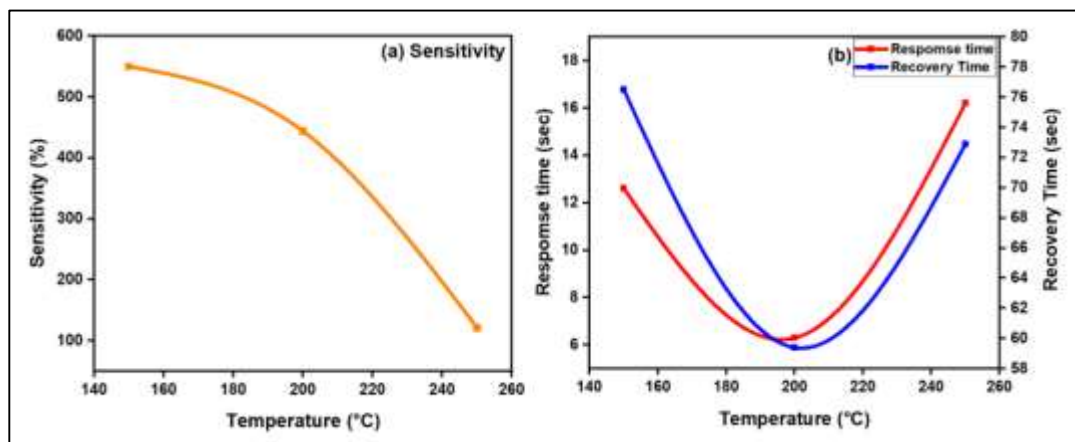


**Figure (4.70): (a) H<sub>2</sub>S gas sensitivity versus operating temperatures for SnO<sub>2</sub>/rGO, and (b) response and recovery times versus operating temperatures.**

**Table (4.23): SnO<sub>2</sub>/rGO gas sensors parameters with different operation temperatures.**

Sample	Operating Temperature (°C)	Sensitivity (%)	Response time (sec)	Recovery time (sec)
SnO <sub>2</sub> /rGO	150	550	12.6	76.5
	200	443.75	6.3	59.4
	250	120.68	16.2	72.9

#### 4.12.2.2 SnO<sub>2</sub>/ CuO Sensor Measurements

Figures (4.71) and (4.72) display the sensitivity, response time, and recovery time of the SnO<sub>2</sub>/CuO sensors when exposed to 50 ppm of H<sub>2</sub>S gas at various operating temperatures (200 °C, 250 °C). This sensor exhibits neglected response at room and low temperatures, with the initial response at 200 °C. Subsequently, increased sensitivity was seen with increasing temperature, and high response was observed at 250 °C as depicted in figure (4.72-a). Figure (4.71) demonstrates that the addition of SnO<sub>2</sub> to the CuO thin film enhances the sensitivity of CuO. CuO is classified as a p-type semiconductor, while SnO<sub>2</sub> is an n-type semiconductor. Consequently, n-p junctions are created, causing a depletion region to occur at the interface.

This results in a confined pathway for the conduction of charge carriers, leading to a high value of sensor resistance [46].

Nevertheless, the addition of CuO to the SnO<sub>2</sub> film leads to more significant reduction in sensor resistance when exposed to H<sub>2</sub>S gas. This can be due to the improved transfer of H<sub>2</sub>S gas molecules onto the surface of SnO<sub>2</sub>, facilitated by the presence of CuO catalysts which accelerates the reaction with H<sub>2</sub>S. The selectivity characteristic may be due to more active sites for H<sub>2</sub>S adsorption dispersed throughout the film [188]. Table (4.24) summarizes the sensor's estimated sensitivity, response, and recovery times. It is important to point out that at 250°C, the time taken by SnO<sub>2</sub>/CuO thin film sensor to achieve 90% of the total resistance was 12.6 sec, while the time required to return to baseline resistance was 46.8 sec. This sensor was more sensitive to H<sub>2</sub>S gas than NH<sub>3</sub> gas. These results were lower than that obtained by [188] and better than that obtained by [189].

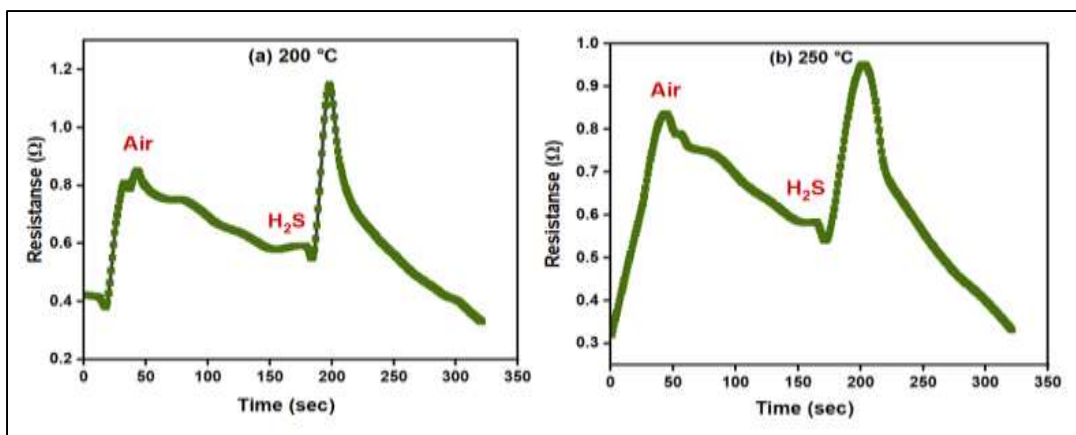


**Figure (4.71): Dynamic response of SnO<sub>2</sub>/CuO toward 50 ppm H<sub>2</sub>S gas at different working temperatures; (a) 200 °C, and (b) 250 °C.**

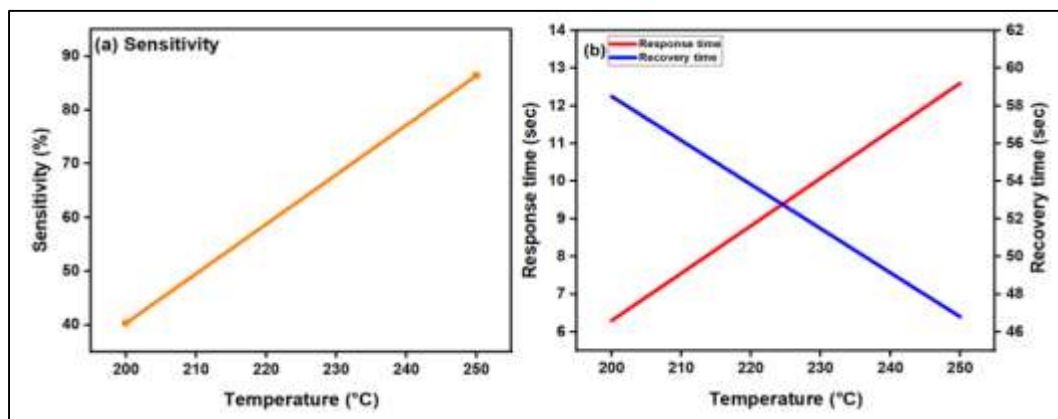


Figure (4.72): (a) H<sub>2</sub>S gas sensitivity versus operating temperatures for SnO<sub>2</sub> /CuO, and (b) response and recovery times versus operating temperatures.

Table (4.24): SnO<sub>2</sub>/ CuO gas sensors parameters with different operating temperatures.

Sample	Operating Temperature (°C)	Sensitivity (%)	Response time (sec)	Recovery time (sec)
SnO <sub>2</sub> /CuO	200	40.29	6.3	58.5
	250	86.41	12.6	46.8
SnO <sub>2</sub> /CuO	200	40.29	6.3	58.5
	250	86.41	12.6	46.8

#### 4.12.2.3 SnO<sub>2</sub>/ CuO- rGO Sensors Measurements

The sensitivity, response time, and recovery time of the SnO<sub>2</sub>/ CuO- rGO sensors when exposed to 50 ppm of H<sub>2</sub>S gas at different operating temperatures (150 °C, 200 °C, 250 °C) are shown in figures (4.73) and (4.74), (4.75), and (4.76). These sensors display neglected response at room temperature and low temperatures, with the initial response at 150 °C. SnO<sub>2</sub>/ S4 and SnO<sub>2</sub>/ S5 sensors showed higher values of sensitivity as the temperature increased at 200 °C as depicted in figures (4.74-a) and (4.76-a)



with rapid response time for the two sensors; then, the sensitivity dropped to low value at 250 °C.

SnO<sub>2</sub>/ S4 sensor with low amount of GO exhibited high response compared to SnO<sub>2</sub>/S5 sensor. In air, the resistance of SnO<sub>2</sub>/ S4 increases due to the presence of heterojunctions within the ternary heterojunctions (specifically n-p junctions), which enhance the adsorption and decomposition of O<sub>2</sub>. As a result, a larger concentration of chemisorbed oxygen is formed on the surface, increasing the thickness of the depletion layer. After exposure to H<sub>2</sub>S gas, it reacts with surface negative oxygen species, and releases electrons to the conduction band of SnO<sub>2</sub>. Additionally, electrons enter the conduction band of rGO and CuO, resulting in an increased conductivity.

The presence of heterojunctions enhances catalytic activity by increasing adsorption sites. The SnO<sub>2</sub>/S4 surface exhibits higher adsorbed oxygen vacancies, that contributed to increased charge density near the valence and conduction bands, narrowing the band gap of SnO<sub>2</sub> and facilitating gas adsorption and activation [185]. The mesoporous structure of S4 incorporated SnO<sub>2</sub>, the higher BET surface area, and the high surface roughness contributes to the gas diffusion. This gives oxygen molecules more sites to interact with inner grains and lowers the activation energy of gas sensing, which accelerates the reaction between H<sub>2</sub>S and oxygen molecules that have been adsorbed [33].

Table (4.25) illustrates the sensor's sensitivity, response time and recovery time.

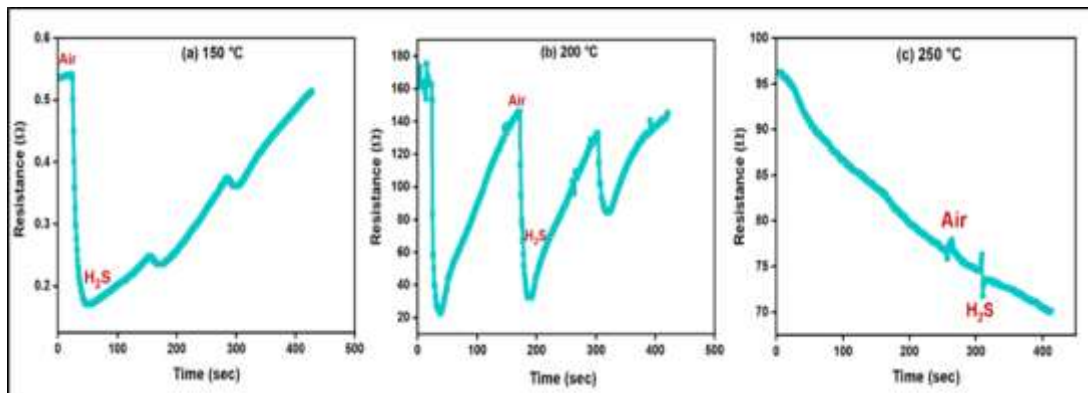


Figure (4.73): Dynamic response of SnO<sub>2</sub>/ S4 toward 50 ppm H<sub>2</sub>S gas at different working temperature; (a) 150 °C, (b) 200 °C and (c) 250 °C.

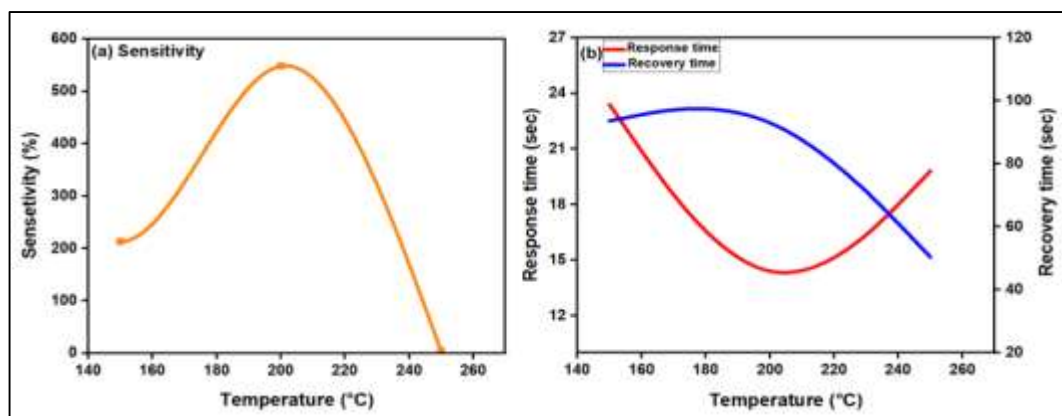


Figure (4.74): (a) H<sub>2</sub>S gas sensitivity versus operating temperatures for SnO<sub>2</sub>/S4, and (b) response and recovery times versus operating temperatures.

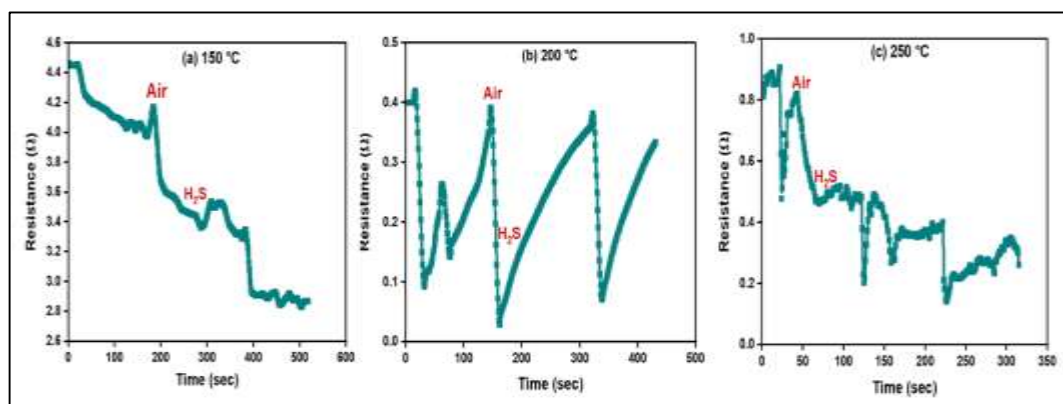


Figure (4.75): Dynamic response of SnO<sub>2</sub>/ S5 toward 50 ppm H<sub>2</sub>S gas at different working temperature; (a) 150 °C, (b) 200 °C and (c) 250 °C.

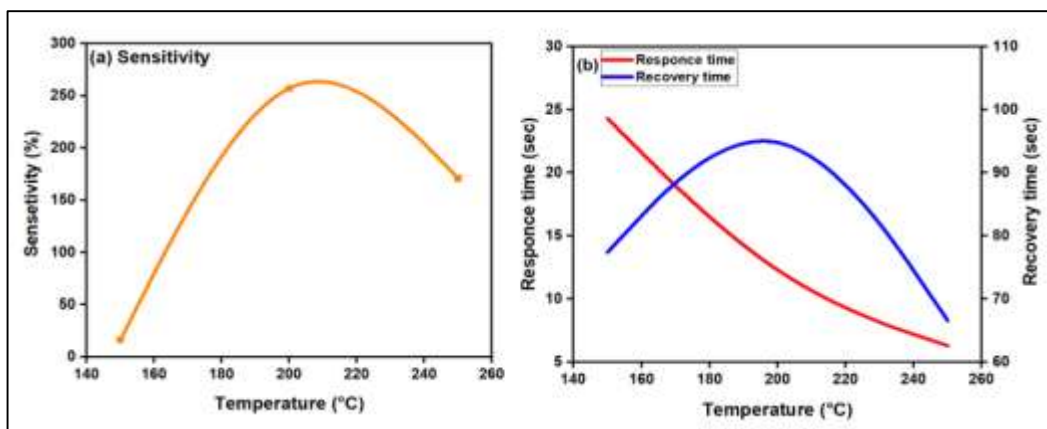


Figure (4.76): (a) H<sub>2</sub>S gas sensitivity versus operating temperatures for SnO<sub>2</sub>/S5, and (b) response and recovery time versus operating temperatures.

Table (4.25): SnO<sub>2</sub>- rGO/ CuO gas sensors parameters with different operating temperatures.

Sample	Operating Temperature (°C)	Sensitivity (%)	Response time (sec)	Recovery time (sec)
SnO <sub>2</sub> /S4	150	212.71	23.4	93.6
	200	547.99	10.8	103.5
	250	3.711	19.8	50.4
SnO <sub>2</sub> /S5	150	16.20	24.3	77.4
	200	257.14	11	106.2
	250	170.92	6.3	66.6

### 4.13 Conclusions

- 1-The thermal reduction approach is preferred for preparing rGO nanoparticles.
- 2- It was found from XRD results that rGO can be completely reduced at 200 °C.

- 3- Hydrothermal method can be recommended to prepare CuO nanorods and CuO- rGO nanoparticles in a low cost and simple way.
- 4- Higher preparation temperatures and annealing improve the nanostructure crystallinity.
- 5- The crystallite size of nanoparticles increases for all samples after annealing to 400 °C and the main peaks of rGO, CuO, and SnO<sub>2</sub> were noted after deposition of SnO<sub>2</sub> layer by PLD.
- 6- BET measurements show that rGO prepared at 200 °C has a surface area of 195 m<sup>2</sup>/g which is more than GO, CuO pure and CuO- rGO.
- 7- The FESEM and TEM analysis reveal the presence of rod-shaped structures in CuO, S1, and S4, which became spherical shapes with increasing the weight of GO in the nanocomposites. The rGO material exhibits a plate-like morphology with curved textures and an increase number of pores, like slits.
- 8- UV-visible spectroscopy reveals a reduction in the energy gap of the binary CuO- rGO, and a slight decrease is observed for the three layers structures.
- 9- The CuO sensors exhibit the low sensitivity to NH<sub>3</sub> gas which is improved after incorporation with SnO<sub>2</sub> toward NH<sub>3</sub> and H<sub>2</sub>S gases.
- 11- Low response has been observed for CuO- rGO toward NH<sub>3</sub> gas.
- 12- The SnO<sub>2</sub>/rGO sensor has the high sensitivity toward NH<sub>3</sub> gas.
- 13- The SnO<sub>2</sub>/CuO-rGO, SnO<sub>2</sub>/rGO, and SnO<sub>2</sub>/CuO sensors are selective to H<sub>2</sub>S gas, but the SnO<sub>2</sub>/rGO sensor has the highest sensitivity.
- 14- SnO<sub>2</sub>/ CuO- rGO sensors are the best sensors toward both gases which were improved after adding rGO.

15- It was observed that SnO<sub>2</sub>/ CuO- rGO sensors respond more quickly after incorporation than the other samples such as, rGO, SnO<sub>2</sub>/rGO, and SnO<sub>2</sub>/CuO.

16- The working temperature for SnO<sub>2</sub> was reduced after incorporation with CuO and rGO.

#### **4.14 Suggestions for Future Work**

1- Testing our device with oxidizing gases, such as NO<sub>2</sub>.

2- Decorating carbon nanotubes with CuO-SnO<sub>2</sub> nanostructures and testing by our gas sensor device toward NH<sub>3</sub> and H<sub>2</sub>S gases.

3-Deposition of three layers sensors (SnO<sub>2</sub>/CuO/SnO<sub>2</sub>) layer by layer using PLD only and testing by our gas sensor device.

4- Studying the effect of several laser pulses on the structures and thus the performance of sensor devices (SnO<sub>2</sub>/CuO/SnO<sub>2</sub>).

## References

- [1] G. Korotcenkov, “Handbook of Gas Sensor Materials.”, Springer, Gwangju Institute of Science and Technology, Gwangju, Korea, Republic of South Korea, 2013, doi: 10.1007/978-1-4614-7165-3.
- [2] R. Leghrib, “Design, Fabrication and Characterization of Gas Sensors Based on Nanohybrid Materials”, Ph.D. thesis, University of Rovira Virgili, Tarragona, 2010.
- [3] L. Liu, Y. Wang, Y. Liu, S. Wang, T. Li, S. Feng, S. Qin and T. Zhang, “Heteronanostructural Metal Oxide-Based Gas Microsensors,” J. Microsystems and Nanoengineering, vol. 8, no. 85, pp. 1–22, 2022, doi: 10.1038/s41378-022-00410-1.
- [4] Z. Yunusa, M. Nizar Hamidon, A. Kaiser, “A review: Gas Sensors”, J. Sensors and Transducers, vol. 168, no. 4, pp. 61-75, 2014.
- [5] F. Ezahra Annanouch, “Design, Optimization and Characterization of Metal Oxide Nanowire Sensors,” Ph.D. thesis, University of Rovira Virgili, Tarragona, 2016.
- [6] M. Alvarado Pérez “Development of Flexible Gas Sensors Based on Additive Fabrication Processes “, Ph.D. thesis, University of Rovira Virgili, Tarragona, 2020.
- [7] G. Neri, “First Fifty Years of Chemoresistive Gas Sensors,” J. Chemosensors, vol.3, no.1, pp.1-19, 2015, doi:10.3390/chemosensors3010001.

- [8] G. Lei, C. Lou, X. Liu, J. Xie, Z. Li, W. Zheng, J. Zhang, “Thin Films of Tungsten Oxide Materials for Advanced Gas Sensors,” *J. Sens Actuators B Chem*, vol. 341, p. 129996, 2021, doi: 10.1016/j.snb.2021.129996.
- [9] E. Brauns, E. Morsbach, S. Kunz, M. Bäumer, and W. Lang, “A Fast and Sensitive Catalytic Gas Sensors for Hydrogen Detection Based on Stabilized Nanoparticles as Catalytic Layer”, *J. Sens Actuators B Chem*, vol. 193, pp. 895–903, 2014, doi: 10.1016/j.snb.2013.11.048.
- [10] A. Farquhar, G. Henshaw, and D. Williams, “Understanding and Correcting Unwanted Influences on the Signal from Electrochemical Gas Sensors,” *J. ACS Sens*, vol. 6, no. 3, pp. 1295–1304, 2021, doi: 10.1021/acssensors.0c02589.
- [11] J. Baranwal, B. Barse, G. Gatto, G. Broncova, and A. Kumar, “Electrochemical Sensors and Their Applications: A Review,” *Chemosensors*, vol. 10, no. 9, pp. 1–22, 2022, doi: 10.3390/chemosensors10090363
- [12] R. Bogue, “Detecting Gases with Light: A Review of Optical Gas Sensor Technologies,” *J. Sensor Review*, vol. 35, no. 2, pp. 133–140, 2015, doi: 10.1108/SR-09-2014-696.
- [13] J. Wu, G. Yue, W. Chen, Z. Xing, J. Wang, W. Wong, Z. Cheng, S. Set, G. Senthil Murugan, X. Wang, and T. Liu, “On-Chip Optical Gas Sensors Based on Group-IV Materials,” *J. ACS Photonics*, vol. 7, no. 11, pp. 2923–2940, 2020, doi: 10.1021/acsp Photonics.0c00976.
- [14] Z. Xi, K. Zheng, C. Zheng, H. Zhang, F. Song, C. Li, W. Ye, Y. Zhang, Y. Wang and K. Frank “Near-Infrared Dual-Gas Sensor System for Methane

and Ethane Detection Using a Compact Multipass Cell,” *J. Front. Phys*, vol. 10, pp. 1–9, 2022, doi: 10.3389/fphy.2022.843171.

[15] C. Chen, Q. Ren, and Y. Wang, “Review on multi gas detector using infrared spectral absorption technology,” *J. Appl Spectrosc Rev.*, vol. 54, no. 5, pp. 1–20, 2018, doi: 10.1080/05704928.2018.1474766.

[16] J. Liu and Y. Lu, “Response mechanism for surface acoustic wave gas sensors based on surface-adsorption,” *J. Sensors*, vol. 14, no. 4, pp. 6844–6853, 2014, doi: 10.3390/s140406844.

[17] P. Patial and M. Deshwal, “Systematic Review on Design and Development of Efficient Semiconductor Based Surface Acoustic Wave Gas Sensor,” *J. Trans. Electr. Electron. Mater.*, vol.12, pp. 385-393, 2021, doi: 10.1007/s42341-021-00332-1.

[18] C. Schultealbert, T. Baur, A. Schütze, S. Böttcher, and T. Sauerwald, “A novel approach towards calibrated measurement of trace gases using metal oxide semiconductor sensors,” *Sens Actuators B Chem*, vol. 239, pp. 390–396, 2017, doi: 10.1016/j.snb.2016.08.002.

[19] N. Isaac, I. Pikaar, and G. Biskos, “Metal oxide semiconducting nanomaterials for air quality gas sensors: operating principles, performance, and synthesis techniques,” *J. Microchimica Acta*, vol. 189, no. 196, pp. 1-22, 2022, doi: 10.1007/s00604-022-05254-0.

[20] M. Verma, A. Chowdhuri, K. Sreenivas, and V. Gupta, “Comparison of H<sub>2</sub>S sensing response of hetero-structure sensor (CuO – SnO<sub>2</sub>) prepared by rf sputtering and pulsed laser deposition,” *J. Thin Solid Films*, vol. 518, no. 24, pp. e181–e182, 2010, doi: 10.1016/j.tsf.2010.03.162.



- [21] D. Jundale, S. Pawar, M. Chougule, P. Godse, and S. Patil, "Nanocrystalline CuO Thin Films for H<sub>2</sub>S Monitoring: Microstructural and Optoelectronic Characterization," *J. Sensor Technology*, vol.1, no. 2, pp. 36–46, 2011, doi: 10.4236/jst.2011.12006.
- [22] S. Choi, J. Zhang, K. Akash, and S. Kim, "H<sub>2</sub>S sensing performance of electrospun CuO-loaded SnO<sub>2</sub> nanofibers," *J. Sens Actuators B Chem*, vol. 169, pp. 54–60, 2012, doi: 10.1016/j.snb.2012.02.054.
- [23] N. Hu, Z. Yang, Y. Wang, L. Zhang, Y. Wang, X. Huang, H. Wei, L. Wei and Y. Zhang "Ultrafast and sensitive room temperature NH<sub>3</sub> gas sensors based on chemically reduced graphene oxide," *J. Nanotechnology*, vol. 25, no. 2, pp. 1-9, 2014, doi: 10.1088/0957-4484/25/2/025502.
- [24] M. Kumar and V. Gupta, "SnO<sub>2</sub> – CuO nanocomposite thin film sensor for fast detection of H<sub>2</sub>S gas," *J. Experimental Nanoscience*, vol. 8, no. 3, pp. 326-331, 2013, doi: 10.1080/17458080.2012.680930.
- [25] A. Katoch, J. H. Kim, and S. S. Kim, "CuO/SnO<sub>2</sub> mixed nanofibers for H<sub>2</sub>S detection," *J. Nanoscience and Nanotechnology*, vol. 15, no. 11, pp. 8637–8641, 2015, doi: 10.1166/jnn.2015.11505.
- [26] Z. Li, N. Wang, Z. Lin, J. Wang, W. Liu, K. Sun, Y. Qing Richard Fu, and Z. Wang, "Room-Temperature High-Performance H<sub>2</sub>S Sensor Based on Porous CuO Nanosheets Prepared by Hydrothermal Method," *J. ACS Appl Mater Interfaces*, vol. 8, no.32, pp.20962–20968, 2016, doi: 10.1021/acsami.6b02893.
- [27] B. Sakthivel, L. Manjakkal, and G. Nammalvar, "High Performance CuO Nanorectangles-Based," *IEEE Sensors J.*, vol. 17, no. 20, pp. 6529–6536, 2017, doi: 10.1109/JSEN.2017.2749334.

- [28] W. Li, X. Li, L. Cai, M. Sun, and D. Xie, "Reduced Graphene Oxide for Room Temperature Ammonia (NH<sub>3</sub>) Gas Sensor," *J. Nanoscience and Nanotechnology*, vol. 18, no. 2, pp. 7927–7932, 2018, doi: 10.1166/jnn.2018.15563.
- [29] L. Yin, H. Wang, L. Li, H. Li, D. Chen, and R. Zhang, "Microwave-assisted preparation of hierarchical CuO@ rGO nanostructures and their enhanced low-temperature H<sub>2</sub>S-sensing performance," *J. Appl Surf Sci*, vol. 476, pp. 107-114, 2019, doi: 10.1016/j.apsusc.2019.01.019.
- [30] F. Peng, Y. Sun, W. Yu, Y. Lu, J. Hao, R. Cong, M. Ge, J. Shi and N. Dai, "Studies on sensing properties and mechanism of CuO nanoparticles to H<sub>2</sub>S gas," *J. Nanomaterials*, vol. 10, no. 4, pp. 1–14, 2020, doi: 10.3390/nano10040774.
- [31] Z. Boroun, M. Ghorbani, R. Mohammadpour, and A. Moosavi, "Importance of N-P-N Junction in H<sub>2</sub>S Sensing Process of SnO<sub>2</sub>-CuO Heterostructure: A Theoretical Macroscopic Approach," *IEEE Sensors J.*, vol. 21, no. 6, pp. 7123–7129, 2021, doi: 10.1109/JSEN.2020.3046785.
- [32] D. Jung, S. Hwang, H. Kim, and J. Han, "Characterization of Porous CuO Films for H<sub>2</sub>S Gas Sensors," *J. Materials*, vol.15, no. 20, pp. 1–10, 2022, doi: 10.3390/ma15207270.
- [33] T. Chen, J. Sun, N. Xue, W. Wang, Z. Luo, Q. Liang, T. Zhou, H. Quan, H. Cai, K. Tang, and K. Jiang, "Cu-doped SnO<sub>2</sub> / rGO nanocomposites for ultrasensitive H<sub>2</sub>S detection under low temperature", *J. Microsystems and Nanoengineering*, vol. 9, no. 69, pp.1-19, 2023, doi:10.21203/rs.3.rs-2332849/v1.

- [34] P. Chaiyo, "Fast Response Ammonia Gas Sensor Based on SnO<sub>2</sub> Nanoporous Synthesized by the Simple Heat-Up Method," *Science Essence J.*, vol. 39, no.1, pp. 76-87, 2023.
- [35] N. Ahmad and T. Ahmad, "Tin Oxide Based Hybrid Nanostructures for Efficient Gas Sensing," *J. Molecules*, vol. 27, no. 20, p.7038, 2022, doi:10.3390/molecules27207038.
- [36] E. Effiong Bassey, "Development and Characterization of Metal Oxide Gas Sensors" Ph.D. thesis, Auckland University of Technology, 2014.
- [37] B. Bilge, R. Lontio and S. Nahirnia, "Review: Influences of Semiconductor Metal Oxide Properties on Gas Sensing Characteristics," *J. Frontiers Sensors*, vol. 2, pp.1-23, 2021, doi: 10.3389/fsens.2021.657931.
- [38] H. Ji, W. Zeng, and Y. Li, "Gas sensing mechanisms of metal oxide semiconductors: A focus review," *J. Nanoscale*, vol. 11, no. 47, pp. 22664–22684, 2019, doi: 10.1039/c9nr07699a.
- [39] M. Nikolic, V. Milovanovic, Z. Vasiljevic, and Z. Stamenkovic, "Semiconductor gas sensors: Materials, technology, design, and application," *J. Sensors*, vol. 20, no. 22, pp. 1–31, 2020, doi: 10.3390/s20226694.
- [40] A. Borhaninia, A. Nikfarjam, and N. Salehifar, "Gas sensing properties of SnO<sub>2</sub> nanoparticles mixed with gold nanoparticles," *J. Transactions of Nonferrous Metals Society of China*, vol. 27, no. 8, pp. 1777–1784, 2017, doi: 10.1016/S1003-6326(17)60200-0.
- [41] D. Mohanta and M. Ahmaruzzaman, "Tin oxide nanostructured materials: an overview of recent developments in synthesis, modifications

and potential applications” J. Royal Society of Chemistry, vol.6, pp. 110996–111015, 2016, doi: 10.1039/c6ra21444d.

[42] D. Shaker, N. Abass, and R. Ulwall, “Preparation and study of the structural, morphological and optical properties of pure tin oxide nanoparticle doped with Cu,” Baghdad Science J., vol. 19, no. 3, pp. 660–669, 2022, doi: 10.21123/BSJ.2022.19.3.0660.

[43] Y. Gebreslassie and H. Gebretnsae, “Green and Cost-Effective Synthesis of Tin Oxide Nanoparticles: A Review on the Synthesis Methodologies, Mechanism of Formation, and Their Potential Applications,” J. Nanoscale Res Lett, vol.16, no. 97, pp. 1-16, 2021, doi: 10.1186/s11671-021-03555-6.

[44] R. Casali, J. Lasave, N. Scientific, and C. A. Ponce, “Ab initio and shell model studies of structural, thermoelastic and vibrational properties of SnO<sub>2</sub> under pressure,” J. Physics. Condensed matter, vol. 25, no. 13, pp.1-11, 2013, doi: 10.1088/0953-8984/25/13/135404.

[45] M. Hijazi, “Sensitive and selective ammonia gas sensor based on molecularly functionalized tin dioxide working at room temperature”, Ph. D. thesis, Université de Lyon, 2017.

[46] S. Steinhauer, “Gas Sensors Based on Copper Oxide Nanomaterials: A Review,” J. Chemosensors, vol. 9, no 3, pp.1-20, 2021, doi: 10.3390/chemosensors9030051.

[47] S. Sagadevan, J. Lett, G. Weldegebrieal, S. Garg, and W. Oh, “Enhanced Photocatalytic Activity of rGO-CuO Nanocomposites for the Degradation of Organic Pollutants,” J. Catalysts, vol.11, no.8, 2021, pp.1-13 doi: 10.3390/catal11081008 021.

- [48] N. Yusoff, "Synthesis of functionalized graphene/copper oxide (CuO) nanocomposites and their catalytic activity / Norazriena binti Yusoff," Ph. D. thesis, University of Malaya, Kuala Lumpur, 2013.
- [49] K. Ungeheuer, K. Marszalek, M. Perzanowski, P. Jelen, and M. Marszalek, "Influence of Cr Ion Implantation on Physical Properties of CuO Thin Films," *Int J. Molecular Science*, vol. 23, no. 9, pp.1-14, 2022, doi: 10.3390/ijms23094541.
- [50] W. Ghann, H. Kang, J. Uddin, F. Chowdhury, SI. Khondaker, M. Moniruzzaman, M. Kabir, and M. Rahman, "Synthesis and characterization of reduced graphene oxide and their application in dye-sensitized solar cells," *J. Chem Engineering*, vol. 3, no. 1, pp. 1–13, 2019, doi: 10.3390/chemengineering3010007.
- [51] G. Oxide, F. Electrodes, M. Nakagawa, A. Ahammad, and T. Islam, "Preparation of reduced Graphene Oxide (rGO) assisted by microwave irradiation and hydrothermal for reduction methods", *J. Materials Science and Engineering*, vol. 434, 2018, pp. 1-9, doi: 10.1088/1757-899X/434/1/012079.
- [52] I. Sengupta, S. Chakraborty, and M. Talukdar, "Thermal reduction of graphene oxide : How temperature influences purity," *J. Material Research*, vol. 33, no. 23, pp. 4113-4121, 2018, doi: 10.1557/jmr.2018.338.
- [53] M. Eluyemi, M. Eleruja, A. Adedeji, B. Olofinjana, O. Fasakin<sup>1</sup>, O. Akinwunmi<sup>1</sup>, O. Ilori, A. Famojuro, S. Ayinde, E. Ajayi, "Synthesis and Characterization of Graphene Oxide and Reduced Graphene Oxide Thin Films Deposited by Spray Pyrolysis Method," *J. Graphene*, vol. 05, no. 03, pp. 143–154, 2016, doi: 10.4236/graphene.2016.53012.

- [54] H. Liu, “Modified Thermal Reduction of Graphene Oxide”, Ph.D. thesis, University of Nottingham, 2014.
- [55] T. Smith, A. Chance, S. Zeng, B. Liu, and L. Sun, “Synthesis, properties, and applications of graphene oxide/reduced graphene oxide and their nanocomposites,” *J. Nano Materials Science*, vol. 1, no. 1, pp. 31-47, 2019, doi: 10.1016/j.nanoms.2019.02.004.
- [56] V. Sharma, Y. Jain, M. Kumari, R. Gupta, S. Sharma, and K. Sachdev, “Synthesis and Characterization of Graphene Oxide (GO) and Reduced Graphene Oxide (rGO) for Gas Sensing Application,” *J. Macromol Symp*, vol. 376, no. 1, pp. 1–5, 2017, doi: 10.1002/masy.201700006.
- [57] I. Sengupta, S. Kumar, S. Pal, and S. Chakraborty, “Characterization of structural transformation of graphene oxide to reduced graphene oxide during thermal annealing,” *J. Materials Research*, vol. 35, pp. 1197–1204, 2020, doi: 10.1557/jmr.2020.55.
- [58] F. Khan, M. Khan, S. Kamal, M. Arshad, S. Ahmad, and S. Nami, “Recent advances in graphene oxide and reduced graphene oxide-based nanocomposites for the photodegradation of dyes,” *J. Materials Chemistry C*, vol. 8, no. 45, pp. 15940–15955, 2020, doi: 10.1039/d0tc03684f.
- [59] M. Shaban, S. Ali, and M. Rabia, “Design and application of nanoporous graphene oxide film for CO<sub>2</sub>, H<sub>2</sub>, and C<sub>2</sub>H<sub>2</sub> gases sensing,” *J. Mater Research Technology*, vol. 8, no. 5, pp. 4510–4520, 2019, doi: 10.1016/j.jmrt.2019.07.064.
- [60] A. Oliveira, G. Braga, C. Tarley, and A. Pereira, “Thermally reduced graphene oxide: synthesis, studies and characterization,” *J. Material Science*, vol. 53, no. 17, pp. 12005–12015, 2018, doi: 10.1007/s10853-018-2473-3.

- [61] H. Imran, K. Hubeatir, K. Aadim, and D. Abd, "Preparation Methods and Classification Study of Nanomaterial: A Review," *J. Physics Conference Series*, vol.1, , pp.1-10, 2021, doi: 10.1088/1742-6596/1818/1/012127.
- [62] D. Bokov, A. Jalil, S. Chupradit, W. Suksatan, M. Ansari, I. Shewael, H. Valiev, and E. Kianfar, "Nanomaterial by Sol-Gel Method: Synthesis and Application," *J. Advances in Materials Science and Engineering*, vol. 2021, pp. 1-21, 2021, doi: 10.1155/2021/5102014.
- [63] M. Parashar, V. Kumar, and S. Ranbir, "Metal oxides nanoparticles via sol – gel method: a review on synthesis, characterization and applications," *J. Materials Science: Materials in Electronics*, vol. 31, pp. 3729–3749, 2020, doi: 10.1007/s10854-020-02994-8.
- [64] E. Modan and A. Plaiasu, "Advantages and Disadvantages of Chemical Methods in the Elaboration of Nanomaterials," *J. Metallurgy and Materials Science*, vol. 43, no. 1, pp. 53–60, 2020, doi: 10.35219/mms.2020.1.08.
- [65] D. Zappa, V. Galstyan, N. Kaur, H. Munasinghe Arachchige, O. Sisman, E. Comini "Metal oxide -based heterostructures for gas sensors: A review," *J. Anal Chim Acta*, vol. 1039, pp. 1-23, 2018, doi: 10.1016/j.aca.2018.09.020.
- [66] M. Sabzi, S. Mousavi Anijdan, M. Shamsodin, M. Farzam, A. Hojjati-Najafabadi, P. Feng and U. Lee "A Review on Sustainable Manufacturing of Ceramic-Based Thin Films by Chemical Vapor Deposition (CVD): Reactions Kinetics and the Deposition Mechanisms," *J. Coatings*, vol. 13, no. 1, pp.1-16, 2023, doi: 10.3390/coatings13010188.

- [67] A. Garzón, “Synthesis of Metal Oxide Nanoparticles for Superconducting Nanocomposites and Other Applications”, Ph. D. thesis, University of Autonomia, 2016.
- [68] S. Ahmadi, N. Asim, M. Alghoul, F. Hammadi, K. Saeedfar, N. Ludin, H. Zaidi, and K. Sopian, “The role of physical techniques on the preparation of photoanodes for dye sensitized solar cells,” *Int J. Photoenergy*, vol. 2014, pp.1-19, 2014, doi:10.1155/2014/198734.
- [69] Y. Gan, A. Jayatissa, Z. Yu, X. Chen, and M. Li, “Hydrothermal Synthesis of Nanomaterials,” *J. Nanometer*, vol. 2020, pp. 1-3, 2020, doi: 10.1155/2020/8917013.
- [70] C. Pohshna, D. Rao Mailapalli, “Modeling the particle size of nanomaterials synthesized in a planetary ball mill”, *J. Open Nano*, vol.14, pp. 1-16, 2023, doi: 10.1016/j.onano.2023.100191.
- [71] M. Sherif El-Eskandarany, A. Al-Hajji, A. Al-Duweesh, N. Ali and F. Al-Ajmi, “Mechanical milling: A superior nanotechnological tool for fabrication of nanocrystalline and nanocomposite materials,” *J. Nanomaterials*, vol. 11, no. 10, 2021, doi: 10.3390/nano11102484.
- [72] T. Yadav, R. Manohar, and D. Singh, “Mechanical Milling: a Top Down Approach for the Synthesis of Nanomaterials and Nanocomposites,” *J. Nanoscience and Nanotechnology*, vol. 2, no. 3, pp. 22–48, 2012, doi: 10.5923/j.nn.20120203.01.
- [73] S. Kumar Sharma, “Handbook of Materials Characterization”, Springer, 2018, doi:10.1007/978-3-319-92955-2



- [74] D. Lundin and K. Sarakinos, "An introduction to thin film processing using high-power impulse magnetron sputtering," *J. Material Research*, vol. 27, no. 5, pp.1-13, 2012, doi: 10.1557/jmr.2012.8.
- [75] M. Ali, W. Hung, and F. Yongqi, "A Review of Focused Ion Beam Sputtering," *Int. J. Precision Engineering Manufacturing*, vol. 11, no. 1, pp. 157–170, 2010, doi: 10.1007/s12541-010-0019-y.
- [76] A. Veerbhadra, S. Ramakrishna, and G. Angadi, "Development of polyvinyl acetate thin films by electrospinning for sensor applications," *J. Appl Nanoscience*, vol.7, pp. 355-361, 2017, doi: 10.1007/s13204-017-0576-9.
- [77] S. Zhang, Z. Jia, T. Liu, and G. Wei, "Electrospinning Nanoparticles-Based Materials," *J. Sensors*, vol.19, no. 3977, pp.1-24, 2019, doi:10.3390/s19183977.
- [78] J. Huotari, J. Lappalainen, J. Puustinen, T. Baurb, C. Alépéc, T. Haapalainen, S. Komulainen, J. Pylvänäinen, and A. Lloyd Spetz, "Pulsed Laser Deposition of Metal Oxide Nanoparticles, Agglomerates, and Nanotrees for Chemical Sensors," *J. Procedia Engineering*, vol. 120, pp. 1158–1161, 2015, doi: 10.1016/j.proeng.2015.08.745.
- [79] H. Jadhav, S. Suryawanshi, M. More, and S. Sinha, "Pulsed laser deposition of tin oxide thin films for field emission studies," *J. Applied Surface Science*, vol.419, pp.764–769,2017,doi:10.1016/j.apsusc.2017.05.020.
- [80] X. Zhou, X. Zhou, and H. Zhang, "Optimizing Laser-Induced Voltage Signal in SnO<sub>2</sub> Thin Films by Changing Oxygen Pressure," *J. Advances in Materials Science and Engineering*, vol. 2022, pp.1-6, pp. 5–9, 2022.

- [81] N. Bintiyusoff, "Synthesis of functionalized graphene / copper oxide (CuO) nanocomposites and their catalytic activity," MSc. thesis, University of Malaya, Kuala 2013.
- [82] S. Sharma, D. Verma, L. Khan, S. Kumar, and S. Khan, Handbook of Materials Characterization. Springer, Gwangju Institute of Science and Technology, Gwangju, Korea, Republic of South Korea, 2018. doi: 10.1007/978-3-319-92955-2.
- [83] A. Munshi, M. Foroughi, and M. Munshi, "Modified Scherrer Equation to Estimate More Accurately Nano-Crystallite Size Using XRD," World J. Nano Science and Engineering, vol. 2, no. 3, pp. 154–160, 2012, doi: 10.4236/wjnse.2012.23020.
- [84] A. Abbas Ramadhan, "Characterization of CuPcTs/PEDOT: PSS, Alq<sub>3</sub> bulk heterojunction blend for sensor application", Ph.D. thesis, University of Baghdad, 2017.
- [85] P. Ebere Eze-Idehen, "The Development of Sensors for the Detection of Hydrocarbons in Oil spills", Ph. D. thesis, University of Manchester, 2021.
- [109] J. Park, "Nanostructured semiconducting metal oxides for use in gas sensors," Ph. D. thesis, University of Wollongong , 2010.
- [86] L. Amber Horsfall, "Modification of n-type and p-type semiconducting metal oxide gas sensors for the purpose of explosive detection", Ph. D. thesis, University College London, 2019.
- [87] H. Hamdi Nayel, "Synthesis, Characterization and Gas Sensor Performance of In<sub>2</sub>O<sub>3</sub> – Ag<sub>x</sub>O nano Composites Prepared by Chemical Bath Deposition", MSc. thesis, University of Anbar, 2016.

- [88] A. Mariana Negrescu, S. Killian Raghu, P. Schmuki, and A. Cimpan, “Metal oxide nanoparticles: synthesis, characterization and Biological Effects,” *J. Functional Biomater*, vol.13, no.4, pp. 1– 47, 2022, doi: 10.3390/jfb13040274.
- [89] Q. Zhao, L. Ma, Q. Zhang, C. Wang, and X. Xu, “SnO<sub>2</sub> -Based Nanomaterials: Synthesis and Application in Lithium-Ion Batteries and Supercapacitors,” *J. Nanomaterials*, vol. 2015, no. 6, p.6, 2015, doi:10.1155/2015/850147.
- [90] H. Song, M. Seo, K. Choi, M. Jo, J. Yoo, and J. Yoon, “High-Performance Copper Oxide Visible-Light Photodetector via Grain-Structure Model,” *J. Scientific Report*, vol. 9, no.1, pp. 1–10, 2019, doi: 10.1038/s41598-019-43667-9.
- [91] Q. Jiang, X. Zhang, and J. You, “SnO<sub>2</sub>: A Wonderful Electron Transport Layer for Perovskite Solar Cells,” *J. Nano Micro Small*, vol. 14, no.31, pp. 1–14, 2018, doi: 10.1002/sml.201801154.
- [92] H. Soonmin, “A Review of Metal Oxide Thin Films in Solar Cell Applications,” *Int. J. Thin Film Science Technology*, vol. 11, no. 1, pp. 37-45, 2022, doi:10.18576/ijtfst/110105.
- [93] A. Zedan, A. Mohamed, and M. El-shall, “Tailoring the reducibility and catalytic activity of CuO nanoparticles for low temperature CO oxidation,” *J. RSC Advances*, vol. 8, no. 35, pp. 19499–19511, 2018, doi: 10.1039/c8ra03623c.
- [94] N. Bellier, P. Baipaywad, N. Ryu, J. Lee, and H. Park, “Recent biomedical advancements in graphene oxide and reduced graphene oxide-

based nanocomposite nanocarriers,” *J. Biomater Research*, vol. 26, no.1, pp. 1–23, 2022, doi: 10.1186/s40824-022-00313-2.

[95] A.Reghu, “Surface Reaction and Diffusion Kinetics in Semiconducting Metal Oxide Film Gas Sensors,” Ph. D. thesis, University of Maine, 2018.

[96] H. Chai, Z. Zheng, K. Liu, J. Xu, K. Wu, Y. Luo, H. Liao, M. Debliquy, and C. Zhang “Stability of Metal Oxide Semiconductor Gas Sensors: A Review,” *IEEE Sens J*, vol. 22, no. 6, pp. 5470–5481, 2022, doi: 10.1109/JSEN.2022.3148264.

[97] D. Zappa, V. Galstyan, N. Kaur, H. Munasinghe Arachchige, O. Sisman, and E. Comini, “Metal oxide -based heterostructures for gas sensors- A review,” *J. Analytica Chimica Acta*, vol. 1039, pp. 1–23, 2018, doi: 10.1016/j.aca.2018.09.020.

[98] A. Dey, “Semiconductor metal oxide gas sensors: A review,” *J. Materials Science and Engineering B*, vol. 229, pp. 206–217, 2018, doi: 10.1016/j.mseb.2017.12.036.

[99] N. Hossain, M. Hosne Mobarak, M. Akter Mimona, M. Aminul Islam, A. Hossain, F. Tuz Zohura, and M. Asaduzzaman Chowdhury “Advances and significances of nanoparticles in semiconductor applications – A review”, *J. Results in Engineering*, vol. 19, pp. 1-18, 2023, doi: 10.1016/j.rineng.2023.101347.

[100] Z. Yunusa, M. Nizar Hamidon, A. Kaiser, and Z. Awang, “Sensors and Transducers Gas Sensors: A Review,” *J. Sensors and Transducers*, vol. 168, no. 4, pp. 61-75, 2014.

- [101] P. Raju, "Review: Semiconductor Materials and Devices for Gas Sensors," *J. Electrochem. Soc.*, vol.169, no. 5, pp. 1-37, 2022, doi: 10.1149/1945-7111/ac6e0a.
- [102] J. Ko, Q. Xu, and Y. Jang, "Emissions and Control of Hydrogen Sulfide at Landfills: A Review," *J. Critical Reviews in Environmental Science and Technology*, vol. 45, no. 19, pp. 2043–2083, 2015, doi: 10.1080/10643389.2015.1010427.
- [103] F. Mazloun, and A. Amini, "Metal oxide- based gas sensors for the detection of exhaled breath markers," *J. Medical Devices Sensors*, vol.4, no.1, pp. 1–11, 2021, doi: 10.1002/mds3.10161.
- [104] L. Zhang, Q. Tan, H. Kou, D. Wu, W. Zhang, and J. Xiong, "Highly Sensitive NH<sub>3</sub> Wireless Sensor Based on Ag-RGO Composite Operated at Room-temperature," *J. Science Report*, vol. 9, no. 1, pp. 1–10, 2019, doi: 10.1038/s41598-019-46213-9.
- [105] Y. Wang, L. Zhang, N. Hu, Y. Wang, Y. Zhang, Z. Zhou, Y. Liu, S. Shen and C. Peng, "Ammonia gas sensors based on chemically reduced graphene oxide sheets self-assembled on Au electrodes," *J. Nano Express*, vol. 9, no.1, pp. 1–12, 2014, doi:10.1186/1556-276X-9-251.
- [106] B. Sakthivel and G. Nammalvar, "Selective ammonia sensor based on copper oxide/reduced graphene oxide nanocomposite," *J. Alloys Compd*, vol. 788, pp. 422–428, 2019, doi: 10.1016/j.jallcom.2019.02.245.
- [107] M. Mathew, P. Shinde, R. Samal, and C. Rout, "A review on mechanisms and recent developments in p-n heterojunctions of 2D materials for gas sensing applications," *J. Material Science*, vol. 56, no. 16, pp. 9575–9604, 2021, doi: 10.1007/s10853-021-05884-4.

- [108] D. Barreca, C. Maccato, and A. Gasparotto, "Metal Oxide Nanosystems as Chemoresistive Gas Sensors for Chemical Warfare Agents: A Focused Review," *J. Advanced Material Interfaces*, vol. 9, pp.1-27, 2022, doi: 10.1002/admi.202102525.
- [109] L. Jin, W. Chen, H. Zhang, G. Xiao, C. Yu, and Q. Zhou, "Characterization of reduced graphene oxide (rGO)-loaded SnO<sub>2</sub> nanocomposite and applications in C<sub>2</sub>H<sub>2</sub> gas detection," *J. Applied Sciences*, vol. 7, no. 9, pp.1-15, 2017, doi: 10.3390/app7010019.
- [110] Z. Yuan, C. Yang, and F. Meng, "Strategies for improving the sensing performance of semiconductor gas sensors for high-performance formaldehyde detection: A review," *J. Chemosensors*, vol. 9, no. 7, pp. 1-25, 2021, doi: 10.3390/chemosensors9070179.
- [111] A. Naik, I. Parkin, and R. Binions, "Gas sensing studies of an n-n hetero-junction array based on SnO<sub>2</sub> and ZnO composites," *J. Chemosensors*, vol.4,no.1,pp.1–17,2016,doi: 10.3390/chemosensors4010003.
- [112] Y. Deng, "Semiconducting Metal Oxides for Gas Sensing," *J. Engineering Reports*, vol. 3, pp. 23–51, 2019, doi: 10.1007/978-981-13-5853-1.
- [113] Z. Yuan, C. Yang, and F. Meng, "Strategies for improving the sensing performance of semiconductor gas sensors for high-performance formaldehyde detection: A review," *J. Chemosensors*, vol. 9, no. 7, pp. 1-25, 2021, doi: 10.3390/chemosensors9070179.
- [114] L. Yin, H. Wang, L. Li, H. Li, D. Chen, and R. Zhang, "Microwave-assisted preparation of hierarchical CuO@ rGO nanostructures and their

enhanced low-temperature H<sub>2</sub>S-sensing performance,” *J. Appl Surf Sci*, vol. 476, pp. 107-114, 2019, doi: 10.1016/j.apsusc.2019.01.019.

[115] F. Anjum, M. Shaban, M. Ismail, S. Gul, E. Bakhsh, M. Ali, U. Sharafat, S. Khan, and M. Khan, “Novel Synthesis of CuO/GO Nanocomposites and Their Photocatalytic Potential in the Degradation of Hazardous Industrial Effluents,” *J. ACS Omega*, vol.8, no. 20, pp.17667–17681, 2023, doi: 10.1021/acsomega.3c00129.

[116] Y. Deng, “Semiconducting Metal Oxides for Gas Sensing,” *J. Engineering Reports*, vol. 3, pp. 23–51, 2019, doi: 10.1007/978-981-13-5853-1.

[117] A. Yasir, Fabrication of Glucose Biosensor Using ZnO Nanostructure Coated By Silver Nanoparticles, MSc. thesis, University of Kerbala, 2022.

[118] A. Naik, I. Parkin, and R. Binions, “Gas sensing studies of an n-n hetero-junction array based on SnO<sub>2</sub> and ZnO composites,” *J. Chemosensors*, vol.4,no.1,pp.1–17,2016,doi: 10.3390/chemosensors4010003.

[119] B. Sakthivel and G. Nammalvar, “Selective ammonia sensor based on copper oxide/reduced graphene oxide nanocomposite,” *J. Alloys Compd*, vol. 788, pp. 422–428, 2019, doi: 10.1016/j.jallcom.2019.02.245.

[120] J. Sultana, S. Paul, A. Karmakar, G. Dalapati, and S. Chattopadhyay, “Optimizing the thermal annealing temperature: technological route for tuning the photo-detecting property of p-CuO thin films grown by chemical bath deposition method,” *J. Materials Science: Materials in Electronics*, vol. 29, no. 2, pp. 12878–12887, 2018, doi: 10.1007/s10854-018-9407-3.

[121] Z. Lu, Z. Ma, P. Song, and Q. Wang, “Facile synthesis of CuO nanoribbons/rGO nanocomposites for high-performance formaldehyde gas

sensor at low temperature,” *J. Materials Science: Materials in Electronics*, vol. 32, no. 14, pp. 19297–19308, 2021, doi: 10.1007/s10854-021-06449-6.

[122] A. Puthran, Y. Kumar, S. Olivera, C. Vidyasagar, “Development of Multipurpose CuO–GO Nanocomposites for Heavy Metals Adsorption and Super Capacitor Applications,” *J. Energy and Environment Focus*, vol. 5, no. 4, pp. 305–315, 2017, doi: 10.1166/eef.2016.1225.

[123] S. Pourbeyram, R. Bayrami, and H. Dadkhah, “Green synthesis and characterization of ultrafine copper oxide reduced graphene oxide (CuO/rGO) nanocomposite,” *J. Colloids Surface A*, vol. 529, pp. 73–79, 2017, doi: 10.1016/j.colsurfa.2017.05.077.

[124] P. Gokuladeepan and A. Karthigeyan, “Effect of annealing temperature on oxygen reduction reaction of reduced graphene oxide incorporated cobalt oxide nanocomposites for fuel cell applications,” *J. Applied Surface Science*, vol. 449, pp. 705–711, 2018, doi: 10.1016/j.apsusc.2017.12.153

[125] K. Phiwdang, S. Suphankij, W. Mekprasart, and W. Pecharapa, “Synthesis of CuO nanoparticles by precipitation method using different precursors,” *J. Energy Procedia*, vol. 34, pp. 740–745, 2013, doi: 10.1016/j.egypro.2013.06.808.

[126] R. Vijayalakshmi, S. Kanchana, J. Santhanalakshmi, “Green synthesis and characterization of copper oxide nanoparticles - reduced graphene oxide nano composites for facile electrochemical oxidation of ponceau 4r and alizarin red dyes in aqueous medium,” *J. Water Environmental Nanotechnology*, vol. 6, no. 3, pp. 241–251, 2021, doi: 10.1016/j.colsurfa.2017.05.077.



- [127] S. Alam, N. Sharma, and L. Kumar, "Synthesis of Graphene Oxide (GO) by Modified Hummers Method and Its Thermal Reduction to Obtain Reduced Graphene Oxide (rGO)," *J. Graphene*, vol. 6, no. 1, pp. 1–18, 2017, doi: 10.4236/graphene.2017.61001.
- [128] J. Kim, J. Eum, J. Kang, O. Kwon, H. Kim, and D. Kim, "Tuning the hierarchical pore structure of graphene oxide through dual thermal activation for high-performance supercapacitor," *J. Scientific Reports*, vol. 11, no. 1, pp. 1–10, 2021, doi: 10.1038/s41598-021-81759-7.
- [129] M. Oleksandr M. Slobodian, P. Lytvyn, A. Nikolenko, V. Naseka, O. Khyzhun, A. V. Vasin, S. Sevostianov and A. Nazarov, "Low-Temperature Reduction of Graphene Oxide: Electrical Conductance and Scanning Kelvin Probe Force Microscopy," *J. Nanoscale Research Lett*, vol.13, no.139, pp.1-11, 2018, doi 10.1186/s11671-018-2536-z.
- [130] M. Eluyemi, M. Eleruja, A. Adedeji, B. Olofinjana, O. Fasakin, O. Akinwunmi, O. Ilori, A. Famojuro, S. Ayinde, E. Ajayi, "Synthesis and Characterization of Graphene Oxide and Reduced Graphene Oxide Thin Films Deposited by Spray Pyrolysis Method," *J. Graphene*, vol. 5, no. 3, pp. 342-344, 2016, doi: 10.4236/graphene.2016.53012.
- [131] S. Archana, K. Yogesh Kumar, S. Olivera, B. Jayanna, H. Muralidhara, A. Ananda, and C. Vidyasagar, "Development of Multipurpose CuO–GO Nanocomposites for Heavy Metals Adsorption and Super Capacitor Applications," *J. Energy and Environment Focus*, vol. 5, no. 4, pp. 305–315, Mar. 2017, doi: 10.1166/eef.2016.1225.

- [132] A. Singh, N. Sharma, M. Arif, and R. Katiyar, "Electrically reduced graphene oxide for photovoltaic application," *J. Materials Research*, vol. 34, pp. 652–660, 2019, doi: 10.1557/jmr.2019.32.
- [133] V. Țucureanu, A. Matei, and A. Avram "FTIR Spectroscopy for Carbon Family Study," *Crit Rev Anal Chem*, vol. 46, no. 6, pp. 502–520, 2016, doi: 10.1080/10408347.2016.1157013.
- [134] K. Qaiser Ali, A. Shaur, T. Ali Khan, Y. Joya, M. Awan, and L. Narayana Suvarapu. "Characterization of Reduced Graphene Oxide Produced through a Modified Hoffman Method." *J. Cogent Chemistry*, vol. 3, no. 1, 2017, doi:10.1080/23312009.2017. 1298980.
- [135] X. Mei, X. Meng, and F. Wu, "Hydrothermal method for the production of reduced graphene oxide GO colloidal solution GO lamellar solid sample for conductivity test," *J. Physica E*, vol. 68, pp. 81–86, 2015, doi: 10.1016/j.physe.2014.12.011.
- [136] S. Archana, K. Yogesh Kumar, S. Olivera, B. Jayanna, H. Muralidhara, A. Ananda, and C. Vidyasagar, "Development of Multipurpose CuO–GO Nanocomposites for Heavy Metals Adsorption and Super Capacitor Applications," *J. Energy and Environment Focus*, vol. 5, pp. 1–11, 2016, doi: 10.1166/eef.2016.1225.
- [137] Z. Jabar and M. Hassouni, "Preparation and Characterization of Copper Oxide Nanoparticles by Precipitation Method for Photonics and Optoelectronics," *Iraqi J. Applied Physics*, vol. 19, no. 3, pp. 37–42, 2023.
- [138] S. Sagadevan, Z. Zaman Chowdhury, M. Rafie Johan, F. Abdul Aziz, E. Marina, A. Hawa and R. Rafique, "A one-step facile route synthesis of copper oxide / reduced graphene oxide nanocomposite for supercapacitor

applications,” *J. Experimental Nanoscience*, vol. 13, no. 1, pp. 302–313, 2018, doi: 10.1080/17458080.2018.1542512.

[139] Y. Zhao, X. Song, Q. Song, and Z. Yin, “A facile route to the synthesis copper oxide / reduced graphene oxide nanocomposites and electrochemical detection of catechol organic pollutant”, *J. Crystl Engineering Communication*, vol.14, pp.6710–6719, 2012, doi:10.1021/acsomega.8b00334.

[140] M. Abood and B. Hasan, “FTIR Analysis and Characterizations of (SnO<sub>2</sub>:Ga<sub>2</sub>O<sub>3</sub>, CeO<sub>2</sub> /Cu<sub>2</sub>S/c-pSi) Heterojunctions Solar Cells,” *Iraqi J. Science*, vol. 64, no. 5, pp. 2282–2296, 2023, doi: 10.24996/ijjs.2023.64.5.16.

[141] A. Fernandez, P. Sakthivel, K. Kumar, and J. Jesudurai, “A New Approach towards Gas Sensing through A.C. Conductivity of Tin Oxide-Copper Oxide Composite,” *Int. J Engineering Science Research and Technology*, vol.3, pp. 324-33, 2014, doi:1039/c2ce25509j.

[142] Y. Wang, L. Zhang, N. Hu, Y. Wang, Y. Zhang, Z. Zhou, Y. Liu, S. Shen and C. Peng, “Ammonia gas sensors based on chemically reduced graphene oxide sheets self-assembled on Au electrodes,” *J. Nano Express*, vol. 9, no. 251, pp. 1–12, 2014, doi: 10.1186/1556-276X-9-251.

[143] M. Brycht, A. Leniart, J. Zavašnik, A. Nosal–Wiercińska, K. Wasiński, P. Półrolniczak, and S. Skrzypek, “Synthesis and characterization of the thermally reduced graphene oxide in argon atmosphere, and its application to construct graphene paste electrode as a naptalam electrochemical sensor,” *J. Anal Chim Acta*, vol.1035, pp.22–31, 2018, doi: 10.1016/j.aca.2018.06.057.

[144] C. Ho and H. Wang, “Characteristics of thermally reduced graphene oxide and applied for dye-sensitized solar cell counter electrode,” *J. Applied SurfaceScience*, vol.357, pp.147–154, 2015, doi:10.1016/j.apsusc.2015.09.016.

- [145] I. Sengupta, S. Chakraborty, M. Talukdar, S. Pal, and S. Chakraborty, “Thermal reduction of graphene oxide: How temperature influences purity,” *J. Material Research*, vol. 33, no. 23, pp. 4113–4122, 2018, doi: 10.1557/jmr.2018.338.
- [146] N. Abass and R. Ulwali, “Preparation and study of the Structural, Morphological and Optical properties of pure Tin Oxide Nanoparticle doped with Cu”, *Baghdad Science J*, vol. 19, no. 3, pp. 660–669, 2022, doi:10.21123/bsj.2022.19.3.0660.
- [147] H. Byeon, K. Haribabu, G. Karadoc, V. Sreenivasan, M. Sivaprakash, S. Richard and J. Sunil, “Evaluation of physiochemical and electrochemical behavior of reduced graphene functionalized copper nanostructure as an effective corrosion inhibitor,” *J. Chemical Society of Ethiopia*, vol. 38, no. 1, pp. 269-280, 2024, doi: 10.4314/bcse. v38i1.20.
- [148] M. Jarvin, S. Inbanathan, D. Rosaline, A. Prabha, S. Martin Dhas, “A study of the structural, morphological, and optical properties of shock treated SnO<sub>2</sub> nanoparticles: removal of Victoria blue dye doped with Cu”, *J. Heliyon*, vol. 8, no. 6, p. e09653, 2022, doi: 10.1016/j.heliyon. 2022.e09653.
- [149] U. Chasanah, W. Trisunaryanti, H. Oktaviano, Triyono, I. Santoso, and D. Fatmawati, “Study of green reductant effects of highly reduced graphene oxide production and their characteristics,” *J. Communications in Science and Technology*, vol. 7, no. 2, pp. 103–111, 2022, doi: 10.21924/cst.7.2.2022.906.
- [150] F. Xiaowei, X. Huai, J. Wang, L. Jing, T. Wang, J. Liu, and H. Geng “Low surface roughness graphene oxide film reduced with aluminum film deposited by magnetron sputtering,” *Nanomaterials*, vol. 11, no. 6, pp.1-13, 2021, doi: 10.3390/nano11061428.

- [151] N. Dahham, “Annealing temperature effect on the Structure, Morphology and Optical properties of Copper Oxide CuO thin Films,” *Tikrit J. Pure Science*, vol.22,no.6, pp.115-124, 2017, doi:10.25130/tjps.v22i6.799.
- [152] R. Cheedarala, E. Park, Y. Bin Park, and H. Park, “Highly wettable CuO: graphene oxide core-shell porous nanocomposites for enhanced critical heat flux,” *J. Physica Status Solidi (A) Applications and Materials Science*, vol. 212, no. 8, pp. 1756–1766, 2015, doi: 10.1002/pssa.201431858.
- [153] M. Norizan, N. Abdullah, N. Abdul Halim, S. Zulaikha, N. Demon and I. Mohamad, “Heterojunctions of rGO/Metal Oxide Nanocomposites as Promising Gas-Sensing Materials-A Review” *J. Nanomaterial*, vol. 12, no. 2278, pp. 103–111, 2022, doi: 10.21924/cst.7.2.2022.906.
- [154] F. Xiaowei, X. Huai, J. Wang, L. Jing, T. Wang, J. Liu, and H. Geng “Low surface roughness graphene oxide film reduced with aluminum film deposited by magnetron sputtering,” *J. Nanomaterials*, vol. 11, no. 6, pp.1-13, 2021, doi: 10.3390/nano11061428.
- [155] J. Meena, N. Kumaraguru, N. Sami veerappa, P. Shin, J. Tatsugi, A. Kumar, and K. Santhakumar, “Copper oxide nanoparticles fabricated by green chemistry using *Tribulus terrestris* seed natural extract-photocatalyst and green electrodes for energy storage device,” *J. Scientific Report*, vol. 13, no. 1, pp. 1-15, 2023, doi: 10.1038/s41598-023-49706-w.
- [156] Z. Lu, Z. Ma, P. Song, and Q. Wang, “Facile synthesis of CuO nanoribbons/rGO nanocomposites for high-performance formaldehyde gas sensor at low temperature,” *J. Materials Science: Materials in Electronics*, vol. 32, no. 14, pp. 19297–19308, Jul. 2021, doi: 10.1007/s10854-021-06449-6.

- [157] Z. Zhang, H. Schniepp, and D. Adamson, "Characterization of graphene oxide: Variations in reported approaches," *J. Carbon*, vol. 154, pp. 510–521, 2019. doi: 10.1016/j.carbon.2019.07.103.
- [158] J. Kim, J. Eum, J. Kang, O. Kwon, H. Kim, and D. Kim, "Tuning the hierarchical pore structure of graphene oxide through dual thermal activation for high-performance supercapacitor," *J. Scientific Report*, vol. 11, no. 1, pp.1-10, 2021, doi: 10.1038/s41598-021-81759-7.
- [159] N. Touka, D. Tabli, and K. Badari, "Effect of annealing temperature on structural and optical properties of copper oxide thin films deposited by sol-gel spin coating method," *J. Optoelectronics and Advanced Materials*, vol. 21, no. 11, pp.698-701, 2019, doi:10.25130/tjps. v22i6.799.
- [160] N. Touka, D. Tabli, and K. Badari, "Effect of annealing temperature on structural and optical properties of copper oxide thin films deposited by sol-gel spin coating method" *J. Procedia Materials Science*, vol. 10, pp. 292-300, 2015, doi: 10.1016/j.mspro.2015.06.053.
- [161] S. Siddique, M. Waseem, T. Naseem, A. Bibi, M. Hafeez, S. Ud Din, S. Haq, and S. Qureshi "Photo-Catalytic and Anti-microbial Activities of rGO/CuO Nanocomposite," *J. Inorganic Organomet Polymer Material*, vol. 31, no. 3, pp. 1359–1372, 2021, doi: 10.1007/s10904-020-01760-x.
- [162] F. Anjum, M. Shaban, M. Ismail, S. Gul, M. Bakhsh, M. Ali Khan, U. Sharafat, S. Bahadar Khan, and M. Khan, "Novel Synthesis of CuO/GO Nanocomposites and Their Photocatalytic Potential in the Degradation of Hazardous Industrial Effluents," *J. ACS Omega*, vol. 8, no. 20, pp. 17667–17681, 2023, doi: 10.1021/acsomega.3c00129.

- [163] Z. Lu, Z. Ma, P. Song, and Q. Wang, "Facile synthesis of CuO nanoribbons/rGO nanocomposites for high-performance formaldehyde gas sensor at low temperature," *J. Materials Science: Materials in Electronics*, vol. 32, no. 14, pp. 19297–19308, Jul. 2021, doi: 10.1007/s10854-021-06449-6.
- [164] Z. Zhang, H. Schniepp, and D. Adamson, "Characterization of graphene oxide: Variations in reported approaches," *J. Carbon*, vol. 154, pp. 510–521, 2019. doi: 10.1016/j.carbon.2019.07.103.
- [165] Z. Ren, Y. Shi, T. Song, and X. Yu, "Flexible low-temperature ammonia gas sensor based on reduced graphene oxide and molybdenum disulfide," *J. Chemosensors*, vol. 9, no. 12, 2021, doi:10.3390/chemosensors9120345.
- [166] S. Saleem, A. Hasan, M. Hasnain, A. Rehman, Z. Hashim, A. Hashim, Z. Ghaffar, S. Abdul, R. Adel Pashameah, E. Alzahrani, and S. Salit, "Enhancement in structural, morphological, and optical properties of copper oxide for optoelectronic device applications", *J. Nanotechnology Reviews*, vol. 11, no. 1, pp. 2827-2838, 2022, doi: 10.1515/ntrev-2022-0473.
- [167] M. Shaker, A. Jaafar, "Study the Effect of Annealing on the, Structural. and Optical Properties of Nano SnO<sub>2</sub> Thin Films Prepared by Spray Pyrolysis Technical," *J. Iraqi Al-Khwarizmi Society*, vol. 4, pp. 57-66, 2020.
- [168] K. Biswas, Y. Mohanta, and A. Mishra, "Wet chemical development of CuO/GO nanocomposites: its augmented antimicrobial, antioxidant, and anticancerous activity," *J. Material Science: Material Medical*, vol. 32, no. 151, 2021, doi:10.1007/s10856-021-06612-9.

- [169] T. Yarb, R. Sami, A. Saleh, and F. Saleh, “Study the effect of annealing on the Structural and Optical properties of Copper oxide films prepared by Sol-Gel Spin Coating” *Tikrit J. Pure Science*, vol. 21, no. 5, pp.148-153, 2023, doi: 10.25130/tjps.v21i5.1041.
- [170] G. Dalapati, H. Sharma, A. Guchhait, N. Chakrabarty, P. Bamola, Q. Liu, G. Saianand, A. Mounik, S. Mukhopadhyay, A. Dey, T. Wong, S. Zhuk, S. Ghosh, S. Chakraborty, C. Mahata, S. Biring, A. Kumar, C. Ribeiro, S. Ramakrishna, A. Chakraborty, S. Krishnamurthy, P. Sonar and M. Sharma., “Tin oxide for optoelectronic, photovoltaic and energy storage devices: A review,” *J. Materials Chemistry A*, vol. 9, no. 31, pp. 16621–16684, 2021. doi: 10.1039/d1ta01291f.
- [171] S. Siddique, M. Waseem, T. Naseem, A. Bibi, M. Hafeez, S. Ud Din, S. Haq, and S. Qureshi “Photo-Catalytic and Anti-microbial Activities of rGO/CuO Nanocomposite,” *J. Inorganic Organomet Polym Material*, vol. 31, no. 3, pp. 1359–1372, 2021, doi: 10.1007/s10904-020-01760-x.
- [172] V. Naganaboina and S. Singh, “CdS based Chemiresistor with Schottky Contact: Toxic Gases Detection with Enhanced Sensitivity and Selectivity at Room Temperature,” *J. Sensors and Actuators B: Chemical*, vol. 357, pp.1-36, 2022, doi: 10.1016/j.snb.2022.131421.
- [173] S. Zhu, H. Sun, X. Liu, J. Zhuang, and L. Zhao, “Room-Temperature NH<sub>3</sub> sensing of graphene oxide film and its enhanced response on the laser-Textured silicon,” *J. Scientific Report*, vol. 7, no. 1, pp. 1-8, 2017, doi: 10.1038/s41598-017-15270-3.
- [174] A. Rivadeneyra, D. Gerardo, F. Romero, V. Toral, S. Vásquez, M. Costa-Angeli, C. Moraila-Martínez, D. Morales, and N. Rodríguez



“Demonstration of bare Laser-reduced Graphene Oxide sensors for Ammonia and Ethanol,” *IEEE Sensors J*, vol. 55, pp. 1-10, 2023, doi: 10.1109/JSEN.2023.3298823.

[175] B. Sakthivel, L. Manjakkal, and G. Nammalvar, “High Performance CuO Nanorectangles-Based Room Temperature Flexible NH<sub>3</sub> Sensor,” *IEEE Sensors J*, vol. 17, no. 20, pp. 6529–6536, 2017, doi: 10.1109/JSEN.2017.2749334.

[176] C. Wang, L. Yin, L. Zhang, D. Xiang, and R. Gao, “Metal oxide gas sensors: Sensitivity and influencing factors,” *J. Sensors*, vol. 10, no. 3, pp. 2088–2106, 2010. doi: 10.3390/s100302088.

[177] B. Sakthivel and G. Nammalvar, “Selective ammonia sensor based on copper oxide/reduced graphene oxide nanocomposite,” *J. Alloys Compound*, vol. 788, pp. 422–428, 2019, doi: 10.1016/j.jallcom.2019.02.245.

[178] Z. Sima, Z. Ma, P. Song, and Q. Wang, “Ultra-low concentration detection of NH<sub>3</sub> using rGO/Cu<sub>2</sub>O nanocomposites at low temperature,” *J. Materials Science: Materials in Electronics*, vol. 32, no.17, pp. 22617-22628, 2021, doi:10.1007/s10854-021-06746-0.

[179] S. Yenorkar, “Full Proceeding Paper ammonia gas (NH<sub>3</sub>) sensing of SnO<sub>2</sub>-CuO mixed oxide thick film at operating temperature”, *National conference on recent Advances in Physical Sciences*, vol.8, no.1, pp. 42-45, 2020.

[180] M. Verma and V. Gupta, “SnO<sub>2</sub>-CuO nanocomposite thin film sensor for fast detection of H<sub>2</sub>S gas,” *J. Experimental Nanoscience*, vol. 8, no. 3, pp. 326–331, 2013, doi: 10.1080/17458080.2012.680930.

- [181] Q. Feng, X. Li, and J. Wang, "Percolation effect of reduced graphene oxide (rGO) on ammonia sensing of rGO-SnO<sub>2</sub> composite based sensor," *J. Sens Actuators B Chem.*, vol.243, pp.1115–1126, 2017, doi: 10.1016/j.snb.2016.12.075.
- [182] Y. Chen, W. Zhang, and Q. Wu, "A highly sensitive room-temperature sensing material for NH<sub>3</sub>: SnO<sub>2</sub>-nanorods coupled by rGO," *J. Sens Actuators B Chem*, vol. 242, pp. 1216–1226, 2017, doi: 10.1016/j.snb.2016.09.096.
- [183] J. Sun, N. Xue, K. Jiang, T. Zhou, and H. Quan, "Cu-doped SnO<sub>2</sub>/rGO nanocomposites for ultrasensitive H<sub>2</sub>S detection under low temperature," *J. Microsystems and Nanoengineering*, vol.9, no.1, pp.1-11, 2022, doi: 10.21203/rs.3.rs-2332849/v1.
- [184] Z. Song, Z. Wei, B. Wang, Z. Luo, S. Xu, W. Zhang, H. Yu, M. Li, Z. Huang, J. Zang, F. Yi, and H. Liu "Sensitive Room-Temperature H<sub>2</sub>S Gas Sensors Employing SnO<sub>2</sub> Quantum Wire/Reduced Graphene Oxide Nanocomposites," *J. Chemistry of Materials*, vol. 28, no. 4, pp. 1205–1212, 2016, doi: 10.1021/acs.chemmater.5b04850.
- [185] J. Sun, N. Xue, K. Jiang, T. Zhou, and H. Quan, "Cu-doped SnO<sub>2</sub>/rGO nanocomposites for ultrasensitive H<sub>2</sub>S detection under low temperature," *J. Microsystems and Nano engineering*, vol.9, no.1, pp.1-11, 2022, doi: 10.21203/rs.3.rs-2332849/v1.
- [186] B. Bhangare, N. S. Ramgir, A. Pathak, K. R. Sinju, A. K. Debnath, S. Jagtap, N. Suzuki, K. Muthe, C. Terashima, D. Aswal, S. Gosavi, and A. Fujishima, "Role of sensitizers in imparting the selective response of SnO<sub>2</sub>/RGO based nanohybrids towards H<sub>2</sub>S, NO<sub>2</sub> and H<sub>2</sub>," *J. Material*

Science Semiconductor Process, vol. 105, pp. 1-23, 2020, doi: 10.1016/j.mssp.2019.104726.

[187] Z. Song, Z. Wei, B. Wang, Z. Luo, S. Xu, W. Zhang, H. Yu, M. Li, Z. Huang, J. Zang, F. Yi, and H. Liu “Sensitive Room-Temperature H<sub>2</sub>S Gas Sensors Employing SnO<sub>2</sub> Quantum Wire/Reduced Graphene Oxide Nanocomposites,” J. Chemistry of Materials, vol. 28, no. 4, pp. 1205–1212, 2016, doi: 10.1021/acs.chemmater.5b04850.

[188] D. Faisal, W. Kalef, E. Salim, and F. Alsultany, “Synthesis of CuO/SnO<sub>2</sub> NPs on quartz substrate for temperature sensors application,” J. Ovonic Research, vol. 18, no. 2, pp. 205–212, 2022, doi: 10.15251/jor.2022.182.205.

[189] P. Leangtanom, A. Wisitsoraat, K. Jaruwongrangsee, N. Chanlek, A. Tuantranont, S. Phanichphant and V. Kruefu, “Highly Sensitive and Selective Sensing of H<sub>2</sub>S Gas Using Precipitation and Impregnation-Made CuO/SnO<sub>2</sub> Thick Films,” J. Nanoscale Research Lett, vol. 16, no. 1, pp.1-11, 2021,doi:10.1186/s11671-021-03530-1.

## الخلاصة

تم تحضير التراكيب النانوية SnO<sub>2</sub>/ CuO- rGO كمستشعر للغاز باستخدام تقنيات مختلفة في هذه الدراسة. حيث تم تحضير التراكيب النانوية rGO, CuO-rGO و CuO بالطريقة الحرارية المائية ثم ترسيبها على ركائز الزجاج باستخدام تقنية الطلاء بالغمس. تم ترسيب الطبقة الثالثة من المركب SnO<sub>2</sub> بواسطة تقنية الترسيب بالليزر النبضي. تمت دراسة الخواص التركيبية والمورفولوجية والحرارية والبصرية للتراكيب المصنعة باستخدام تقنيات XRD، و FTIR، و FESEM، و EDX، و TEM، و BET، و AFM، و TGA، و UV و I-V.

اظهرت نتائج حيود الاشعة السينية (XRD) ان GO تم اختزاله بشكل كامل عند درجة حرارة تحضير ٢٠٠ درجة مئوية وتمت ملاحظة قمم حيود ضعيفة ل rGO في العينات rGO/CuO. ازداد التبلور والحجم البلوري لجميع العينات المحضرة بعد التلدين الى ٤٠٠ درجة مئوية لمدة ساعتين. ظهرت القمم الرئيسية الخاصة ب SnO<sub>2</sub> و rGO, CuO في الغشاء الرقيق ذي الطبقات الثلاثة SnO<sub>2</sub>/CuO-rGO. تم استخدام تحليل ال TGA لتحديد درجات حرارة التلدين ومدى استقرارية العينات المحضرة. حيث اظهرت النتائج ان rGO اكثر استقرارا من GO وان استقرارية التراكيب النانوية CuO-rGO تقل مع زيادة كمية GO في المركب النانوي. اما المركب النانوي CuO كان اكثر استقرارا. اظهرت مطيافية الاشعة تحت الحمراء FTIR لكلا من GO و rGO و CuO و SnO<sub>2</sub> و CuO-rGO العديد من القمم المقابلة ل O-H, C-H, C=C, C=O=C و aromatic, C-C, CO- C-H and Cu-O, Sn-O bonds. وقد لوحظ انخفاض طفيف في شدة القمم في المركب النانوي CuO-rGO.

اوضحت نتائج المجهر الالكتروني الماسح FESEM والنافذ TEM ان اوكسيد الكرافين GO يظهر في شكل طبقات مطوية متداخلة في حين يظهر rGO في شكل يشبه الألواح مع انحناءات والكثير من المسامات في هيئة شقوق. ظهرت عينات CuO في شكل قضبي. اما عينات CuO-rGO فظهرت في شكل قضبي وكروي اعتمادا على كمية GO في المركب النانوي. اما SnO<sub>2</sub> فظهر في شكل كروي مع الكثير من التكتلات. التحليل الطيفي لتشتت الطاقة EDX ل GO و rGO اشار الى ان النسبة الذرية ل O:C في GO قد تناقصت عند الاختزال في ٢٠٠ درجة مئوية كنتيجة لعملية الاختزال وفقدان المجاميع الوظيفية. كشف تحليل EDX لعينات CuO عن وجود النحاس والأكسجين دلالة على تكون اوكسيد النحاس. تحليل EDX للمركب النانوي CuO-rGO بين ان

النحاس والاكسجين والكاربون هي العناصر الاساسية في المركب النانوي وليس هناك شوائب اخرى.

اظهرت نتائج مجهر القوة الذرية AFM ان خشونة الغشاء الرقيق GO المملدن قد قلت بعد الاختزال في حين ان خشونة الغشاء الرقيق CuO المملدن قد ازدادت مع زيادة درجة حرارة التحضير. لقد لوحظت خشونة عالية للاغشية الرقيقة CuO-rGO المملدنة والمحضرة بدرجة ٢٠٠ درجة مئوية مقارنة بتلك المحضرة ب ١٠٠ درجة مئوية. اظهرت نتائج تحليل المساحة السطحية BET ان المساحة السطحية لأكسيد الكرافين قد ازدادت بعد الاختزال في حين ان المساحة السطحية لأكسيد النحاس قد قلت وزاد معدل قطر المسامات. أظهرت عينات CuO-rGO مساحة سطحية متوسطة ذات قطر مسام مرتفع مقارنةً ب CuO. كشف التحليل الطيفي للأشعة المرئية وفوق البنفسجية UV-visible ان جميع العينات لها فجوة طاقة مباشرة حيث كانت فجوة الطاقة للمركب النانوي CuO-rGO اقل اما فجوة الطاقة للمركب النانوي SnO<sub>2</sub>/ CuO-rGO فقد كانت اعلى قليل. كشفت خواص منحنى ال I-V عن اتصال شوتكي لجميع العينات.

اظهرت فحوصات مستشعر الغاز ان اوكسيد النحاس كان الاقل حساسية لغاز الامونيا بينما اوكسيد الكرافين المختزل اظهر حساسية عالية نسبيا في حين ان SnO<sub>2</sub>/rGO كان الاعلى حساسية. ان مستشعرات الغاز الاكثر انتقائية لغاز H<sub>2</sub>S هي CuO و SnO<sub>2</sub>/CuO و SnO<sub>2</sub>/rGO و SnO<sub>2</sub>/CuO-rGO المختزل لكن SnO<sub>2</sub>/rGO هو الاكثر حساسية لغاز H<sub>2</sub>S. ان افضل المستشعرات لكلا الغازين هو مستشعر SnO<sub>2</sub>/ CuO-rGO والتي تم تحسينها بعد اضافة اوكسيد الكرافين المختزل حيث استجابت بسرعة اكبر من العينات الاخرى.



جامعة كربلاء

كلية العلوم

قسم الفيزياء

تحضير تراكيب ( $\text{SnO}_2/\text{CuO} - \text{rGO}$ ) النانوية وتوصيف ادائها لتحسس الغاز

رسالة مقدمة الى

مجلس كلية العلوم – جامعة كربلاء

وهي جزء من استكمال متطلبات نيل درجة الدكتوراه

علوم في الفيزياء

من قبل

انعام عبد حمود

بكالوريوس جامعة كربلاء ٢٠١١

ماجستير جامعة كربلاء ٢٠١٥

اشراف

أ.د. نور جواد رضا

أ.د. خولة جميل طاهر

٢٠٢٤ م/ ايلول

١٤٤٦ هـ / ربيع الاول